Epoxy Adhesives, Correlation between Strain Whitening and Damage Using a Macroscopic Optical Method

by

Luis Fernando Trimiño Rincón

A thesis
presented to the University of Waterloo
in fulfillment of the
thesis requirement for the degree of
Doctor of Philosophy
in
Mechanical Engineering

Waterloo, Ontario, Canada, 2019

Examining Committee Membership

The following served on the Examining Committee for this thesis. The decision of the Examining Committee is by majority vote.

External Examiner	Dr. Franck Lauro Professeur des Universites Laboratoire d'Automatique, de Mécanique et d'Informatique et Humaines University of Valenciennes Hainaut-Cambresis
Supervisor	Dr. Duane S. Cronin, P. Eng. Professor, Department of Mechanical and Mechatronics Engineering Canada Research Chair in Trauma Biomechanics and Injury Prevention Director, Impact Mechanics and Material Characterization Laboratory University of Waterloo
Internal Member	Dr. Michael Worswick, P. Eng. Professor, Department of Mechanical and Mechatronics Engineering Canada Research Chair in Light Weight Materials Under Extreme Deformation: Forming and Impact University of Waterloo
Internal Member	Dr. Hamid Jahed, P. Eng. Professor, Department of Mechanical and Mechatronics Engineering Director, Fatigue and Stress Analysis Laboratory University of Waterloo
Internal-External Member	Dr. Scott Walbridge, P. Eng. Associate Professor, Department of Civil and Environmental Engineering Director, Architectural Engineering Program Supervisor, Metal Structure Assessment and Repair Group University of Waterloo

Author's declaration

This thesis consists of material all of which I authored or co-authored: see Statement of Contributions included in the thesis. This is a true copy of the thesis, including any required final revisions, as accepted by my examiners.

I understand that my thesis may be made electronically available to the public.

Statement of contributions

This thesis contains material that has been co-authored. The following paragraphs state the particular contributions made by me and by other authors were applicable.

Chapter 3 of this thesis consist of a paper that was co-authored by myself and my supervisor Dr. Cronin and published in the Journal of Dynamic Behaviour of Materials. Dr. Cronin choose the topic of the paper while I carried out the tensile testing experiments, collected and analyzed the experimental data. I also implemented the material models and the numerical simulations. The writing was done by me but was assisted by Dr. Cronin for the final edits. Technician Jeff Wemp and Chris Tom help with sample manufacturing and sample testing.

Chapter 4 consist of a paper co-authored by myself and my supervisor Dr. Cronin and published in the Journal of Adhesion and Adhesives. The topic of the paper was selected by me although Dr. Cronin help to define the scope of the experiments. Experiment methodology, data collection and analysis were developed and carried out by myself. Both Dr. Cronin and I contributed to the final version of the text. Data collection was assisted by students Yogesh Nandwani and Eric Hetherington.

Chapters 5 was written in manuscript format and was co-authored between me and my supervisor. Dr. Cronin assisted with data interpretation edits to the final version of the material and suggested the use of the digital microscope for surface observation under load. The experiments were designed, planned and carried out by myself as well as the data collection and analysis. Technicians Jason Benninger, and Neil Griffett assisted with sample manufacturing and machine set up for load-unload respectively.

Chapters 6 was written in manuscript format and was co-authored between me and my supervisor. Dr. Cronin suggested the use of a Lagrangian frame of reference for the analysis of the strain whitening. The experiments were planned and carried out by myself. Data collection and analysis was also my responsibility. The code used for image analysis during strain whitening was solely developed by myself using the Mathematica language.

Abstract

The success of lightweight automotive multi-material assemblies depends on selecting appropriate joining techniques that can provide the expected day-to-day operational strength while delivering occupant protection during crash scenarios and long-term durability performance. Epoxy-based adhesives provide an important joining method to increase structural stiffness and enable the joining of dissimilar materials for multi-material assemblies. However, the design of adhesive joints requires mechanical data to support integration in vehicles and computer aided engineering design. The objective of this research was to address a deficit in the identification and quantification of damage in epoxy adhesive materials under applied loading, which is critical for constitutive models that can be used in the numerical representation of structural epoxy adhesive materials.

Three structural epoxy adhesive formulations: a non-toughened single-part epoxy (EC-2214, 3M); a two-part toughened epoxy (DP-460NS, 3M); and a high toughness single-part epoxy (SA-9850, 3M); were tested to failure under tension and shear loading conditions over a range of strain rates (0.002–100 s^{-1}). The measured mechanical data was implemented in constitutive models using two approaches (cohesive zone model and continuum solid element formulation) and verified using finite element simulations of the experiments. This study provided understanding regarding the mechanical response of structural adhesives to loading and the relationship between shear and tensile strength, differences in non-recoverable mechanical response, and the mode of failure for different adhesive formulations (localization and brittle failure, development of strain whitening and ductile failure). Adhesives strength increased with increases in strain rate for all three materials, and limitations in current modeling approaches such as the use of a von Mises yield surface and assuming coupling of strain rate effects between different modes of loading, were identified. Importantly, strain whitening was observed on the surface of the specimens during testing, and exhibited varying intensity and distribution depending on the strain rate and material type. A paucity of damage data for structural adhesives was identified in the literature. This information is necessary to define or enhance failure criteria in finite element simulations, which in turn can improve the physical representation of adhesive materials in numerical simulations.

A follow-on study investigated the viability of using Vickers microhardness measurements as a forensic technique to quantify damage in structural adhesives. The study used tensile specimens machined from bulk adhesive and tested to failure over a range of strain rates (0.002-100 s^{-1}). Pre-test reference

microhardness measurements were compared to post-test hardness measurements along the gauge length of the test specimens. The changes in microhardness were used to indirectly measure damage in the materials. In general, for toughened epoxies, the damage extended over much of the sample gauge length, while the un-toughened epoxy demonstrated damage localization at the failure location. Increasing strain rate led to an increase in the damage localization for a given material. Out of the three tested materials, the two-part toughened epoxy (DP-460NS) demonstrated the most complex behavior during the straining process including variations in microhardness with strain rate, development of strain whitening with load, and further evolution towards shear banding at high levels of deformation. Although microhardness did provide a reliable method for damage measurement, the procedure was not practical to obtain continuous strain-damage data, as is required for material constitutive models. However, the microhardness data support the premise that strain whitening in the tested specimens was associated with the measured microhardness changes and therefore damage in the toughened epoxies.

A follow-up study using the two-part toughened adhesive (DP-460NS) was conducted to further understand the nature of the strain whitening process and its connection to damage through microscopic observations of the material surface during loading. This study also established damage reference values using traditional techniques (changes in stiffness and strength after load-reload) and determined that the observed changes in color (strain whitening) were linked to changes in the morphology of the surface in the strained material. Microscopic observations identified that the morphological changes caused by increases in tensile loading were due to the development of crack opening, cavitation, growth of plastic zones around cracks, and later the development of shear bands. Although the morphological change (21% change in the amount of pixels that describe the morphology of the free surface) was comparable to damage values calculated using traditional techniques (19% from changes in modulus, and 18% using changes in strength), the implementation suffered from the same shortcomings that affected the use of microhardness. That is, impracticality to obtain continuous damage data over the strain history of the material and limitations resulting from the small area observed in the material using the microscope.

The previous studies led to the development of a macroscopic optical technique to quantify the evolution of damage in real time. The technique used images captured during tensile testing to assess damage through the change in average color on the material surface with strain. The two-part toughened epoxy was used to asses the implementation. The results were compared against damage data from the previous studies using the same material and damage calculated using other reference techniques. The

reference techniques included volumetric strains, changes in modulus of elasticity, and changes in microhardness. Damage measurements from the optical method ranged between 15 and 25% at failure, which agreed (15 to 21%) with the reference techniques (microhardness changes, modulus changes with load-unload and microscopic observations). There was a difference between the damage predicted using changes in volumetric strains (8%) and all other measures of damage. It was hypothesised that the lower value was associated with the volume conserving nature of the shear banding deformation process. In other words, any damage that can occur in parallel with or that can be associated with the shear banding process, was captured by all other techniques (changes in microhardness, changes in modulus of elasticity, microscopic images, change in color) while the volumetric strains fail to capture this contribution to the overall damage in the material. This was due to the lack of detectable changes in volume resulting from the shear banding process. In addition to the numerical agreement between optical damage values with the reference techniques (except for volumetric strains), the implemented optical method can predict the location of the actual fracture zone, quantify the damage level at different locations along the area of analysis, besides providing a continuous strain-damage curve.

Damage measurement using optical measurement of changes in average color constitutes an accurate and robust experimental technique for structural adhesives that offers a new method to identify and quantify damage evolution in polymeric materials exhibiting strain whitening. The proposed technique can provide strain-damage curves, which are much needed information for the implementation of constitutive material models for structural adhesives and other polymeric materials. Although the method is limited to strain whitening materials, the measurement can be implemented for testing in tensile loading at any strain rate as long as a suitable image-capturing device is used.

Acknowledgements

I would like to thank my supervisor, Professor Duane Cronin, for giving me the opportunity to pursue the first steps in building an academic career. This chance not only opened up the door to a better understanding of natural phenomena but also broadened my knowledge in fields that directly affect modern engineering. Such fields include project management and the design of experiments and machinery. I am very grateful for Duane's guidance, his insight and his confidence in my ability to get to term this research project.

The experimental portion of this work required the assistance from the technical staff of the MME department at UW. Many thanks to Andy Barber, Jason Benninger, Karl Janzen, Tom Gavel, and Jeff Wemp. Without them lending me a hand in the use of lab equipment, sample preparation, machining expertise, and photography knowledge, this would have been a more lengthy and tortuous road.

This research would not have been possible without the financial support of the Natural Sciences and Engineering Research Council of Canada our industry partner 3M, and the Initiative for Advanced Manufacturing Innovation and Automotive Partnerships Canada.

Dedication

For my beloved Shannon and Nadia.

Shannon, your support and confidence steadied my course when I was faltering.

Nadia, you may never read these pages but know that every one of your smiles provided a beautiful light to keep me going. Every dream is possible with determination, will and smart work.

Table of Contents

List of Figures

Figures Appendix A

Figures Appendix B

Figures Appendix C

Figures Appendix D

List of Tables

Tables Appendix A

Tables Appendix B

Tables Appendix C

Tables Appendix D

List of Equations

Equations Appendix C

Equations Appendix D

Nomenclature

ΔC	Change in pixel color
ΔT	Change of temperature
ΔV	Change of volume
ε, ε_{xx} or e_{xx}	Strain or strain in a direction xx
$\bar{\varepsilon}$	Average strain
ε_{elas}	Elastic strain
ε_{plas}	Plastic strain
ε_D	Strain threshold for initiation of damage
ε_V	Volumetric strain
$\dot{\varepsilon}$	Strain rate
γ	Shear strain
ρ	Density
σ	Stress
$\pm\sigma$	Standard deviation
σ_e or $\bar{\sigma}$	Effective stress
σ_y	Yield stress
ν	Poisson's ratio
A or A_0	Area
A_D or A_v	Area of voids in a damaged material
$A_{TSC}\tau$	Area traction separation curve in shear
AOI	Area of interest
C^P	Heat capacity at constant pressure
$\bar{C}\ or\ \bar{C}_o$	Average pixel color or initial average pixel color
$\overline{C_t}$	Average pixel color at time t
δ	Displacement
δ_{fail}	Displacement at failure
d	micro indentation diagonal length
D	Damage
$\overline{D}$	Average damage

D_A or D_{Ai}	Damage in a particular area
D_{fz}	Damage at the fracture zone
$D_{\Delta A}$	Damage from area of voids in the fracture plane
$D_{\Delta E}$	Damage from changes in modulus of elasticity
$D_{\Delta MHV}$	Damage from changes in material microhardness
$D_{\Delta\sigma}$	Damage from changes in effective stress
$D_{\Delta Smic}$	Damage from changes in microscopic surfaces
E or E_o	Modulus of elasticity
E_D or $E **$	Modulus of elasticity in a damaged material
F	Force
f_{Ai}	Damage fraction at an area i
G_I	Energy release rate in mode I (Tension)
G_{II}	Energy release rate in mode II (Shear)
H	Hardness of the material post-loading
H_0	Hardness of the material
HV or HVN	Vickers' material microhardness
k	Stress concentration factor
l	Crack length
r	Crack tip radius
R^2 or r^2	Regression coefficient
SNR	Signal to noise ratio
T_{crit}	T-test critical threshold value for statistical decision
T_{obs}	T-test observed value for statistical decision
V or V_0	Volume
V_D or V_v	Volume of voids in a damaged material
V_I	Coefficient of variation (%)
Y	Yield strength
U	Ultimate strength

Chapter 1
Introduction

1.1 Motivation

In an effort to improve energy efficiency and sustainability, manufacturers of such systems have been required to improve fuel efficiency while upholding current safety standards. Current Corporate Average Fuel Efficiency (CAFE) goals for fuel consumption was set at 41 miles per gallon for 2016 and the future 2025 goal is set to the even higher efficiency of 60 MPG for passenger vehicles [1–3]. Occupant protection requirements have been also evolving since their first introduction in 1969 [4]. The current New Car Assessment Program (NCAP) requires a vehicle to comply with minimum ratings for head injury criteria, chest deceleration, femur load among others to determine the crashworthiness and rollover safety of the vehicle [5]. To achieve these goals, designers must not only consider structural and energy absorbing materials but also the joining methods that ultimately determine if the assembly and performance of such a structure is even possible. Typically, optimization design for both weight and safety is best achieved with multi-material structures. However, the use of dissimilar materials can introduce stresses due to mismatches in thermal expansion, while differences in galvanic potentials can lead to corrosion. Traditional mechanical fasteners and welding can only partially address some of these problems, but the use of bonding can at least, reconcile the galvanic differences by acting as a barrier between different materials. At the same time, a bonded union can provide a continuous joint that stiffens the structure and potentially enhances the energy absorption ability of the assembly[6,7]. Besides these basic requirements, current engineering practices also require that other performance aspects of bonded components be evaluated; including fatigue life, performance under load-unload scenarios, exposure to extreme temperature differentials, and lastly performance in crash scenarios where the dynamic deformation response of the structure, that is response under different rates of loading, is of great importance for safety concerns.

Modern engineering design encompasses the extensive use of numerical simulation, which is not only economical but also practical. On the one hand, the use of numerical methods has substantially reduced design cycle times [8] while at the same time reducing the number of resources devoted to testing concepts and prototypes. In order to develop numerical models that can accurately predict the performance of bonded structures, a designer needs two pieces of information: first, a constitutive model that can accurately represent the mechanical response of the adhesive material [9] under diverse load scenarios; second, the mechanical properties and parameters that can be used to implement the

selected constitutive model [10]. Such mechanical properties can encompass stress-strain response under different modes of loading (tension, compression, shear) and at different strain rates, strains to failure, fracture toughness and damage data depending on the complexity of the model.

Although the development of constitutive models is a challenging field, its development cannot proceed without a basic understanding of the mechanical response and damage mechanisms present in adhesive materials nor without experimental measurements. Current literature in adhesive materials is typically focused in three areas. One is the chemical composition and atomic structure and their relation to mechanical response to deformation [11–18] . The second corresponds to measured mechanical properties for adhesive materials, bonded joints and the testing methodology required [18–20]. This body of literature typically covers strength, stress-strain response, and fracture toughness under different loading modes. As of lately, this type of literature also incorporates a wide range of strain rates as opposed to only the quasi-static response [21–23]. The last field considers the numerical representation of adhesive materials [24–26]. Adhesives can be represented using different numerical methods, each one of which varies in complexity [24]. The simplest method available is a contact definition [27]. This implementation ties nodes with a critical stress failure criterion or crack opening displacement approach to predict failure. Although numerically efficient and requiring very little information for implementation, this type of elements are known to be problematic due to numerical instabilities (often termed unzipping). Cohesive elements [28,29], the next level of complexity, were designed to eliminate the shortcomings of contact definitions. Cohesive elements also enhance the accuracy of adhesive representation by including strain rate effects on strength, mixed load, and principles of fracture mechanics to predict element response and failure. Finally, continuum solid elements formulations can also be used to represent adhesive materials. This type of implementation can describe the mechanical response of materials in complex loading scenarios by incorporating all relevant experimentally observed effects in one model [30]. In many cases, the most sophisticated continuum implementations [31] incorporate damage mechanics formulations to predict damage growth, crack initiation and growth, and ultimate failure.

Considering the needs of engineering design, the current implementation of constitutive materials for modeling and the available data in the literature, a survey determined that there is a significant deficit in the practical identification and quantification of damage in epoxy adhesive materials. This survey produced175 results out of which 73 were relevant after filtering non-related topics (e.g. reinforce concrete, bridge decks, etc.). Most of the surveyed literature contained sparse information in regards to

experimental data in a few epoxy materials [32–34] and a large portion of the survey considered either simulation or constitutive models with a damage implementation [35–37]. In some instances, the proposed constitutive models were used to infer the damage in the material from the mechanical response to load. Experimental techniques that address damage detection and measurement are available in the literature nonetheless. Some of these techniques include Ultrasonics [38,39], CT-Scan [40], Laser light scatter [41], Thermal tomography [42], Infrared Imaging [43], repetitive load-unload [44,45], volumetric strains [33,46,47], and electrical changes [48] among others. However, many challenges need to be addressed before implementing these techniques. For example, the existence of rate-dependent effects (visco-elasticity) inherent to polymeric materials [14,49] need to be consider while implementing mechanical testing [50]. Electrical changes can be difficult to measure due to the non-conductive nature of polymeric materials, or the time scale required to capture data for a given methodology (e.g. CT-Scan) could introduce creep effects [40]. More often than not, repetitive testing or the use of out-of-reach, specialized equipment with complex data analysis can be required before continuous damage-deformation data is generated.

1.2 Objective

It is known that certain polymeric materials can exhibit strain whitening during loading, i.e. the material can appear lighter in color compared to the original unloaded material; such a change in appearance is attributed to damage mechanisms such as crazing, crack openings, plastic zones, cavitation in particles and shear banding. The evolution of such features causes light scatter and hence a change in the hue of color in the material surface. The appearance of such features can be considered as damage since the capacity of the material to sustain further increases in load or absorb energy can be compromised. The aim of this thesis is to present an experimental method developed to quantify the strain whitening in the surface of structural adhesive materials so damage is measured in an indirect way. The proposed method is inexpensive and easy to implement, it also closes an experimental gap in the literature for a practical measurement method that provides damage measurements for a structural epoxy adhesive in a continuous fashion. The strain-damage data can be used with constitutive models that include continuum damage mechanics to define failure criteria, or to modify the effective material response under load. The damage data is also useful to model irreversible conditions that affect unloading/reloading paths.

1.3 Outline of thesis

This thesis consists of seven chapters. The first chapter is this introduction and describes the motivations for, and objective of, the thesis. Chapter two provides an overview of the relevant literature and background related to epoxy adhesives, mechanisms of failure in polymers, and damage. Chapters three to six summarize the research carried out to identify the important aspects of damage in structural adhesives and to develop a methodology to measure damage. The contents of each chapter are based in separate articles as shown below:

- Chapter 3. Characterization of the mechanical response in tension and shear for three epoxy adhesives (EC-2214, DP-460NS and SA-9850) at various strain rates (quasi-static to 1000 1/s). The mechanical data was used to identify the capabilities and limitations of current material models used to represent adhesives in numerical simulations.

  Trimiño L, Cronin D. Evaluation of Numerical Methods to Model Structural Adhesive Response and Failure in Tension and Shear Loading, Journal of Dynamic Behavior of Materials, February 2016; 2, 122-137.

- Chapter 4. Changes in microhardness were used as a first step to understand damage in epoxy adhesives subjected to uniaxial tensile loading. The work included assessing three adhesives tested under different strain rates (0.002 to 100 1/s), so the impact of strain rate on damage could be understood.

  Trimiño L, Cronin D. Damage Measurements in Epoxy Structural Adhesives Using Microhardness. International Journal of Adhesion and Adhesives, January 2018; 82, 211-220.

- Chapter 5. In-situ microscopic observations were used to assess surface changes during uniaxial loading using the DP-460NS adhesive. In parallel, measurements of damage were conducted using more traditional detection techniques such as changes in modulus of elasticity. The observed changes on the surface of the material with load were linked to cavitation and shear banding. Additionally, the surface change was quantified using image processing. Image segmentation was applied to identify changes between successive images

and the pixel differences between images were expressed as percentual changes. The surface image percentual change values (~ 21%) were compared with the available measurements of damage (18 and 19% respectively) and found to be in good agreement.

- Chapter 6. Introduction of a new experimental optical technique for the measurement of damage. During tensile loading of toughened epoxy adhesive materials, damage occurs through mechanisms that favor strain whitening (particle debonding, cavitation and/or shear banding). With the strain whitening, the loaded material appears lighter in color when compared to the base material. In this study, the color change on the surface of a tensile sample was measured using image processing techniques and calibrated with the fraction of voids from the fracture zone. This provided a method to indirectly measure damage in the material with changes in strain. Results were compared with damage values calculated using other techniques such as damage from volumetric strains, changes in modulus of elasticity, and changes in microhardness.

The last chapter (Chapter 7), provides conclusions, highlights the contributions of this work, and briefly discusses opportunities for future work.

Chapter 2
Literature review

Epoxy systems are adhesive compounds typically used in structural joints; they can provide the required performance to satisfy the structural demands of the automotive industry [6,51]. This chapter focuses on three main sections: a general description of bonded joints and epoxy adhesives; failure mechanisms in polymeric materials; and lastly a discussion of damage mechanics and a survey of the experimental techniques currently available for the characterization of damage in materials, and their limitations.

2.1 Adhesive systems

2.1.1 Bonded joints

Adhesives can be defined as a chemical compound that is used to bond or join an interface between two surfaces (Figure 2-1). The adherends (that is the material or materials to be joined) can be of a varied nature, i.e., they can be ceramics, metals, polymers, organic materials or a combination of these. Depending on the application, that is the type of adherends, and the expected level of load and service conditions, certain types of adhesives may be more suitable than others. Bonded joints can be loaded in many ways, but the main result is that the material selected to provide the bonding has to transfer tension, compression, shear loads, or a combination of these without failure, so the integrity of the assembly is maintained.

Bonded systems have two potential failure mechanisms while transferring loads: one is the rupture of the adhesive material itself by the failure of its own cohesive strength[52][1].The other is debonding at the interface between the adhesive and one of the bonded surfaces due to the failure of the adhesive forces [52][2].

2.1.2 Principles of adhesion

According to Kinloch [53] adsorption is the most widely applicable theory to explain adhesion. Adsorption proposes that provided enough molecular contact exists at the interface, materials will adhere because of interatomic and intermolecular forces. The most common forces are van der Waals

[1] Cohesive strength: Strength of the chemical and physical forces that hold together a mass of material
[2] Adhesive strength: Strength of the interface between the adhesive material and the bonded surface of the adherend material

forces where hydrogen bonds can play a significant role in establishing adhesion. In addition, ionic and covalent bonds can also play a role, however the development of these links are highly dependent upon the chemistry of the interface. There are other three main mechanisms of adhesion [53,54]: diffusion theory, electronic theory, and mechanical interlocking. Diffusion states that the adhesion of materials is due to mutual diffusion of molecules across the interface. Electronic theory postulates that there is some electron transfer on contact to balance Fermi levels, which will result in the formation of an attractive electrical charge in the interface. Lastly, mechanical interlocking proposes that the topography and roughness of the materials provide the irregularities that lock the materials and provides the major source of intrinsic adhesion.

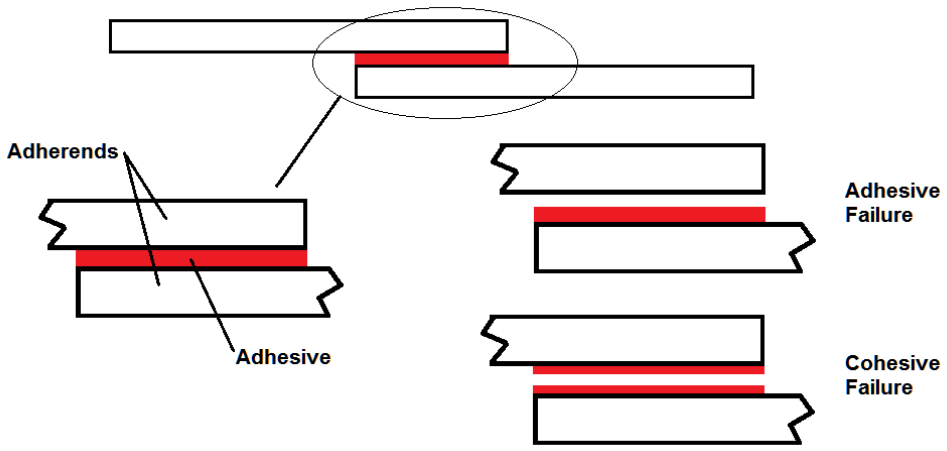

Figure 2-1: Schematic of a bonded joint and its modes of failure

2.1.3 Epoxy Adhesives

Although, in general, adhesives can have a wide range of compositions (vegetable or animal emulsions, casein glues, albumen glues) [55], epoxy adhesives are considered as synthetic polymers due to their chemical composition and structure [55]. Polymers can be classified into three groups [56]:

- **Thermoplastics:** Linear or branched polymers which melt upon heating. They can be further categorized into crystalline or amorphous depending on the presence or lack of a definite structure, or regular pattern, in their molecular composition.

- **Thermosets:** Rigid, highly cross-linked polymers which degrade rather than melt when exposed to heat.
- **Rubbers:** Lightly cross-linked polymers which have elastomeric properties.

Epoxy adhesives have been used to replace more traditional methods of joining like bolts, rivets, welding, crimping, brazing, and soldering [53]. Due to their versatility, structural adhesives can be used to provide optimized joints which are lighter and stronger than the traditional counterparts [53], provide joints with uniform stress distributions, and the ability to join almost any material [57]. In addition, epoxy adhesives can be chemically tailored to perform in adverse environments (oxygen, UV, water, salt-spray, temperature and radiation) [54,58] where other methods of joining may not be appropriate or desired. For structural applications, the best-known and mostly widely used adhesives are epoxides [54]. Epoxy adhesive systems typically contain several chemical elements that interact by complex chemical reactions, but the essential component is the epoxy resin around which the adhesive was formulated [59]. Resins can be made synthetically by reacting two or more chemicals; these chemical compounds can be aromatic or aliphatic, cyclic or acyclic [60]. The most common type of functional building block in epoxy resins is the oxirane group [61], a three-membered group containing oxygen (Figure 2-2). Oxirane, or Ethylene oxide, is an organic compound with the formula C_2H_4O, which describes a cyclic ether. Cyclic ethers consist of an alkane[3] with an oxygen atom bonded to the two carbon atoms of the alkane forming a ring. Because of its unique molecular structure, ethylene oxide readily participates in addition reactions[62,63]; e.g., opening its ring and thus easily polymerizing. Polymerization and cross-linking is not only important for determining the cohesive strength of an adhesive [54], it can also play a role in the capability to incorporate other resin types that can improve the mechanical performance of the bulk material (Service temperature, shear/peel strength, toughness) [60].

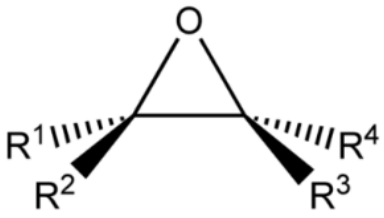

Figure 2-2: Oxirane group [64]

[3]Alkane: Chemical compound compose solely of hydrogen and carbon atoms with single bonds in an open chain.

Another common type of resin is Phenoxy, which in terms is based on Bisphenol-A (Figure 2-3). This last compound is used in many cases either as standalone or as a secondary component in the resin [65]. Because of the number of secondary hydroxyls present in the compound, it promotes higher cross-link densities, and higher chemical resistance [66] and superior adhesion with a variety of substrates can be achieved by the increased potential for hydrogen bonding compared to Oxirane-based resins.

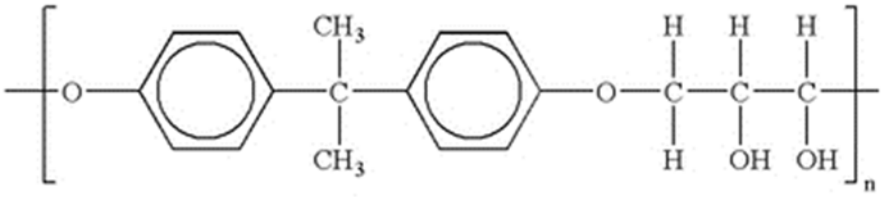

Figure 2-3: Phenoxy, chemical composition [67]

Typically, epoxy adhesives can be obtained in two forms: a two-part formulation, which are combined at the time of application, or a one-part heat-cured paste. Two-part adhesives are often manufactured from Bisphenol-A with the addition of a curing agent [59]. The appropriate selection of a curing agent can satisfy specific requirements for an epoxy system such as curing temperature, strength, chemical resistance, etc. [65,66]. Also, these compounds can be formulated so the curing process can proceed at room temperature, making them quite simple for field use. On the other hand, one-part heat curing epoxy adhesives have higher crosslink densities and better surface wetting capabilities; this results in better adhesive and cohesive strength and better environmental resistance. In addition, heat-cured one-part epoxies are much more consistent from the standpoint of final cured properties (e.g. modulus of elasticity and/or mechanical strength) [68] than room temperature two-part epoxies. In two-part epoxies, variations in mixing ratios can affect the final properties. Although epoxy properties may be varied, there are a few characteristics common to all epoxy adhesives:

- Upon cure, some shrinkage of the bond takes place, a phenomenon common to all polymerizing systems. The amount of shrinkage can result in residual stresses in the bond [69].
- Epoxy-based adhesives display good adhesion to a wide variety of materials, such as wood, ceramics, metals, and plastics [20,70].
- In service conditions that can require functionality under different environments, including exposure to water or solvents, the formulation can be tailored for these conditions. For example,

Petrova [71] reported that when an aluminum powder was used as a filler in epoxy adhesives, the water uptake by cured films was lower than that of the unfilled adhesive.

An epoxy system can be further modified to change its physical properties by the addition of solvents to reduce the viscosity; fillers and reinforcements such as glass fiber, alumina, silica sand, clay or metal powders to change properties such as heat and electrical resistance, strength and/or change adhesion to specific substrates and materials [72]. One addition that is relevant for impact related events are plasticizers. This addition generally results in a minor reduction in strength but with a significant increase in the fracture toughness of the adhesive, which improves the impact resistance, flexibility, and energy absorption in joints. Typically, butadiene (rubber) or other polymers are included as microscopic particles that provide a toughening mechanism [73]. In this case, the toughening mechanism is provided by the softer phase, which arrests crack propagation and therefore increases the fracture toughness of the material [74,75]. A transmission electron microscopy (TEM) micrograph of such a compound is illustrated in Figure 2-4. The reason for the phase separation in the figure is that most polymers are immiscible in one another. Although Figure 2-4 illustrates a highly ordered composite material, it must be noted that the actual appearance of a toughened epoxy can be very irregular and is influenced not only by the amount of toughening phase, but also by the curing temperature as demonstrated by Pillai [76] (Figure 2-5).

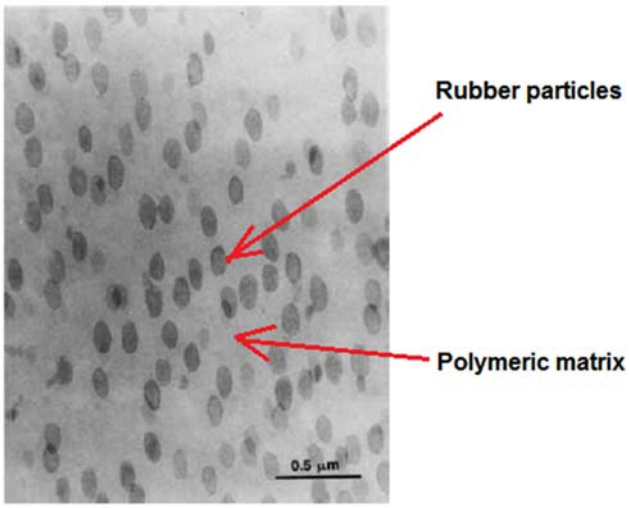

Figure 2-4: TEM micrograph of epoxy with rubber toughening adapted from [73]

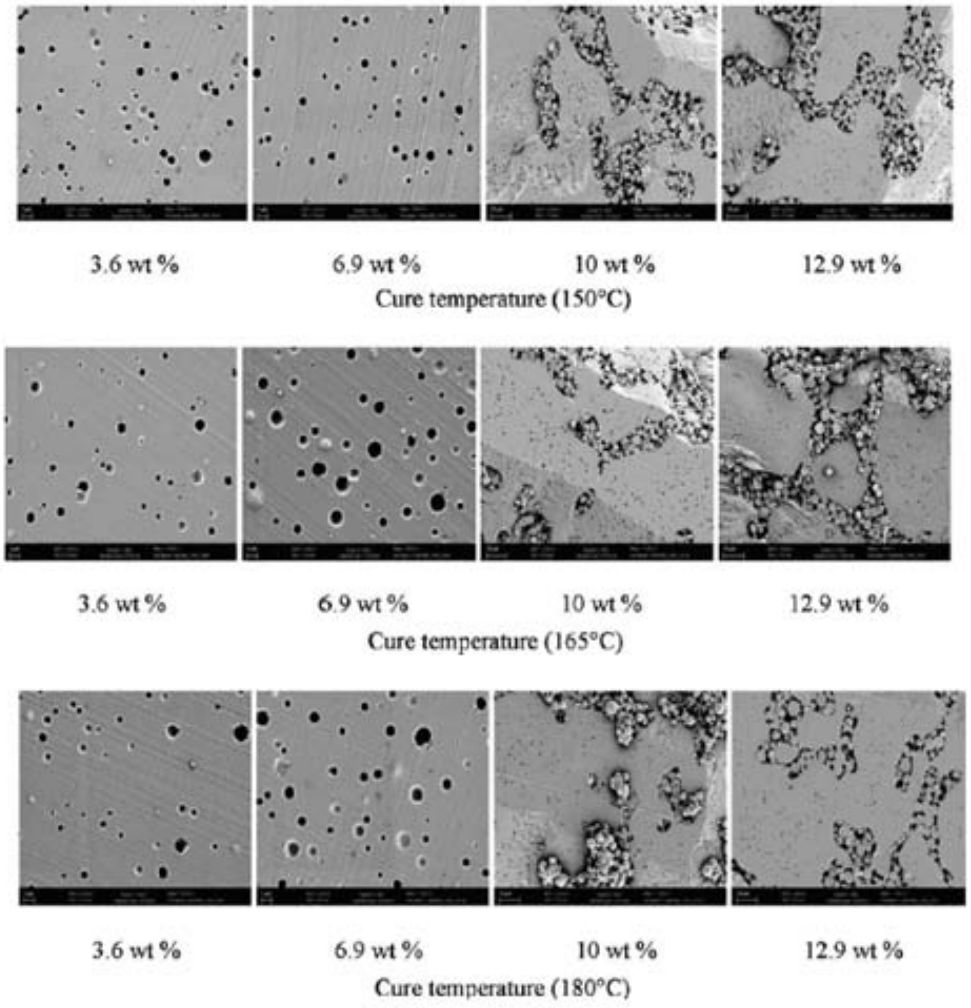

Figure 2-5: SEM pictures describing the effects of curing and blend ratio in the morphology of a toughened epoxy. Reprinted with permission from [76]. Copyright 2012 American Chemical Society

2.2 Polymer response to load

Polymers exhibit a wide range of mechanical properties depending upon their structure and the testing conditions. Polymers, as many other engineering materials, demonstrate elastic behavior for small deformations, and in some cases viscoelastic response, but this response is highly dependent on the microstructure and chemical composition of the polymeric material [77]. In polymers with semi-crystalline structure, that is polymers with some degree of regularity between the chains that form their structure; deformation takes place essentially through the bending and stretching of aligned polymer

backbone bonds, which requires high forces [78–80]. In the case of some isotropic polymers; the molecules can be coiled, randomly oriented and locked in the structure so elastic deformations induce bond rotations which require lower forces [78]. Polymers exhibit a distinctive mechanical behavior in the way they respond to an applied stress or strain depending upon the rate or time period of loading [56,81]. Elastic materials obey Hooke's law and have the capacity for storing energy, whereas a viscous material, such as liquids, tend to obey Newton's law where the stress is proportional to strain-rate and independent of strain [56]. In general, the behavior of many polymers can be thought of as being somewhere between that of elastic solids and viscous liquids (i.e. viscoelastic) [82]. It must be noted that the term viscoelastic is also used to denote materials whose mechanical properties are dependent upon their past deformation history which is also applicable to polymers.

2.2.1 Load-deformation response

The load response in polymers can be as varied as their chemical composition [83] as is shown in Figure 2-6. Polymers can have a linear-elastic response for small deformations, e.g PMMA (Polymethyl methacrylate); they could have viscous effects that are reflected as dampening and are a consequence of internal friction between deforming chains which is noticed as local peaks in the load curve as it is shown for an epoxy (Bisphenol-A type) and for PA (Nylon 6,6). The plastic behavior could be perfectly plastic or highly non-linear with either hardening (epoxy) or softening (PVC) or even both.

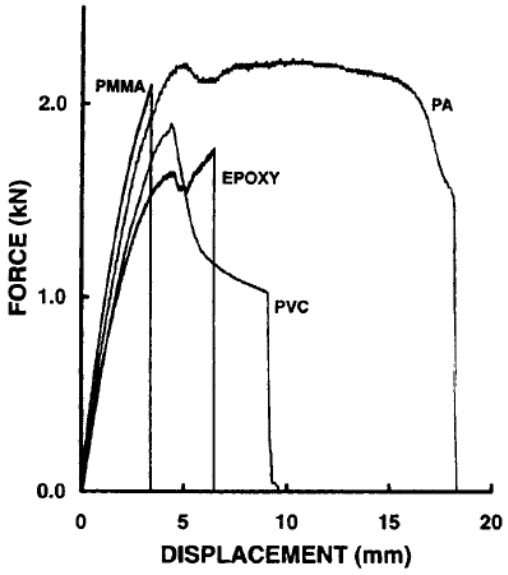

Figure 2-6: Force-displacement response for different polymers [83]

Epoxies typically demonstrate linear elastic behavior with limited ductility and small strains to failure [21,84]. However, incorporation of other elements in the formulation (plasticizers, toughening particles) can significantly modify the response [15,84–86] by enhancing the strain to failure, fracture toughness, and energy absorption but at the price of reducing the strength to failure.

2.2.2 Strain rate effects

Generally, materials are tested at quasi-static loading conditions (e.g. 0.01 1/s strain rate), where the rates of change in the loads and inertia effects are negligible; however, scenarios of interest for the use of adhesives (i.e. crashworthiness of bonded structures) are better described by including dynamic conditions. Under dynamic conditions both the loading rate and inertial effects can affect the measured behavior of a material or structure [87]. Strain rate effect is a phenomenon that has been extensively researched in different polymeric materials (PMMA, PC, PVC, Epoxy adhesives) [79,88]. The phenomenological behavior observed in different polymeric material testing [9,22,88–90] is similar to that of metals, in that the strain rate effect can be identified as an increase in strength and decrease in the strain to failure. For polymers in particular, changes in modulus of elasticity can also be observed as a consequence of type of loading (i.e. tension or compression) and strain rate effects [22]. Figure 2-7 illustrates some of these effects for Nylon 101, it is noticeable that the strength of the material is higher as the strain rate of the test is increased for both tension and compression loading.

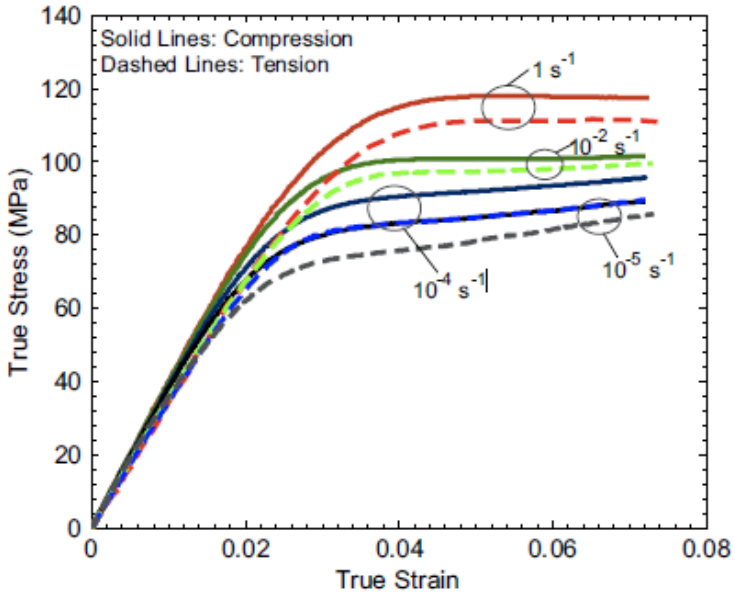

Figure 2-7: Strain rate effects on Nylon 101 [22]

A variety of constitutive models, derived from work in metallic materials, can be used to describe the flow stress of polymeric materials loaded at different strain rates [89]. One compelling fact for the use of this type of models, is that they are ready available in many commercial codes for numerical simulation; also they require limited amount of experimental data for implementation when compared to viscoelastic models based on combinations of springs and dashpots, e.g. Maxwell model,Kelvin model, or Prony series [77,82]. When the strength of the material is proportional to the logarithm of the strain rate one of such models from metals that seem suitable to predict strain rate behavior in epoxy polymers is the Cowper-Symonds (C-S) model [91]. Although this equation is broadly used due to its practicality, it is important to mention that sometimes the C-S equation is not able to predict material behavior over a broad range of strain rates. To circumvent this limitation, authors have propose to use coefficient changes [92]. Also, in certain instances this model is not appropriate since it cannot capture viscoplastic effects that could be noticeable in certain polymeric materials (bi-component epoxy adhesive[89]). As is well explained by Morin [90], "The evolution of the stress for a given plastic strain as a function of strain rate is a highly non-linear phenomenon and classical models (e.g. C-S) only give parallel behavior laws". Goglio [89] proposed the use of Poly-linear fittings to circumvent these challenges.

2.2.3 Mechanisms of failure in polymers

In terms of deformation and failure, very distinct phenomena can be observed in polymers, depending on chemical composition and structure [93]. The first mechanism of failure is a brittle fracture (Figure 2-8, top left), which occurs at temperatures below the glass transition temperature ($\leq 0.8\ T_g$) or high strain rates. Glass Transition Temperature (Tg) is the point at which a material alters state. Below this temperature materials are relatively hard and inflexible, and above it they are soft and flexible [54]. During a brittle failure, the elongation is small (strains to failure in the range of 0.5% to 2% [94]), and catastrophic failure by fracture occurs very suddenly without any large-scale plastic deformation, although it is generally thought that brittle failure is initiated by localized shear yielding or crazing [93]. Both shear banding (also known as shear yielding) (Figure 2-8, lower left) and crazing (Figure 2-8, top right) occur by localization of strains [95,96].

Shear banding is a process that can lead to plastic deformation; it takes place at constant volume and leads to a permanent change in specimen shape and can occur in either tension or compression [95,97,98]. Shear bands will form if a material exhibits strain softening, most polymers have a tendency to form shear bands, but it is stronger in some more than in others, and this is observed by a difference

in the geometry of the formed bands [79]. One author suggests that the rate of strain softening and the strain-rate sensitivity of the flow stress can be related to characteristics of the bands [79] such as their width and length. The shear band mechanism generates viscoelastic and plastic deformations that can increase the toughness of the material [99].

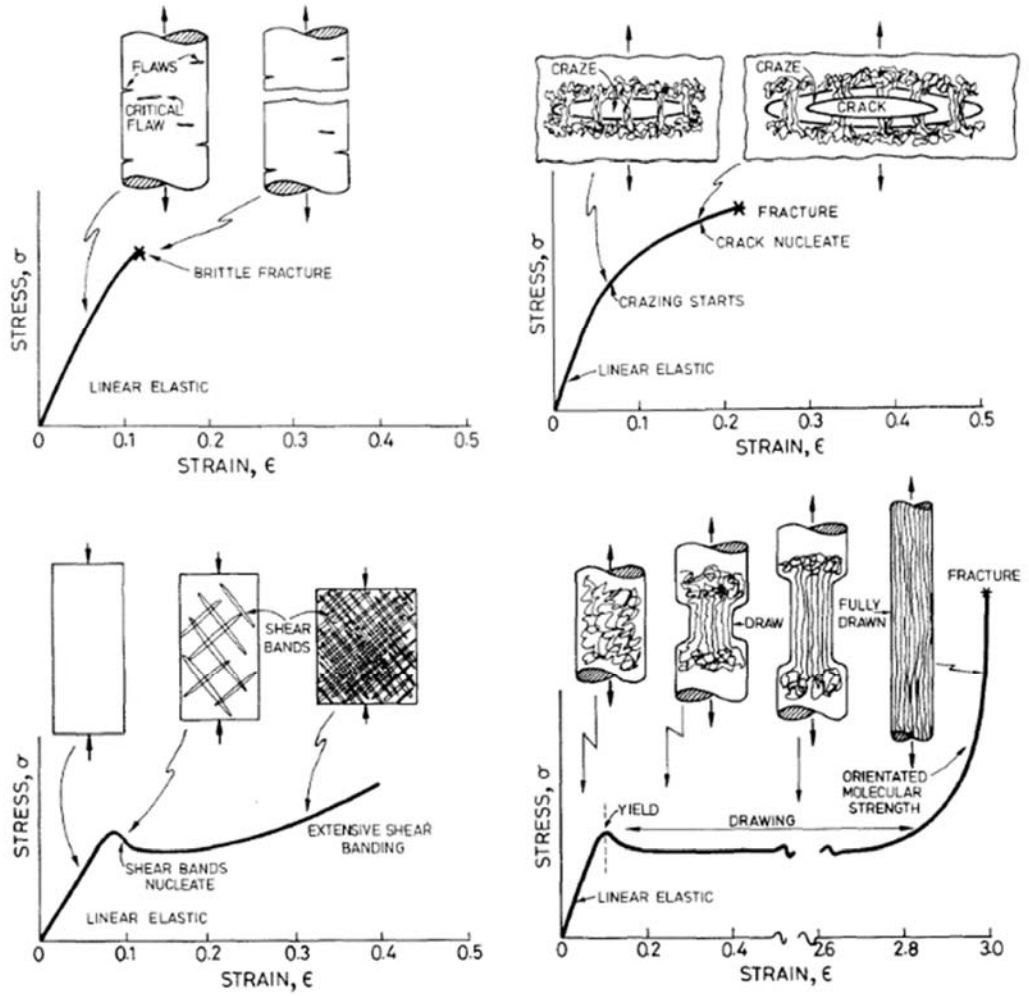

Figure 2-8: Failure mode mechanisms in polymers [93]. Adapted by permission from Springer 1998

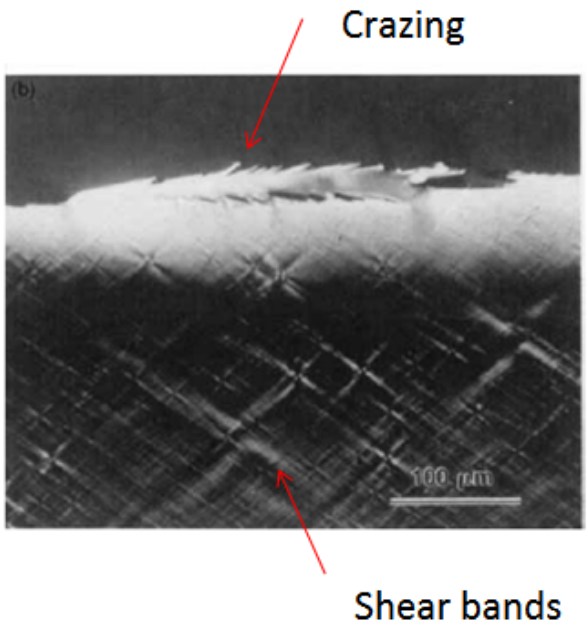

Figure 2-9: Crazing and shear bands in epoxy adapted from [73]

Crazing can be considered as micro-cracks bridged by fibrils (crazes) [100], and their formation is accompanied by an increase in specimen volume. Crazing is favored in polymers with a high level of molecular mobility or systems with low crosslink density [96,99]. Craze development has been reported in materials such as polystyrene, high impact polystyrene, methylmetacrylate and polycarbonate. For crazes to develop, there must exist a hydrostatic tensile state of stress that favors void nucleation and crack opening, compressive states of stress do not develop crazes[101]. Crazes usually initiate and grow oriented perpendicular to the maximum principal stress, and they preferentially nucleate at points of stress concentration such as notches, rough surfaces [46], or defects inside the volume of the material. This has lead to the use of rubber particles to toughen polymeric materials by crazing[16,102,103]. Also, for crazes to form, the tensile strain needs to exceed a critical value[77,101]. Multiple crazes can lead to general yielding and act as a toughening mechanism in polymers. Crazing can be observed at the macro scale by a whitening of the material surface [46,104,105]. Although crazing is a significant damage mechanism in toughened thermoplastics [41], it is a controversial topic in epoxy materials. While some authors acknowledge the possibility of crazing in epoxies [106]; others [107] dispute the presence of this mechanism. To further complicate the subject, craze-like damage in toughened epoxies has been reported in the literature [108].

Craze-like damage, is described as load carring fibrils or tendons that arrest crack growth initiated from scattered cavitation in the core-shell particles (Butadiene particles surrounded by a hard shell material) used to modify an epoxy matrix [108]. Cavitation in this context (damage in materials), can be understood as the creation and propagation of voids inside a solid due to a high hydrostatic, or tri-axial, tensile stress [109]. Particle cavitation can also manifest as strain whitening [110]. In this case, the cracks and voids created by the cavitation at a particle are responsible for reflecting light and can explain the changes towards a whitened color.

Both shear bands, crazing and craze-like mechanisms (caviation) are examples of strain inhomogeneity that can form inside polymeric materials. Since neither one of these mechanisms involve relaxation inwards of the sides of the specimen (necking) they can develop in thin sections and can form distinct regions entirely inside the specimen, provided that the shear or normal displacements are small [79]. Shear banding and crazing can be considered as competing mechanisms [111], but they can develop in parallel as shown in Figure 2-9 [73] for a core-shell rubber modified epoxy. Crazing can also act as a precursor to shear banding [112]. Which one dominates depends on chemistry, load conditions (i.e., state of stress and strain rate), as well as the composition of the material. As an example of this, Berger [113,114] has reported that highly entangled polymers (entanglement density > 11.0×10^{25} strands /m^3) deform primarily by shear banding while less heavily cross-linked polymers (entanglement density < 4.0×10^{25} strands /m^3) prefer crazing.

For completeness, one last mechanism to discuss is drawing (Figure 2-8, lower right). In a ductile regime, polymers can show yield stress followed by a constant drawing or shearing plateau. Both the yield stress and drawing stress depend on temperature, strain rate, and hydrostatic pressure. Drawing can be seen as a process of chain lengthening and disentanglement resulting from tensile loading. It has been noticed by Liu and Piggot that the shear strength when measured using a punching test, is approximately the same as the yield strength in tension[83], and therefore suggests that in shear most polymers (LDPE, HDPE,UHPE, PP, PA, PVC, PMMA, PC and Epoxy) can ultimately fail in tension by a process of chain disentanglement. Broadly speaking each failure mechanism has a typical range of polymer composition, temperature, state of stress and strain and of strain rate in which is dominant.

Consideration needs to be given to the role that strain rate effects can play in the development of damage mechanisms in polymers. Although most literature is concerned with the measurement of mechanical properties (e.g. strength to failure, fracture toughness) and their variation with strain rate [9,22,88–90]

or variation with chemical formulation [75,115,116]; scarce information can be found in regards to variations in the modes in failure that can be triggered by changes in the rate of loading. Wu et al. [117] reported that in polybutylene terephthalate (PBT) polycarbonate (PC) blends, the key toughening mechanism under quasi-static loading (interfacial debonding of particles and cavitation) was disabled during impact loading. In this particular case, the constrain of the PBT matrix promoted brittle failure of the PC. In the case of epoxy systems modified with iron particles, Kytopolous [118] had shown that actual velocity and direction of crack propagation can be correlated to highly localized energy dissipative processes at the crack-front as well as to local inertial molecular mass effects.

2.2.4 Observation of mechanisms of failure in polymers

It is essential to be able to identify and understand fracture and failure in materials [81,99,119,120]. Elucidating damage mechanisms not only provides insight into the conditions that trigger failure under a specific mode of loading [81,119,120]; such knowledge can also lead to the selection of materials that are better suited to a particular application, or determine the requirements that need to be fulfilled in the development of a new material. The main tools available for this type of analysis are the use of optical microscopy [121], Scanning Electron Microscopy (SEM) [122] and Transmission Electron Microscopy (TEM) [123]. Each technique has its own advantages as well as limitations, although many challenges arise with the last two when studying polymeric materials.

SEM can be problematic due to sample preparation requirements [122]. Artifacts may be created during the specimen preparation. Damage can be introduced due to polishing preparation and, metallic coatings may not be capable of following all the deformations in the polymer. Lastly, there is the possibility that the interaction between the scanning electron beam and the observed material, may affect the nature of the sample by either eroding the material or changing bonds due to the interplay of the electrons (e.g., promotion of crosslinking).

TEM also presents particular challenges due to the nature of the required sample [123]. In this case, the surface for observation must be microtomed (10-400 nm in thickness), possibly requiring chemical staining to allow phase contrast and in some cases also require cryogenic cooling to inhibit reactivity of the sample during irradiation.

Although the role of optical microscopy has been displaced by the advent of SEM and TEM [124], optical microscopy is mostly ready available, and several different methods of observation (polarization, differential interference contrast, fluorescence, etc.) make it a powerful tool for the

analysis of polymeric surfaces. Also, optical microscopes can be more suitable to implement in situ observations of materials under load. Although optical microscopy can be limited to a narrow depth of field, the use of newer digital optical microscopes can circumvent this problem by capturing images that are fully focused in the field of view, but also provide 3D mapping and measurements of surface roughness without the interaction of a contact tool or electron beam with the specimen.

2.3 Numerical representation of adhesive materials

In order to describe the mechanical response of bonded joints using numerical methods, different options are currently available to describe adhesive materials [125,126]. Depending on the degree of accuracy desired, and available computational resources for a solution, different representations are available. These representations include, in increasing order of complexity, the use of tied contact surfaces, cohesive elements and lastly continuum formulations.

2.3.1 Tied contact definition

A tied contact [127–129], or Tie-Break element, can be best described as a spring joining two nodes, where each node belongs to a different body. The Tie-Break constrains how the bodies move relative to each other, and the mechanical response of the Tie-Break can be implemented in several different ways depending on the capabilities of the software. Typically, failure is defined as a function of normal or shear components or a combination of both [130]. In the case of adhesives, the Tie-Break is ideal to simulate debonding between two joined surfaces using very few computational resources. Although the Tie-Break provides benefits, mostly corresponding to ease of implementation and low computational demands, sometimes the physical response and behavior of the joint is not completely captured [131,132]. One good scenario to describe this is crack propagation. During crack propagation the first element in the crack front carries a significant portion of the load, once it fails that load is immediately passed on to the next element causing a sudden load increase that can immediately overload the element. This behavior will continue from one element to the next causing what is termed “numerical unzipping”. Depending on the code implementation this behavior can be addressed using a critical opening. Only when the displacement between nodes reaches a critical value the element is deleted preventing sudden changes in load. This type of element also lacks the inclusion of strain-rate effects since the defined strength value is independent of the strain rate that can be experienced by the element during the actual simulation.

2.3.2 Cohesive elements

Cohesive elements have emerged as a more sophisticated implementation to overcome the limitations of the Tie-Break. This type of element can be described as a number of springs joining two surfaces [130]; three springs are included, one normal and two in the shear directions. Cohesive elements are implemented by defining an element between the joined surfaces and then assigning a material model to it [28,29,132–134]. The material definition typically requires properties that are dependent on the fracture behavior of the material. Specifically, the fracture toughness or energy release rate is required, but also a curve that defines traction in relation to displacement or separation [134]. The use of a cohesive element permits designers to link the energy absorbed during deformation with the volume of the material, which is directly linked with fracture mechanics principles. Also, using a traction-displacement curve links the displacements with the initiation of damage in the material. Newer implementations can incorporate strain rate effects [132] and in certain cases try to emulate the irreversible effects of damage [135]. Damage can be introduced by enforcing loading and unloading paths that come from or point to the origin of the traction-separation curve [130]. This implementation of damage, although practical, can miss viscoelastic effects and non-linear behavior in the unloading response of an epoxy adhesive**.**

2.3.3 Continuum formulations

Solid elements paired with constitutive models are the more sophisticated solution to the numerical representation of materials when compared to the contacts or cohesive implementation. Their mathematical formulations incorporate concepts from continuum mechanics that allows them to capture many more nuances of a material response to load. This numerical representation of materials can describe linear-elastic-plastic behavior, viscoelasticity, and viscoelastic-plastic behavior. In addition, the implementation can include different options that allow them to capture asymmetric yield behaviors (i.e. dependence with type of loading) [30], but also represent anisotropy, viscoelasticity [136], strain rate effects [137] and failure. More advanced constitutive models [138–140] incorporate concepts from damage mechanics [141] or void nucleation and propagation [142,143] to modify the mechanical response of the material with load. Damage mechanics principles can also be used to trigger damage growth and failure [144,145] as well as allowing the description of unloading and reloading behavior [47,146–150].

2.4 Damage

2.4.1 Concepts in damage mechanics

Engineering materials subject to mechanical loading undergo microstructure changes. At some point, these changes can impair the mechanical response, and it can be said that the material is "damaged" [141]. Damage can be viewed as a progressive physical process on two different scales that ultimately ends when the material breaks. At the micro-scale level, damage is concerned with stresses at interfaces and defects that lead to the breaking of bonds within polymers. At the next scale (~ 1 mm for polymers), damage is considered in terms of micro-voids and micro-cracks and describes the coalescing and growing of defects within a representative volume element (RVE) to ultimately initiate a crack. Once a detectable crack is formed, the material response can be described using fracture mechanics. As explained by Lemaitre [141]: the RVE must be small enough to avoid smoothing of high gradients, but large enough to represent an average of the micro processes. A more concise definition by the same author [44] states that a "representative" volume is the smallest volume on which a density may represent a field of discontinuous properties. The same work also defines the linear size of representative volume elements for different materials (Table 2-1).

Material	Linear size RVE
Metals	0.05to 0.5 mm
Polymers	0.1 to 1.0 mm
Wood	1.0 to 10.0 mm
Concrete	1.0 to 100.0 mm

Table 2-1: Representative volume element (RVE) linear size [44]

Damage (D) can then be interpreted as the creation of discontinuities within the material by the breaking of atomic bonds and/or the enlargements of cavities. These processes can be approximately quantified in two ways [141]: the area of all the flaws that intersect with a plane (Equation 2-1), or the volume of micro voids inside an RVE of the material (Equation 2-2).

$$D = \frac{A_D}{A}$$

Equation 2-1: Damage definition in terms of area

$$D = \frac{V_D}{V}$$

Equation 2-2: Damage definition in terms of volume

It follows from the previous definitions that damage is a scalar variable, and is bounded by 0 and 1, where D=0 is an undamaged material, and D=1, a fully broken material in two parts. In fact, failure generally occurs for D<1 through an instability process [141]. When the material is loaded, there is a point at which the applied stress in the material will induce rupture of the atom bonds, and this corresponds to some critical value of damage, at which crack initiation starts. When the damage is initiated, the micro-voids and cracks already present in the material must start to grow and coalesce. This point not only corresponds with some level of stress in the material but also must correspond with some level of strain; below this strain threshold (ε_D) there is no damage (Equation 2-3).

$$\varepsilon < \varepsilon_D \rightarrow D = 0$$

Equation 2-3: Strain threshold for damage initiation

Our understanding of loads in materials comes from the general concept of stress, which is the force divided by the nominal area in which the load is applied (Equation 2-4).

$$\sigma = \frac{F}{A}$$

Equation 2-4: Definition of stress

In this concept it is assumed that the material is a continuum with no flaws, correspondingly, we can include the damaged area in the surface by defining the effective stress (σ_e) as:

$$\sigma_e = \frac{F}{A - A_D}$$

Equation 2-5: Definition of effective stress

Replacing Equation 2-1 into Equation 2-5, the effective stress can be redefined in terms of damage [141] as:

$$\sigma_e = \frac{F}{A(1 - \frac{A_D}{A})} = \frac{\sigma}{1 - D}$$

Equation 2-6: Definition of effective stress in terms of damage

In polymers, the damage occurs when the bonds between chains are broken [141], which can be caused by the relative movement of the chains due to translations or rotations. In both cases, as damage is increased, the elastic properties are directly influenced by the damage. Since the number of bonds has decreased, changes in the modulus of elasticity could be measured. Then using the definition of effective stress and Young's law, we can define the elasticity modulus of the damaged material, E_D, as:

$$E_D = \frac{\sigma_e}{\varepsilon} = E(1 - D)$$

Equation 2-7: Damage in the elasticity modulus

The previous expression could be derived through the strain equivalence principle[141]: any strain constitutive equation for a damaged material may be derived in the same way as for the undamaged material except that the usual stress is replaced by the effective stress.

Since the areas of resistance decrease, damage also influences plastic strains. Therefore the plastic modulus can be defined in the same manner. It must be noticed that damage can start before strains reach the plastic region.

2.4.2 Measurement of damage in materials

Measurement of damage in materials can be separated into two distinct areas: first, direct observation of the affected surface or volume and second, indirect measurements from the mechanical response of the material [44,141].

Direct observation of damage consists of defining the surface density of micro-cracks and cavities in a plane by visual inspection with the use of micrographs. The inspection can be done manually or with the aid of image analysis tools such as segmentation [151]. However, this type of measurement can be inaccurate due to the irregular shapes contained in the image and can lead to artifacts and errors in area measurement [124,152]. Furthermore, sample preparation may affect the observed area. Current advances in X-ray tomography techniques allow for direct measurements in the actual volume of the material [40] without the need for sample destruction. Unfortunately, this type of equipment is expensive, not necessarily available, and may require long duration of exposure during scanning which

can heat the sample and alter the microstructure. Also, the scanning of low absorbent polymeric materials is challenging due to the low attenuation in the X-rays necessary to construct the image, which can affect the final image quality [40].

Indirect methods take advantage of measuring some physical quantity that is directly affected by damage in the material. In this case, the techniques can be destructive or non-destructive. Among these techniques, the following are the most relevant:

- Measuring changes in modulus of elasticity [44]. This technique is the "gold standard" for measuring damage and has been used to test a variety of materials: concrete [153], metals[154,155], polymers[45] and composites [156,157]. However, it requires extensive testing to obtain statistically relevant data over the expected range of strain.
- Measuring changes in properties that depend on the density of the material, for example:
    - Changes in resistivity [44]
    - Changes in wave speed propagation (acoustic techniques) [44,153,158]
- Measuring changes in physical properties of the material, such as:
    - Changes in microhardness [44,96,159]
    - Changes in material transparency to infrared radiation [42,43,160], or light transmission. Schirrer et al. [41] used laser light transmission to identify damage in polymethyl methacrylate (PMMA). However, the technique is limited to translucent materials and can only be applied to a small area in the material at a time.
- Measuring the dilation of the RVE using the strain field [46,161,162]. This method was initially developed by video measuring strains in the material but the application of more modern techniques that can define the entire strain field in the material surface, such as digital image correlation [163], virtual fields method [164] or Sigma-epsilon-epsilon-dot method [165], can improve the accuracy of the results. Although damage measurements with DIC can be of high quality (comparable to direct CT-scan measurements) and useful to test at different rates of strain[166], the implementation relies on the results of the image correlation. The accuracy of the image correlation, and therefore the measured strains, can be impacted by a number of factors such as the applied speckle pattern [167,168], image resolution, optical distortions and out of plane motions [169,170]; as well as intrinsic systemic errors such as high order interpolations [171]. Additionally, DIC analysis can be limited by decorrelation at large

deformations (e>20%) [172,173] or from temporal under-sampling of a rapidly evolving phenomena [174].

- Surface pictographic analysis of materials has also been used to conduct measurements of damage taking advantage of the crazing phenomena, Luo [175,176] demonstrated a procedure in which the morphological changes in translucent PMMA (presence of micro-cracks in the material surface) were successfully quantified to determine damage, but the measurement requires an elaborate microscope setup and highly specialized computer subroutines were necessary for identification and measurement in the images.

2.4.3 Implementation of damage in numerical models

Damage is implemented in the constitutive representations of materials in different manners. Cohesive element implementations try to emulate the irreversible effects of damage [135] by enforcing loading and unloading paths that come from or point to the origin of the traction-separation curve [130]. However, damage data can be used to drive improvements in this approach. In constitutive materials coupled with solid elements, the simplest implementations use damage data to modify the material response. This is typically accomplished by implementing the strain equivalence principle. The principle is used to modify the modulus of elasticity of the material (Equation 2-7) or the stress response (Equation 2-6) if necessary. For example, SAMP-1 [30] uses this methodology to implement damage response in the constitutive equations to describe material changes during unload. Other models (Gurson RC-DC [142], Huang [139]) rely on complex formulations in which the damage rate is described by a mathematical function dependent on parameters such as critical strain to initiate damage, the current state of stress, initial amount of voids and other parameters that can be used to mathematically describe damage evolution with load. The calculated damage is then used to modify the stiffness tensor or the stress tensor as required by the load state or by specified conditions that trigger the use of damage in the implementation.

Chapter 3

Mechanical Response and Constitutive models to Model Bulk Adhesive Response in Tension and Shear Loading

This chapter is based on the following published paper:

Trimiño L, Cronin D. Evaluation of Numerical Methods to Model Structural Adhesive Response and Failure in Tension and Shear Loading, Journal of Dynamic Behavior of Materials, March 2016, Volume 2, Issue 1, pp 122-137. (DOI: 10.1007/s40870-016-0045-7)

3.1 Overview/Abstract

Improved energy efficiency in transportation systems can be achieved with multi-material lightweight structures; however, joining often requires the use of adhesive bonding and design efforts are challenged by the paucity of data required to represent adhesives in numerical models. The data for three epoxy structural adhesives tested in tension and shear over a range of strain rates (0.001 to 1000 1/s) is reported. The range of experimentation addresses normal operation and extreme conditions (crash scenarios) for vehicles. The data was implemented with cohesive and solid elements, and the models were assessed on their ability to reproduce adhesive material response.

Good agreement was achieved using both approaches. In average the coefficients of determination (r^2) between measured experimental response and simulations were 0.81 for tension and 0.59 for shear, with 2% difference in the prediction of stress at failure. The cohesive formulation was computationally efficient and reproduced rate effects, but was limited in representing the response of the non-toughened epoxy. The solid element formulation required longer simulation times but yielded similar accuracy for tension (2% difference in stress to failure and r^2 values of 0.98, on average). However, the shear response accuracy (r^2=0.53) was reduced by coupling between shear and tension strain rate effects.

Numerical simulation of structural adhesives requires constitutive models capable of incorporating uncoupled deformation rate effects on strength. The results of this study indicate that a cohesive model can provide adequate representation of an adhesive joint for tensile and shear loading across a range of deformation rates.

3.2 Introduction and background

Increasing requirements for improved energy efficiency in transportation systems have led to the introduction of lightweight materials and multi-material structures. These structures have been enabled by the use of adhesives for joining. Traditional joining methods such as fasteners or welding restrict the use of dissimilar materials and/or thin gage components that are key to producing light weight structures[177,178].The adoption of adhesive joining not only reduces the overall weight of the structure; but also provides joints that are continuous and therefore stronger with reduced stress concentrations [51]. Although joining with structural adhesives is currently in use by some automobile manufacturers[178,179] and bonded structures have been tested under operational conditions[180–184]; a major obstacle to incorporating adhesive joints in designs is the lack of appropriate data to characterize and represent adhesive joints in numerical models and simulations to support Computer Aided Engineering (CAE) [89]. Incorporation of adhesive joints in numerical models can be undertaken with relatively simple implementations using tied nodes between the adherends and a critical stress criterion, to the more comprehensive, cohesive element and solid element constitutive models. These representations vary in complexity and the amount of data required for implementation, with corresponding requirements for mechanical testing. The required properties can range from simple strength values to full traction-separation curves, and the incorporation of deformation rate effects. Typically, strain-stress curves for tension, compression, and shear at different strain rates; values for fracture toughness in Modes I and II, traction-separation behavior, damage response and strain to failure are required. Mechanical properties in adhesives are generally measured using bonded joints subjected to uniaxial tension, or peal [185] or by using thin lap shear tests [186].

Measuring the mechanical properties of adhesives can be undertaken using many different methods; a search of the ASTM standards [187] for the mechanical testing of adhesives identified 517 documents pertaining to testing, out of which 94 are different active standards. These standards include 15 different test protocols for adhesion, 24 for tension; 8 for compression; and 15 different tests for shear. Generally, these tests require the preparation of a bonded specimen and subsequent testing in order to measure the desired mechanical property. Unfortunately, many of the configurations produce results that are influenced by the adherend material stiffness, strength, and joint geometries [188] resulting in stress concentrations and complex modes of loading [189] affecting the measured properties [190]. The variability in measured results can be observed in published data for adhesive testing using lap-shear and T-peel test [191,192].

Untoughened epoxy adhesives typically exhibit relatively high strength at failure (≥70 MPa), low strain to failure (≤0.1) [21] and low fracture toughness (~0.4 J m^{-2}) [28,73,83,193–195]. Toughened epoxy formulations incorporate a second toughening phase, typically butadiene or another polymer (EPM, ABS, polyolefins) [73,196,197], and demonstrate increased ductility (≥0.1 mm/mm at failure) and fracture toughness (≥ 1.5 J m^{-2}). This type of adhesive is ideal for applications where the bonded joints are required to maintain integrity under high deformation, which is generally the case in crashworthiness scenarios for transportation systems. Crashworthiness and other load case scenarios result in a range of deformation rates, and under such conditions, it is vital to consider strain rates effects in the constitutive model. In particular for adhesives, the literature reports changes in the mechanical response; typically increase in the stress to failure and decrease in the strain to failure [17,22,47,184,198–200], and in some cases changes in modulus of elasticity. Conflicting information is reported for fracture toughness. In some instances, increases with strain rate have been reported [201,202] while others have found that there are no noticeable changes [195], and still, others report decreases with increasing strain rate [203–205]. Many different constitutive models can be used for modeling adhesives, ranging from simple elastic models, metal plasticity models, and viscoelastic models [24,27,125]. Failure is often incorporated using a critical stress or fracture toughness criterion. Three common numerical implementations include: directly tied nodes with a critical stress failure criterion or crack opening displacement approach to predict failure, cohesive element formulations incorporating traction separation curves and material toughness, and solid continuum element formulations. Simple implementations involving tied nodes, although numerically efficient and requiring very little information for implementation, are known to be problematic due to numerical instabilities (often termed unzipping). Although the incorporation of a damage criterion can mitigate this issue, deformation rate effects are generally not considered in this approach. Further, this approach can misrepresent the joint stiffness, which is determined from the adherend materials and not from the adhesive itself. In recent years [29,132], advances in cohesive element formulations have incorporated traction-displacement curves to provide a better description of the material response to load and fracture mechanics concepts to predict failure. Cohesive elements allow for progressive failure in ductile adhesive materials, avoiding the numerical instabilities that are generally observed with tied nodes. In addition to incorporating Mode I (pure tension), Mode II (pure shear) and mixed-mode response, recent cohesive formulations [132,206] include strain rate effects and are numerically efficient. Discretization using solid continuum elements and an appropriate constitutive model is considered to be the most accurate representation of an adhesive joint if the finite element size is sufficiently small. This approach

can require a large number of elements, making it computationally expensive. Constitutive models for use with solid elements include: elastic with failure, metal plasticity models, plasticity models with strain rate effects, viscoelasticity and continuum damage models. In general, these models require a relatively large of material properties and data to accurately represent the adhesive joint. Limitations include a lack of accounting for rate effects, material asymmetry and prediction of failure. For example, an elastic model with failure can predict the elastic response of the material but fails to describe the damage in the material. Metal plasticity models can incorporate strain rate effects and damage but often rely on von Mises or other yield criteria applicable to metals to link the tensile response to the compression or shear response, which can be inaccurate for many polymeric materials. Although traditional viscoelastic models account for deformation rate effects, most do not incorporate a description of material damage and failure. Some constitutive models, such as the Semi-Analytical Model for Polymers (SAMP-1) [30] have been developed specifically for polymers, incorporating tension, shear, and compression behavior separately, along with deformation rate effects.

Modeling of structural adhesives is widely discussed in the literature [24,27,125,126,207,208]. Simple representations starting with the use of beam elements to represent the substrate coupled with iso-parametric elements to represent the adhesive was successfully implemented by Wu [209] to generate the stress distribution of different type of joints. Van Hoof [210] used tied nodes between surfaces to represent adhesive joints in the analysis of delamination in composite materials. These simplified methods can be useful to get insight into general behavior in joints under load and in some cases to provide stress distributions, but prediction capabilities are limited due to the limited information that these models require (i.e., stresses to failure). For example, behaviors that depend on the true stiffness in the joint can be biased since the stiffness of a simple tied contact is generally assumed in the implementation [130] and is arbitrarily independent of the true stiffness of the adhesive itself. In contrast, highly sophisticated user defined materials have been used successfully to describe bulk material behavior under linear elastic conditions, strain softening or strain hardening effects, and to predict the effects of strain rate dependency or the effects of damage in the unloading phase [14,126,211]. Although these models can be highly accurate, they require the use of element formulations with refined meshes that are computationally expensive; calculation times can be prohibitive and impractical, e.g., analysis of a complete vehicle [182]. Cohesive elements have been used successfully to accurately describe joint load response and predict the crack propagation of bonded joints in Mode I load conditions [212–214] and in mixed mode loading scenarios [28]. Even though limitations in regards to rate dependencies have been partially addressed [29,132,201,206], other

limitations in cohesive formulations, as identified by Needleman [215] include size effects and the dependence of material parameters on deformation rate. Success in modeling structural adhesives is not only limited to the reproduction of experimental coupons; but also at the structural level [7,182,216,217] under quasi-static and impact loads with good agreement for predicted loads, deformation patterns and modes of failure between simulations and experiments. The techniques have also been used in the analysis of complex joints such as the interface between welds and adhesive materials in hybrid joints [218]. Regardless of the numerical implementation used for the analysis of a bonded joint or a bonded structure, the analysis using numerical methods is not possible without mechanical properties that can describe the adhesive material response. The minimal requirements being the uniaxial tension response or/and pure shear data.

In this study, the mechanical properties of three structural epoxy adhesives (DP-460NS, SA-9850 and EC-2114, 3M Limited, Canada) were measured. The testing was undertaken using bulk material at different strain rates under tension (0.0001 to 1000 1/s) and using thick adherend lap shear samples (0.005 to 50 1/s) to measure the shear properties. This study aims to provide much required mechanical data and an understanding of available numerical implementations for modeling structural adhesive response and failure that can be used in the analysis of bonded structures.

3.3 Methods

3.3.1 Materials

Three commercial structural adhesives were investigated, a traditional non-toughened epoxy, and two toughened epoxies. The non-toughened material was a single part epoxy (EC-2214, 3M Limited Canada) [191,219] with a small percentage of a synthetic elastomer (1 to 5% per weight). The material was cured for an hour at 120 °C. This adhesive was designed to bond metals and high temperature plastics. The second adhesive was a two-part structural epoxy base in a phenolic resin and modified with acrylonitrile butadiene (CTNB) for enhanced strength (7 to 13% per weight) (DP-460NS, 3M Limited, Canada) [192,220]. The manufacturer data sheet shows that best performance is obtained with a curing cycle of 2 hours at 70°C. The last material (SA-9850, 3M Limited Canada) [221] was described by the manufacturer as one part impact resistant adhesive formulated for bonding contaminated or unprepared steel and aluminum materials. From the data sheet, a curing cycle of 1 hour at 170°C was selected. The materials considered, permit to compare a typical epoxy adhesive (EC-2214), an adhesive

with enhanced toughness (DP-460NS) and one that was specifically designed for impact resistance (SA-9850).

3.3.2 Tensile testing

Specimens were extracted from cast adhesive sheets 3 mm in thickness by machining. The coupon geometry has been used previously for high deformation rate tensile testing [222] and was used for the current study so that the same sample geometry could be used over a wide range of deformation rates and maximized the number of samples that could be machined from the cast material [223]. This specimen geometry has been compared to the ASTM type V sample and has provided similar results for metals [222,224]. To ensure that this geometry would not introduce artifacts, results of coupon tensile testing at low strain rates were compared with the ASTM type V geometry [223] for the uniaxial testing of polymers. It was found that the critical values (stiffness, yield strength, strain to failure) were in good agreement for both test geometries.

Materials were tested at quasi-static strain rates (0.001 to 0.7 1/s) using a hydraulic test frame (Instron, Model 1331) in conjunction with a dynamic extensometer (Instron, Model 2620-601) and a load cell (Strain Sert, model FL25U-2DG). At the intermediate strain rates (10 to 100 1/s), a hydraulic frame equipped with a quartz piezoelectric load cell (Kistler model 9321B) and charge amplifier (Kistler type 5010B) was used to measure force. Digital Image Correlation (DIC) [163] was used to measure specimen deformation (VIC-2D [225]) with images captured using a high speed camera (Photron Fastcam SA-4) and LED light source (AADYN Technologies, Jab Bullet model). At high strain rates, 1000 1/s or higher, a Tensile Split Hopkinson Pressure Bar was used (Figure 3-1). All testing was conducted at room temperature.

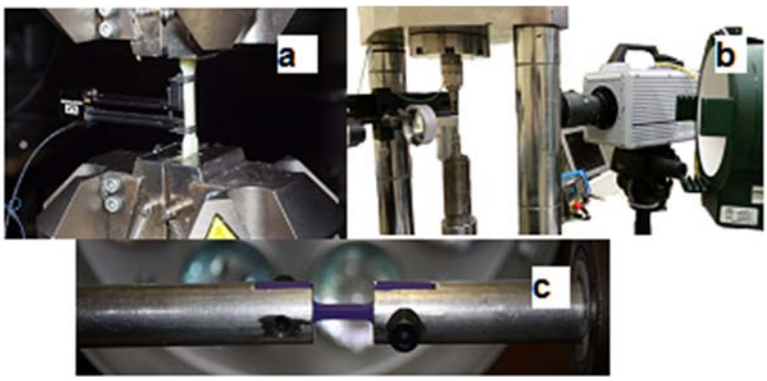

Figure 3-1: Experimental set-up (a) Quasi-Static, (b) intermediate range and (c) high strain rate

3.3.3 Shear testing

The adhesive shear properties were measured using thick lap shear specimens (TLS), based on the ASTM D5656 standard [226]. The samples were constructed by bonding two 3 mm thick steel substrates (SAE 1018 HR) 16mm in width and 25.53 mm in length. The two pieces overlap by 5.8mm to create a 1mm thick adhesive joint, and a fixture was used to maintain the geometrical dimensions of the bond during the curing process. The specimens were used to obtain the shear response of the adhesive; since the adherends were quite rigid compared to the adhesive, it was assumed that the results correspond to those of the bulk material since cohesive failure was present during the test.

The coupons were tested over strain rates ranging from 0.005 up to 50 1/s; and were performed using a hydraulic test frame in conjunction with a load cell (Transducer Techniques, model SWP-20K) and a Linear Variable Differential Transformer (LVDT) (Omega, type LD-320-7.5) mounted on the sample to measure displacement. Custom offset grips were used to maintain the alignment of the sample with the applied load and minimize the introduction of bending moments during the test. Imaging of the test and post-test sample analysis confirmed that there was no misalignment and that the setup did not introduce any measurable bending in the test sample.

3.3.4 Adhesive modeling and CAE implementation

The ability to model the mechanical response and failure of adhesive joints is essential for integration into the design process. One challenge in modeling adhesive joints is the small thickness of the adhesive bond, resulting in relatively small elements. For example, vehicles and substructures are often modeled with elements on the order of 3 to 5 mm in dimension; whereas a typical bond thickness may be 0.15 mm leading to a significant reduction in time step and increased computational cost for solid continuum elements. A second challenge is the level of detail in the material or constitutive model, which determines the mechanical properties that must be measured as inputs to the model. To address the large number of possible combinations, three approaches in order of increasing complexity and computational cost were identified for investigation in this study: tied nodes, a cohesive zone model, and a continuum model.

A computationally efficient approach to modeling adhesive joints is a simple tied interface, where nodes on adjacent adherends are tied to one another and failure is predicted through the use of a stress-based criterion [27,227,228]. Although this method is very computationally efficient and some implementations include apparent ductility of the adhesive through a prescribed displacement corresponding to fully damaged material, this method does not incorporate the actual bond thickness

or adhesive elastic response and can be prone to numerical instability [210]. Further, available implementations in a commercial explicit finite element code (LS-Dyna, LSTC) did not include deformation rate effects, bond thickness, or the compliance of the adhesive. Initial studies identified these aspects as a significant limitation, and this formulation was not pursued further.

Cohesive zone models (CZM) provide a computationally efficient, albeit incomplete, formulation to represent two important modes of loading on an adhesive joint: tension and shear. Further, the adhesive bond thickness is included as is the compliance of the adhesive. In this study, a cohesive element formulation incorporating tensile, shear, fracture and damage properties was investigated [132]. Importantly, this implementation also included deformation rate effects and an interpolation to consider mixed-mode loading. The measured parameters included the tensile traction displacement curve, the shear traction displacement curve, Mode I fracture toughness, and deformation rate effects in tension characterized by an increase in material strength with increasing deformation rate. The Mode II fracture toughness was not directly measured and was determined from the shear tests as described in the methods section.

Continuum approaches incorporating solid elements have been used to investigate stress gradients in a joint and can aid the design engineer to understand the adhesive performance in a particular joint configuration[7,208], but are not often used for large structures due to the high computational cost. Specifically, multiple elements are required through the small thickness of the adhesive leading to a large number of elements and increased solution time for a given model. A continuum approach requires a constitutive model to describe the material response, often providing stress as a function of strain history and strain rate. There are many material models that may be considered, and the use of a particular model is dictated by the sensitivity of a material to deformation rate, damage, and mode of loading. Classes of materials investigated included: elastic, viscoelastic, viscoplastic, metal plasticity, and polymer-specific models. In general, the experimental test results determined that the constitutive model was required to incorporate elastic response, damage or plastic response, deformation rate effects, asymmetry in tension and compression, and shear response. Although many different models exist with some or all of these aspects, noted limitations included incorporation of deformation rate effects, the asymmetric yield surface [229], and the general ability to fit the wide range of data available from the experimental tests. Following an investigation of several different models, the Semi-Analytical model for Polymers (SAMP-1) constitutive model developed by Kolling et. all [30] and implemented in a commercial finite element solver (LS-DYNA) [230] code was identified for use in the current

study. The SAMP-1 model incorporates specific stress-strain curves for different modes of loading (tension, shear, and compression) and incorporates strain rate effects.

3.3.5 Implementation of experimental test data in constitutive models

Multiple tests were undertaken for each mode of loading and deformation rate; the experimental data was used in whole or in part as required to implement the various constitutive models used in this study. In the case of the cohesive element, the models required strength data as a function of strain rate; this information was extracted from the experimental test data by cross-referencing stress at failure against strain rate. The strain rate effects were described with the use of a log-linear model. Mode I fracture toughness was measured by the manufacturer using the tapered double cantilever beam tests [231] and the average value from the measurements[221] was used in the cohesive constitutive model. Mode II data was first approximated using an expression (Equation 3-1) that relates the maximum shear strength (τ) with the displacement at failure (δ_{fail}), the area under the normalized shear stress-strain curve (A_{TSC}) and the energy release rate. In the case where no shear data is available, the value of Mode II energy release can be approximated as 2 to 10 times the Mode I value [232,233]. In cases where the initial Mode II approximation (Equation 3-1) did not predict the material strain to failure accurately; the value was recalculated using an inverse method. The method consisted in varying the Mode II value until the response of a single element in pure shear at the lowest strain rate followed that of the experimental data and there were no differences in strain to failure. Cohesive elements require a curve to describe the traction separation response in the material, the literature [213,233–236] suggest the use of bilinear or bilinear with plateau curves; although some authors have claimed that the shape does not have a significant effect on the response [213]. The traction separation curve was determined by normalizing the shear response at the lowest strain rate. The normalization process consisted of dividing the measured curve by the maximum measured stress and strain values respectively in each axis to obtain the normalized traction-displacement curve.

$$\delta_{fail} \cong \frac{G_{II}}{A_{TSC}\tau}$$

Equation 3-1: Energy release rate for mode II [81]

In the case of the implemented solid formulation and constitutive model (SAMP-1), the model required true stress as a function of plastic strain to define the material response for tension and shear. For the tensile tests, the measured experimental stress-strain data for each specimen at each strain rate was processed as follows. The elastic (linear) region was identified, and the elastic modulus was determined

for each test. The end of the linear region (yield strength) was identified with the aid of Equation 3-2 to determine when the plastic strain was greater than zero, using the modulus measured in the linear region of the response. The stress-strain response was then separated into elastic and plastic components (Equation 3-2) and the resulting plastic strain versus stress data was fit using an empirical relationship between stress and strain (Equation 3-3), which resulted in good quality fits and coefficients of determination (e.g., $r^2 > 0.95$). Finally, the plastic strain-true stress curves were averaged in a point-wise manner (Equation 3-4), and the strains at failure were determined from averaging the failure strains for all the tests, denoted by the counter i, at a particular strain rate, denoted by the counter j (Equation 3-5). The same procedure was followed with the shear data, although in this case, a polynomial curve type fit (Equation 3-6) was more appropriate ($r^2 > 0.90$). It is worth noting that the described procedure was successful at preserving the integrity of the physical response in the material, which was not the case when all the available data for a single strain rate was curve fitted into a single expression.

$$\varepsilon = \varepsilon_{elas} + \varepsilon_{plas}$$
$$\varepsilon_{elas} = \frac{\sigma}{E}$$

Equation 3-2: Strain decomposition

$$\sigma = A + B * e^{-C\varepsilon} \sinh^{-1}(\varepsilon + D)$$

Equation 3-3: Mathematical expression for curve fitting in tension

$$\sigma_{avg}|\dot{\varepsilon}_j = \frac{\sum_1^n \sigma_i|\dot{\varepsilon}_j}{n}$$

Equation 3-48: Average curve for a particular strain rate $\dot{\varepsilon}_j$

$$\varepsilon_{fail}|\dot{\varepsilon}_j = \frac{\sum_1^n \varepsilon_{fail\,i}|\dot{\varepsilon}_j}{n}$$

Equation 3-5: Strain to failure in the average curve for a particular strain rate $\dot{\varepsilon}_j$

$$\tau = A + B\gamma^{\frac{1}{2}} + C\gamma + \cdots + G\gamma^7$$

Equation 3-6: Mathematical expression for curve fitting in shear

Additionally, both models require values for modulus of elasticity in tension, in shear, density and Poisson's ratio. This information was readily available from the manufacturer and was verified in the experimental tests.

3.3.6 CAE modeling

Single element simulations were used for a first level assessment of the constitutive models. In these simulations, the boundary conditions were implemented to obtain pure tension and pure shear (Figure 3-2). In the second stage of this implementation, the actual test samples used in the experiments (TSHB and TLS) were simulated and subjected to the same loading as the experimental test conditions. The TLS used both CZM and continuum elements while the TSHB geometry used solid elements only (Figure 3-2).

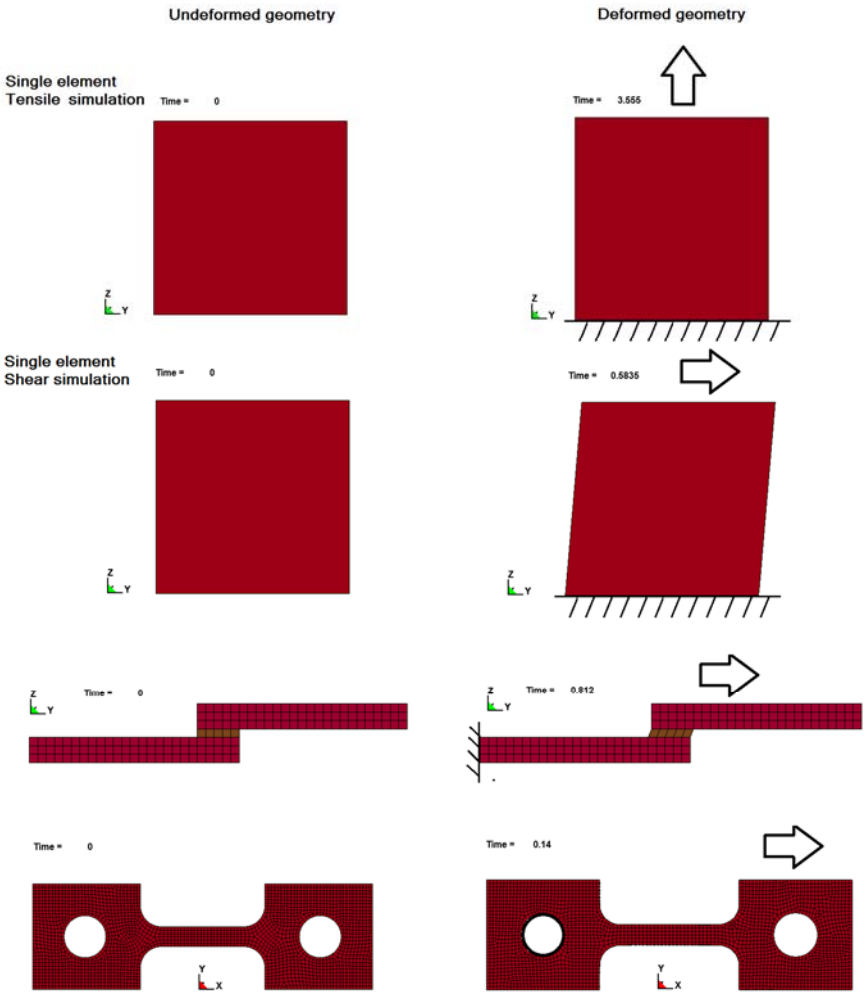

Figure 3-2: Single element cases (Top), TLS geometry (Bottom Left) and TSHB geometry (Bottom right)

3.4 Results

3.4.1 Experimental test results

The tensile and shear test results showed that all three adhesive materials demonstrated significant strain rate sensitivity for both tension and shear modes of loading. Figure 3-3 describes a data set from the testing showing strain dependency for one of the materials in tension as well as the relative strength between all three adhesives under quasi-static loading. The complete set of experimental results and material properties is provided in Appendix A

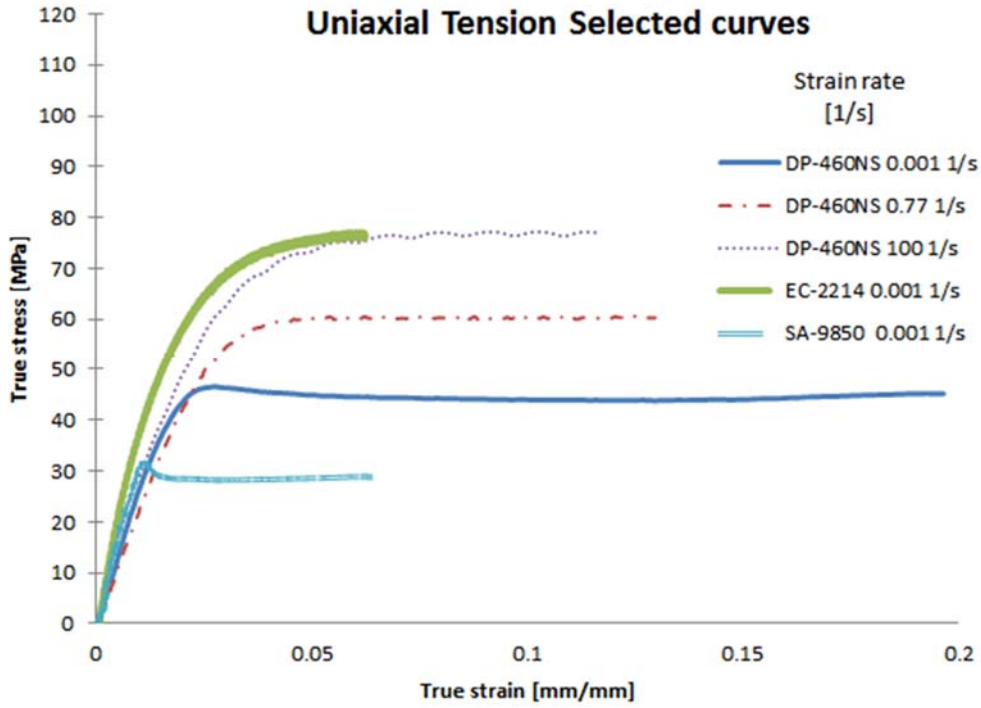

Figure 3-3: Selected test results for tension in three structural adhesive materials

The dependency of material ultimate strength on strain rate for both tension and shear (Figure 3-4) was quantified by fitting a log-linear curve (Table 3-1). In metallic materials, the strain rate effects are typically log-linear [237] [82], but for these three polymeric materials, a non-linear fit may provide improved coefficients of determination. Non-linearity has been reported in the literature [90,92,198] for polymers and epoxy adhesives. However, a linear fit was required for the cohesive constitutive model implementation. It was noted that variability in the data contributed to lower coefficients of

determination and should be investigated in future studies. The EC-2214 and DP-460NS adhesives demonstrated the highest dependence on strain rate, based on the coefficient of the log-linear curve fit to the tensile strength data.

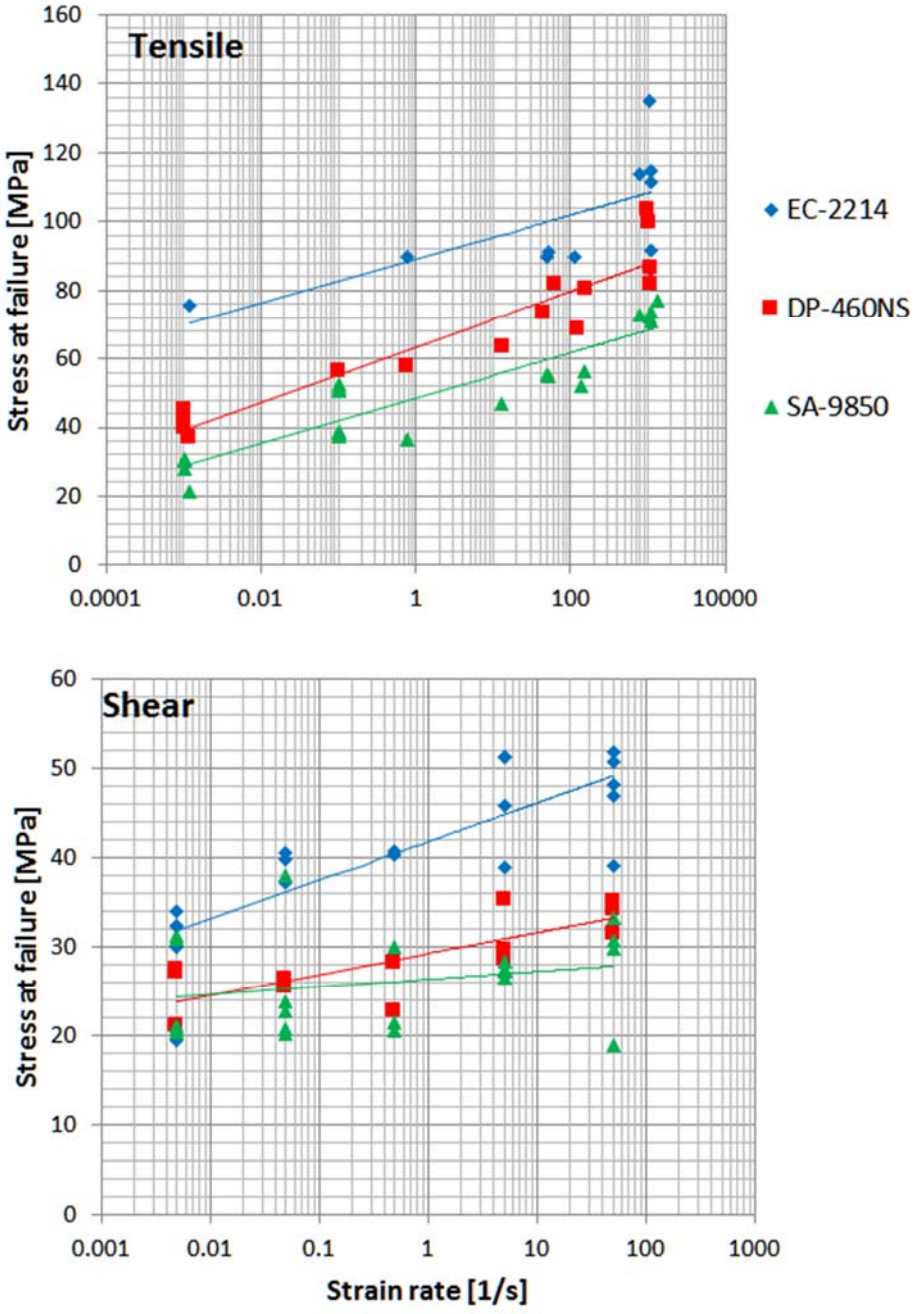

Figure 3-4: Strain rate effects in the stress to failure for tensile and shear modes of loading

Material	Tensile Data Linear fit	r^2	Shear Data Linear fit	r^2
EC-2214	3.06 ln($\dot{\varepsilon}$) + 83.46	0.66	1.88 ln($\dot{\varepsilon}$)+ 41.78	0.68
DP-460NS	3.45ln($\dot{\varepsilon}$) +62.87	0.88	1.02 ln($\dot{\varepsilon}$) +29.27	0.66
SA-9850	2.68 ln($\dot{\varepsilon}$) + 46.75	0.82	0.38 ln($\dot{\varepsilon}$) + 26.36	0.06

Table 3-1: Linear models for tensile and shear strength from Figure 3-4

The shear response was different for each material as described by the stress-strain curves. In shear, the strain rate effects on the shear stress to failure were relatively small for DP-460NS while an increased sensitivity was noted in the curve fit for both EC-2214 and SA-9850 below strain rates of 50 1/s. The three materials also showed slight changes in modulus of elasticity with strain rate (Table A1-1, Figure A1-1), where the modulus of elasticity was determined following the procedures described by the ASTM E-11-04 standard [238]. These changes in modulus were not incorporated in the numerical models but should be investigated in future studies.

3.4.2 CAE Implementation

3.4.2.1 Cohesive zone model

The cohesive element formulation was implemented using the measured data from the tension and shear tests to describe the strain rate effects on the strength of the material (Table 3-1). Also, the modulus of elasticity and shear modulus used matched those published by the manufacturer and confirmed during the experimental testing (Table A1-2). The required fracture toughness values in Mode I and Mode II were obtained from the manufacturer or the literature, or as previously explained any values not directly available were determined by matching the response of the cohesive model using a single element, to that of the measured data in the experiments. The complete sets of parameters for the cohesive models as implemented in a commercial finite element code (LS-DYNA) can be found in Tables A2-1 to A2-3 in section 2 of Appendix A. The material properties were defined in the mm-sec-tonne-Newton unit system [130], commonly used in vehicle and structural models.

The response of the cohesive model using a single element was compared to the experimental results for the individual strain rates measured during testing (Figure 3-5). In general, the CZM demonstrated good prediction of stress at failure. The results also showed excellent agreement in the elastic regime; individual results are illustrated in section 3 of Appendix A (Figure A3- to A3-3). The coefficient of

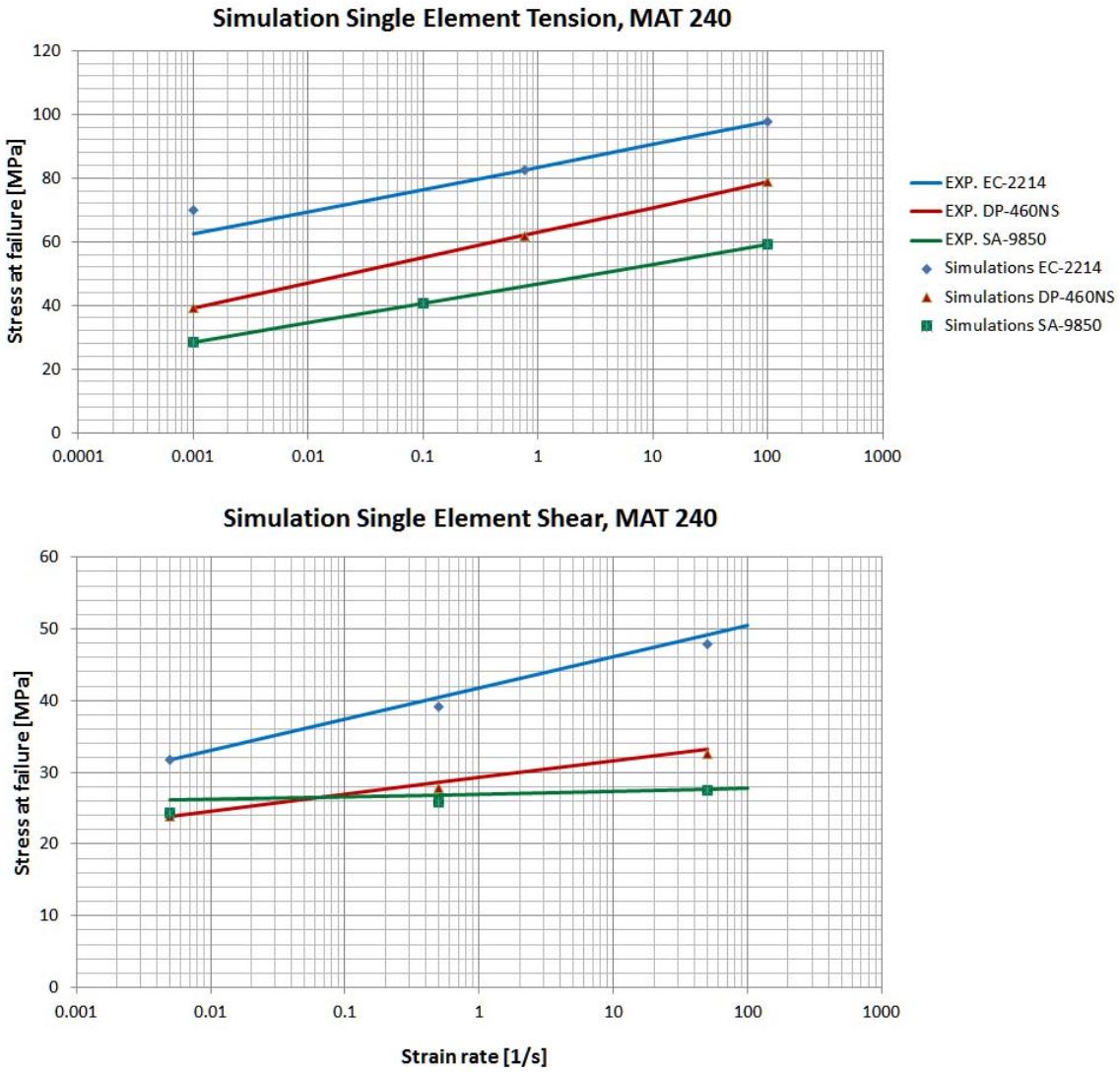

Figure 3-5: Single element simulations results, CZM

determination (r^2) value was calculated between the simulation response and the average stress-strain curve of the material for each of the strain rates tested. In general, there was good agreement between the models and the experimental data for both tension and shear loading; the calculated regression coefficients had a high value, typically around 0.8 under tension. The average value for shear loading was much lower (r^2=0.59), attributed to the poor fit at higher strain rates between the average shear curve and the model response. At low strain rates, the calculated r^2 values were much higher (~0.9). Differences in the prediction of failure stress were 1.5% on average for tension and 2.39% for shear

(Table 3-2) in the cohesive model; and for each individual case, the predicted stress value at failure was generally within one standard deviation of the experimental data average value. Tables A3-1 to A3-6 (Appendix A, section 3) contains all the metrics for each of the simulations to calculate the averages presented in Table 3-2 for the cohesive model (stress at failure, the standard deviation of experimental data, measured error, and r^2). In a few cases, the difference was higher, around 12%, but this was due to the differences between the curve fit used to predict the strain rate effect on the stress and the average stress value calculated from the available data points at those particular strain rates.

After the single element verification, the cohesive model was further investigated with the TLS geometry using rigid elements to represent the adherends. The response of the TLS models was identical to those of the single element simulations for DP-460NS, the same result was observed for the other two adhesives.

3.4.2.2 Continuum model

The response of a continuum model using solid elements using the SAMP-1 constitutive model was evaluated using single element models and with simulations of the TLS and TSHB geometries. During the tensile single element simulations, all cases showed good agreement between model and experimental data although there was a small difference in the predicted plastic behavior, which increased with increasing strain rate. Even though in the implemented model the stress during the plastic deformation was slightly lower than the measure (Table 3-2, Figure 3-6).

One specific assumption in the SAMP-1 model is that the material behaves linear elastically until yield, defined as the departure from linearity. Further, the model predicts the departure from the linear-elastic region of the material to occur at the strength corresponding to the lowest deformation rate provided (i.e., the first strength value of the plastic curve with lowest strain rate in the implementation) and did not initially follow the strength versus plastic strain data provided. In essence, the model uses the first yield from the lowest strain rate curve and then interpolates the plastic behavior using the provided curves at different deformation rates. This caused the differences noted in the transition region from elastic to plastic behavior.

In the shear loading cases, at low strain rates (~0.005 1/s), the simulation response was in very good agreement with the actual elastic and plastic response from the test data (<2% difference in maximum stress value, see Tables A4-1 to A4-6 in appendix A for each case results). In addition, the regression coefficients between the experimental data and the simulation were higher than 0.90, but as the strain rate increased the difference in stress prediction increased up to 40% in some cases and the regression

Model	Adhesive	Tensile response		Shear Response	
		Difference %	Average r^2	Difference %	Average r^2
Cohesive model	EC-2214	4.08	0.70	1.90	0.53
	DP-460NS	0.18	0.91	1.58	0.61
	SA-9850	0.00	0.83	3.68	0.64
	Overall	1.42	0.81	2.39	0.59
SAMP-1 model	EC-2214	4.03	0.96	22.64	0.43
	DP-460NS	0.61	0.99	14.61	0.55
	SA-9850	1.23	0.98	3.00	0.61
	Overall	1.96	0.98	13.42	0.53

Table 3-2: Model summary response metrics in single element simulations

coefficient diminished in all cases (<0.5). It was noted that the SAMP-1 model used the tensile strain rate sensitivity to scale both tension and shear loading response. In case of shear loading, the strain rate was calculated using the von Mises flow rule [30], linking the applied shear deformation to the provided uniaxial tension curves and hence did not accurately represent the strain rate effects for shear loading. Further verification of the SAMP-1 model was pursued using simulations of the tested samples (i.e., tensile sample and thick adherend lap shear). In both cases, a mesh convergence study was performed. Convergence was evaluated using the stress-strain response, element stress in a selected region, as well as the measured modulus of elasticity and shear modulus. From the study results, it was determined that elements between 1.5 mm and 1mm in characteristic length provide a converged solution for the tensile coupon while a smaller size (0.25 mm) was required for the TLS. The mesh size in the TLS model was constrained by the 1mm adhesive bond used in the actual experiment, at least 3 elements across the joint thickness are recommended when using single integration point elements to capture any possible bending effects and the resulting stress gradient [27].

Further verification of the SAMP-1 model was pursued using simulations of the tested samples (i.e., tensile sample and thick adherend lap shear). In both cases, a mesh convergence study was performed. Convergence was evaluated using the stress-strain response, element stress in a selected region, as well

as the measured modulus of elasticity and shear modulus. From the study results, it was determined that elements between 1.5 mm and 1mm in characteristic length provide a converged solution for the tensile coupon while a smaller size (0.25 mm) was required for the TLS. The mesh size in the TLS model was constrained by the 1mm adhesive bond used in the actual experiment, at least 3 elements across the joint thickness are recommended when using single integration point elements to capture any possible bending effects and the resulting stress gradient [27].

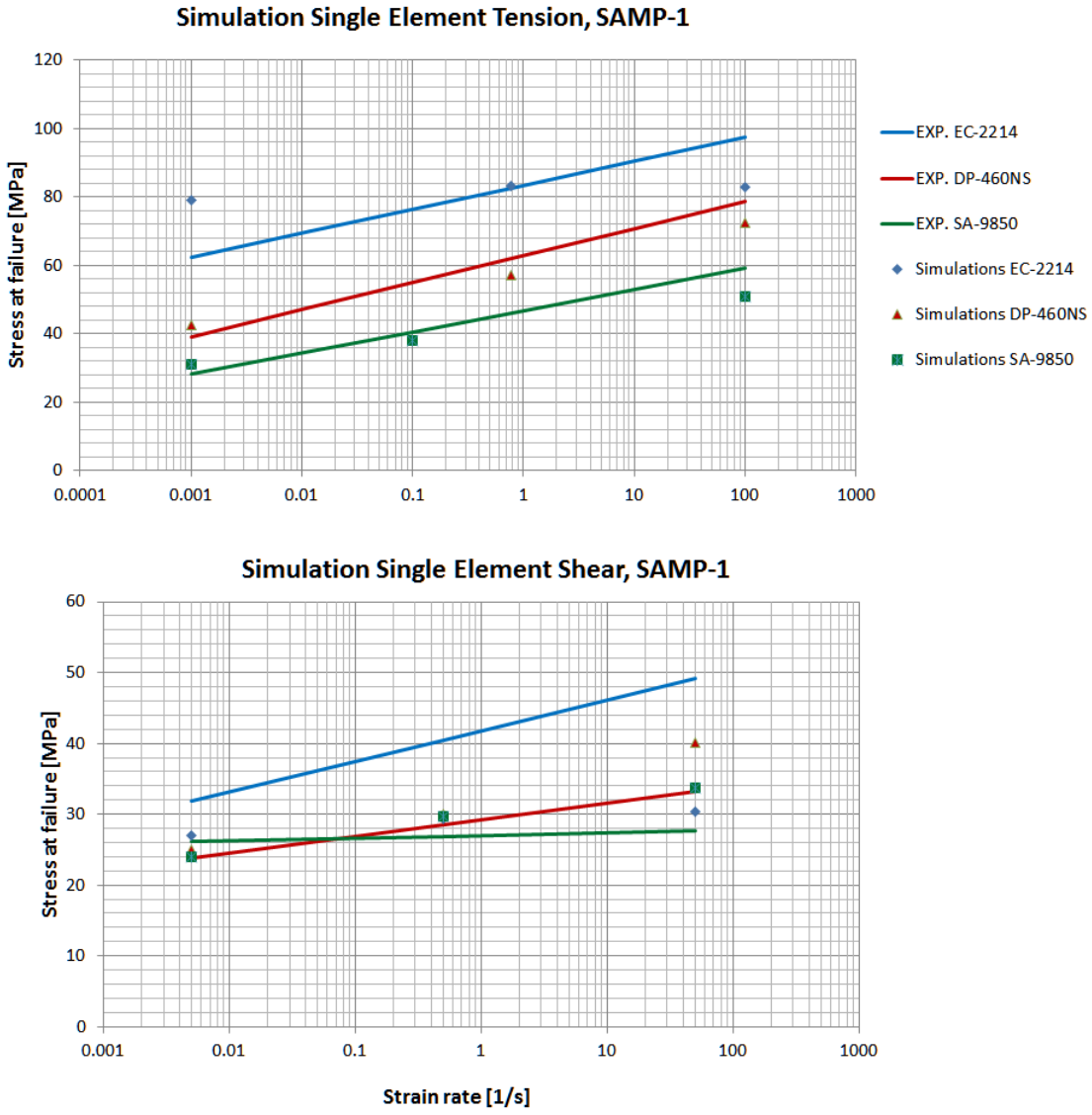

Figure 3-6: SAMP-1 Single element simulation results

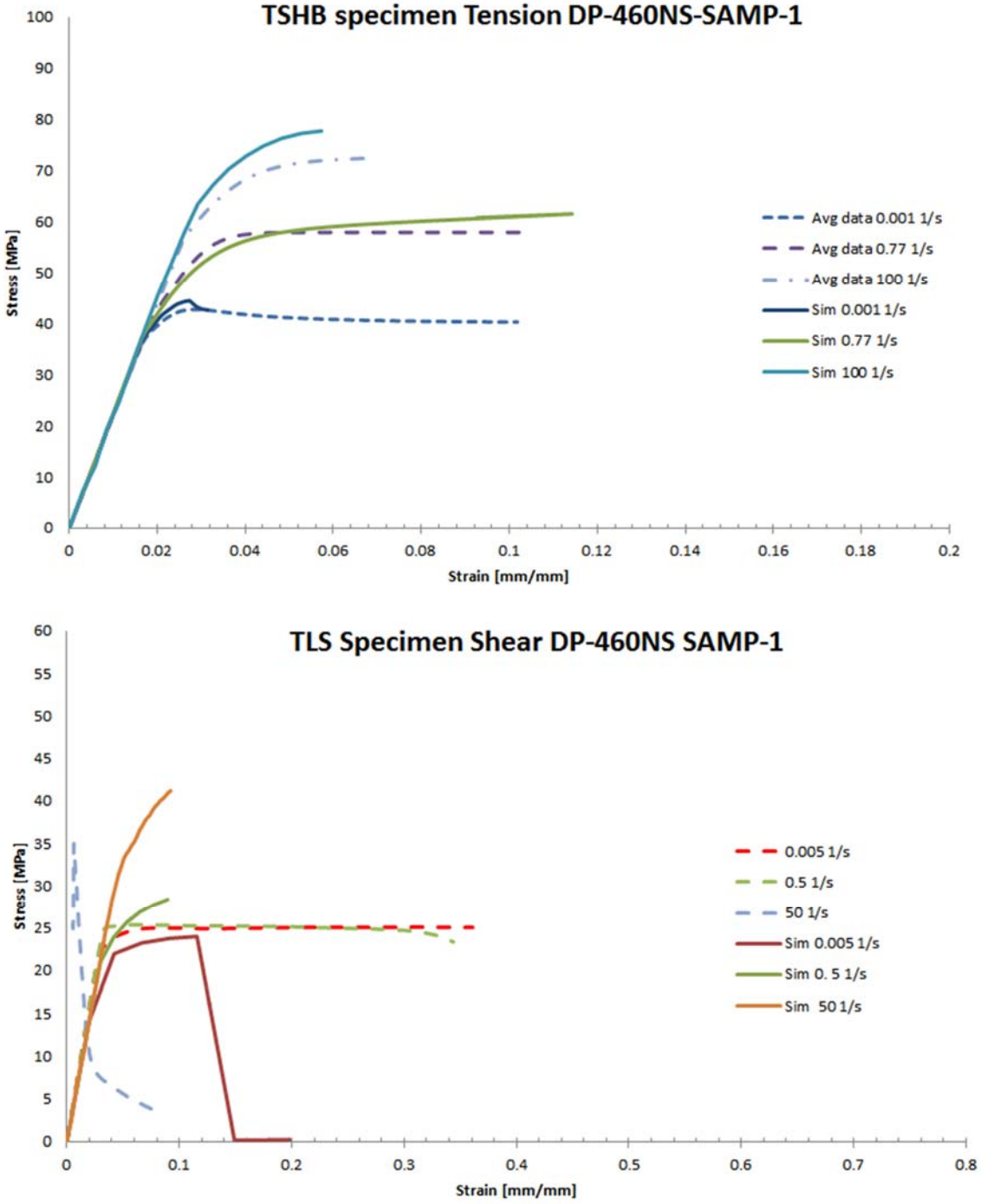

Figure 3-7: Simulation results vs. testing. Uniaxial tension (Top), Thick lap shear (Bottom)

Figure 3-7 shows the stress-strain results for DP-460NS at three different strain rates (0.001, 0.77 and 100 1/s) for tension and rates of 0.005, 0.5 and 50 1/s for shear. In all tension cases, the response of the

SAMP-1 model was adequate, properly predicting the elastic response, the stress to failure as well as providing a good approximation to the transition between elastic and plastic behavior.

The implemented strain to failure criteria in the model was close to the specified parameters (below 13% error, Table 3-3). The TLS simulation presented the same type of limitations noticed in the single element simulations. That is, a good response at low strain rates, but a departure from the measured behavior at higher strain rates. Simulations for SA-9850 and EC-2214 materials using the testing geometries was not pursued.

Tensile response				Shear Response			
Strain rate [1/s]	**Stress Difference %**	**Strain to fail Diff. %**	**r^2**	**Strain rate [1/s]**	**Stress Difference %**	**Strain to fail Diff. %**	**r^2**
0.001	3.93	N/A	0.97	0.005	4.53	N/A	0.89
0.77	5.90	5.07	0.92	0.5	10.59	N/A	0.65
100	2.36	17.07	0.93	50	15.37	N/A	0.05

Table 3-3: SAMP-1 simulations results for experimental geometries

3.5 Discussion

3.5.1 Experimental testing

Three different epoxy adhesive materials where tested under uniaxial tension using bulk samples and under shear loading using a thick lap shear sample geometry across a range of strain rates. The experimental results were of good quality, but some challenges were identified during high strain rate testing. Under tensile loading using the Split Hopkinson Bar with the proposed geometry showed that the specimen was susceptible to non-equilibrium conditions. Even though the sample geometry is acceptable for testing metals, and impedance compatible aluminum bars were used; the sample gauge length was too long so that dynamic equilibrium was not achieved. Reducing the gauge length was not considered since previous testing has demonstrated the required reduction in length would not allow for uniform stresses to develop in the sample. The reported ultimate strength of the adhesive follows the trend from lower strain rates (Figure 3-4). Efforts are underway to investigate modifications to the

test using low impedance polymeric bars, pulse shaping techniques [239–241], or the atypical setup implemented by Rae [241].

Challenges were also noted with the shear testing at high strain rates, in this case, high frequency oscillation was identified in the response at strain rates of 50 1/s and higher, attributed to vibration in the test apparatus. To address this challenge, it is proposed that an alternate sample geometry (e.g., ASTM B831-14 [242]), be investigated. In general, most of the challenges identified were related to displacement or strain measurement while the measured load, particularly the maximum load, was found to be representative, since the differences between the calculated average stress at peak load and the shear data measured by the manufacturer (Table 3-4) are less than 5% in difference for both DP and EC materials.

Material	Manufacturer Shear [MPa]	TLS Shear [MPa]	Difference %
EC-2214	31.02 (ASTM D-1002)	31.82	2.51
DP-460NS	24.82 (ASTM D-1002)	23.86	3.86
SA-9850	19.00 (ISO 4587)	24.34	21.93

Table 3-4: TLS results vs. manufacturer data

The SA-9850 adhesive shear result from the manufacturer was lower, but the manufacturer data reported adherend failure. Hence the actual adhesive property will be higher.

It is clear from the experimental data that all three materials were sensitive to strain rate for both tension and shear loading, exhibiting an increase in strength with increasing strain rate. To describe the effects of strain rate in the mechanical properties of these adhesives, the use of traditional log-linear models, as implemented for metals provided a reasonable fit to the data (Table 3-1). Previously, Nagai [198] demonstrated that the Cowper-Symonds model could be used to describe the effects on the compressive stress of DP-460 (a variant of DP-460NS as used in the current study), but over a limited range of strain rates (≤ 100 1/s).

A similar result was found for the data in this work. Out of the three materials tested, only DP-460NS showed an improvement in the correlation coefficient when the strain rate range was narrowed. This is partially due to the scatter in the data, and may also support the possibility of a non-linear relationship between strength and strain rate effects for this particular material. It is recommended that future testing

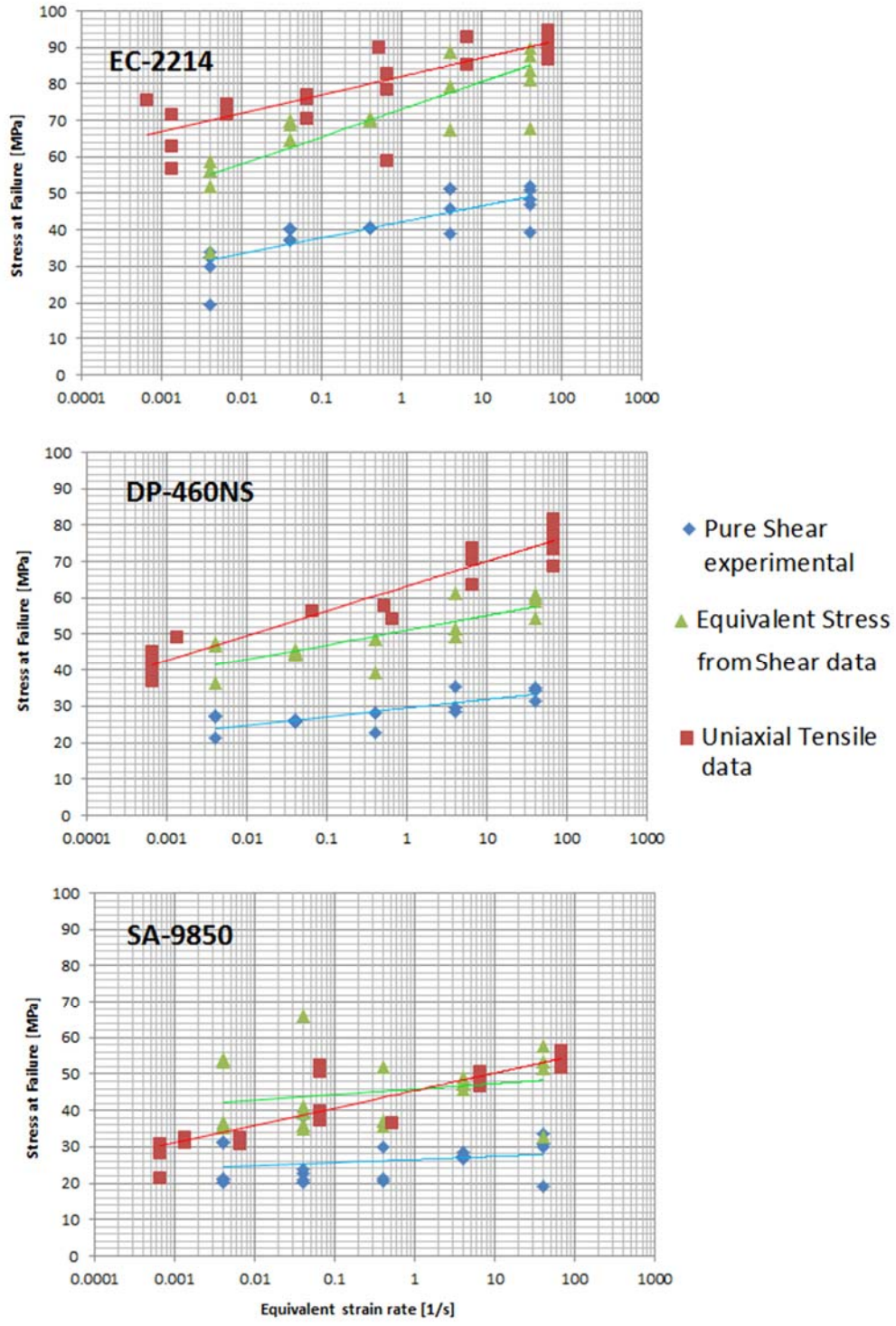

Figure 3-8: Equivalent tensile stress from shear stress against experimental tensile data

consider non-linear models; however, this was not investigated in the current study since the constitutive models used could only account for linear variation in strength with the log of strain rate. Other authors have also highlighted the importance of considering non-linear models when selecting constitutive models to represent polymeric materials [92,243].

Another important finding is that traditional yield criteria (e.g., Tresca or von Mises) that link tensile and shear properties are not applicable to the materials investigated in this study. For example, the shear response cannot be accurately predicted from the tensile data (

Figure 3-8), and the stress transformation (using von Mises theory) confirms that the strain rate effect is clearly not the same between the tensile and the shear data. As a result, complex concave yield surfaces may be required to adequately capture and predict the yield behavior under load [229]. More elaborate test apparatus (e.g., the modified Arcan [28,244]) that can subject the samples to mixed mode loading will be required to fully define the actual yield surface.

3.5.2 CAE Implementation and evaluation

Two constitutive models, a cohesive zone model and a continuum approach using solid elements, were implemented to describe the measured mechanical behavior of three epoxy adhesives. Although both models were capable of describing the material response under the considered load conditions, some limitations were identified. From the experimental testing, it was clear that the strain rate effects may not follow a log-linear relationship across the entire strain rate range; however, in cases where the range of strain rates encountered was limited to only a few decades, a log-linear description of strain rate effects was found to be adequate.

Some authors have noted that [203,204,245,246] the energy release rate for a polymer can be strain rate dependent or that the shape of the traction displacement curve changes with the strain rate. In particular, for this work, the single element simulation for DP-460NS at higher strain rates other than quasi-static (0.77 and 100 1/s) in tension demonstrated that it was not possible to obtain a match to the experimental response unless either the energy release rate was increased or the traction curve was modified. Although the cohesive model considered in this study allows for energy release rate to depend on the deformation rate, there was no experimental data to support the incorporation of this in the present study. Although the individual response under tension and shear was very good, further investigation is needed to evaluate the model under mixed mode loading conditions.

In the case of the solid element formulation, the accuracy of the response was limited due to issues with strain rate effects implementation; in particular when loaded in pure shear at high strain rates or under

mixed mode loading conditions. As noted in the model description, the shear response was scaled from the strain rate effects defined for tension, which is a limitation of the model. The strain rate dependency for these two modes of loading is not the same in the investigated materials (
Figure 8). This has been acknowledged as a limitation of the SAMP-1 [30] and further highlighted in the current study, particularly when considering intermediate to high strain rate effects in shear or under complex states of stress. It was also noted that similar challenges might be encountered for strain rate effects in compression based on the data measured by Nagai [198]. The Nagai data shows the dependency of the modulus of elasticity and stress to failure with strain rate. If symmetric behavior between tension and compression stress to failure were to be assumed; the compressive data measured by Nagai [198,211] overestimates the stress to failure in tension when compared against the measured data in this study. Therefore the strain rate effects could also be decoupled between tension and compression. Although these tests concentrated on DP-460, a variation of DP-460NS, similar effects may be expected for DP-460NS. Work by other researchers, Chen [240] and Farrokh [22]; has demonstrated an asymmetric response in other epoxy materials between tension and compression for a wide range of strain rates. Considering the possible highly asymmetric nature of the yield surface based on the tensile and shear results, Tresca or von Mises yield theories are not applicable, and models such as Coulomb-Mohr or Drucker-Prager may be considered. Ideally, the models need to incorporate more flexibility in regard to load decoupling. Although the implemented strain to failure criteria in the model works well under pure tension, again issues with coupling affect the shear strain to failure, nevertheless the SAMP-1 model is the only available material model that can address some of the idiosyncrasies of polymeric materials and seems to be a good starting point for modeling structural adhesives using solid elements.

3.6 Conclusions

In this study, three different epoxy adhesives were mechanically tested under tension, and shear modes of loading across a range of strain rates and the properties were implemented in two numerical formulations.

Tensile testing was undertaken using samples machined from the bulk material, and the stress-strain data demonstrated increasing failure strength, and decreasing failure strain, with increasing strain rate. The modulus of elasticity did not vary significantly with strain rate and was in good agreement with the reported values from the supplier. Variability in the quasi-static tests was low, but higher variability

was noted for intermediate and high strain rate test data. Further, it was found that the samples were not in equilibrium for the high rate testing (~1000 1/s). However, the measured strength values followed the log-linear relationship established at the lower strain rates and were therefore reported in this study. Further testing is recommended to measure the complete stress-strain response for high deformation rate loading. The adhesive shear response was measured using a thick adherend lap shear test, also demonstrating an increase in strength with increasing strain rate. The Mode I fracture toughness was previously measured using tapered double cantilever beam testing, while the Mode II energy release rate was determined from the shear test data. Future studies should include direct measurement of Mode II toughness and the dependence of toughness on deformation rate.

Implementation of the mechanical properties required average curves which were established for a given loading condition and deformation rate through an empirical curve fit followed by a point-wise average of the plastic strain-stress curves. The effect of deformation rate was incorporated through a linear relationship between the material strength and the deformation rate. The strength values were adequately described with a log-linear relationship; typical coefficients of determination (r^2) were 0.8 for tension and 0.6 for shear.

Two different numerical implementations were considered in this study and verified using single element simulations, followed by a simulation of the actual test samples. A cohesive zone model using a cohesive element and the associated constitutive model, incorporating deformation rate effects provided a computationally efficient method of representing the adhesive joint dimensions, stiffness and failure response. It was noted, for the adhesives considered in this study, the incorporation of deformation rate effects was essential to accurately represent the material properties. In general, the cohesive model was able to reproduce the experimental test data for pure tension and pure shear for the toughened epoxy adhesives (DP-460NS and SA-9850), with less than 8% difference on average. The cohesive zone model was able to reproduce the material strength of the non-toughened epoxy adhesive (EC-2214) but did not accurately reproduce the stress-strain response. Further investigations should consider the evaluation of the cohesive model under mixed-mode loading.

Modeling was also undertaken using solid continuum elements and a constitutive model developed for polymeric materials. The solid elements were computationally more expensive, with the benefit of improved prediction of the stress conditions in the joint, when the mesh was sufficiently small (1mm for the tensile test simulation, and 0.25 mm for the thick lap shear simulation). The SAMP-1 constitutive model was accurate for stress prediction and stress-strain response for all adhesive materials when pure tension at different strain rates was considered. Under shear loads at low strain

rates, around the nominal strain rate of the provided data, the response was very close to the experimental data. One of the primary limitations of this model, the use of strain rate effects in tension to describe shear rate effects, was identified using the single element test cases. For all materials tested in this study, the effect of deformation rate on strength (i.e., log-linear slope) differed for tension and shear. It was shown that the model could produce significant errors in the shear response at high strain rates, and this is also expected to affect results for mixed mode loading conditions. Additionally, it was shown that the shear stress could not be linked to the tensile stress by the use of traditional theories (e.g., von Mises). The three tested materials demonstrated the need to have at least both tensile and shear data available for proper modeling; it is possible that this is the general case for structural epoxies. Numerical simulation of structural adhesives requires a constitutive model capable of calculating uncoupled strain rate effects for tension and shear loading, and deformation rate effects on strength must be considered if dynamic conditions are expected. The results of this study indicate that a cohesive zone model can provide an adequate representation of an adhesive joint for tensile and shear loading across a range of deformation rates.

During numerical simulation, damage data was not used directly in the material constitutive model definition. Failure was defined by the fracture toughness values and the traction-displacement curve in the cohesive element while the solid element used strain to failure values. Even though the selected models have damage capabilities, the implementations can be limited. In the case of cohesive elements, damage effects (irreversibility) are consider by enforcing loading and unloading paths that come from or point to the origin of the Traction-separation curve. This solution, although practical, can miss viscoelastic effects and non-linear behavior in the unloading response of an epoxy adhesive. Solid formulations can include more sophisticated damage implementations [31,142,143,247] and incorporate damage mechanics principles [141] to modify the stress response as a function of damage, or use mathematical formulations that describe the internal damage evolution as a function of different parameters that modify the material response. Such parameters can be the initial void fraction, the current state of stress (or tri-axiality), plastic strains, and other values or mathematical descriptions tied to the initiation, growth and propagation of voids. Regardless off this, the implementation or validation of such damage capable models require strain-damage data that was not ready available. This highlights the necessity for experimental damage data that cannot only support the development and validation of numerical models but also further the understanding of the underlying damage mechanisms that evolve

under load for adhesive materials. In the next chapter, damage in adhesives will be explored by using microhardness measurements in the three studied epoxy materials.

Chapter 4

Damage Measurements in Epoxy Structural Adhesives using Microhardness

This chapter is based on the following published paper:

Trimiño L, Cronin D.; Damage Measurements in Epoxy Structural Adhesives Using Microhardness. International Journal of Adhesion and Adhesives, January 2018, volume 82, pp 211-220 . (https://doi.org/10.1016/j.ijadhadh.2018.01.014)

4.1 Overview/Abstract

The design of adhesively joined components requires the ability to predict and model the joint response under expected operating conditions, including crash events for vehicle structures. Specifically, quantifying adhesive material damage accumulation from static and dynamic loading is essential to predict the response of bonded components in such scenarios. In this study, Vickers microhardness measurements were used as a forensic technique to quantify damage in bulk tensile samples for three structural epoxy adhesive materials: a non-toughened epoxy (EC-2214); a toughened epoxy (DP-460NS); and a high toughness epoxy (SA-9850). The samples were tested to failure over a range of strain rates (0.002–100 s^{-1}), and hardness measurements were taken post-test along the gauge length. In general, for toughened epoxies, the damage extended over much of the sample gauge length, while the un-toughened epoxy demonstrated damage localization at the failure location. The hardness data support the contention that mechanisms such as crazing and shear banding play a role in microhardness changes in toughened epoxies. Increments in strain rate led to an increase in the damage localization. Microhardness measurements were a valuable tool to quantify damage, with the limitation that the magnitude of change in hardness could be adhesive-specific, hypothesized to be related to competing damage mechanisms. The benefits of this approach include the ability to spatially quantify damage, to detect strain rate effects and to carry out measurement of damage post-test in support of constitutive modeling and failure analysis.

4.2 Introduction and background

Engineering design of adhesively joined components and structures requires the modeling of structural adhesives with appropriate constitutive models to describe the mechanical response and failure under aggressive loadings, such as crash scenarios in vehicle applications [248]. The study of adhesives and adhesive joints to support modeling presents challenges as the stress state, strain rates, and joint geometry can influence the measured properties and active damage mechanisms in the adhesive [190,201]. Accordingly, quantifying the damage distribution and the relationship to deformation rate is necessary for defining constitutive models that can accurately predict adhesive joint response in bonded components. Adhesives can have a wide range of chemical composition, with epoxies and toughened epoxies commonly used for structural applications. Toughened epoxies are modified to improve the adhesive strain to failure and fracture toughness [107,249], using rubber (butadiene) and/or high stiffness particles as toughening agents. Rubber toughening agents typically comprise particle sizes from 0.1 μm to 0.9 μm in diameter occurring as a suspended phase. However, the particle size depends on the amount of material used for the precipitate and also the relative viscosities between the adhesive components [76,194]. Epoxy adhesive materials can exhibit different deformation and failure mechanisms depending on the mode and rate of loading. In unmodified epoxies, brittle failure is observed, attributed to the existence of micro voids or small stress concentrations in the material [110]. In the case of toughened epoxies, many different mechanisms [107,110] can be active, including cavitation and fracture of rubber toughening particles; debonding and tearing of other embedded constituents that act like particles (EPM, ABS, polyolefins, etc.); crack deflection by hard particles; plastic zones at crack tips; and shear band/craze interactions. Shear banding and crazing are considered the dominant damage mechanisms for toughened epoxies [250].

Ductile polymers, with strains to failure above 25% [251], typically deform by shear banding, identified by birefringent areas oriented at well-defined angles, typically 45°. Shear bands may initiate at stress concentration points or in areas of high compressive stress. High magnitude localized strains develop within the shear bands [79], without the creation of voids [251].

Crazing, also referred to as strain whitening, occurs through the widening of pre-existing micro cracks as well as the initiation and opening of new cracks in the material [252,253]. Typical craze opening sizes are less than 1 μm in high-impact polystyrene [254], and approximately 2 μm for styrene butadiene-modified polypropylene [194]. The phenomenon may occur at a local area or may extend

along the load-bearing area, depending on the chemical composition of the polymer, microstructure, and presence of microdefects [107,110,194]. Thus, crazing can be considered as damage (D) in its most simple interpretation, as the creation and coalescence of voids within a volume of material [141].

Damage may be defined or measured as the ratio between the volume of voids (V_v) and the original material volume (V_o). Similarly, damage can also be defined on an area basis as the ratio of the area of voids (A_v) to the total area (A_o) of undamaged material in a given cross-section (Equation 4-1), as proposed by Woo [255].

$$D = \frac{V_v}{V_o} \; or \; D = \frac{A_v}{A_o}$$

Equation 4-1: Definition of damage

Direct measurement of voids is a formidable task, especially if in-situ measurements are desired during loading. Damage is then generally measured by indirect methods, such as [141]: changes in modulus of elasticity; variations in electrical resistivity; changes in wave speed; and changes in hardness. These methods are related to the density of the material, and therefore intrinsically related to the voids inside the volume of material. Tang *et al*. [45]measured changes in modulus of elasticity and Poisson's ratio to quantify damage for polystyrene (PS) toughened with rubber particles (HIPS).

The use of microhardness to characterize metals and damage in metallic materials is well established [141,256], but the use of micro-indentation in polymers has been relegated mostly to a simple, non-destructive production control test that indicates cure or chemical composition [257]. Nevertheless, there are studies that demonstrate the flexibility and usefulness of indentation techniques to determine the mechanical properties for viscoelastic materials [258,259], to measure changes in polymeric materials, such as polymorphic transitions due to loading [257], or to identify craze initiation [96]. A possible method, then, to measure the effect of damage in materials is through hardness measurements at discrete points. Hardness can be measured using a standardized scratch hardness test or a Shore Durometer as described in the literature [260], or with the aid of other indentation devices, such as Brinell, Knoop, Rockwell or Vickers. Where indentation size is limited, for example on small samples or thin bond lines, Vickers microhardness is often used [257]. When measuring hardness, damage can be defined in terms of the original hardness of the material (H_o), and the hardness of the material post-loading (H) (Equation 4-2) [141]. The hardness of a material is often described in test-specific units

(e.g., HV) but can be represented using consistent units of force divided by length squared [257]. Typically, results are expressed in units of megapascals, although the measurements do not represent pressure or stress. It is also necessary to consider that the use of Equation 4-2 does not consider deformation rate dependencies, which are of importance in the description of viscoelastic materials [259].

$$D = 1 - \frac{H}{H_0}$$

Equation 4-2: Damage as a function of hardness

Reported hardness values for polymers can be highly dependent on composition, curing temperature, heat treatments, and test temperature, with typical values ranging from 30 MPa for poly ethyl-ethylene (PEE) [261] up to 1,000 MPa, as reported by Paplham [262] for a carbon fiber epoxy composite. The epoxy resin used in Paplham's study had a measured microhardness of approximately 300 MPa. Stoeckel *et al*. [20], and Zheng and Ashcroft [159] have reported microhardness values in the range of 180–220 MPa for different epoxy adhesives. The microhardness of a material can also be estimated, using Tabor's relation [256], as three times the yield strength (σ_y) of the material (Equation 4-3). This relationship was developed for metals but has been applied to some polymers [257]. Equation 4-3 also neglects strain rate effects. Therefore it may be limited in application due to the viscoelastic nature of polymeric materials, as demonstrated by Lopez [263].

$$\boldsymbol{HV = 3\sigma_y}$$

Equation 4-3: Tabor's relation

Stress-induced changes in microhardness measurements have been reported in the literature, and demonstrate that the material hardness decreases with increasing levels of strain [257,264]. However, it is possible to observe a reversal in this trend, depending on the specific polymer. For example, at high levels of deformation (>40%) PEE microhardness increases, following the notable decrease in microhardness trend for lower strains [261]. The same behavior was reported by Fakirov and Boneva [265] for homo-PBT, but the trend reversal started as low as 10% strain. Baltá-Calleja [257] reports that softening followed by hardening with strain is possible due to "polymorphic" transitions. In such polymorphic transitions, the material changes from an alpha form, in which molecular chains are not fully extended, towards a beta form with chains fully extended. Coiled chains have ductility and produce a lower hardness, while extended chains require more load to deform, hence higher microhardness. In general, for the reviewed literature microhardness measurements made under stress

and after unloading are lower compared to the undamaged material, making application of Equation 4-2 feasible to describe the damage in polymers based on microhardness measurements.

In this study, Vickers microhardness was used to quantify damage and damage extent along the loaded zone for bulk tensile samples of three different epoxy adhesives subjected to uniaxial tensile loading until fracture at different strain rates. With adhesive materials, joint geometry and the state of stress can influence material properties, therefore using the bulk material presents a limitation. Nevertheless, the bulk material provides a controlled and repeatable test to further the understanding of the active damage mechanisms. It also serves as proof of concept for a methodology that can be extended to more complex scenarios. Additionally, the applicability of Tabor's relationship to epoxy adhesives was explored.

4.3 Methods

4.3.1 Materials and testing

Three different epoxy adhesives (EC-2214, DP-460NS and SA-9850; 3M, Minnesota) were investigated. The selected materials made it possible to compare the response of an untoughened epoxy adhesive (EC-2214) with a toughened epoxy (DP-460NS) and a material specifically designed for impact resistance (SA-9850). Both DP-460NS (two-part epoxy) and SA-9850 (single-part epoxy) were toughened epoxies with a polymeric phase, while EC-2214 was a single-part epoxy. Table 4-1 provides a general overview of the chemical composition of each material based on available data from the manufacturer [266]. To quantify the material microstructural inhomogeneity (measure the average size and shape of the visible phases), length scale observations were made for all three materials at intermediate magnification (100–200x) using an opto-digital microscope (ODM) (Keyence VHX-5000).

Epoxy sheets were manufactured by casting the adhesive material between two glass plates followed by oven curing. Curing temperature and time were set to the manufacturer specifications to develop optimal strength for each material: one hour curing cycle at 120°C for EC-2214; two hours at 70°C for DP-460NS; and one hour at 170°C for SA-9850. Tensile samples were machined from the sheets and loaded in uniaxial tension to failure at different strain rates (0.002, 0.01, 0.1 and 100 s^{-1}). In recent research [248] these materials were identified to exhibit increasing strength and reduced strain to failure

with increasing strain rate (Table 4-2). During uniaxial loading, both DP-460NS and SA-9850 demonstrated strain whitening, but EC-2214 did not (Figure 4-1).

Material	Matrix	Phase 2	Phase 3	Phase 4
EC-2214	Epoxy Resin 30–60%	Al pigment 15–40%	Elastomer 1–5%	n/a
DP-460NS	Phenol Resin 60–100%	Butadiene 7–13%	Silicones 1–5%	n/a
SA-9850	Epoxy resin 30–60%	Phenoxy resin 7–13%	Elastomer 10–30%	Al 5–10%

Table 4-1: Epoxy composition, weight percentages as a ratio of the controlled product

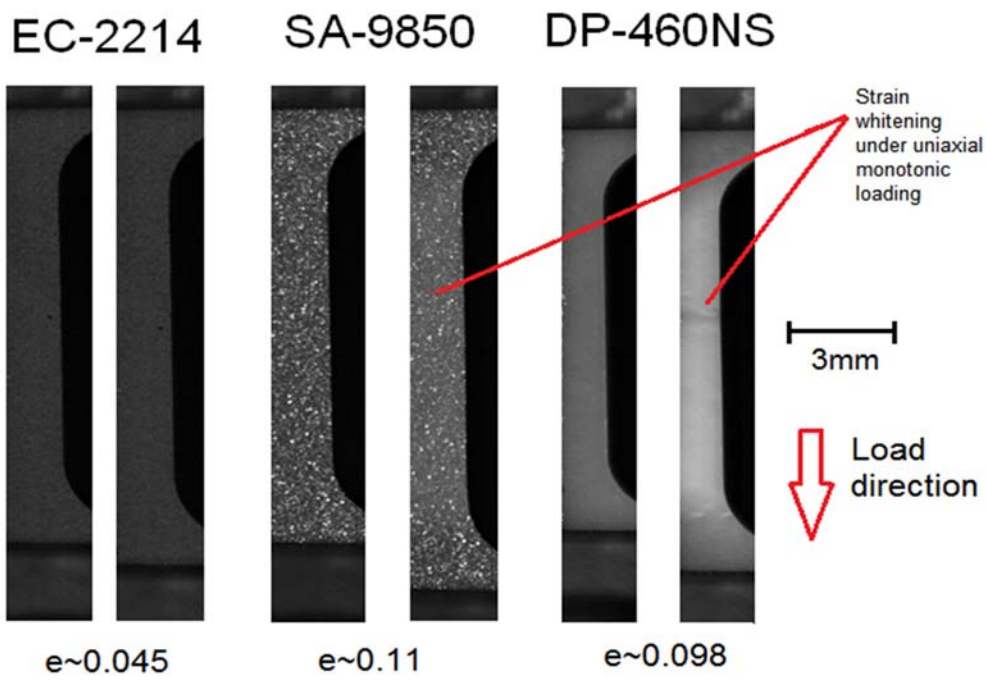

Figure 4-1: Strain whitening (crazing) for three structural adhesives

The DP-460NS material was further investigated for damage features that relate to the strain whitening, such as micro-cracks and shear bands. The toughening agent (butadiene) in DP-460NS is commonly used as a toughening agent [76,110,194,251,267,268], and the particle sizes were comparable to those

present in SA-9850. Therefore, this material represented typical feature size relative to the indentation size and, from a Linear Elastic Fracture Mechanics perspective (fracture toughness, Table 4-2), DP-460NS will generally produce damage features that are larger in size than the non-toughened epoxy (EC-2214) and that are similar in length to SA-9850.

Material	ρ [kg/m^3]	E [GPa]	ν	Tensile Strength Strain Rate Effects [MPa]	Shear Strength Strain Rate Effects [MPa]	G_I [MPa m]	G_{II} [MPa m]
EC-2214	1540	5.17	0.38	3.1ln($\dot{\varepsilon}$)+83.5	1.9ln($\dot{\varepsilon}$)+41.8	1.82	5.46
DP-460NS	1200	2.13	0.41	3.5ln($\dot{\varepsilon}$) +62.9	1.0ln($\dot{\varepsilon}$)+29.3	2.82	10
SA-9850	1200	2.40	0.41	2.7ln($\dot{\varepsilon}$)+46.8	0.4ln($\dot{\varepsilon}$)+26.4	2.97	15

Table 4-2: Mechanical properties of tested structural adhesives [248]

4.3.2 Microhardness measurements

For this study, the use of a digital Shore durometer was considered (Instron S1 model handheld durometer). However, it was found that the indentation size (1.5 mm in diameter) prevented the possibility of performing a significant number of measurements across the width of the coupon samples (3 mm) for statistical analysis. Nano-indentation could provide better measurement resolution across the width of the samples, and measurements on the order of the size of the damage features but this technique was not pursued but should be considered in the future. The goal of this study, however, was to undertake material hardness measurements at a microscopic scale to determine average changes in hardness and material damage. Therefore, a Micro Vickers Hardness Machine (Leco MHD-200 model) was used to measure the material hardness. The device provided repeatable measures, and the small indentations (~200 μm) enabled multiple measurements in a small area, which is required for statistical analysis. The indentations were measured with the optical filar micrometer. At a later stage in the study, measurement of the indentations was undertaken with the ODM to improve measurement consistency. When using Vickers microhardness [257], the size of the micro indentation diagonal (d) in millimeters and the load applied in Newtons can be related to the hardness of the material (HV) (Equation 4-4).

$$HV = \frac{1.854 * Load}{d^2}$$

Equation 4-4: Microhardness definition

Micro-indentation testing in metals is typically conducted by mounting the specimens in Bakelite or some other support material [269]. In the case of micro-indentation of polymers, Baltá-Calleja [257] and Smith [124] made some recommendations regarding sample mounting and testing. In general, an epoxy resin can be used for mounting polymers because it will have similar mechanical properties as the material to be tested. When mounted in this way, samples need to be cleaned and polished, and a cold-mount resin is required to avoid thermal effects on the material to be measured. To address these challenges, an aluminum support fixture was manufactured to support the samples during the micro-indentation process. A preliminary study was conducted to determine if the support fixture produced results different from those of a sample mounted using an epoxy resin. It was concluded that the use of the support fixture did not influence the hardness results. This same study also determined the ideal load to use during micro-indentation for each material (see Appendix B, section B1).

The samples' microhardness was measured before and after uniaxial loading. Three measurements were made in the grip zone before testing, and these served to verify the previously measured basic reference values for each material. To evaluate the effects of loading in the material, microhardness measurements were made in the sample gauge length following uniaxial tensile testing (3 measurements across the width, at 2 mm increments along the gauge length). The indentations started at 0.5 mm from the fracture plane, and a minimum distance of 350 μm was maintained between indentations in the same plane (Figure 4-2) to minimize interaction between measurements.

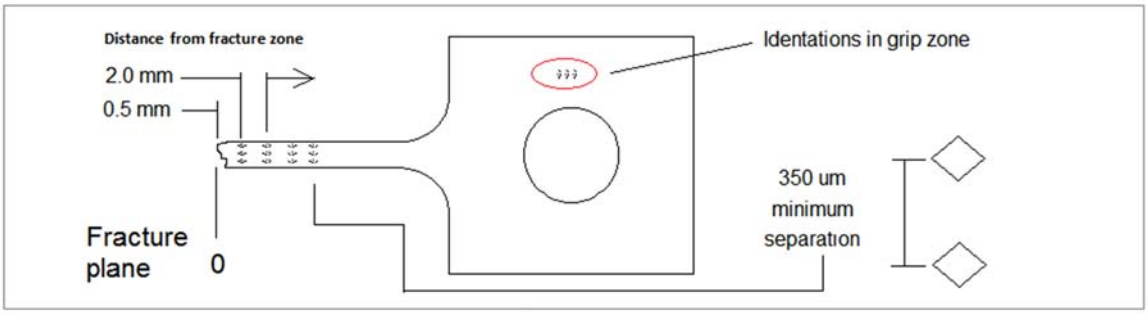

Figure 4-2: Microhardness measurement locations in samples

4.4 Results

4.4.1 Epoxy material microstructure measurements

Table 4-3 summarizes particle size analysis for all three materials. In the analysis, the first phase was the epoxy matrix, and therefore no particle results are reported. In EC-2214 and SA-9850, the micrographs pointed to a microstructure composed of reflective circular particles corresponding to the aluminum aggregates, typically 10 μm in diameter. Dark areas were identified as the elastomeric phase in both materials, with a mean diameter of approximately 20 μm. In both materials, the particle distribution was typically even along the observed surfaces, and the particle spacing (edge to edge) was on the order of 10 μm. Although DP-460NS is described by 3 different phases in the chemical constitution (Table 4-1), it was only possible to identify 2 phases with the ODM: phenol matrix in the background; and a mix of circular and amorphous butadiene, identified as a darker component. The butadiene particle distribution was random over the material surface; particle separation, measured from edge to edge, varied between 2 μm and 25 μm. It is worth noting that some of the butadiene particles demonstrated internal inhomogeneity (lighter colored areas). This may indicate that the unidentified third silicone phase could be partially distributed within the second phase.

Material	**Phase 2** Mean Dia. [μm]±σ	**Phase 3** Mean Dia. [μm]±σ	**Phase 4** Mean Dia. [μm]±σ
EC-2214	17±7	24±9	-
DP-460NS	13±9	-	-
SA-9850	-	10±7	20±17

Table 4-3: Inclusion size evaluation in the epoxy materials

4.4.2 Strain whitening development in the adhesives

During uniaxial load testing, DP-460NS and SA-9850 showed strain whitening, but EC-2214 did not. For DP-460NS, as the load was applied to the material at very low strain rates, the material first developed small areas of lighter color compared to the base material; the size of these areas grew and coalesced with increasing strain. Eventually, the whitened regions linked and formed inclined bands of whiter color. For DP-460NS, the development of white areas started well before the end of the elastic range (e~0.015) and transitioned towards well-defined bands after reaching the maximum stress (45

MPa); the strain (e~0.03) was below the strain to failure (e≥ 0.10) at this point. At low strain rates, the strain whitening occurred over the entire gauge length of the sample, with the development of numerous shear bands. However, as the strain rate was increased, localization of whitening in the vicinity of the fracture zone was identified. After failure, there was strain whitening in the gauge for the quasi-static samples, yet it was only noticeable in the region of failure for the high strain rate samples.

In the case of the SA-9850 adhesive, the behavior was similar, although the transition from crazing to shear bands was delayed well into the plastic region with high strains (e≥ 0.05), and the shear bands were not as well defined as in DP-460NS. The whitening was distributed along the entire gauge length of the material sample and was noticeable at all strain rates tested. In SA-9850 the strain whitening was noticeable in the gauge length even after final failure; this was also identified in the high strain rate samples.

4.4.3 In-situ damage feature measurement in DP-460NS

The DP-460NS material was observed using the ODM during tensile loading to identify the characteristic lengths of features such as micro-cracks and shear bands. The initial typical surface of DP-460NS consisted of the elastomeric phase and pre-existing cracks. From ODM image measurements it was determined that surface defects, such as cracks, were typically less than 3 μm opening. During loading, these features could open up to 4 μm. A crack in the sample area imaged began at 26 μm in length and grew to a length of 51 μm under load. It was noted that cracks often coalesced during the loading stage. Shear band orientation ranged between 28° and 30° relative to the loading direction, and the shear bands were approximately 50 μm in width. Figure 4-3 illustrates the material surface during load, as well as measurements made on the shear bands and at crack features.

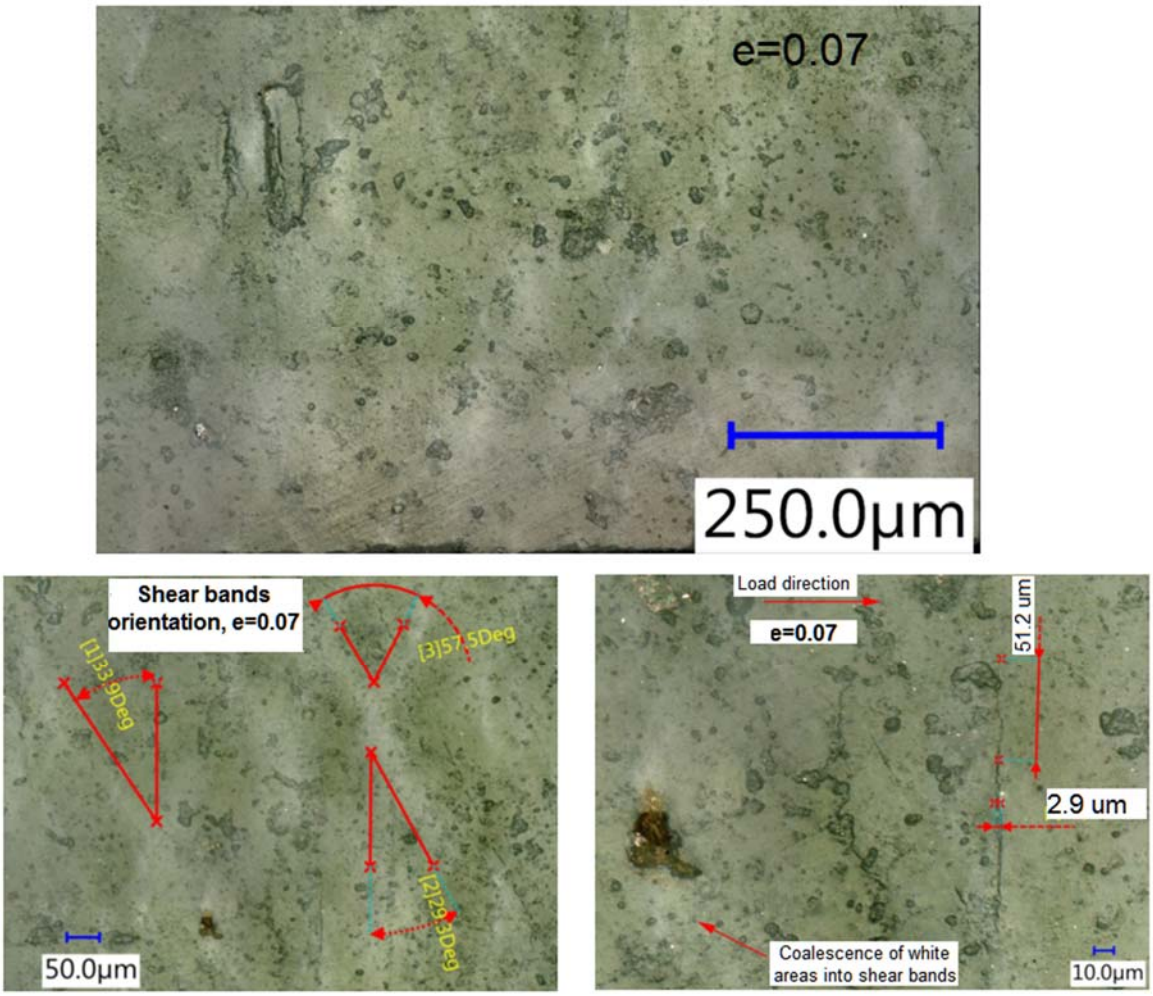

Figure 4-3: DP-460NS, evolution of surface features and damage under tensile loading

4.4.4 Microhardness baseline measurements

Microhardness baseline values for each individual adhesive material were established for reference (Table 4-4). Also reported are the yield strength and the ultimate strength. Values for Tabor's ratio between yield strength and measured microhardness were calculated using Equation 4-3. The calculation was also performed using the ultimate strength of the materials (Table 4-5). Micro-indentation diagonal length varied with the materials (Table 4-4), and in certain cases evaluation with the optical filar was challenging (Figure 4-4). The ODM facilitated the identification of micro-indentations using variable depth of field imaging and 3D image processing (Figure 4-5).

Material	Mean Hardness & ±σ. [MPa]	Indentation diagonal length & ±σ [µm]	Yield Stress [MPa] @ 0.002 s^{-1} [248]	Ultimate Stress [MPa] @ 0.002 s^{-1} [248]
EC-2214	251.06±38.04HV300	150±10.12	53.02	62.32
DP-460NS	120.10±7.20HV200	176±4.96	35.54	39.03
SA-9850	102.90±10.80HV500	301±15.92	24.70	28.24

Table 4-4: Microhardness of cured structural adhesives prior to testing

Material	Tabor's HV/Y	Modified Tabor's HV/U
EC-2214	4.73	4.02
DP-460NS	3.37	3.07
SA-9850	4.13	3.64

Table 4-5: Tabor's relation using yield strength and ultimate strength

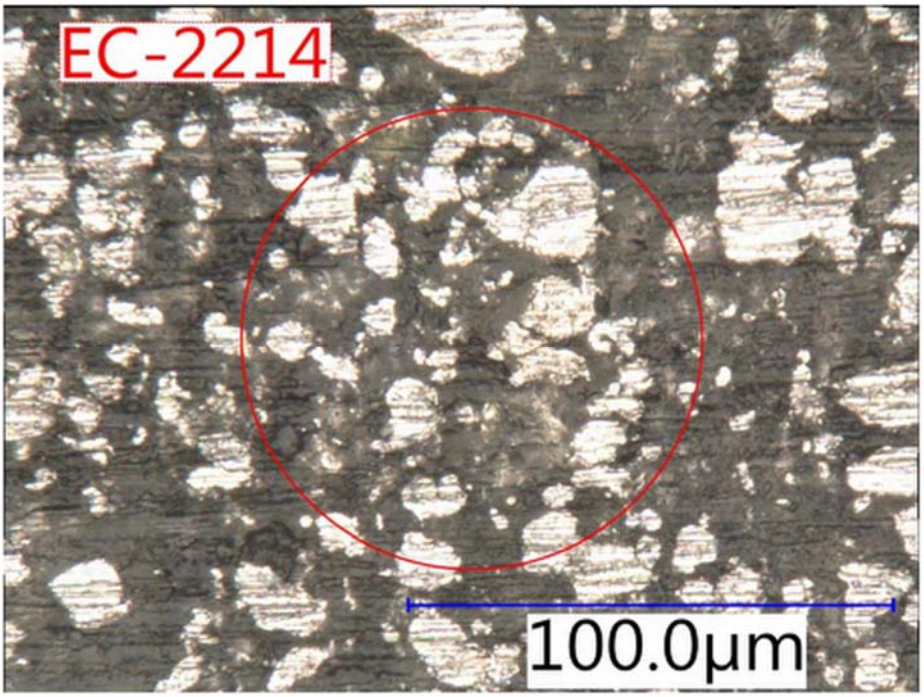

Figure 4- 4: Vickers microhardness indentations in three epoxy materials

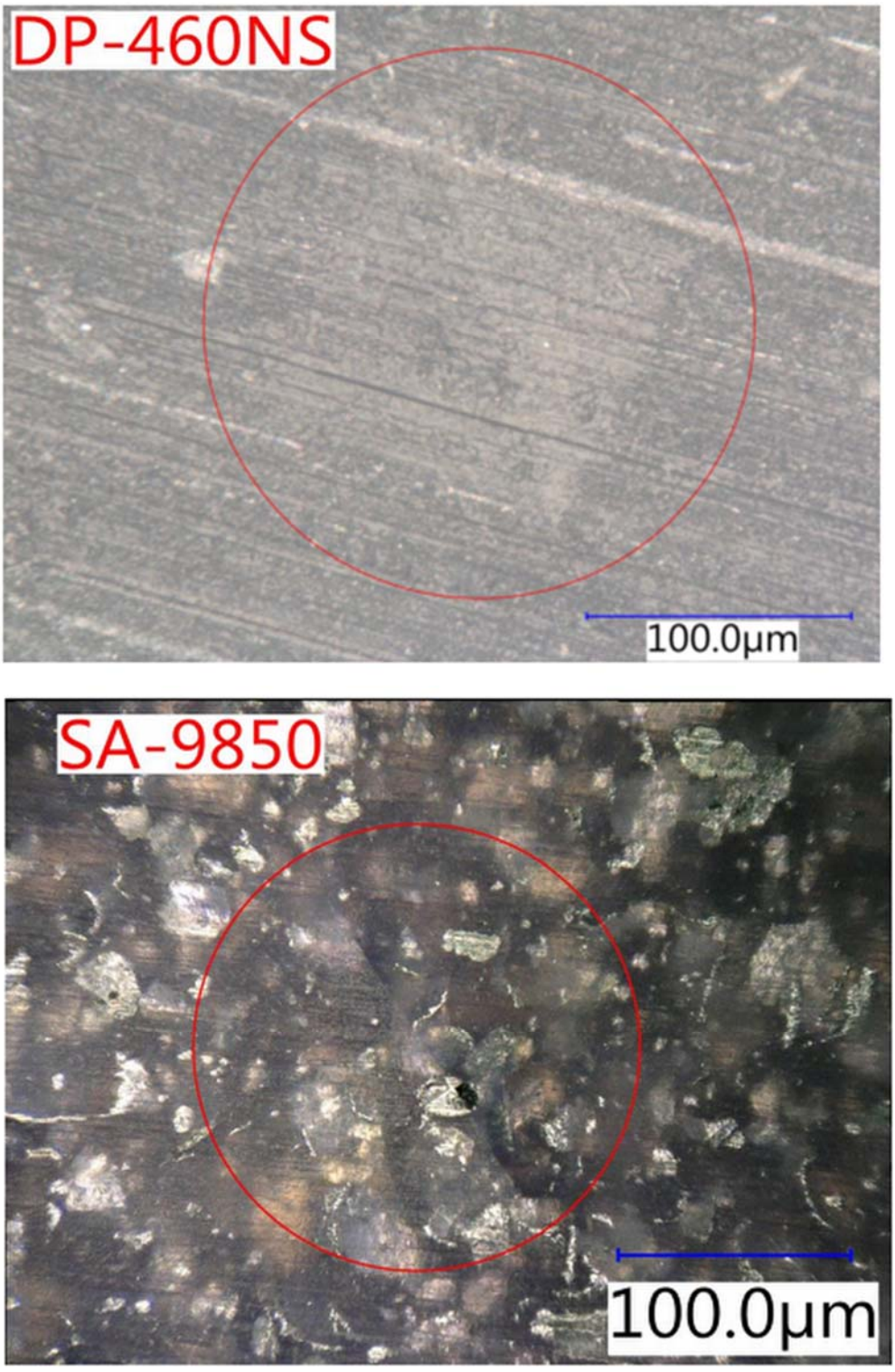

Figure 4- 4: Vickers microhardness indentations in three epoxy materials (continued)

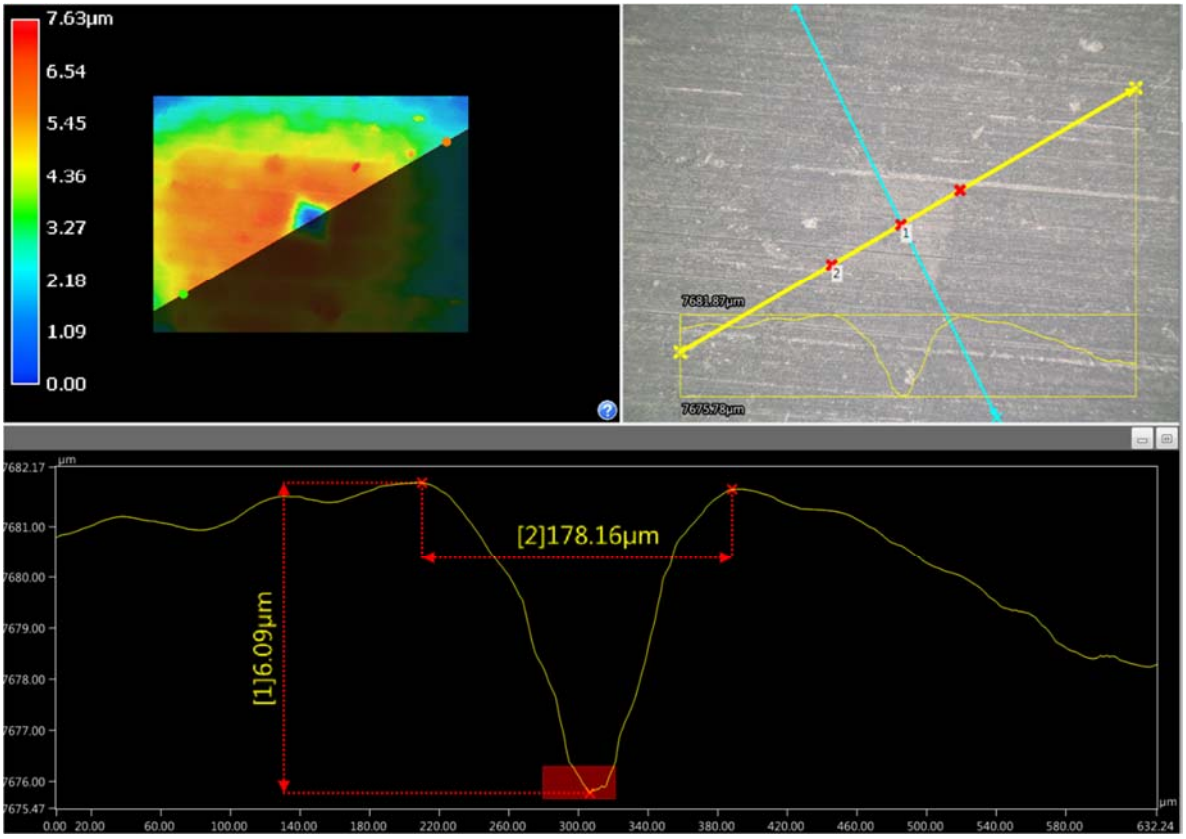

Figure 4-5: Indentation identification and measurement using an ODM

4.4.5 Post-test microhardness and effect of strain rate

The microhardness profile along the gauge length of the sample, beginning at the fracture zone, was determined for the three different materials (Figures 4-6 to 4–8). The figures include box whisker plots that summarize the data at each measurement location. Each box includes a horizontal bar to depict the mean value, the upper and lower fence, and 75% and 25% quartiles. Each figure also includes a corridor indicating the undamaged material mean microhardness values (solid line, data from Table 4-4) and three standard deviations from the mean (dashed lines).

At each tested location, measurements were compared with those of the undamaged material average microhardness (Table 4-4), using a T-test with a significance level of 95%. The tables in section B2 of Appendix B summarize the analysis results for each material at each measured location. Statistically different locations from the mean are identified with the star symbol in Figures 4-6 to 4-8.

The microhardness measurements were lower, on average, for the tested samples compared to the base material values (Table 4-4). The EC-2214 material had microhardness values statistically similar to the

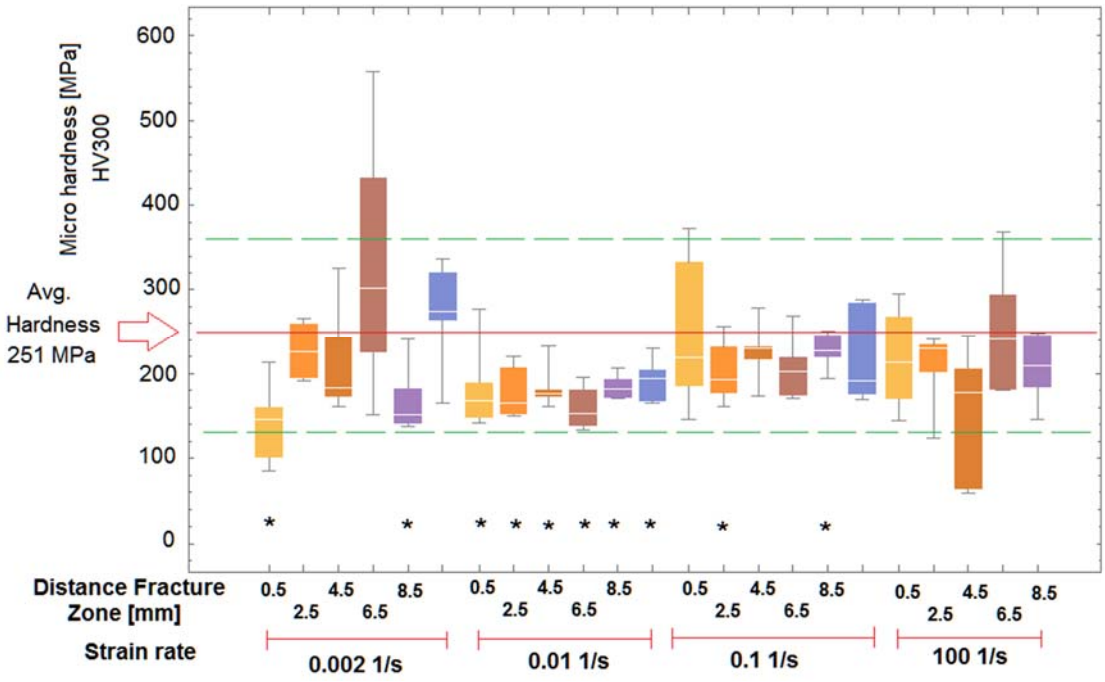

Figure 4-6: Measured hardness of EC-2214. Undamaged material average microhardness (solid line) with ± three standard deviations (dashed line)

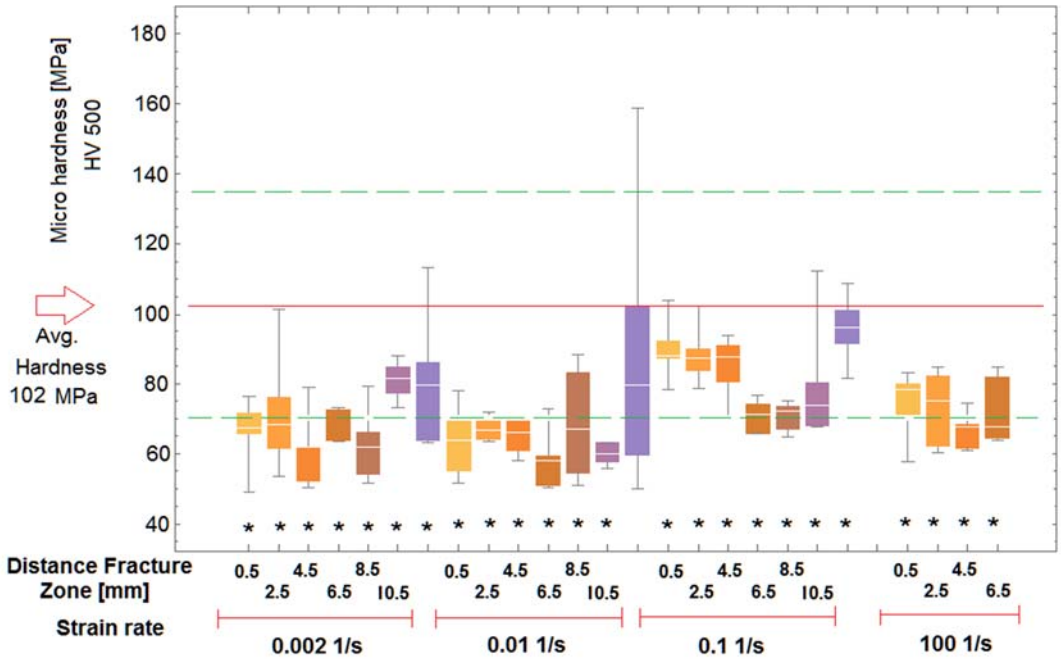

Figure 4-7: Measured hardness of SA-9850. Undamaged material average microhardness (solid line) with ± three standard deviations (dashed line)

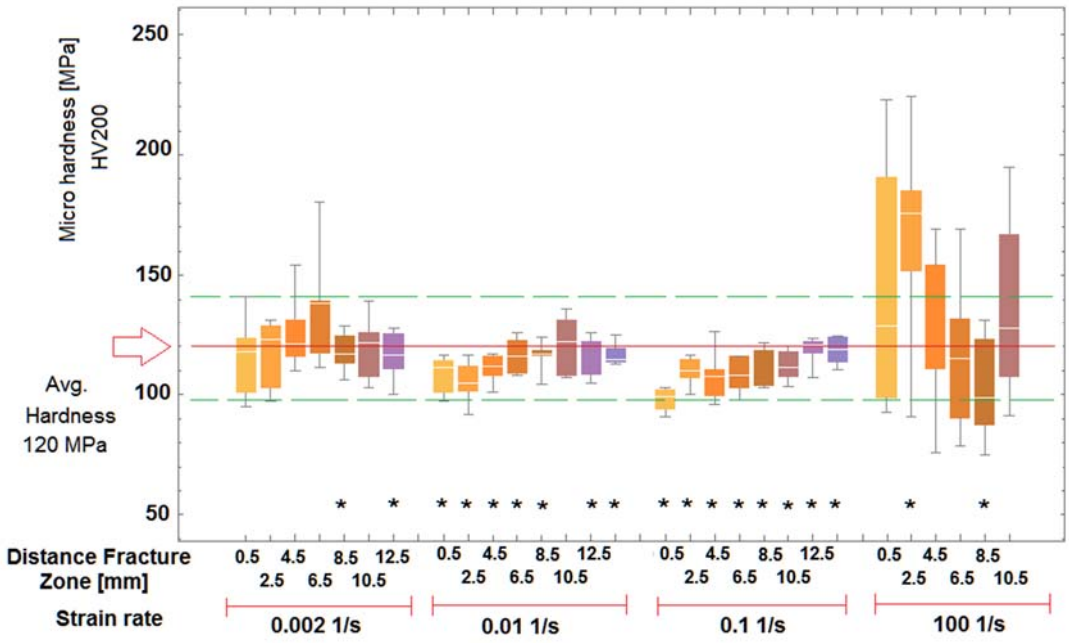

Figure 4-8: Measured hardness of DP-460NS. Undamaged material average microhardness (solid line) with ± three standard deviations (dashed line)

base material, except near to the fracture zone, while both DP-460NS and SA-9850 exhibited a more even distribution of the microhardness values along the sample gauge length. DP-460NS exhibited wide variability in hardness at the two extremes of the strain rates tested, and at the highest strain rate, the average value of microhardness (135 MPa) was higher than that of the undamaged material mean (120 MPa). Due to the variability of the DP-460NS samples at the highest strain rate (100 s^{-1}), the individual samples were investigated in detail to clearly understand the reason for this change and variability (Appendix B, Figure B3-1, and Table B3-1).

4.4.6 Damage Calculation

From the microhardness measurements (Figures 4-6 to 4–8), and assuming that the material base microhardness was a constant (Table 4-4), the damage at each measurement location was calculated (Equation 4-2). Damage values were calculated considering only softened material, which is a limitation of the analysis. The calculated damage was summarized using whisker boxes (Figures 4-9 to 4–11). Note that only information for locations that were statistically significant (identified by * in Figures 4-6 and 4-7) was included for EC-2214 and SA-9850, whereas all the measured data was used for the DP-460NS damage calculation.

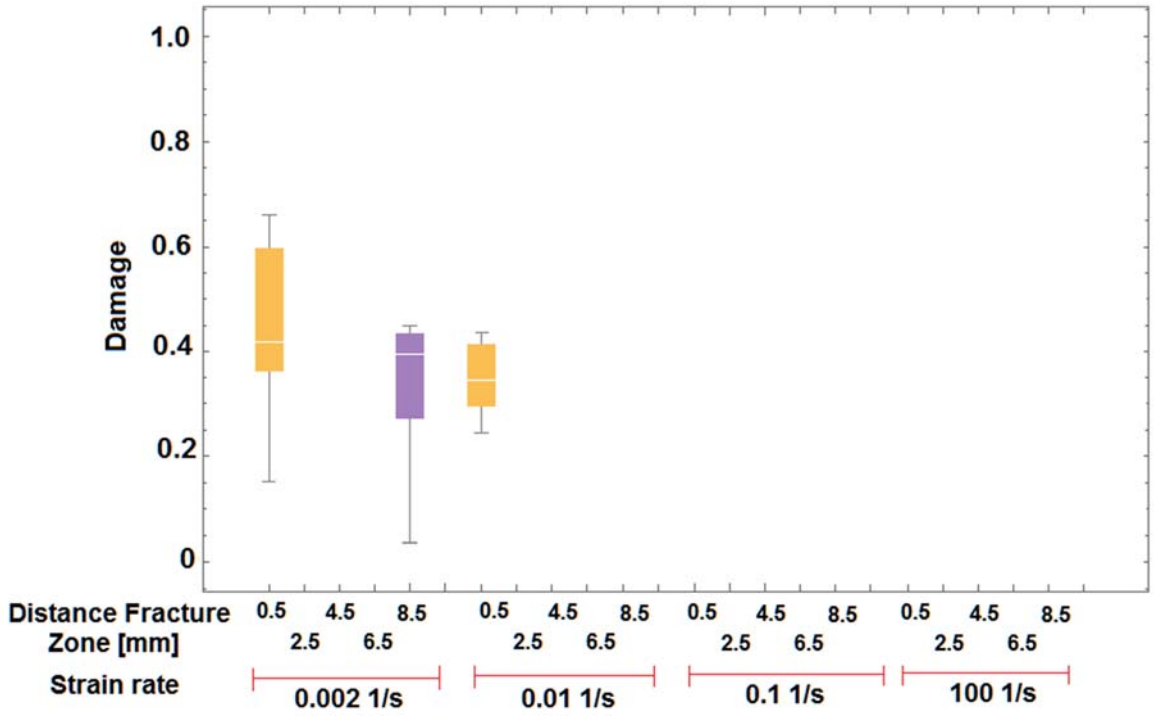

Figure 4-9: Damage calculated from hardness measurements in EC-2214

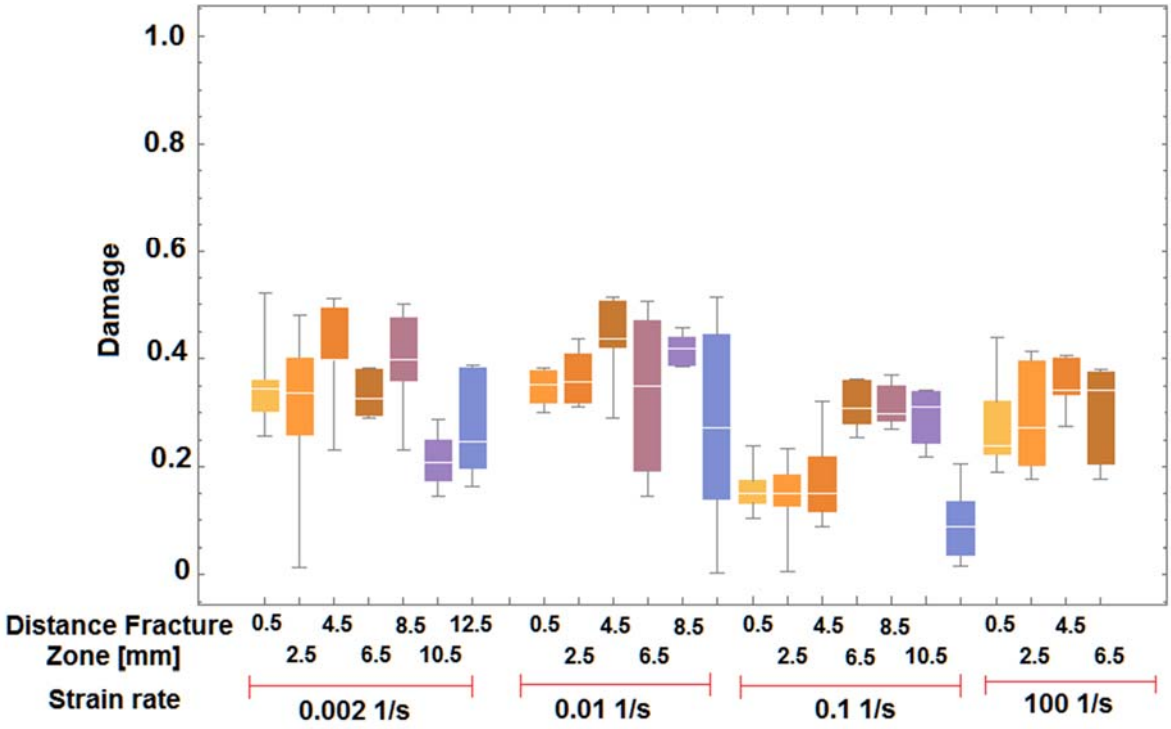

Figure 4-10: Damage calculated from hardness measurements in SA-9850

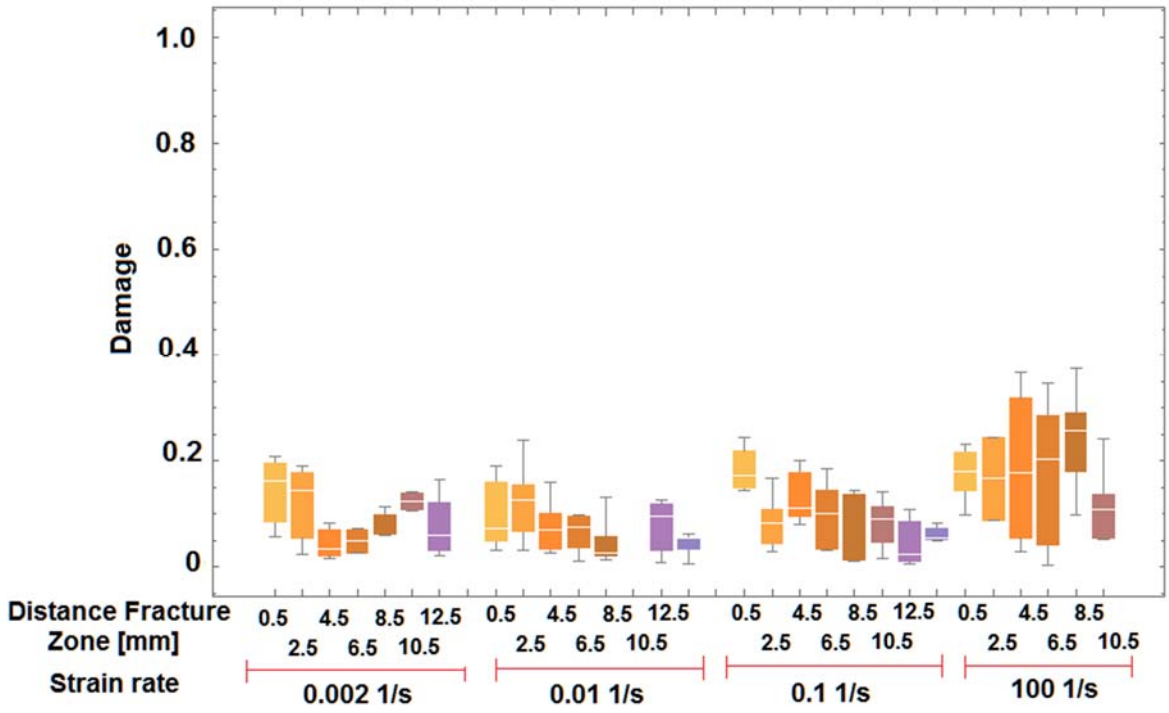

Figure 4-11: Damage calculated from hardness measurements in DP-460NS

According to the damage calculations from microhardness, for EC-2214 (Figure 4-9) the average damage value at quasi-static rates was 43%. There was great variability in the calculated damage, and the reported values could be as low as 15% and as high as 66%. Moving away from the fracture zone the calculated damage always decreased. At the next strain rates (0.01 and 0.1 s^{-1}) the trend was repeated, with higher damage detected towards the fracture zone than in the furthest location reported. Two trends in the calculated damage were noticed: with increases in strain rate the amount of damage decreased; and increasing differences between the value at the fracture zone and the other locations were also detected.

In the case of SA-9850 (Figure 4-10), the calculated damage value varied around an average of 37% and was independent of strain rate up to a strain rate of 0.01 s^{-1}. The damage was more or less distributed evenly along the length gauge of the specimens, although increased variability and trends towards lower values were detected further away from the fracture zone. At higher strain rates, localization began to appear in the vicinity of the fracture zone, and the calculated damage was reduced to 25% on average. The samples at 0.1 s^{-1} had a trend not noticed anywhere else. For this data, the calculated damage was greater further away from the fracture zone (30% on average), than closer to the fracture zone (20% on

average). Further review of the microhardness values (Figure 4-7) indicated that for this particular sample group, there was a reverse in the microhardness trend close to the fracture zone.

The DP-460NS damage data (Figure 4-11) reflected a trend towards higher damage in the region of the fracture zone. The calculated damage was 20% on average closest to the fracture zone for all strain rates. The damage was typically higher towards the fracture zone and then tapered off towards a lower value (5–10%) moving away from the fracture zone. At the highest strain rate tested (100 s^{-1}), the damage closest to the fracture zone was also around 20% on average, but there was variability along the gauge length. Fluctuations between 16% and 25% in average value were detected in these zones. Finally, at the furthest location average damage was calculated as 10%.

4.5 Discussion

4.5.1 Measurement of microhardness in epoxy materials

The traditional equipment used to measure microhardness can have difficulty identifying indentations in certain materials, specifically polymeric materials with aggregates that appear dark under microscope light (Figure 4-4, SA-9850 and EC-2214 materials). Although measurements with a filar micrometer and a regular confocal microscope were possible, it required high skill, and in some cases, it proved challenging to properly identify the location or the boundaries of the indentation. Identification can be enhanced with the use of a contrasting medium (marker ink), but this approach remains limited because while it can aid in identifying the presence of an indentation, it cannot clearly delineate the boundaries. In this study, an opto-digital microscope (ODM) was used to verify previous measurements gathered with a traditional filar micrometer and regular confocal microscope imaging. Importantly, the ODM capability to measure surface profiles facilitated the identification and measurement of indentation features (Figure 4-4 far left vs. Figure 4-5), especially in low contrast conditions.

4.5.2 Length scales

The damage calculations assumed that each adhesive could be treated as a continuum. Such an assumption must be supported by demonstrating that the material microstructure, inhomogeneity and the length of the damage features were sufficiently smaller than the size of the microhardness indentation.

For the EC-2214 and SA-9850 adhesives, the material microstructure can be considered as an aggregate of particles (Figure 4-4, center and far right). Such particles were typically circular in shape and 3–37 μm in diameter (Table 4-3). In DP-460NS, micrographs showed a random distribution of the elastomeric phase in both particle shape and size. Particle analysis in this material identified sizes up to 22 μm in diameter in the observed region. Measurements of damage features identified micro-cracks in DP-460NS up to 4 μm in width and up to 50 μm in length, while shear bands were typically 50 μm in width and oriented at 30°. The measurements were reasonably close to the reported data in the literature for crazing crack openings, on the order of 1–2 μm [114,194,252–254] in different polymeric materials. From a fracture mechanics perspective, given the similarity in mechanical properties (Table 4-2) and particle sizes (Table 4-3) across the toughened materials (DP-460NS and SA-9850), the reported crack sizes should be a representative length scale of damage features for both materials. For the regular epoxy (EC-2214), given the lower fracture toughness, the characteristic length of damage features are expected to be smaller than the measured values in DP-460NS. Microhardness indentation sizes ranged between 140 μm and 316 μm (Table 4-4) in diagonal length. Typical micro-indentations are depicted in Figure 4-4 inside the red circle. From the ODM results (Figure 4-5), a value of 6 μm can be considered as a representative magnitude of the indentation depth. The microhardness diagonal length scale is at least 3 times larger than the largest microstructure features, and ~300 times larger than the smallest features in the material. Not considering the depth of indentation, the materials could be treated as a continuum for damage characterization and interpretation of the hardness measurements.

4.5.3 Measured microhardness values

Microhardness measurements made in the undamaged materials were lower than the typical expected range for epoxy resins (~300 MPa), but this can be expected as the tested epoxy adhesives incorporate different levels of elastomeric materials in their chemical composition. The EC-2214 epoxy with the lowest amount of toughening agent (< 5% per weight) exhibited the highest microhardness (250 MPa). This value is below that reported by Paplham [262], but well within the approximate expected range of epoxy materials (165–300 MPa). Both DP-460NS (120 MPa) and SA-9850 (102 MPa) had a higher content of toughening agent, which was reflected in lower microhardness measurements. Tabor's relation was also evaluated using the undamaged material measured microhardness, and compared to the measured yield strength and ultimate strength. For all three materials the calculated ratios were between 3.3 and 4.7 using the yield strength, and between 3 and 4 using the ultimate strength. Given these values, we consider that the Tabor relationship can provide a reasonable approximation of the

strength for the epoxy adhesives examined in this study. Conversely, since yield values for polymeric materials are scarce in the literature, the ultimate strength could be used to obtain a reasonable approximation for the microhardness of the material when needed. Baltá-Calleja [257] linked microstructure with the Tabor findings and explained that materials with hardness to strength ratios close to 3 are representative of polymers with high crystallinity. Clearly, the measured ratios in this case cannot be interpreted in terms of crystallinity alone because epoxy resins are generally considered to be amorphous glassy polymers.

4.5.4 Strain rate effects on the microhardness

The microhardness indentation data were used to investigate the effect of strain rate on the hardness of the structural epoxy adhesive materials.

In general for the EC-2214 material, changes in microhardness were highly localized at the fracture zone and no other statistically significant changes were identified along the gauge length, although variability was present in the results. Microscope observations of the material (Figure 4-4, middle) show that the micro-indentations can cover regions that include the aluminum additive used in the material formulation, which could play a role in the variability. For the single-part EC-2214 epoxy, the microhardness data (Figure 4-6) and the T-test analysis demonstrated that for the two lowest strain rates tested (0.002 and 0.01 s^{-1}), the microhardness had lower values at, and adjacent to, the fracture zone. For the 0.1 s^{-1} data, two locations were found to be statistically different from the untested material (Figure 4-6). However, this result was attributed to sample composition variability and not linked to actual changes in hardness caused by loading. At these two locations the measured microhardness averages (227.95±20.79 MPa and 201.83±35.99 MPa) were within one standard deviation of the virgin material microhardness (251.06±38.04 MPa). A T-test with increased significance level to 99% reports that at the two locations, the microhardness was the same as the base material. Similarly, at the higher strain rate (100 s^{-1}) no statistically significant changes in the measured microhardness were detected.

For the SA-9850 adhesive, the T-test confirmed that the microhardness trend was towards values that were statistically lower than that of the undamaged material (Figure 4-7). A noticeable change in the material microhardness trend with strain rate was detected: at low strain rates (< 0.01 s^{1}) the microhardness ranged from 60 MPa to 70 MPa, while at higher strain rates microhardness ranged from 70 MPa to 80 MPa. In both cases, these fluctuations were statistically different, and lower than the undamaged material microhardness of 102 MPa. They were also statistically different from each other.

Of the three tested materials, the DP-460NS results were most challenging to interpret, a difficulty attributed to the damage mechanisms active during deformation. For the lowest strain rate, the statistical T-values reported both significant and non-significant values, with no observable trend. The changes in significance for the T-values along the test gauge can be explained by the observed changes in the material caused by the loading history. At very low strain rates, the material first experienced crazing, which then transitioned to well-defined shear bands as deformation progressed. During the initial craze formation stage, groups of voids developed that softened the material. As the strain was increased, the development of shear bands caused a significant stretch in the polymeric chains, leading to re-hardening of the material. The occurrence of these two potentially competing damage mechanisms led to no noticeable changes in the material microhardness (Figure 4-4 to 4-8). This type of effect in the microhardness, i.e., re-hardening with strain, has been reported in the literature for other materials [257,261,265]. The wide fluctuation in microhardness between softer and harder material along the test sample gauge length can be due to pockets of softer crazed material among hardened shear-banded regions, hence the changes in significance for the T-values along the test gauge. It is also important to consider that the many damage mechanisms available for toughened epoxies, as described in the Introduction, can play a significant role in the variability of the measured values. Furthermore, as pointed out by Bucknall [250], differences in particle size can also influence the balance between crazing and shear banding across regions of the material, further complicating the possible reasons for the variability. At the next two tested strain rates (0.01 and 0.1 s^{-1}), the material had less chance to develop a transition between shear banding and crazing, hence the trend in lower microhardness towards the fracture zone. At the highest strain rate, the average microhardness (132.5 MPa) was statistically higher than the material mean microhardness value (Appendix B, Table B3-1, 100 s^{-1} T-test results), although high variability in the data was noted (Figure 4-8, right). The individual sample measurements (Appendix B, Figure B3-1, and Table B3-1) confirmed the same phenomenon detected in the samples tested at the quasi-static strain rate. For areas where crazing development was evident, the microhardness decreased. At zones where shear bands were present, the microhardness increased.

4.5.5 Calculation of damage in the epoxy materials

According to the damage calculations from microhardness, the calculated post-test damage ranged between 20% and 42% in the materials. Although the average tolerance for damage in EC-2214 (34–42%) seems comparable to the other two adhesives, one should consider that the calculated damage, according to the statistics, can be as low as 15% in the fracture zone (Figure 4-9). The concentration of

damage in a small area of the test sample and low strains to failure demonstrated the brittle nature of this material. In the case of the toughened epoxies, the damage tolerance was demonstrated by the capacity of the materials to propagate damage along the test sample gauge section. This was favoured by the capacity of the materials to develop crazing, due to the presence of toughening agents. Calculated damage values along the sample gauge length for both SA-9850 (30–40% damage, Figure 4-10) and DP-460NS (20% damage, Figure 4-11) demonstrated the ability of these materials to tolerate damage across a large area of the loaded material. At higher strain rates the capacity to absorb damage was reduced in SA-9850 (20% damage) but remained constant in DP-460NS. Although, at the higher strain rates, DP-460NS demonstrated the initiation of localization, while SA-9850 maintained some of its capacity to tolerate and distribute damage along the test gauge. The differences between low strain rates and high strain rates can be explained by a reduction in the ability of the materials to develop crazing to the same extent as possible during quasi-static loading.

Intuitively, one would expect damage values to be higher in the toughened materials than in the brittle epoxy, as was the case with the PS and HIPS data [45]. In this regard, the shear banding present in the toughened epoxies had a re-hardening effect in the measured hardness value that biased the damage calculation towards a lower result. It is possible to circumvent this issue by extrapolating the undamaged material microhardness as proposed by Lemaitre [141] for the case of materials where damage and strain hardening occur simultaneously. Using a reference hardness value (H_o) of 300 MPa, typical of a pure epoxy resin, the damage of the toughened epoxies would be on the order of 60–80%, given the range of measured microhardness after failure in both DP-460NS and SA-9850. This is more in accord with the values presented for HIPS [45]. Although the calculated values for damage were not unreasonable for the plain epoxy adhesive (EC-2214), further consideration needs to be given to damage evolution and measurement in toughened epoxy materials (DP-460NS and SA-9850). Both softening and hardening were coupled, and both effects need to be quantified in order to obtain an improved calculation of material damage.

4.6 Conclusions

Three different epoxy adhesive materials (EC-2214, DP-460NS and SA-9850 3M, Minnesota) were tested under tensile load at different strain rates and were evaluated using microhardness measurements as a means to measure material damage. Traditionally, micro-indentations for microhardness

measurements were measured with a filar micrometer or with the aid of a confocal microscope. In this study, the use of an opto-digital microscope (ODM) was explored, and it proved to provide a significant advantage for identification and measurement of microhardness indentations, particularly for low contrast surfaces where the traditional filar micrometer or optical microscopes may not be adequate to measure the size of the indentation. The microhardness measurements demonstrated that changes along the gauge length were dependent on both strain rate and the chemistry of the adhesive. In a non-toughened epoxy (EC-2214), the damage was highly localized around the fracture zone. In toughened epoxies (DP-460NS and SA-9850), the damage extended over much of the sample gauge length and the microhardness variations were linked to the deformation mechanisms, i.e., crazing and shear banding. In these two materials, the shear banding generally increased the measured hardness, while crazing decreased the measured hardness, offsetting one another and ultimately affecting the damage results. With increments in strain rate, localization increased.

Even though there was a localization effect on the measured damage that prevented measuring hardness, and therefore damage data at high strain rates, microhardness measurements were a valuable tool to quantify damage for epoxy adhesive materials subjected to tensile loading under a wide range of strain rates. The microhardness data along the test sample gauge length were also used to generate damage profiles (Figures 4-9 to 4–11), which cannot be easily obtained by other traditional means to measure damage, such as detecting changes in the modulus of elasticity using load-unload cycles. The Tabor relationship applied to polymeric materials was also explored, and the results suggest that it can be used with toughened epoxy adhesive materials to provide an estimate of strength from hardness values. The microhardness information can be used as an additional verification point for assessing damage prediction capabilities of constitutive models for use in analysis, design and computational models that include adhesive materials.

Out of the tested materials, only DP-460NS exhibited strain whitening tied to two different mechanisms (crazing and shear banding). Although strain whitening is typically associated with crazing [270,271], the actual underlying mechanism that causes the optical change needs to be fully identified, quantified and compared against known measurements of damage. Chapter 5 will explore in depth the evolution of damage in the two-part epoxy adhesive material using microscopic observations and changes in modulus of elasticity. Even tough SA-9850 demonstrated strain whitening and other traits that deserve

further investigation (e.g. better damage propagation at higher strain rates), lack of availability for this material precluded further studies.

Chapter 5
Strain Whitening and Damage Correlation in a Toughened Epoxy Adhesive

5.1 Overview/Abstract

Owing to the increased use of toughened epoxy adhesives in current transportation light weighting efforts, it is critical that the damage mechanisms observable as strain whitening in these materials are understood and quantified. Quantification of damage is needed for finite element constitutive models used in structural design; however, thin bond lines in adhesive joints limit direct observation of the adhesive. In this study, microscope observations of bulk material specimens subjected to tensile loading were linked to strain whitening and damage in a toughened epoxy adhesive. Cracks on the surface were observed to open during loading, with strain whitening observed at the crack tips and with the initiation and propagation of shear bands were identified. The stresses approximated at the crack tips suggested that particle cavitation could be occurring in these regions. Image analysis showed that strain whitening was present at crack tips and that these areas served to initiate shear-bands.

Changes in tensile specimen stiffness and strength were evaluated during load-unload and reload testing, and were linked to the presence of crack growth, as well as the formation of shear bands. Considering changes in strength, the predicted damage level before failure (D~18%) was lower than that predicted using traditional load-unload stiffness (D~35%), attributed to short-term viscoelastic effects; however, damage calculated from load-reload material stiffness (D~19%) was in good agreement with the damage estimated from changes in strength. A new approach, calculating damage from direct image analysis of strain whitening on the free surface (D~21%) was in good agreement with damage quantified by changes in strength and stiffness, with the benefit of quantifying damage over the loading history of the test sample and identifying areas of damage localization.

5.2 Introduction and background

The use of modern structural adhesives makes it possible to join dissimilar materials when traditional joining methods (e.g. welding) may not be feasible or when the potential for galvanic corrosion exist (e.g., steel to aluminum). Also the use of adhesives allows for continuous joints with benefits [51,177,178,272,273] relative to traditional discontinuous mechanical joints (bolts, rivets, spot-welds, etc.) because they result in structures that are stiffer, can absorb more energy under extreme deformation, and also reduce unwanted vibrations and stress concentrations at joints [51,183]. Due to the relevance of toughened structural adhesives in current light weighting efforts, it is critical that designers and engineers understand the mechanisms that lead to their failure so that these materials can be used effectively and in accordance with the expected loading demands associated with the intended use of the bonded structure.

Although it is important to acknowledge the potential differences between thin bonds and bulk adhesive materials [271], recent investigations in regards to identification of material properties in epoxy adhesives tend to favor the use of bulk samples. Previous studies by different authors using bonded joints have reported that stress concentrations caused by geometry (fillets) [190,274], complex states of stress (i.e. triaxiality) associated with adhesive thickness [275,276], strain rate effects [201,203,277], and agglomeration of particles in thin bonds [278], can influence the development of different failure mechanisms in adhesive systems. On the other hand, the use of bulk samples is amenable to the implementation of different experimental techniques that can directly identify the stress-strain response (e.g. Hopkinson bar [21,166], optical techniques [46], grid methods [23,165]) or other parameter of interest such as microhardness [263,279] or fracture toughness [166]). Some of these techniques cannot be implemented otherwise due to the impracticality and constrains imposed by thin bond lines (complex states of stress, stress concentrators, clearance and geometric constrains, etc.). However, the use of bulk samples is limited by the difficulty to obtain pore-free samples [280]. Nevertheless, the use of bulk samples provide results that are independent of the tested geometry, the adherent properties, and avoid the use of reverse identification procedures [280].

A common observation in toughened polymeric materials under tensile loading is the development of strain whitening. Strain whitening then, can be considered as a manifestation of the damage mechanisms that are active in a polymeric material. Although strain whitening is generally associated with crazing [270,281], other phenomena such as cracks, particle debonding and cavitation [41,282] , and shear banding can cause light scattering and manifest as strain whitening.

Structural adhesives can have many different formulations (urea, melamine, epoxy, toughened epoxy with rubber particles, toughened epoxy with hard particles, etc.) [20] which explains the rich mechanical responses that can be observed in these materials when subjected to load (e.g. high elasticity modulus with brittle failure, ductile response with large deformation, differences in fracture toughness) [85,86,107]. In previous studies [248,279] three different adhesive formulations (a one part epoxy, a two part toughened epoxy, and a one part toughened epoxy) were tested under load. However, the two-part phenol resin epoxy with a thermoplastic phase and silicone content for toughening (DP-460NS) demonstrated unique characteristics in its mechanical response: high stress to failure (~40 MPa), large deformation accompanied with the development of both strain whitening and shear banding. At ultimate failure (e~0.2), the material typically exhibited the characteristics of a brittle fracture at the failure plane. Given these mechanical characteristics and the relevance of toughened adhesives in modern engineering design [20,51,182,183], this adhesive was selected to further investigate the causes of strain whitening and quantification of damage.

Toughened polymeric materials can contain initial defects (e.g., cracks, surface non-uniformities, etc.) which serve as initiation points for the development of damage mechanisms such as crazing, particle cavitation and shear banding. Crazing can be described as the development of fibrils/tendons that delay crack opening and allow the material to absorb more deformation energy prior to ultimate failure. Although crazing is a significant failure mechanism in toughened thermoplastics [9], it is a controversial topic in epoxy materials. While certain authors acknowledge the possibility as presented by Yee and Pearson [106]; others as presented by Garg [107] dispute the presence of this mechanism. To further complicate the subject, craze-like damage in toughened epoxies has been reported in the literature [73,108].

Craze-like damage was explained by Sue [108] as load carrying fibrils or tendons that arrest crack growth initiated from scattered cavitation in the core-shell particles used to (Butadiene particles surrounded by a hard shell material) modify an epoxy matrix. Cavitation in this context (damage in materials), can be understood as the creation and propagation of voids inside a solid due to a hydrostatic, or tri-axial, tensile stress.

Damage due to particle cavitation can also manifest as strain whitening. In this case, the voids created by the cavitation at a particle are responsible for reflecting light and can explain the changes towards a

whitened color. The critical stress to initiate void nucleation and cavitation in a particle depend on the initial size, modulus of elasticity and the fracture energy of the embedded particle material [109]. A critical stress value (σ_c) to initiate cavitation can be approximated by the modulus of elasticity (E) for rubber inclusions (Equation 5-1) ranging from 0.5 μm to 1 mm in diameter [109].

$$E_{d\sim 1mm} \leq \sigma_c \leq 3E_{d\sim 0.5\mu m}$$

Equation 5-1: Approximate cavitation stress for rubbery inclusions [109]

Light scattering in crack tips can also contribute to the strain whitening. However, the development of plastic zones around crack tips can play a role in energy absorption and delaying failure in polymeric materials [107,110]. For microscopic cracks, Gent [283] investigated the expression developed by Inglis [284] (Equation 5-2) to calculate the stress concentration factor (k) in terms of the crack length (l) and the tip radius (r). Gent explains that the most severe edge flaws which might occur by chance in smooth machined surfaces, would be about 100 μm long and about 10Å in tip radius. This corresponds to a value for k of about 200. However, Gent proposed stress concentration values ranging from 10 to 50 [283] as a more reasonable figures for edge flaws in normal tensile test-pieces. Patterson proposed a stress concentration factor of 25 [285].

$$k = 1 + 2\sqrt{\frac{l}{r}}$$

Equation 5-2: Stress concentration factor [284]

Ductile polymers can also deform by developing shear bands [93,98,110,268]. Shear bands are traditionally identified by areas that are birefringent and are oriented at well-defined angles, typically 45° relative to the principal axis of loading. Shear bands generally initiate at stress concentration points and can develop locally high strains, well above the nominal strain in the material [95,97,98].

The consequence of physical damage to a toughened polymer in the form of cracks, cavitation and shear bands can be described in a quantitative manner using the concept of damage (D). A widely-used definition of damage is a process in which voids and defects grow inside a volume of material until fracture is unavoidable, quantified as the ratio between the volume of voids (V_D) in a representative volume of material (V) (Equation 5-3). Alternatively, the ratio between the area of voids (A_D) that intersect a plane and area of the plane (A) [141].

$$D = \frac{V_D}{V} or\ D = \frac{A_D}{A}$$

Equation 5-3: Damage calculated based on voids in defects in a representative volume or area

According to Lemaitre [44,141], the average damage experienced by a material can be calculated indirectly by using the changes between the material modulus of elasticity (E_o) and the modulus of elasticity during unloading (E_u) (Equation 5-4). Load-unload has been used repeatedly in the literature to measure damage in polymers [166,209,286,287].

$$\overline{D} = 1 - \frac{E_u}{E_o}$$

Equation 5-4: Damage as a function of changes in modulus of elasticity

In addition to changes in modulus of elasticity, variations in effective stress can also be used to determine the amount of damage that a material has sustained. If all defects are open such that there are no forces acting on the surfaces of the defects, then an effective stress ($\bar{\sigma}$) can be related to the ultimate strength of the material (σ_{UTS}) and therefore damage (Equation 5-5) [141].

$$D = 1 - \frac{\bar{\sigma}}{\sigma_{UTS}}$$

Equation 5-5: Damage as a function of changes in effective stress

Although the literature reports the effects of damage in adhesive joints such as changes in fatigue performance [288,289], crack growth prediction [37], strain fields in patched repairs [290,291], and failure analysis of joints [292]. The material is typically link to specific industry applications (composites and composites repair for aerospace [293–296], wind energy [297], boat construction [298], pipe industry [299]) or with the development of health monitoring techniques for field service assessment [300–303]. However, there is paucity of information regarding quantification of the actual damage that the previously described mechanisms (plastic zones at crack tips, particle cavitation, and shear banding) can introduce in actual structural adhesives. In the present study, damage was assessed using bulk samples made from a structural epoxy adhesive by applying uniaxial tensile deformations, enabling both direct and indirect measures of damage. The bulk specimen surfaces were observed using an opto-digital microscope while under tensile loading to determine the causes for the strain whitening and to evaluate observable damage in the material. Damage from traditional indirect measurements

such as changes in modulus and changes in effective stress were used for comparison and to evaluate damage from the optical observation.

5.3 Experimental methods

5.3.1 Material and specimen geometry

A thermoplastic (Methyl Methacrylate-Butadiene-Styrene, MBS) toughened two-part epoxy adhesive (DP-460NS, 3M, Minnesota) (Table 5-1,) was used to investigate damage evolution under quasi-static loading. Epoxy sheets, 3mm in thickness, were manufactured by casting the adhesive material between two glass plates followed by oven curing at 70°C for two hours [192]. The tensile sample geometry (Figure 5-1) consisted of a grip zone and a gauge section, 3 mm in width and 12.5 mm in length. The samples were machined from the cast sheets and tested in uniaxial tension. The tested geometry has been used in previous work [248,279] and demonstrate tensile behavior comparable to that of the ASTM type V geometry [248].

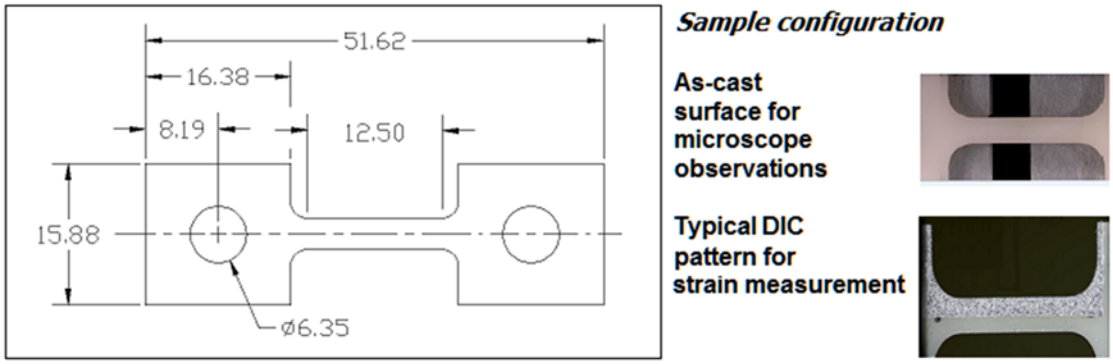

Figure 5-1: Tensile specimen geometry and configurations for testing

ρ [kg/m^3]	E [GPa]	ν	Ultimate Stress [MPa] @ 0.002 s^{-1}
1200	2.52±0.34	0.41	39.03±3.56

Table 5-1: Mechanical properties of DP-460NS adhesive [279]

5.3.2 Microscope observations

Two specimens were loaded in tension to specific strain levels (Table 5-2, Figure 5-2) using a tensile load frame and were observed using an optical digital microscope (ODM) (Keyence VHX-5000, Keyence, Japan). The specimens did not have any previous preparation (Figure 5-1, top right hand) and the illumination setting was fixed for all observations (~75% brightness). A region of the material with an easily distinguishable feature for identification was selected to enable observations at high magnification (> 500x). The region incorporated the entire width of the specimen in the gauge section (3mm) and a length of 1mm. Although the length of the image was limited by the capacity of the ODM to stitch images, the proposed area was large enough to capture the features evolving on the surface of the material due to the damage processes at the microscopic level. The image length was in agreement with the projection of a representative volumetric element (1 mm^3) that could capture the average damage process in polymeric materials as proposed by Lemaitre [141]. The strain levels selected allowed for observation of the material in four key regions of the strain-stress response: elastic, pre-yield, post-yield, and just prior to ultimate failure (Figure 5-2, square points). The yield was assumed to correspond with the extrinsic yield point (Figure 5-2, triangle point), which was determined using *Considères* construction [79].

Measurements made on the observed surfaces were then used to determine the initiation of strain whitening. Changes in images, quantified with the aid of image-processing techniques was used to indirectly determine damage in the material. Additional observations at the surface of a polished sample under tension, and at the shear-banded region of a fractured sample close to the fracture plane were made using the ODM. Lastly, a fracture surface was studied using scanning electron microscopy (SEM).

Strain point	Applied displacement [mm]	Applied strain
1	0.10	0.008
2	0.30	0.024
3	0.55	0.044
4	0.83	0.066

Table 5-2: Applied strain to samples for observation under the ODM microscope

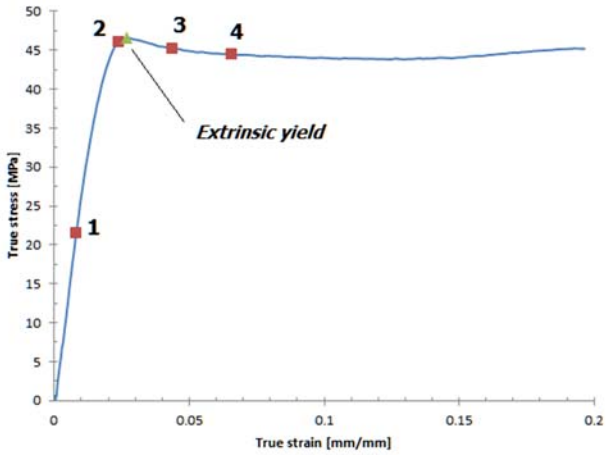

Figure 5-2: DP-460NS quasi-static tensile response with observation points used for microscopy study

5.3.3 Image processing

Image segmentation was used to identify changes caused by strain whitening on the material surface while under tensile load. In the segmented images, white pixels can be considered as features of interest on the surface (defects, cracks, or changes from what is considered as the regular appearance), while the black pixels describe the background (non-strain whitened material in this case). For the image segmentation procedure, a fixed area of interest (AOI) was isolated on the observed surface at high magnification (500x). To assure that the same AOI was always studied regardless of strain; three features on the surface were used to define the corners of a rectangular area. The feature could be a crack, an inclusion or any other noticeable item on the surface image. The same features that defined the original AOI were selected in the captured images for a given sample once deformation was applied.

For each AOI image, the file was first converted into an eight-bit binary image, and then, segmented to separate features of interest (i.e. cracks, regions of stain whitening and shear bands) from the background. Segmentation requires the use of a threshold value, which can bias the results. For procedure consistency, segmentation was done using the IsoData algorithm included with Image J [304]. The IsoData algorithm was selected due to the automatic threshold implementation using histograms [305] and the good rankings (quality of results) that it achieves in different surveys [306–308].The implementation uses an optimal threshold to separate the image pixels into two different classes (object and background). The threshold initial guess is calculated by selecting a region of the image (its four corners) that is most likely to contain only points of the same class (background). The pixel values are averaged to obtain the initial threshold guess. A new threshold is calculated by averaging the integration of the values above and below the previous threshold. The process continues iteratively until the threshold value does not change any more. The image is then segmented into two separate classes using the optimized threshold value. Quantification of the number of black and white pixels after image segmentation determined the relative changes on the material surface. The ratio between the white pixels and the total amount of pixels was used to indirectly capture damage base on the surface changes from load point to load point

5.3.4 Traditional measures of damage

Damage was quantified using two traditional mechanical measures: changes in modulus of elasticity and effective stress during uniaxial tensile loading and subsequent unloading. The resultant stress-strain curves were used to calculate the material modulus of elasticity and to monitor the changes in effective stress. Load-unload measurements used the same test sample geometry as for the microscope observations. A universal hydraulic test machine with a calibrated load cell (Omegadyne model LC-412-500, Omega, Connecticut), a custom software control loop (LabVIEW, National Instruments, Texas) and an electronic controller (MTS FLEX, MTS, Minnesota) were used for the load-unload testing. The control loop made it possible to initiate the cycle at a fixed initial load point, strain the sample to the desired level and then unload the sample back to the initial load point, all under the same constant strain rate ($0.002s^{-1}$). Digital Image Correlation (DIC) [163] software (VIC-2D, Correlated Solutions [225]) was used to measure the test specimen strains using an optical extensometer. Images were captured using high-resolution DSLR cameras (NIKON D3200, 24.7 MP 23.2 x 15.4 mm CMOS sensor, Nikon Corporation, Japan), with a macro lens (SIGMA 105 mm 1:2.8 DG MACRO HSM, Sigma Corporation, Japan) and LED illumination (Lumahawk, AADYN technologies, North Carolina).

Camera and illumination settings were fixed at the same value during the entire test (F8, 1/80 and ISO 1600 for the camera; 95% intensity with 25% temperature for the light source).

During load-unload testing, half of the gauge length of the test sample in the front view included a speckle pattern (Figure 5-1, bottom right hand) for monitoring strain on the surface of the material using the DIC. The uncoated half of the specimen permitted simultaneous macroscopic observations of the strain whitening changes. The load-unload procedure was conducted by loading the testing sample in tension up to a specified level of strain (displacement control) followed by an unloading cycle (displacement control with load monitoring). In between load cycles, the sample was taken out of the grips and the geometrical dimensions measured; this was done for two reasons. Firstly, this method ensured that the sample was unloaded entirely when reference measurements were made. Second, this allowed to account for permanent deformations, and adjust the applied strain for the next load cycle. In this manner, the total amount of applied strain at each cycle was consistent with the first loading. This ensured that no additional damage was introduced. The load-unload cycle was then repeated twice more for a total of three repeats for each test condition. At the beginning of each cycle, the sample was preloaded with a force of 10N to assure proper alignment and eliminate any slack in the grip. Due to equipment limitations in displacement control, caused by the control loop, the applied strain values for load-unload (Table 5-3) were slightly different from those used for microscopy (Table 5-2). Regardless of this limitation, the applied amount of strain for each load-unload condition correctly reflected three of the regions of interest used for the microscopic observations: linear-elastic, before yield, and just prior to the ultimate load.

Strain point	Target strain	Applied displacement [mm]	Actual strain
A	0.008	0.60	0.013
B	0.024	0.90	0.020
C	0.044	1.64	0.070
D	0.066	2.10	0.080

Table 5-3: Target strains applied during load-unload testing

When calculating damage using the stiffness of the material (Equation 5-4), the initial modulus of elasticity (E_o) was determined from the average of the first load cycle in the tested specimens at a particular deformation. The damaged modulus (E_u) corresponded to the average modulus measured during the first unload cycle for a given level of deformation. This follows the traditional convention for the measurements of damage in materials when using the modulus of elasticity [141]. The material modulus of elasticity was determined using the method described in ASTM E11-04 [238]. As previously mentioned load-unload has been investigated in the literature to quantify damage in polymers [166,209,286,287], but viscoelastic effects can present challenges when applying this methodology to polymers. Microhardness data [279] and a side study (Appendix C1), demonstrated that, for this particular material, long term visco-plastic effects were not significant. To minimize strain rate dependencies and viscoelastic effects, the load-unload cycles were carried out under quasi-static conditions. Viscoelastic effects on the recovery portion of the unload cycle were initially considered as non-significant; however, the validity of this assumption was investigated by measuring the load response in subsequent load cycles.

When calculating damage from the strength data (Equation 5-5), the first measure of strength (first load cycle) and the last measure of strength (third load cycle) were used to define the strength of the material (σ) and the effective stress ($\bar{\sigma}$), respectively. For strain values above the extrinsic yield ($e > 0.02$), three load cycles were the maximum number of cycles that could consistently achieve the desired strain levels during testing. Therefore, this number of cycles was used to obtain data that could be subjected to statistical analysis. It was also assumed that after this small number of cycles, viscoelastic effects were eliminated and that the damage was stable.

5.4 Results

5.4.1 Macroscopic strain whitening observations on the surface of a tensile specimen

During uniaxial load testing, the adhesive exhibited strain whitening (Figure 5-3). A qualitative assessment of quasi-static test images determined that as the tensile load was applied, at low strain ($e \leq 0.015$), the material developed small areas of a lighter color compared to the base material. The size of these areas increased, and they coalesced with increasing strain ($0.02 \leq e \leq 0.03$) evidencing further strain whitening in the material. The development of white areas started well before the end of the

elastic range (e~0.015) but the transition towards well-defined and oriented bands did not happen until reaching the maximum stress (45 MPa) and with strains well above 0.04, although the strains were still below the average strain to failure (e~ 0.10) at this point. Localization of strain whitening was noted around the fracture zone of failed samples.

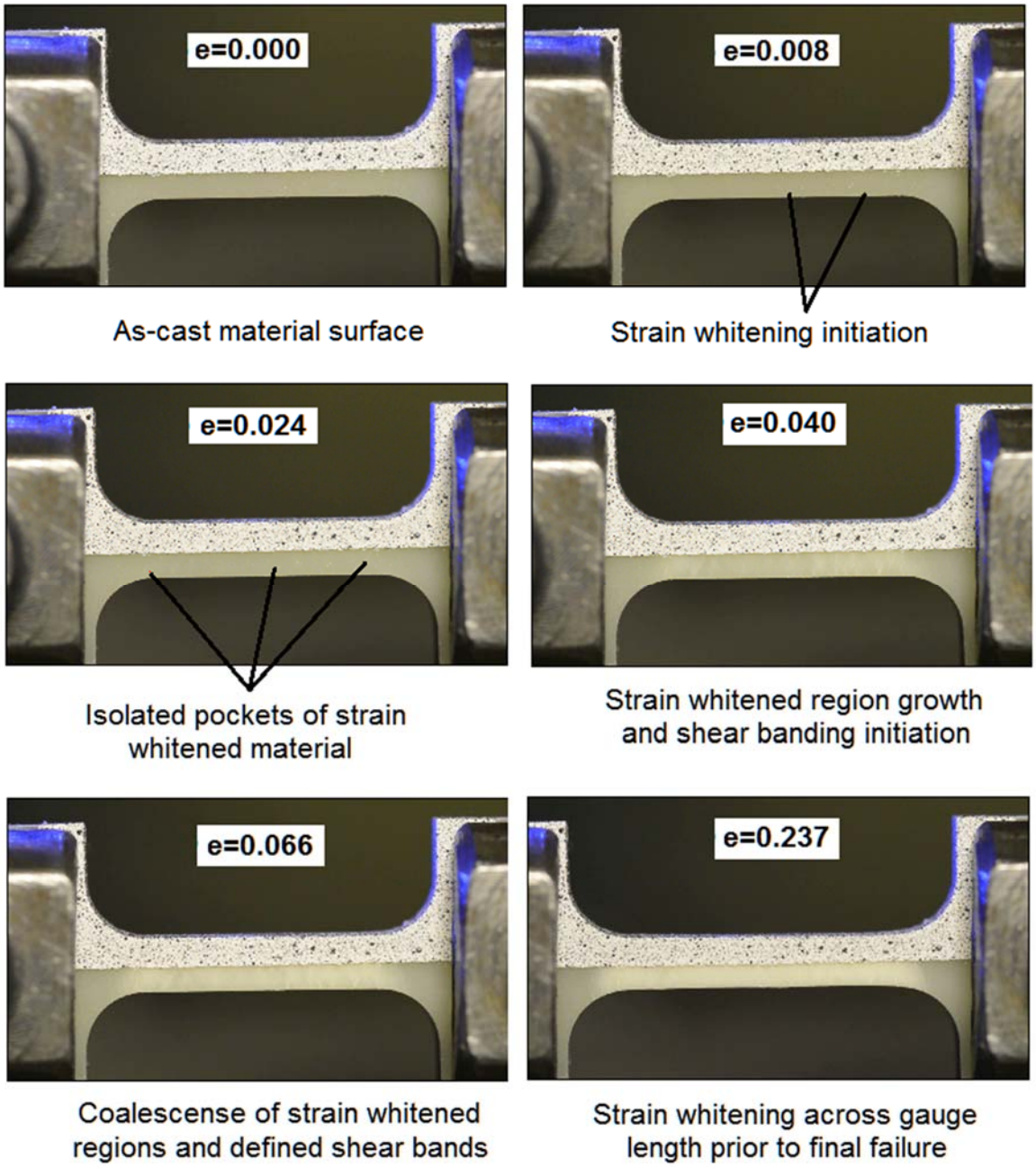

Figure 5-3: Strain whitening observed under tensile loading (0.002 s^{-1})

5.4.2 Microscope observations of test specimen surfaces under tensile load

The material surface was observed under load using an opto-digital microscope. Initial observations at low level magnification (20 to 200x), identified that the observed strain whitening process along the gauge length of the specimen was similar to that observed macroscopically, although it was noted that initial surface changes at low levels of strain ($e<0.01$) were typically initiated at locations that included some sort of surface defect. The source of these defects can be attributed to stresses caused by the curing and casting process. During curing the epoxy needs to go from a liquid to a solid state; this transition requires to physically accommodate the constituents in a given volume limited by the casting setup all of which introduces stresses in the material. For large magnification imaging (500x, Figure 5-4), the observations were concentrated in a small region of the test specimen gauge length. The typical crack evolution in the material (Figure 5-5, 1000x) can be described in the following manner: at low levels of strain ($e<0.008$, linear elastic region) the crack grew very slowly, from its original length of 8.4 μm to 11 μm. At higher strains ($e\sim0.024$, at or just before yield), the crack grew to approximately five times its length ($l\sim50$ μm) due to opening under load and coalescence with other cracks present in the vicinity. At this level of strain, the material whitening developed in small pockets around the boundary of the crack (Figure 5-5, image B). With increased levels of strain ($e\sim0.044$, above yield), the strain whitening grew and spread through the observed surface (Figures 5-4 and 5-5 image C). With further increases in strain ($e\geq0.066$, plastic region), the material transitioned to the formation of well-defined shear bands at a rough orientation of 30° relative to the vertical axis. Geometrical measurements, such as length and width, were made for a crack feature in two individual specimens (Table 5-4); the observations also included calculations for the resultant stress concentration factor *k* (Column 7, Table 5-4; Equation 5-1) and the stress at the tip (Column 8, Table 5-4).

Additional optical observations were made on the material using the ODM. On a polished sample (Appendix C, Figure C2-1), light scattering was detected at a particle (Diameter ~ 167 μm). The color change initiated within the particle and eventually extended beyond the particle boundary towards the epoxy matrix. The observed color change at the particle, which evolved with the strain load may be identified as cavitation.

ODM observations inside the shear band region after failure (Figure 5-6, top right hand) demonstrate the presence of a birefringent surface not observed in the unloaded and undamaged material (Figure 5-6, left hand). Micro-cracks (1 to 5 μm in length and less than1μm in width) and circular particles 3 μm to 20 μm in diameter) were observed in the shear-banded region (Figure 5-6, bottom right). Micro-voids on the surface (≤1 μm) were also present. The propagation of micro-voids and micro-cracks seem

to be roughly oriented between 36 and 55°. Typical shear bands macroscopic orientation was measured between 26º and 30º. The observed shear band surface at high magnifications (Figure 5-6, bottom left) resembled porous material and was similar in appearance to cavitated material in other rubber toughened epoxies [106].

Although the fracture surface under SEM at various magnifications (Appendix C, Figure C2-2) resembles the typical appearance of a toughened epoxy with thermoplastic toughening [86], the morphology of the fracture resembles that of furrows and steps. According to Low and Mei [309], this type of morphology is evidence of crack growth and arrest, and it is similar to those observed in other toughened polymers [115]. No evidence of particle debonding, typically manifested by numerous black voids with a diameter roughly equal to the nominal size of the toughening particles, was evident in the SEM observations.

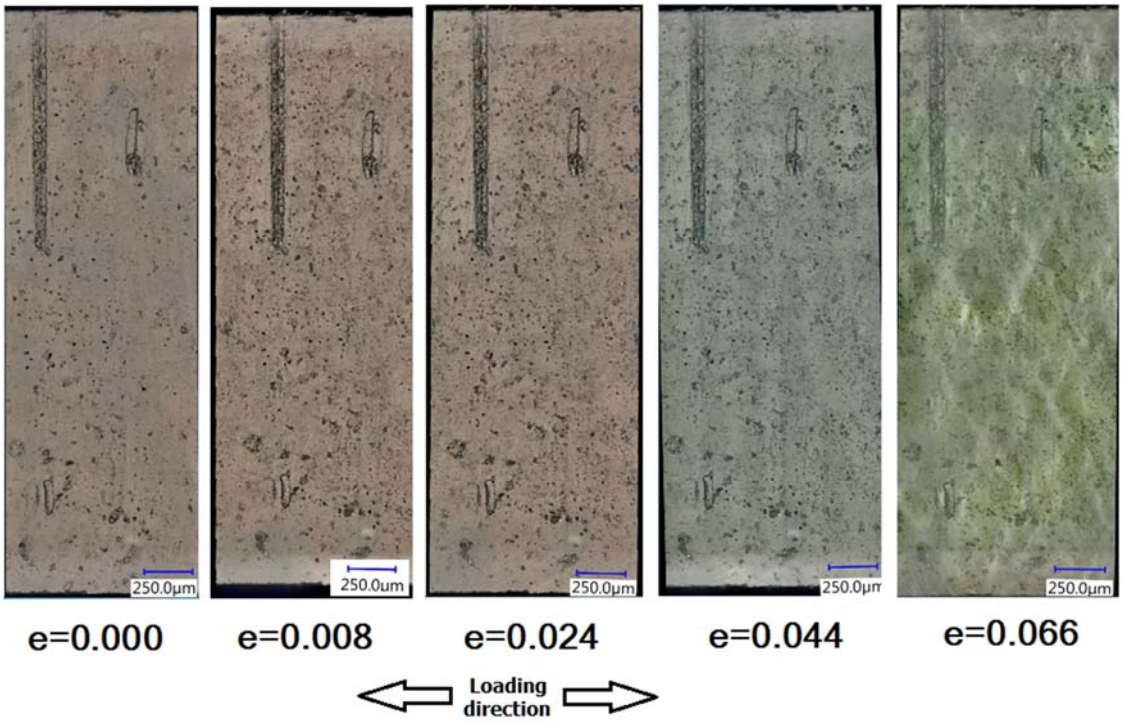

Figure 5-4: Strain whitening under tensile loading in a toughened structural epoxy

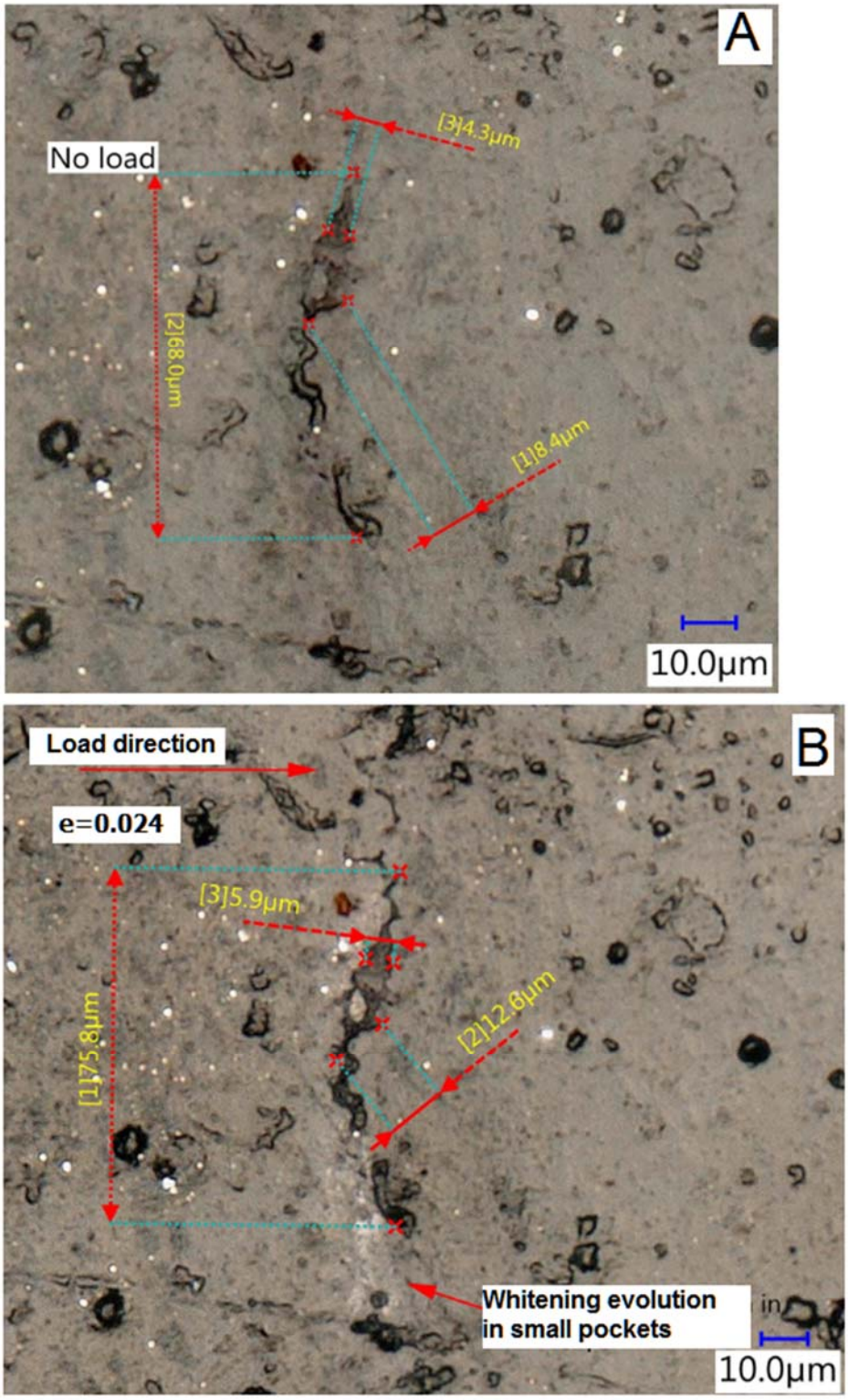

Figure 5-5: Evolution of a crack feature under tensile loading

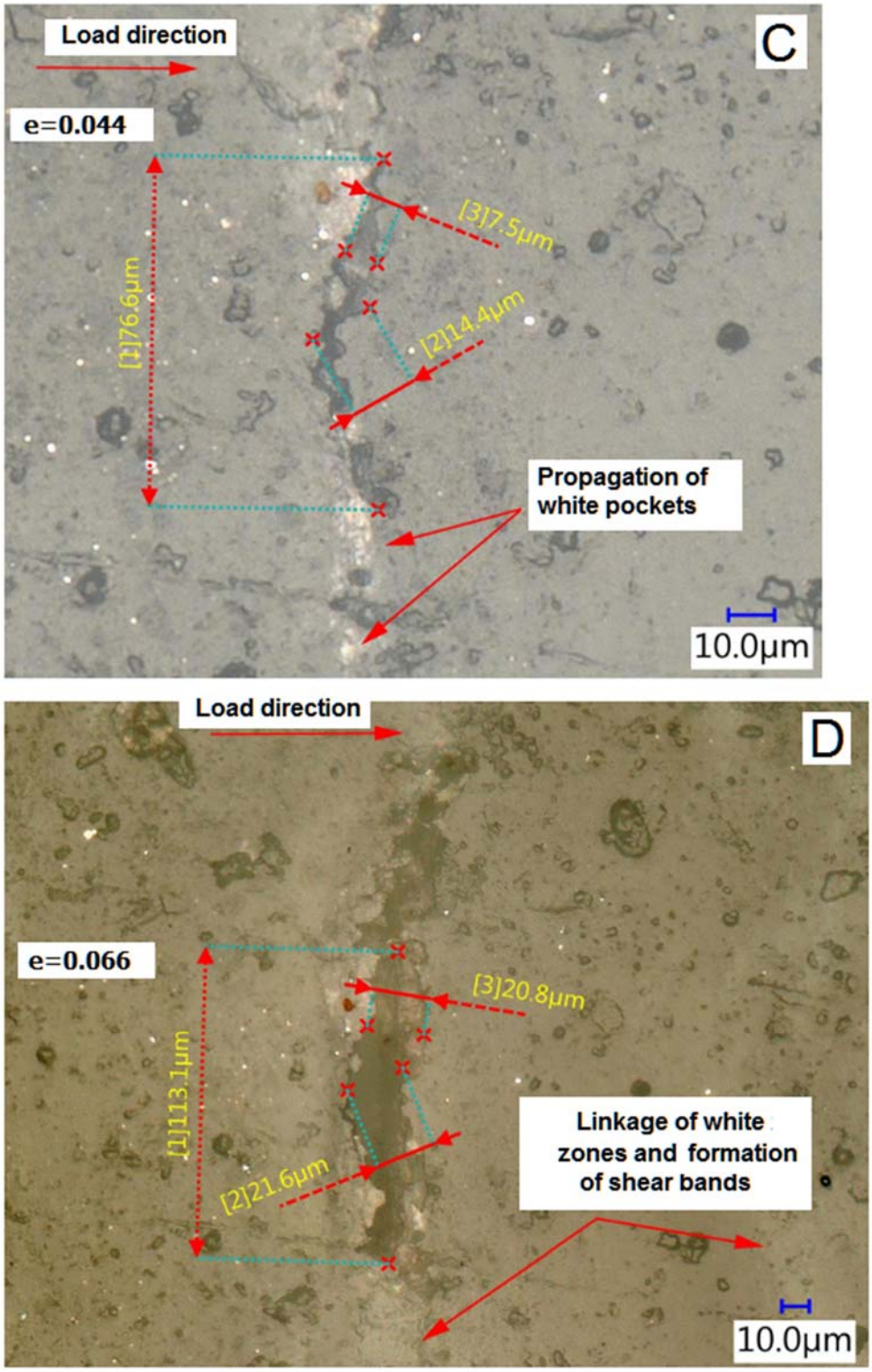

Figure 5-5: Evolution of a crack feature under tensile loading (continued)

Sample	Strain	Av. stress σ [MPa]	Crack length (l) [µm]	Crack width [µm]	Tip radius (r) [µm]	*k* Eq. 5-2	Stress at tip (σ*k) [MPa]	Details
A-OM-2	0.000	0.0	8.4	~1.0	0.1	19	0.0	
	0.008	18.3	11.0	<2.0	0.1	22	402.0	
	0.024	38.6	50.0	< 6.0	1.0	15	584.0	Crack coalescence
	0.040	39.6	50.0	~7.5	2.0	11	436.0	
	0.066	39.4	130.0	~20.8	10.0	8	324.0	
A-OM-4	0.000	0.0	26.1	2.3	0.1	33	0.0	
	0.008	18.3	41.9	3.5	0.1	42	767.0	Crack coalescence
	0.024	38.6	100.0	3.8	1.0	21	811.0	
	0.040	39.6	100.0	2.3	1.0	21	832.0	
	0.066	39.4	100.0	2.9	2.0	15	597.0	

Table 5-4: Measurements of observed crack features for two test specimens under axial loading

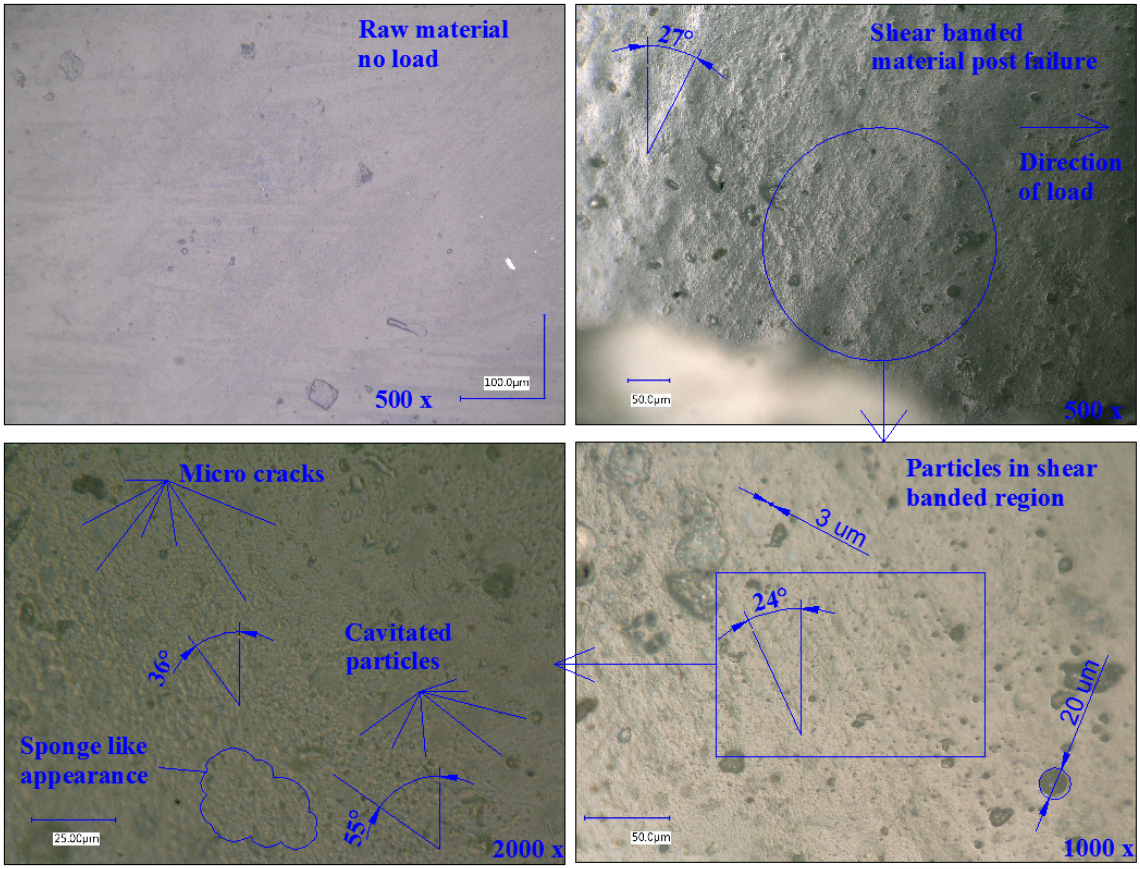

Figure 5-6: Observations of shear banded material. From top left in the clockwise direction: undamaged material. Shear bands after quasi-static tensile failure. Shear banded region at high magnification. Cavitated particles, micro-cracks and porous surface texture.

5.4.3 Tensile specimen surface, microscopic image analysis

Image segmentation was used to isolate the optical changes on the material surfaces resulting from material damage (i.e., color changes on the surface due to crack opening) caused by the applied strains. In the segmented images (Figure 5-7), the background (black pixels) can be considered as original unchanged material, while the white pixels identify changes on the material surface. The number of black and white pixels in the images was monitored and provided a way to quantify the evolution of features on the material surface (Table 5-5). Additionally, the changes in overall AOI dimensions were used to provide a measurement of the local average engineering strain (Column 4, Table 5-5).

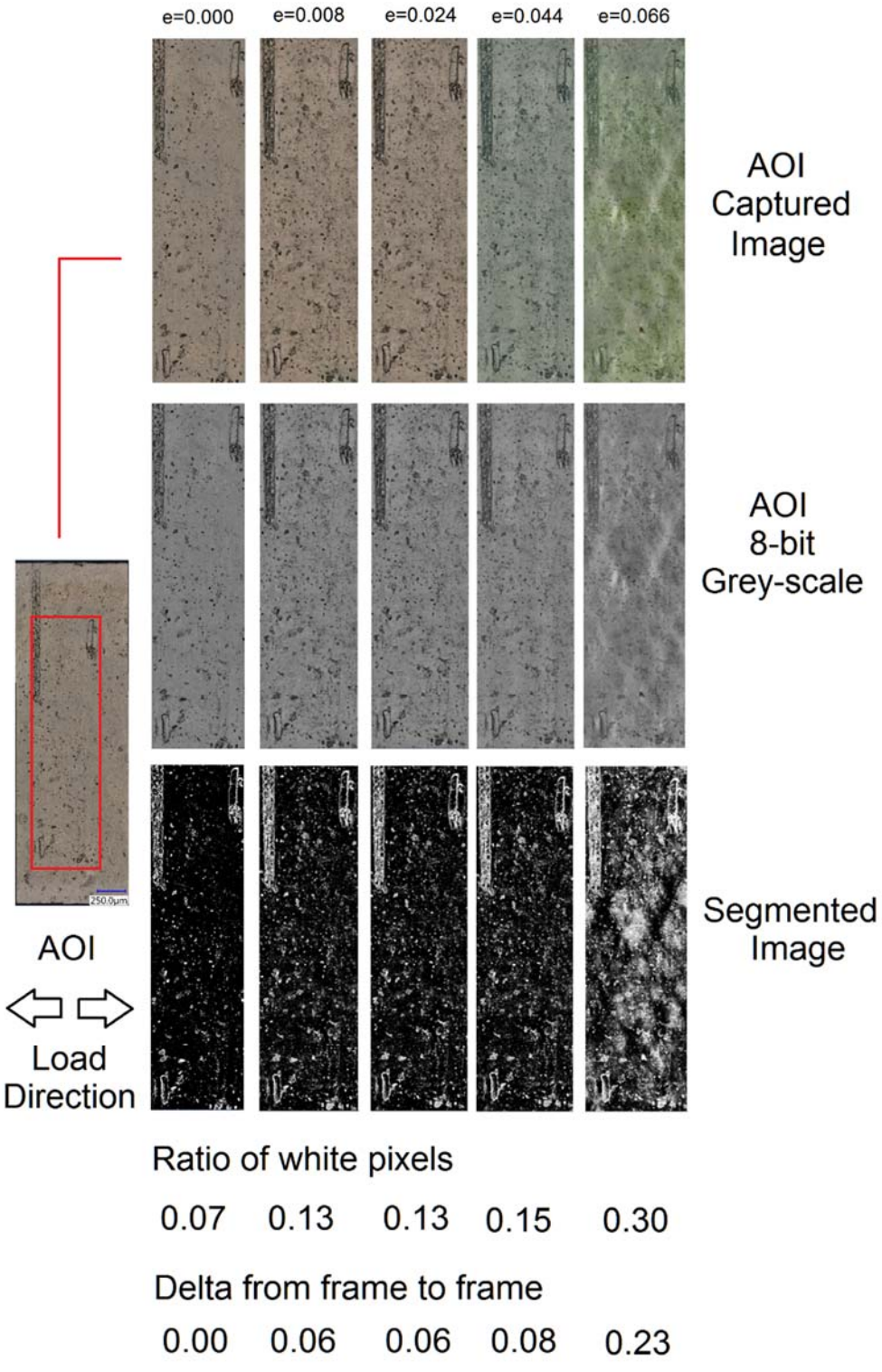

Figure 5-7: Segmented AOI regions in the material surface under ODM observation

Sample	δ [mm]	AOI Length x [µm]	AOI Width y [µm]	Local strain e_{xx}	Local strain e_{yy}	Binary Pixel count Black	Binary Pixel count White	Ratio White pixels to total pixels	D
A-OM-2	0.00	402.1	1,474.5	0.000	0.000	30,112,881	3,417,231	0.10	0.00
	0.10	438.2	1,555.1	0.090	0.055	30,468,682	4,075,958	0.12	0.02
	0.30	512.4	1,836.1	0.274	0.245	29,660,711	4,155,865	0.12	0.02
	0.55	440.0	1,595.3	0.094	0.082	26,053,675	7,632,821	0.23	0.12
	0.83	477.7	1,392.5	0.188	-0.056	21,926,007	8,902,953	0.29	0.19
A-OM-4	0.00	424.7	1,550.8	0.000	0.000	27,515,737	2,103,463	0.07	0.00
	0.10	591.4	2,112.1	0.393	0.362	26,452,977	3,831,823	0.13	0.06
	0.30	537.3	1,930.6	0.265	0.245	26,607,276	3,863,892	0.13	0.06
	0.55	449.8	1,537.5	0.059	-0.009	26,594,626	4,661,438	0.15	0.08
	0.83	464.4	1,536.8	0.093	-0.009	22,351,204	9,533,084	0.30	0.23

Table 5-5: Image binarization results at the AOI

Nucleation, opening, and coalescence of cracks caused surface changes, which manifested as whitening in the material. In addition, the presence of cavitation in large particles (diameter≥ 170 µm) was detected on a polished surface and inside particles within the shear-banded material (Appendix C, Figure C2-1). It could be possible, therefore, to obtain an empirical measure of damage. Changes between the segmented images could be construed as representative of the damage processes in the material, as observed on the free surface of the test specimen. The ratio between the white pixels and the total amount of pixels were used to represent the surface changes from load point to load point (Table 5-5, Column 9). Given that, the initial image contained features represented by white pixels; this initial value was subtracted from the calculated ratios to provide a measure of damage for each observed image (Table 5-5, Column 10). Using this empirical calculation, the predicted damage ranges from 0% up to 20% at the highest tested strain. Although there were changes in the AOI size from load point to load point, the total amount of pixels used for analysis was relatively unchanged (~ 3% in average), and it was considered that no significant error was introduced in the damage calculations.

5.4.4 Changes in modulus of elasticity and strength for load-unload and load-reload

At low strains in the elastic region (e≤0.01, Figure 5-8, top), there was no strain whitening, and the material responded in a linear-elastic manner for all three load cycles. Prior to the extrinsic yield

(e~0.02, Figure 5-8, second diagram from the top), incipient pockets of whitened material were observed, with a small change in the elastic response between cycles (6%), although the whitened material was more noticeable under magnification. At the next strain level (e~0.07, Figure 5-8, second diagram from the bottom), development of strain whitening was easily distinguished in the material. For this level of deformation, subsequent load events demonstrated a reduction of the linear-elastic region extent (from ~30 MPa at a strain of ~ 0.018 to ~12 MPa with a strain ≤0.01) followed by non-linear behavior. At strain levels closer to failure (e~0.11), the strain whitening propagated along the entire gauge length, and well-defined shear bands were recognizable at this stage (Figure 5-8, bottom diagram). The strain whitening process during load-unload was comparable to that described for a sample under tensile load until failure (Section 1.4.1 and Figure 5-3). Damage effects were also noted in the stress-strain response at high deformations: non-linear behavior in the unload portion of the load cycles; and changes in modulus of elasticity between the end of a cycle and the start of the next. Additionally, changes in the material strength between the first load cycle and the next were observed for strains beyond the extrinsic yield (e>0.07).Load-unload and load-reload measurements were made for the adhesive. The modulus of elasticity was calculated [238] from the experimental data for both the loading and unloading portions of the response. In general, the measured modulus of elasticity was well fitted to a linear response. The calculated coefficients of determination (r^2) were 0.99 on average (Appendix C, Table C3-1 to C3-4). During unloading, the entirety of the measured response was considered. For the calculated modulus values in this region, the coefficient of determination fluctuated between 0.97 and 0.99. For all cases, the statistical coefficients comply reasonably well with the limits required by the standard: coefficient of determination (r^2=0.99) and coefficient of variation (V_1≤ 2%). Changes in the modulus of elasticity values between load and unload cycles were detected with increases in strain (Figure 5-9). The modulus values are presented using box-whisker plots. Each box includes a horizontal white line to depict the mean value, black bars for the upper and lower fences, and 75% and 25% quartiles limit the box. The top row of graphs in the figure depicts the loading portion of the cycles, while the middle row summarizes the unload part of the experiments. At the two lowest strains tested (Columns A and B in the figure) there were no statistical differences in the data, but for strains greater than 0.069 (Columns C and D) there was a statistically significant change in stiffness (P-Value ≤$1.7x10^{-6}$, T-Test 95% confidence). The change can be described as a reduction in material stiffness between the first load and the first unload (~37.6% on average). After first unload, the subsequent unload cycles did not record further noticeable reductions in material stiffness and any

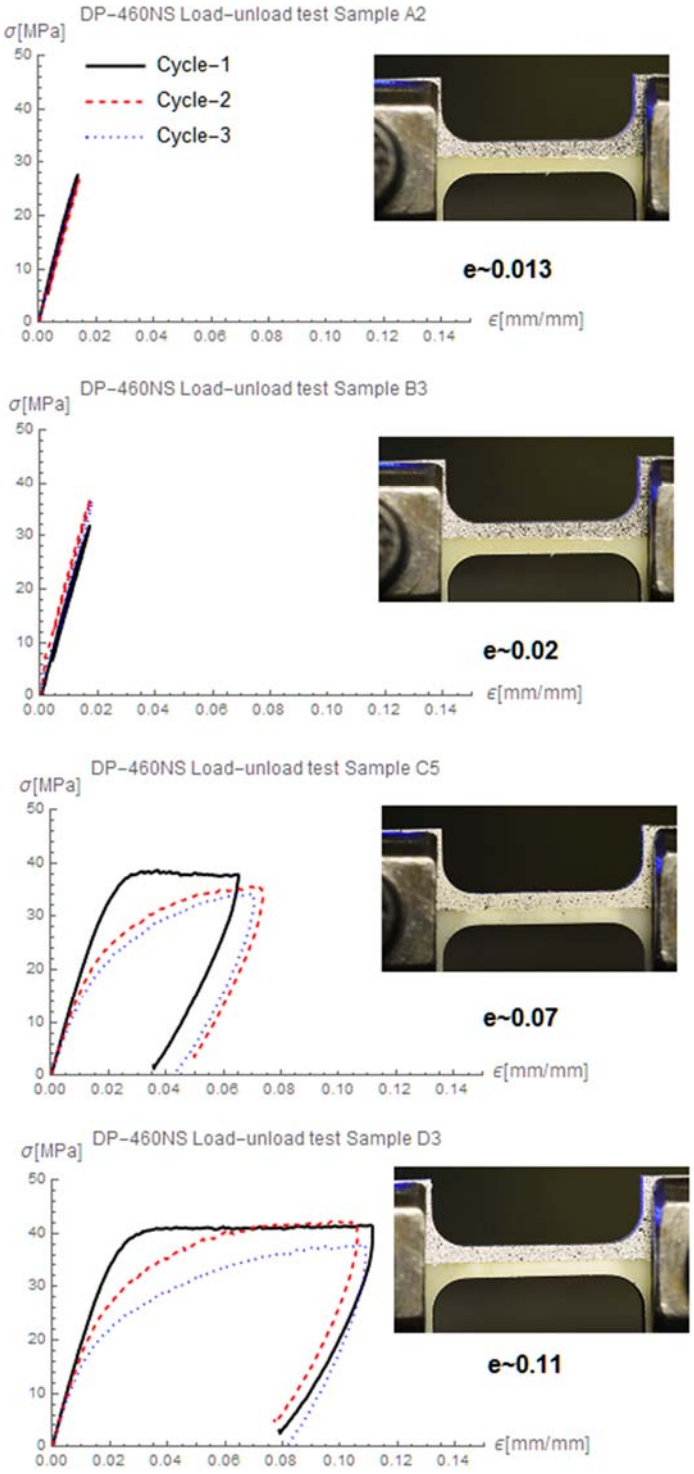

Figure 5-8: Typical load-unload curves and specimen images during load cycles

differences in the recorded mean value of the unload slopes were not statistically significant (T-Test 95% confidence).Changes in stiffness between the successive loading portions of the cycles were also noted (Figure 5-9, first row, Columns C and D). On average, the typical decrease in stiffness between the first load and second load was 17%, while the stiffness decrease between the second and third load cycles was ~5.7%. Since there was a difference in the modulus of elasticity between first unloading (~1.17 GPa) and second load (~1.55GPa) in all cycles that include plastic deformations, the data suggest the presence of a short-term viscoelastic effect that induces recovery in the material. This viscoelastic recovery was no longer present after the second load cycle.

According to the stiffness data using first load (E_o) with first unloading (E_{u1}) in the traditional manner (Figure 5-10 left hand), no damage was present at the very low strains of the elastic region (e<0.013). At strains around the yield point (e~0.02), the damage was calculated as approximately 10%. For strains between the yield point and the first plastic deformation used ($0.02 \leq e \leq 0.07$), there was a sudden increase in damage, but the value stabilized at ~35%. Although the amount of average damage was unchanged at the next strain level (e~0.10, D~35%), there was a larger spread in the data; the upper fence value (D~47%) was higher than in the previous deformation point (e~0.07, D~40%). For strains above 0.069, it was considered that the material had damage saturation and no further increases in damage could occur. Although it can be said that saturation was caused by the applied number of cycles, the statistical analysis of the stiffness measurements does not support this, since:

1. The measured average stiffness between the second and third load cycle (Figure 5-8, top row), were statistically similar.
2. No statistical differences were detected in the unload stiffness between the first unload and subsequent unload cycles for the same amount of strain for any applied strain (Figure 5-8, middle row).

It can be concluded then, that the saturation was due to the applied strain level alone during the first load cycle.

Changes in measured strength were also quantified during load-unload cycles (Figure 5-9, bottom row of graphs). No changes in strength were detected in the elastic region (e~0.013). At strains near the extrinsic yield strength of the material ($e \leq 0.02$), there were no statistical differences (T-test, 95% confidence). At strains higher than the yield of the material and in the plastic deformation zone (Columns C and D), the detected changes in average strength were not statistically significant either. The lack of statistical significance was attributed to the large variability in the measured data (±6.3 MPa). However, the average strength decrease between cycles was calculated at approximately 5%.

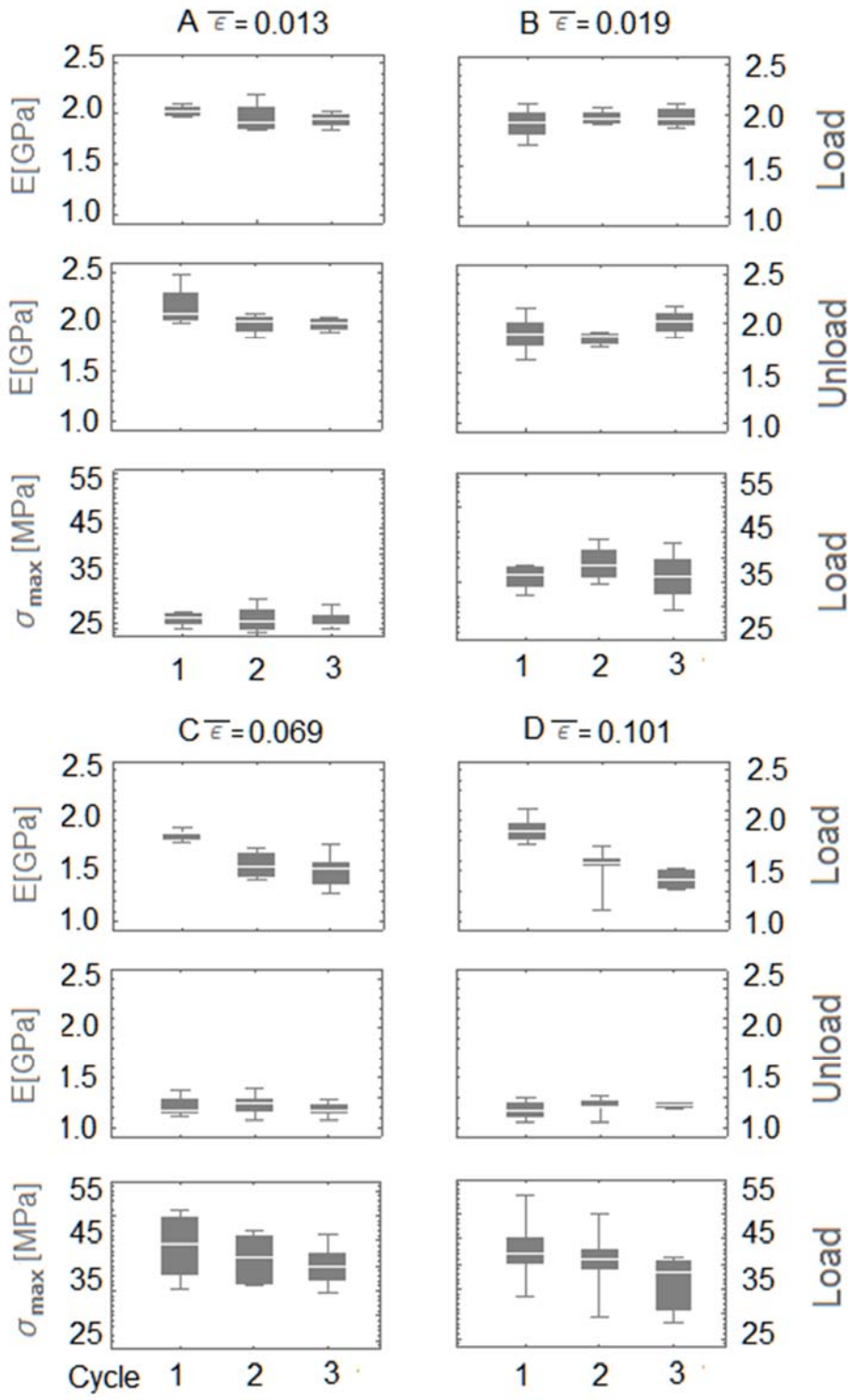

Figure 5-9: Measured changes in the material response for load, unload and reload cycles

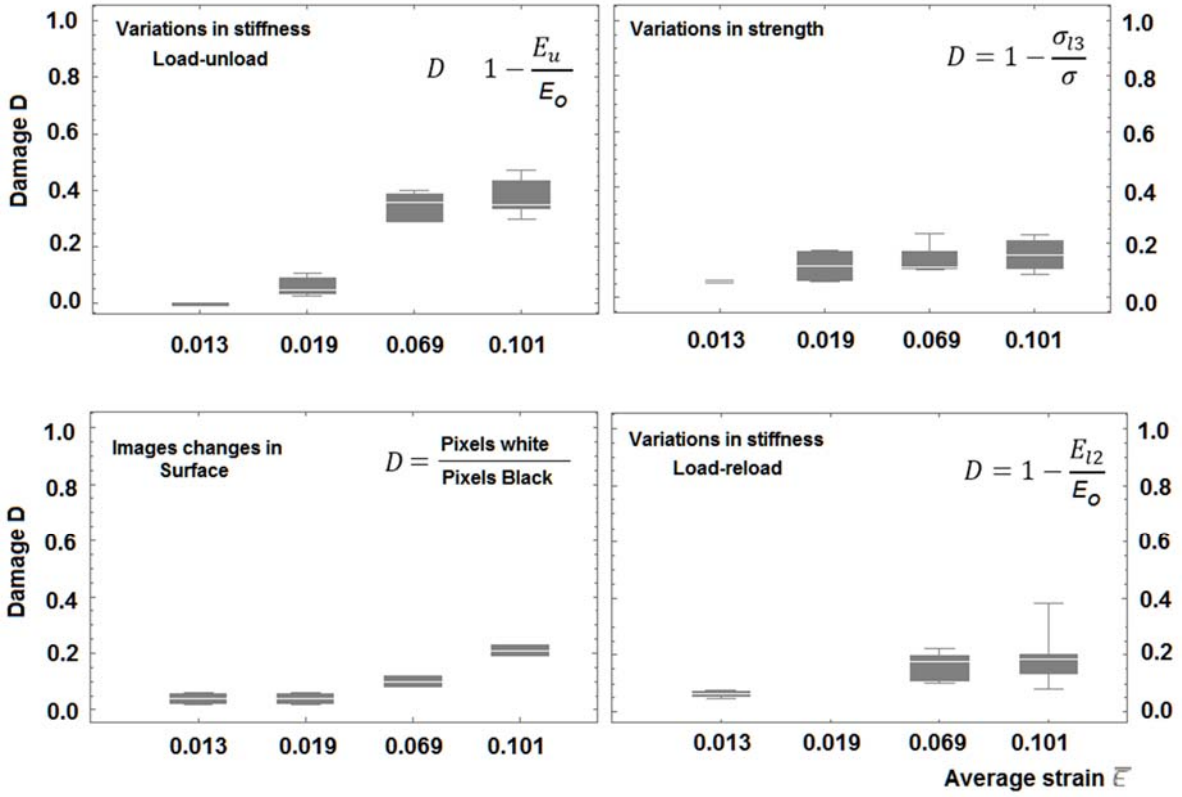

Figure 5-10: Calculated damage in the material

Since no fatigue effects were detected from the changes in modulus of elasticity, it was reasonable to assume that the changes in strength were caused by damage alone, and that the damage was induced in the material with the first deformation cycle. Variations between cycles can be explained by stabilization of damage. Damage was calculated using the difference between the measured strength in the first and third cycle. The damage evolution picture presented by the strength calculation (Figure 5-10, top right) was very different from that depicted by the changes in modulus of elasticity during load-unload. At low strains (<0.01) there was no damage, and the calculated value increased slowly with the increasingly applied strain. The damage value did not grow beyond 15–18% on average.

Damage values from the changes in microscopic surfaces were included for comparison (Figure 5-10, bottom left). Although it would be ideal to have a more significant sample size for statistical analysis (i.e. additional observations using more samples), the calculated values at the different strain levels were in agreement with the calculated damage from changes in strength. The damage values calculated

from the changes in surface pixels were typically within one standard deviation of the average of the damage data from changes in strength.

The traditional damage calculation included viscoelastic effects in the unload portion of the cycle thus the calculated damage values overestimated the actual material damage. This viscoelastic effect was noticed as a recovery in the modulus of elasticity between first unload (1.17 GPa) and the second load (1.54 GPa). Damage calculations were repeated using the modulus of elasticity of the second load cycle (E_{l2}) to eliminate the viscoelastic effects (Figure 5-10, bottom right). In the linear-elastic portion of the material response (e=0.013) the recalculated damage value (~6%) was small and could be attributed to the statistical variations in the elastic modulus. At the next level of deformation (point B, e=0.019), meaningful damage data was not calculated (D<0) but for a single value of 10%. In the plastic deformation region (points C, e= 0.067 and D, e=0.101), the average damage was 16% and 19% respectively although there was much more variation at the largest strain tested (point D,± 9.1%) compared to the variation after the first onset of plastic deformation (point C, ±5.2%). The maximum damage value in the region of plastic deformations was 38.3% (upper fence, point D). The calculated damage figures using load-reload also describe damage saturation in the material during plastic deformation. The average damage values using load-reload, which minimize viscoelastic effects were in good agreement with the damage values calculated from strength variations and microscopic optical surface changes (Table 5-6).

Applied average strain	Damage ΔE (load-unload) ± one std. dev.	Damage Δσ ± one std. dev.	Damage Surface Changes (Average)	Damage ΔE (load-reload) ± one std. dev.
0.000	0.00	0.00	0.00	0.00
0.013	0.00	0.06±0.01	0.04	0.03±0.06
0.019	0.06±0.04	0.11±0.08	0.04	0.10
0.069	0.34±0.05	0.13±0.06	0.10	0.16±0.05
0.101	0.38±0.06	0.15±0.07	0.21	0.17±0.08

Table 5-6: Average damage values calculated by all methods

5.5 Discussion

5.5.1 Microscope observations and optical measurements on the specimen surface

The microscope imaging demonstrated that the material developed strain whitening under load, followed by the development of shear bands. Of importance is the fact that the polished surface observation demonstrated micro-cracking and whitening inside and around an embedded particle (~165 μm in diameter), confirming the presence of cavitation like behavior with increases in strain. SEM analysis revealed the existence of a mechanism for crack arrest, as evidenced by the presence of furrows and steps. The images also discarded the possibility of particle debonding since there was no significant evidence of concave regions with circular or ellipsoidal perimeters with a diameter roughly equal to that of the embedded particle used for toughening. Observations inside a shear-banded region at high magnification demonstrated a porous like surface appearance and the presence of micro voids. Such descriptions are similar to those of cavitated particles in rubber modified epoxy resins as presented by Yee and Pearson [106]. Therefore, it can be assumed that cavitation was the primary damage mechanism in the material. It was possible to calculate the theoretical stresses required to initiate strain whitening by cavitation (Equations 5-1) and to compare those values against the stress concentrations calculated from the measured crack feature in the microscope images (Table 5-4). One limitation of this approach is the fact that the calculations (Equation 5-1) describe a volumetric process while the approximated stress values used a free surface. We considered that the stress field on the free surface was representative of the stress field in the surrounding material.

Equation 5-1 predicted a stress value to initiate a cavitation process in the order of 120 to 360 MPa (for particles between 1mm and 0.5μm in diameter and assuming E~120 MPa). However, the stress range for cavitation can be affected by the chemical composition of the toughening phase. For example, the required cavitation stresses for butadiene particles (E~1-2 GPa) predicted by Equation 5-1, could be in the range of 1000 to 6000 MPa while cavitation for silicon rubber (E~1 MPa) [310], can occur at stresses as low as 1 to 3 MPa.

An average of the crack tip stresses (Table 5-4, Column 8) was used to approximate the stress field around areas of stress concentration. The calculated average (402 MPa) is certainly high enough to satisfy the stress state that can promote internal cavitation (Equation 5-1, 120-360 MPa). As further verification, a balance calculation (Appendix C-4) between the strain energy and the energy required

for a phase transition (from solid to viscous), also predicted that material cavitation was possible. Although Equation 5-1 and the balance calculation are in agreement, this only serve as a first approximation. It has to be acknowledged that the calculated stress values are high for polymers, in the order of 400 MPa, and comparable in magnitude to that of the yield in metals. A fracture mechanics analysis using the stress intensity factor and the derived stress field around a crack tip, may provide a better insight into this problem. This will be consider for future analysis. Even though the proposed analysis is limited, of importance is the fact that even at low strains (e~0.008, well within elastic deformation), the stress concentrations in the material adjacent to a crack as a small as 11 μm in length and with a tip radius less than 2 μm, can be high enough to start the cavitation process in particles with diameters larger than 0.5 μm. The small amount of detectable whitening (surface change ≤ 13%, Table 5-5) observed in the material under high magnification, provides supporting evidence for strain whitening initiation at low levels of load. As a contrast, the variations in stiffness from load-unload did not detect any damage at low strains, but this can be explained by lack of sensitivity and differences in scale between the two methods.

By using image processing during the formation of shear bands, it was possible to determine that the initiation of the shear bands corresponded to areas where strain whitening and crack growth was present (Figure 5-11). From the analysis in the measured data, the stress at the crack tips was high enough, compared to that of the surrounding material, to cause cavitation, develop plastic zones and induce differences in gradients that later on, could favor the formation of shear bands. The local average strain measurement in the AOIs (Table 5-5, Columns 4 and 5), when compared against the applied average strain, also provide evidence of non-uniform strain distributions in the material.

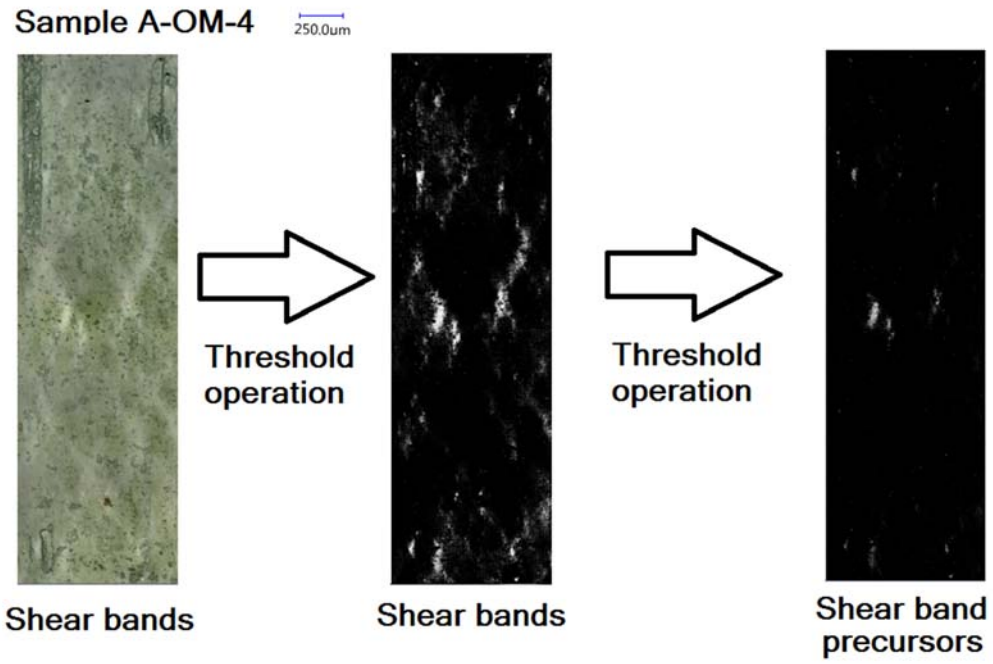

Figure 5-11: Pockets as precursors for shear bands

5.5.2 Changes in modulus of elasticity in the material

At strains well below the yield point and in the linear-elastic region, no statistically significant (T-test 95% confidence) changes in stiffness between load cycles or between consecutive load and unload could be detected, demonstrating that no damage was induced in the material. With increases in strains up to around the yield point ($e \leq 0.02$), no statistically significant changes in stiffness could be detected either. In this strain region, insipient strain whitening was the only phenomenon detected in the material although not enough damage was induced to cause noticeable changes in stiffness. With further increase in strain and within the initiation of plastic deformations ($0.02 < e \leq 0.07$), a significant drop in stiffness (Figure 5-9, Column C) between the first load cycle and the subsequent second load cycle was measured (18% drop) but no changes in stiffness between the second and third load cycles. P-values much smaller than 0.05 (0.0054 and 0.0028, T-Test 95% confidence) pointed to the statistical significance of the initial change. Strain whitening was the dominant phenomenon detected in this region, and the opening and propagation of cracks besides particle cavitation could account for the softening of the material response and the calculated damage. For strains well beyond yield of the material and with significant plastic deformation ($e \geq 0.07$), no additional drop in the stiffness was detected, but the material showed a significant transition towards shear banding. At these levels of strain, there were two distinct

responses in the unloading curve (Figure 5-12). The first portion of the unloading was stiffer (dashed red portion), followed by a transition to a lower stiffness (dotted blue portion). It can be noticed that the respective values for modulus of elasticity (red whisker box and blue whisker box, Figure 5-12 bottom part) were quite distinct among each other and significantly different from the modulus of elasticity measured in the undamaged material (light gray, Figure 5-12 bottom part).

One possible explanation is that the observed behavior can be explained in terms of chains and molecular structure in polymers. At low strains, the material first exhausts easily breakable Van der Waals bonds; this allows the polymeric chains to slip and rotate among each other, and then micro-cracks open to accommodate the deformations. This initial description of the deformation process was derived from basic principles in regards to atomic bonds [311], the basic molecular structure that can be used to describe polymeric materials [312] and descriptions by authors like Bowden [79], Argon [14] and Boyce [17,313]. With further straining, the material develops more openings, although they are governed by particle cavitation and/or development of localized plastic zones; eventually, the material transitions towards shear banding due to the high stress gradients that develop between cracks. The development of high stress gradients between cracks has been previously reported in the literature [314,315], as well as the transition between cavitation and shear banding in reinforced polymers with elastomeric materials [73,108]. While this is happening, further chain slipping occurs and eventually the covalent bonds that interlink chains need to be broken to allow further deformation. In the end, the chains are uncoiled and aligned, and only strong crosslinks that interconnect the main chemical compounds inside the chains are available to support the loading prior to final fracture. When the load direction is reverse just before fracture, the material needs to re-accommodate all the strong bonds first. Hence the brief stiff response detected. Once the principal bonds are repositioned, the unloading process needs to close openings and slide chains relative to one another, which is a process that requires much less force. This process matched the observed behavior described in Figure 5-12. In this figure, with the increase in strain and load cycles, the stiffness to return the material back to the unload condition increased, but this was followed by a constant softer portion in the unloading process. For both portions of the unloading curve the coefficient of correlation was very high (0.97 to 0.98), therefore they can be independently described by linear regression, although the calculated coefficients of variation increased up to 6% in the stiff section of the curve.

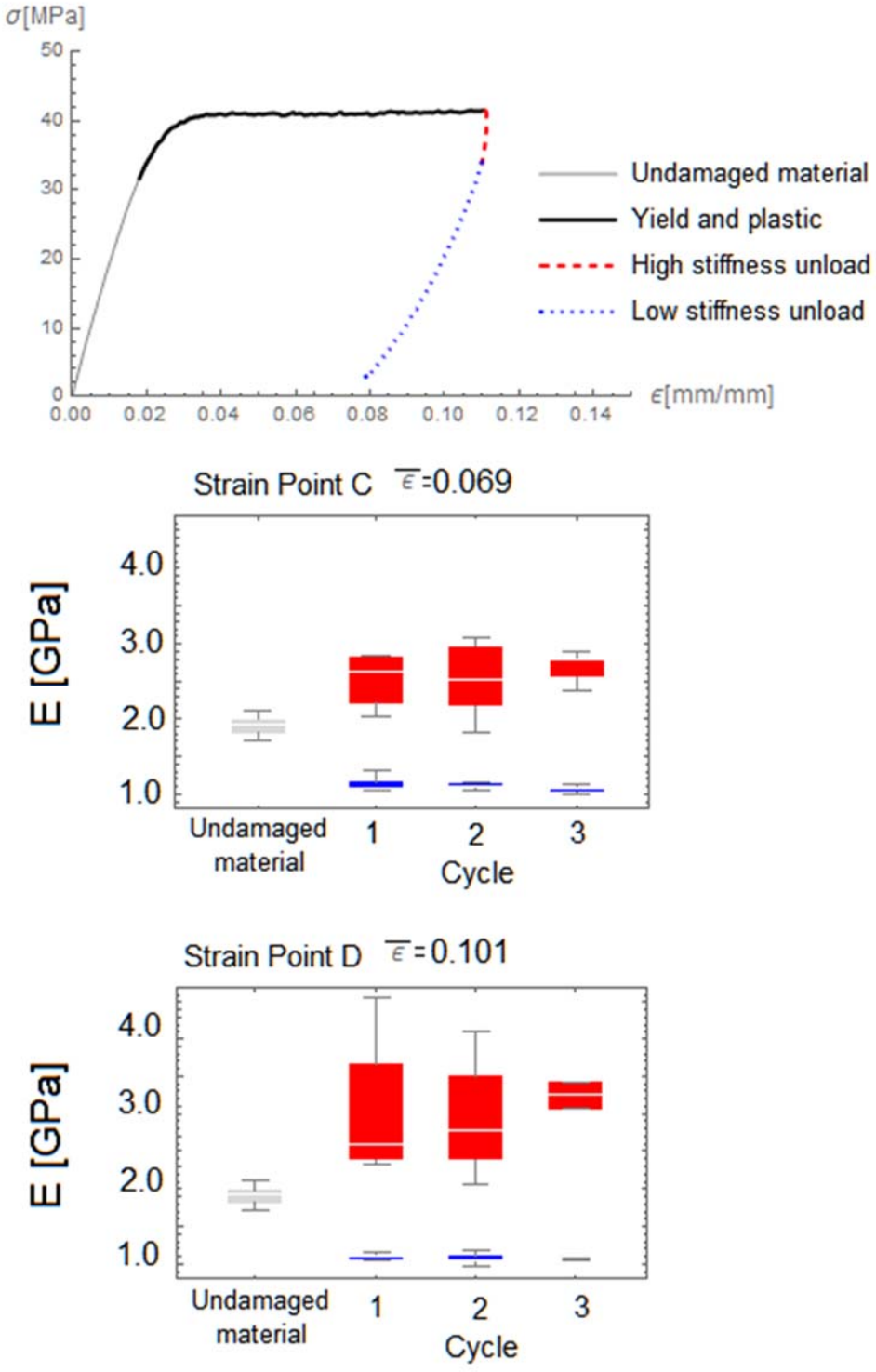

Figure 5-12: Unload response differences in modulus of elasticity

5.5.3 Calculated material damage

A series of load-unload cycles to determine changes in modulus of elasticity were conducted. The data provided a baseline measure to qualify the observed changes in the material surface during uniaxial tension. Damage was calculated for all experimental methods (Figure 5-10 and Table 5-6). The damage process can be accurately described with the use of sigmoidal functions.

For the changes in stiffness with load-unload (Table 5-7, first row; Figure 5-13 blue solid and dot markers) the sigmoidal curve predicts a damage value around 40% for saturation. The damage starts developing when the strain reaches a value in the plastic regime of deformation (e=0.04) and grows very quickly.

Damage calculated from the strength increased up to a value of 15 to 18% on average and a calculated maximum of 22%. The calculated damage can also be represented by a sigmoidal function (Table 5-7, middle row; Figure 5-13 red dashed with square markers). In principle, both methods (stiffness and strength) should predict similar results. In this situation, the discrepancy can be explained by the presence of a short-term viscoelastic effect. Once the viscoelastic effect was considered, by modifying the damage calculation with the use of the stiffness value of the second load rather than the first unload, the calculated average damage was 16 to 19%, with a calculated maximum of 38%. The calculated damage excluding viscoelastic effects was also well described in terms of a sigmoidal function (Table 5-7, bottom row; Figure 5-13 purple dotted and diamond markers).

Method	**Sigmoidal model**	**r^2**
DΔE load-unload	$\frac{0.38}{1 + exp^{16.34-271\varepsilon}}$	0.98
DΔσ	$\frac{0.15}{1 + exp^{4.32-296\varepsilon}}$	0.99
DΔE load-reload	$\frac{0.18}{1 + exp^{3.04-175\varepsilon}}$	0.99

Table 5-7: Damage data (Figure 5-10), sigmoidal function curve fit

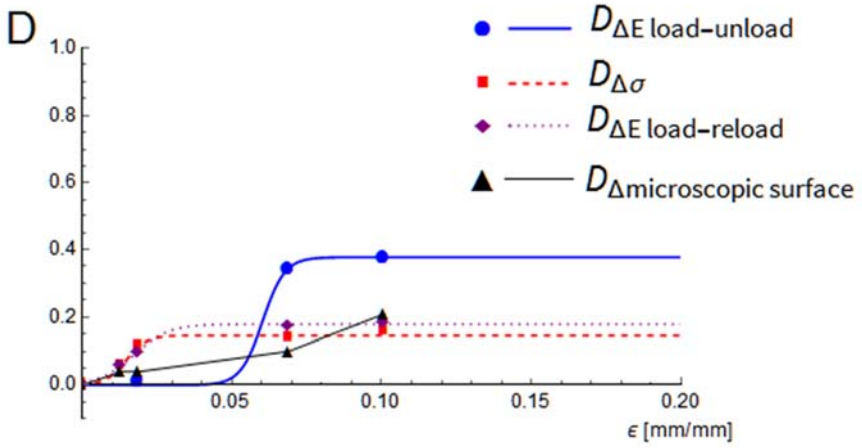

Figure 5-13: Damage data average values vs. sigmoidal functions (Table 5-7)

The damage predicted by changes in microscopic surface could not be fitted to a sigmoidal response (Figure 5-13 black solid line and triangle markers). More sample points that can better describe the spread at each strain point may be required to fit a proper curve to this data. With the current information the behavior is well described by three different linear regions. Nevertheless, the values align well with the measurements from changes in strength and the corrected calculation for stiffness at low strains (e=0.01) and high strains in the plastic region (e>0.07) although is not possible to infer, from the data, the actual saturation detected by the other methods.

From the microscope observations and the measurements of stiffness and strength, crack opening, small plastic zones and cavitation emerged as the most likely and significant damage mechanisms in the material up to well with-in plastic deformation (e≤0.07). At higher strain, the formation of shear bands was more significant. Shear bands cannot be classified under the traditional definition of damage (opening and coalescence of voids); however, there was optical evidence of the presence of micro-cracks, micro-voids and cavitated particles inside the shear-banded regions. In addition, it is necessary to consider that the shear-banding process influenced the material stiffness during the unloading response. The impact was more significant at the last stages of deformation, prior to failure in the material. Traditionally, shear bands are oriented at 45°; in the observed surfaces, the shear bands were oriented between 30° and 40°. It is possible that the presence of micro-cracks and particle cavitation in the disperse phase and/or the chemical composition and chain structure of the material influenced the shear band orientation, but determining this with certainty would require further investigation.

However, Yee and Pearson [106], reported that variations in shear band orientation from 45º could be expected due to the presence of plastic zones and dilatation.

5.6 Conclusions

A toughened structural epoxy adhesive (DP-460NS 3M, Minnesota) was used to measure damage developed during uniaxial tensile loading at different strain levels. Microscope observations confirmed that the material developed strain whitening due to crack opening and particle cavitation and these mechanisms were followed by shear banding in the later stages of deformation (e> 0.04). The shear banding developed from areas that were initially strain whitened. Crack features were monitored and measured during the deformation using microscopy. Typical crack lengths grew approximately 10 times in size (from ~10 up to ~100 μm) while the crack width was relatively constant and rarely grew larger than 10 μm. The crack length and tip radius were used to calculate stress concentration factors. The average stress concentration factor (~20) was in good agreement with those proposed by Patterson (~25) and comparable to those (10 to 50) that can be expected by a polymer that crazes as described by Gent. Patterson's theoretical stress concentration value is a good rule of thumb still applicable today for modern epoxy adhesives. However, the calculated levels of stress using stress concentration are high for polymeric materials, the analysis needs further review using fracture mechanics principles. Nevertheless, the low range of concentrated stresses in the test samples (300 to 400 MPa) were in relative agreement with Gent's theoretical stresses to initiate cavitation in this material (120 to 360 MPa), although the range values from Gent's approximation are highly dependent on the exact value of the modulus of elasticity used for the calculation.

Importantly, it was possible to cause cavitation at relatively low levels of stress (~10 MPa), which is well within the elastic response of this adhesive material. Although the initiation of strain whitening can be influenced by many factors (e.g., chemical composition, associated state of stress) and may not be extrapolated as a general behavior of all toughened epoxies, potential damage in the adhesive at low levels of stress can change the assumed integrity, performance and life expectancy of bonded components. This is yet another complexity that needs to be evaluated when using structural adhesives.

Traditionally, damage measurements are conducted with load-unload testing. This method proved to be effective if the viscoelastic effects are considered. This type of test required the use of multiple samples and was time-consuming for both physical testing and data processing. Further, the

measurement of the modulus was made along the gauge length of the tested samples with a virtual extensometer. Although large gradients were not detected in the DIC results, this approach can only give an average representation of the damage in the material because it does not consider localization phenomena or the changes that occur around the final fracture zone. For materials with large localizations, the damage distribution along the gauge length will be required to characterize the damage process adequately. Microhardness has been explored for this task [279], but it has limitations as the micro-indentations will introduce deformations and additional stress concentrators in the material surface that could skew damage measurements between load cycles. In this work, the changes in material surface (strain whitening and shear banding) were directly linked to damage using an empirical method. The damage was approximated by measuring the changes in image pixel ratios after image segmentation. The calculated damage values were within one standard deviation of the average damage calculated from changes in effective stress. Although the empirical optical method can be used to characterize damage evolution at different locations along the gauge length, implementing this is not practical. The measurements must be conducted in a small area of the material (field view limitation of the microscope) at a specific time in the load history and could require extensive periods of time to complete any image capturing required, which in turn introduces the potential for creep. A natural progression of this work will be the development of an optical method using macroscopic images to continuously measure damage along the specimen gauge length.

Changes in modulus of elasticity and the effective stress in the material were monitored between loading cycles. Changes in stiffness were linked to the presence of strain whitening as well as shear banding. Although the damage calculated using the changes in effective stress was substantially lower (D~18%) than predicted by traditional changes in stiffness (D~35%), the differences were reconciled by accounting for short term viscoelastic effects. The damage figure was recalculated using the load and reload slope (D~19%). This last value was in agreement with the changes in effective stress (D~15 to 18%) as well as the microscopic changes in the material surface (D~21%). The differences in the stiffness of the material caused by viscoelastic effects could be of vital importance for constitutive models that incorporate damage in their formulation. The results indicate that, to predict the behavior of the studied adhesive (DP-460NS), the implementation of a constitutive model with damage needs to be capable of differentiating between load and unload scenarios. The observed types of behavior influencing the effective damage, which are the role of micro-cracks, plastic zones, and cavitated material, cannot be overlooked in the characterization of structural epoxy adhesives.

A natural progression of the microscopic observations is to quantify macroscopic measurements and potentially relate them to damage. Chapter 6 describes the development of a measuring technique that can quantify strain whitening at the macroscopic level, and correlate the measurements with material damage.

Chapter 6
A Macroscopic Technique to Characterize Damage in a Strain Whitening Material

6.1 Overview/Abstract

The success of lightweight multi-material assemblies depends on selecting appropriate joining techniques that can provide the expected structural strength and durability while delivering occupant protection during crash scenarios. Epoxy structural adhesives are important in the design of structural joints in multi-material assemblies. However, the effective design of adhesive joints requires mechanical data to support design and numerical modeling efforts. One set of particularly valuable data is the evolution of damage under loading. Damage data enhances the ability of constitutive models to predict the mechanical behavior of materials and in the case of adhesives, predict the performance of bonded structures under different load conditions such as crash scenarios and unloading. During tensile loading of toughened epoxy adhesive materials, damage can occur through different mechanisms (e.g., cavitation, crack opening, plastic zones, particle debonding, and shear banding). In many cases, the loaded material appears lighter in color when compared to the base material, known as strain whitening. In this study, the color change on the surface of a tensile sample was measured using image processing techniques. The changes in color were calibrated with the fraction of voids from the fracture zone, which is a direct measurement of damage in the material. This provided a method to indirectly determine the damage history of the bulk material as a function of loading. Results were compared against damage calculated using other traditional techniques such as damage from volumetric strains, changes in modulus of elasticity, and changes in microhardness. Damage measurements from the optical method ranged between 15 and 25% at failure, which was in agreement (15 to 21%) with most existing control techniques except for the damage predicted using changes in volumetric strains (8%). The discrepancy was due to limitations in both the volumetric strain technique and the digital image correlation used to measure the field strains. The volumetric measurements can only detect damage related to changes in volume, which doesn't necessarily capture all the damage mechanism that can be active during loading. In addition to the numerical agreement of damage values between changes in

color and the traditional techniques, the implemented optical method can predict the location of the actual fracture zone, quantifying the damage level at different locations along the area of analysis, besides providing a continuous strain-damage curve. Strain-damage data is necessary to implement constitutive models that rely in concepts from damage mechanics to calculate changes in material stiffness and load carrying capacity, determine crack initiation and growth, or predict ultimate failure.

6.2 Introduction

A rational approach to transportation system design requires that the used structure be optimized for weight, due to energy efficiency efforts, while maintaining structural integrity and crashworthiness performance for occupant protection. The design optimization process generally leads to multi-material structures, where the challenges of joining different and possibly incompatible materials can be addressed with the use of adhesives [177]. Part of the optimization process requires finite element analysis where modeling developments using adhesives include elaborate parameters such as fracture toughness and damage[132], to better describe an adhesive material response to loading. Damage is a useful parameter to model ultimate strength, characterize the remaining strength of the adhesive material in a bonded component and to model unloading response. Damage data in adhesive materials is then a necessity and experimental methods that can quantify damage in a representative manner are required.

A search of the current literature indicates that a variety of direct (CT-scan[40] and microtomy [44]) and indirect methods (changes in stiffness [44,45], microhardness [141,257,279], electric conductivity [141], infrared thermography [43]) are available to identify damage in materials. However, careful consideration needs to be given to which method is implemented. For example, CT scanning is expensive, not easily available and limited to events in which changes in the material happen within the scanning frequency of the machine. Changes in stiffness or changes in microhardness can be limited to discrete point measurements and in order to describe a continuous evolution of the damage process; the implementation can be time-consuming and require extensive testing, especially if changes in strain rate also need to be considered.

Structural adhesives have demonstrated strain whitening during axial monotonic loading [279], and the changes in color have been linked to morphological changes in the surface of the material that were attributed to damage (Chapter 5); therefore, the use of an optical technique presents a practical method

to quantify the evolution of damage in real time. Optical techniques to measure damage based on the strain whitening phenomena are not new, although limitations restrict their applicability outside of research environments. Schirrer et al. [41] used laser light transmission to identify damage in polymethyl methacrylate (PMMA). However, the technique was limited to translucent materials and could only be applied to a small area of the material. Luo [175,176] demonstrated a procedure in which the morphological changes in PMMA (microcracks in the material surface) were successfully quantified to determine damage, but the measurement required an elaborate microscope setup and highly specialized computer subroutines were necessary for identification and measurement in the images. Strain measurements with extensometers (contact and optical) have also been used to determine volumetric changes and quantify damage in materials [46,47]. More recently, this method has been enhanced with the implementation of digital image correlation (DIC) [166,316]. Although the damage measurements with DIC can be of high quality (comparable to direct CT-scan measurements) and useful to test at different rates of strain [166], the implementation relies on the results of the image correlation. The accuracy of image correlation, and therefore the measured strains, can be impacted by a number of factors such as the applied speckle pattern [167,168], image resolution, optical distortions and out of plane motions [169,170], besides intrinsic systemic errors such as high order interpolations [171]. Additionally, DIC analysis can be limited by decorrelation at large deformations ($e>0.20$) [172,173] or from temporal under-sampling of a rapidly evolving phenomena [174].

In this work, a macroscopic optical method to quantify damage is proposed. The optical technique, takes advantage of the changes in color caused by the scattering of light due to the opening of cracks and particle cavitation on the surface of the material, to quantify the damage. Development of this optical technique was done using a toughened epoxy (DP-460NS). Results were validated against existing damage data as well as in-situ measurements of volumetric changes using local strains.

6.3 Background

6.3.1 Damage

Damage, most typically denoted by the letter D, can be understood as the quantification of some phenomena that determine when a material fails. In its most simple definition, it can be related to voids inside a material. Following this definition, as damage progresses with loading (voids increase in size),

less material carries the load until fracture and ultimate failure occurs. Such processes, that is the creation, enlargement, and coalescence of voids in a material, can be quantified in two manners (Equation 6-1) [141]: firstly as the ratio between the volume of voids (V_D) and the volume of material considered (V); or, secondly, as a ratio between the area of all voids (A_D) that intersect a plane and the nominal area of such plane (A). According to this approach, damage is then necessarily described by a real number that is bounded between zero and one. Typically, the value is reported as a percentage. In these boundaries, zero indicates no damage while one defines a failed material. However, materials may actually fail during loading before the damage reaches a value of one [141] . For example, Lemaitre [141] reported that steel materials fail when damage reaches a value of approximately 30%.

$$D = \frac{V_D}{V} or\ D = \frac{A_D}{A}$$

Equation 6-1: Definition of damage

From an experimental point of view, damage is not a mechanical variable that can be measured directly. To obtain information that can quantify damage in the manner described by Equation 6-1, microtomy with high magnification microscopy [141] or CT scanning [40] can be used to directly measure and count voids resulting from damage. Most typically, indirect methods are used to measure damage. Indirect methods rely on measuring changes in a mechanical property prior to and after loading, to determine the level of damage in a material. As an example, Equation 6-2 describes damage as a function of the changes in modulus of elasticity. In this equation Eo denotes the modulus of elasticity in the undamaged material, while E* denotes measurements made after subjecting the material to loading [141]. Indirect methods also include measuring changes in microhardness [44,257,279], changes in wave speed [44,317], variations in electrical resistivity [141,318] or changes in thermal conductivity using thermography [43,317,319].

$$D = 1 - \frac{E^*}{E_o}$$

Equation 6-2: Damage as a function of an indirect measurement

Damage can also be determined indirectly by calculating changes in volume using strain field measurements. Since damage in its most elemental form is related with changes in volume, then such change in a representative volume element (RVE) can be detected with the use of the volumetric strain

(Equation 6-3). Tang [47] defined damage in terms of the relative change in volume (ΔV) and the original volume of material (V_o) (Equation 6-4) which can be algebraically manipulated to redefine damage in terms of strains (Equation 6-5). G'Sell [161] reported that this expression (Equation 6-5) matches reasonably well with damage from microscopic analysis in polyethylene. Balieu et al. [166] also demonstrated that the damage evolution resulting from a cavitation process could be described by accounting for the differences in true stress, which in turn can be defined in terms of the longitudinal and transversal strains. The resultant expression for damage is then identical to the expression in Equation 6-5.

$$\varepsilon_V = \varepsilon_{xx} + \varepsilon_{yy} + \varepsilon_{zz}$$

Equation 6-3: Volumetric strain

$$D = \frac{\Delta V}{\Delta V + V_o}$$

Equation 6-4: Damage as a function of changes in volume

$$D = 1 - \exp(-\varepsilon_V)$$

Equation 6-5: Damage as a function of the volumetric strain

6.3.2 Damage in polymers

In polymeric materials, especially in toughened epoxies, particle debonding and cavitation, crack opening, plastic zones at crack tips and shear banding may occur during loading [107]. Cavitation can be described as the development of micro-voids in areas of softened material [109] (Figure 6-1, left-hand top), and it is an energy absorbing mechanism. On the other hand, shear banding (Figure 6-1, left-hand bottom) is an altogether different phenomenon in which the material develops bands at well defined angles [97,98]. Interestingly, for both cases, the material appears lighter in color when compared against the material before it has been subjected to load (Figure 6-1, right hand for two different epoxy adhesives). The different factors that determine how each one of these two mechanisms is initiated have been discussed in the literature but will be briefly explained here.

In the case of cavitation, tensile hydrostatic stress causes a soft phase inside the material to form voids. Therefore, the development of small cracks and openings and in some instances craze-like behavior (crack openings stabilized with joining tendons) [73]. Since an opening is formed, the development of cavitation clearly corresponds with an increase in volume in the material but also with the creation of

damage inside the material. The small openings generated in the material can cause light scattering explaining then the change in color in the material. However, from a mechanical point of view, it is important to highlight that cavitated particles cannot always be considered to be equivalent to particle-sized voids [320].

In the case of shear bands [111,321], this particular mechanism develops due to local variations in the strain field in which zones of amorphous material are stretched and permit to slide relatively to zones of more crystalline material. The concentrated displacement of material also causes light scattering, and these localized deformations (shear bands) are observed as well-structured zones of a different color compared to the original material. The nature of shear bands can be determined by many factors. Zebarjad [322] explained that inter-particle distance in toughened polypropylene can affect dilatational band (shear band) propagation. Tomita and Lu [323], demonstrated through the use of micromechanics simulations, that the volume fraction of the toughening phase in combination with the size of particles used and the state of stress, can determine the type of shear band observed in polymers with second-phase particles. Although shear bands are not traditionally considered as damage [104], is necessary to consider that they tend to grow and nucleate slip surfaces within [324] the material that constitute the shear band. Additionally, shear coalescence of voids has been observed in fracture surfaces of metallic materials [325], which requires to consider if a similar behaviour can be present in polymers. This needs further study as the current understanding of polymers is expanded with the implementation of new experimental techniques. For example, the traditional understanding of PPMA considers that failure occurs by crazing [41,175,326], however a recent in-situ atomic force microscopy study of this material has reported that there is a transition in the failure mechanism from crazing towards shear yielding [327].

The development of voids and micro-cracks during cavitation affects the mechanical response of materials. Therefore the damage can be determined by detecting changes in properties as described by expressions like that presented in Equation 6-2. Previous investigations by the author measured damage in different epoxy adhesives using changes in microhardness [279] and further studied the DP-460NS epoxy adhesive using changes in stiffness, effective stress and microscopic surfaces . Table 6-1 summarizes damage measurements using methods such as changes in stiffness considering viscoelastic effects ($D_{\Delta E}$), changes in effective stress ($D_{\Delta \sigma}$) and changes in surface features using microscopy ($D_{\Delta Smic}$). Figure 6-2 illustrates calculated damage along the sample test gauge after failure under quasi-static uniaxial loading using microhardness ($D_{\Delta MHV}$).

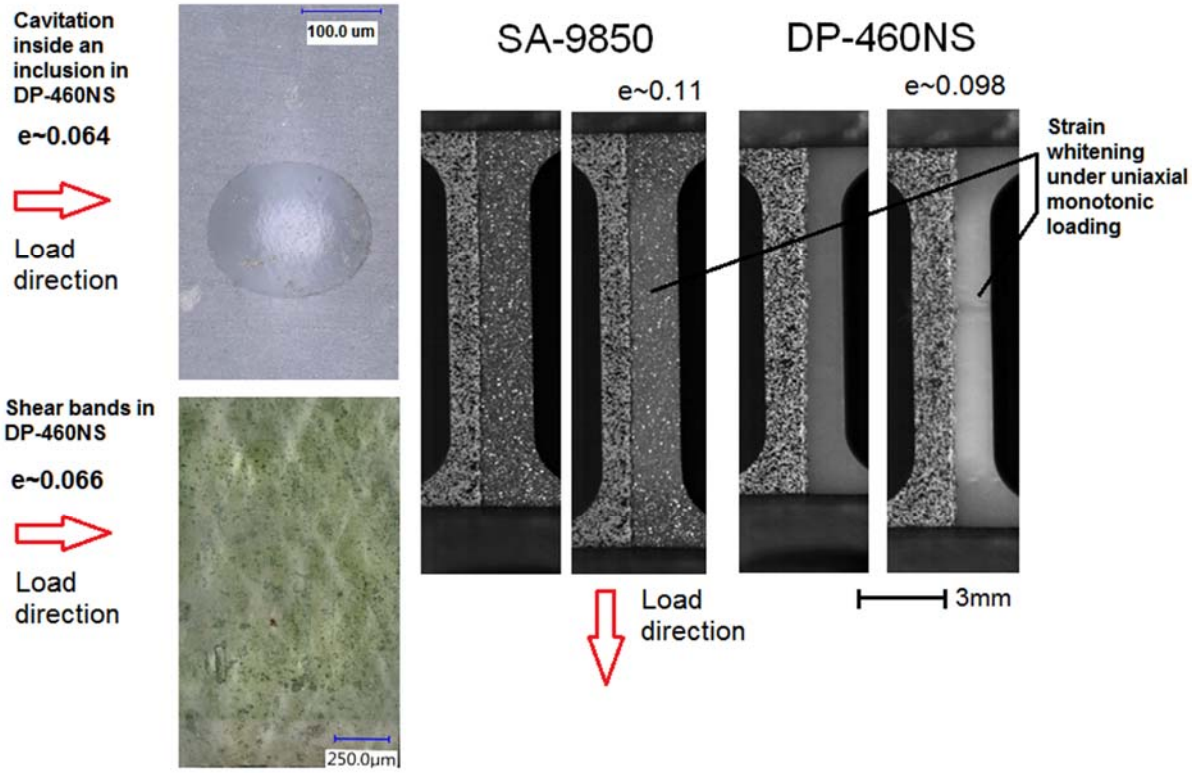

Figure 6-1: Damage mechanisms in polymers: craze in a polymer (top left), shear banding (bottom left) and color change by strain whitening in two epoxy adhesives

Nominal avg. strain [mm/mm]	Average damage with standard deviation		
	Stiffness changes $D_{\Delta E}$	Effective stress changes $D_{\Delta\sigma}$	Surface changes $D_{\Delta Smic}$
0	0.00	0.00	0.00
0.013	0.03±0.05	0.06±0.01	0.04
0.019	0.00±0.13	0.11±0.08	0.04
0.069	0.16±0.05	0.13±0.06	0.10
0.101	0.18±0.09	0.16±0.07	0.21

Table 6-1: Damage measurements in DP-460NS

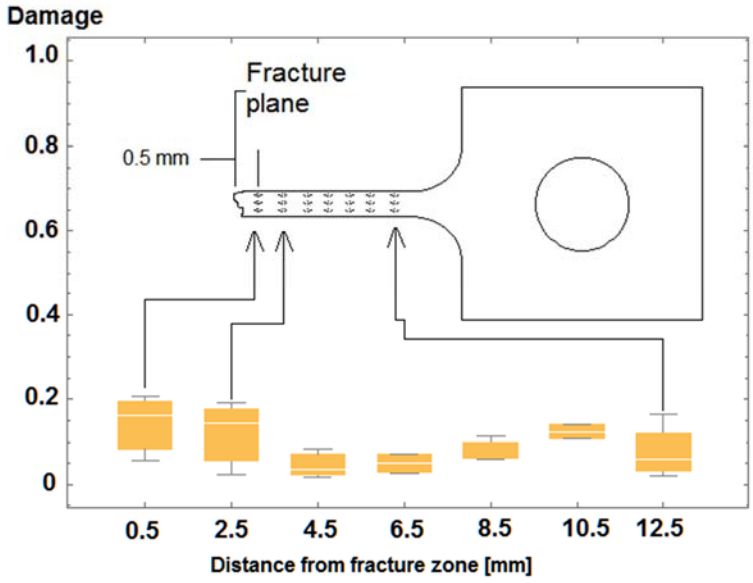

Figure 6-2: Damage from changes in microhardness ($D_{\Delta MHV}$) under quasi-static uniaxial loading along the sample test gauge in DP-460NS

6.3.3 Image processing

Electronic images are typically generated using a two-dimensional array of pixels. The image is mapped into a grid area composed of individual pixels. Each pixel consists of a value describing the color of that region of the image. Typically, in color images, each pixel is defined by an array of three different values representing the relative amount of red, blue and green, traditionally known as RGB color space. RGB images can also be turned into grey scale representations by using a linear combination of the RGB values. When wanting to measure the change in an image different techniques are available [328,329]. The most readily available technique is the use of histograms to identify and quantify changes in image pixel values. Segmentation techniques can be used to differentiate among different regions in an image and mask operations, in which an image is compared to a second image by subtracting one from the other, can also be used to identify areas of change. Typically, the use of these techniques requires a threshold value. A threshold is a quantity that can be used to discriminate and differentiate changes. Defining a proper threshold may not be a trivial matter, and the problem has been treated in the literature[330–332].

Since images are represented by arrays of real numbers, other mathematical considerations can be used to define changes in images. For example, it is possible to look at the average pixel value in a region of

interest or to consider the pixel RGB data as a vector with both direction and magnitude as proposed by Jia [333] making it possible to analyze changes in images using simple vector operations such as dot and cross products.

6.4 Methods

6.4.1 Material, test geometry, and the testing method

A two-part epoxy adhesive (DP-460NS, 3M, Minnesota) toughened with a thermoplastic phase (MBS) was used to investigate the implementation of an optical technique that quantifies damage in materials which develop strain whitening during loading. Non-standard tensile samples were used for the study. Tensile coupons were machined out of bulk material sheets 3 mm thick; the sheets were manufactured by casting the epoxy adhesive between two glass plates and oven cured at 70°C for two hours. The tested geometry (Figure 6-3, left hand) has been used in previous work [248,279], and results were no different to those of testing geometries described in the ASTM standards for tensile testing of polymeric materials [223]. Table 6-2 summarizes the mechanical properties of the material.

ρ [kg/m^3]	**E [GPa]**	**ν**	**Tensile Strength Strain Rate Effects [MPa]**	**Ultimate Stress [MPa] @ 0.002 s^{-1}**	**Mean Hardness & Std. Dev. [MPa]**
1200	2.13	0.41	$3.5\ln(\dot{\varepsilon}) + 62.9$	39.03	120.10±7.20HV200

Table 6-2: Mechanical properties DP-460NS [248,279]

Testing of coupons was performed using a servo-hydraulic controlled test frame (Figure 6-3, right hand). Samples were loaded in uniaxial tension at a constant engineering strain rate of 0.002 1/s until failure. A calibrated load cell (Omegadyne model LC-412-500, Omega, Connecticut), a custom software control loop (LabVIEW, National Instruments, Texas) and an electronic controller (MTS FLEX, MTS, Minnesota) were used as part of the testing set up. During testing, image capture was done using a commercial digital single-lens reflex (DSLR) system (Nikon D-3200, 24.7 MP 23.2 x 15.4 mm CMOS sensor, Nikon Corporation, Japan) with a Macro Lens (SIGMA 105 mm 1:2.8 DG MACRO HSM, Sigma Corporation, Japan). The samples were illuminated using a commercial LED system (Lumahawk, AADYN technologies, North Carolina). Camera and light settings were determined using

a pre-strained sample of DP-460NS material, so the strain whitening phenomenon was detectable in the image; the settings were fixed for the duration of the test (F8, 1/80 and ISO 1600 for the camera; 95% intensity with 25% temperature for the light source). The camera was used in non-interlaced video mode, and individual high-quality images were extracted using Photron FASTCAM viewer software [334]. No additional image processing such as contrast enhancement, histogram manipulation or any other type of modification was used. Two different orthogonal views of the sample, front and side, were captured with the camera equipment.

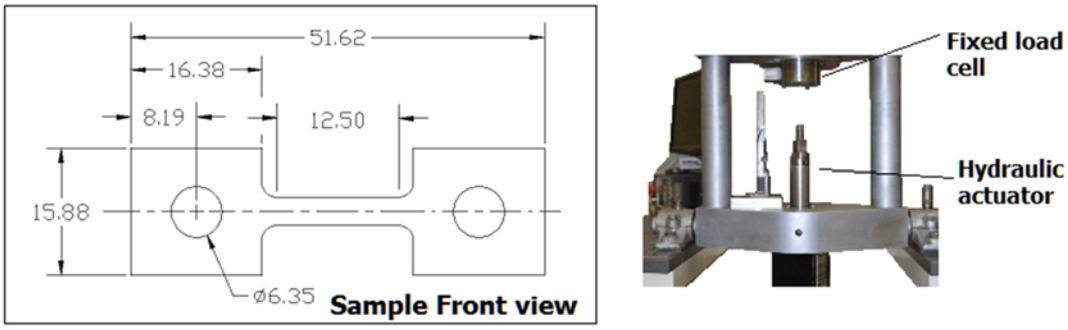

Figure 6-3: Testing sample geometry (dimensions in mm) and testing frame

6.4.2 Quantification of damage

6.4.2.1 Damage by quantifying changes in surface color

Color information is encoded as an RGB vector array for each one of the pixels used to capture an image using digital cameras. For the analysis correlating damage with changes in color, the pixel information needed to be extracted and somehow quantified. For such a task, the Mathematica computing system [335] was used due to its native image processing capabilities combined with its powerful scripting language. A preliminary study was conducted to determine a reasonable procedure to detect and quantify the changes in color that occur in an area of interest (AOI) inside an image (Appendix D). From this preliminary work, the mean average value of pixel color in the AOI was determined as the most reasonable way to quantify the color history as a function of time (or strain). The damage that occurred in a particular area (D_A) due to strain whitening was then defined in terms of the changes between the current average color at a time t ($\bar{C}_t$) and the original average color before the start of the loading ($\bar{C}_o$) (Equation 6-6). For analysis, the strain gauge zone was used as the AOI and it

was discretized using 10 subdivisions. Each subdivision corresponds then to windows approximately 1 mm x 1mm in size for each one of the areas under study (A_i) (Figure 6-4, middle).

$$D_A \propto \overline{C_t} - \overline{C_o}$$

Equation 6-6: Damage related to changes in average pixel color

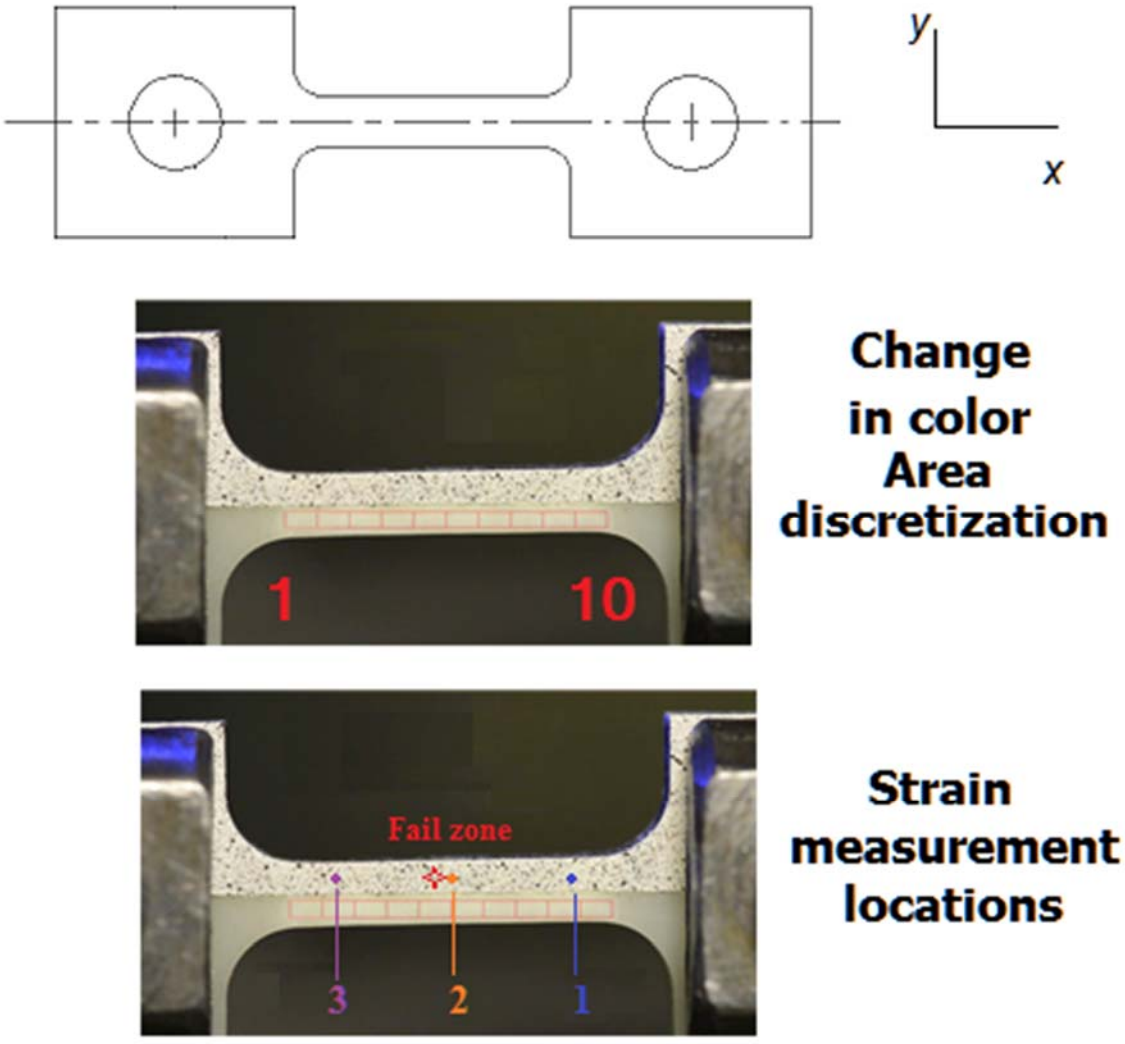

Figure 6-4: Tested sample geometry, analysis zones

Besides tracking changes in color, it was necessary to account for the deformations that occur in the material during loading. The implemented computer algorithm for analysis used a Lagrangian frame of reference to track changes in a user-defined AOI. The algorithm accounted for the deformation by assuming a linear distribution of the displacements along the length of the sample. The closest end of the AOI to the fix grip end was assumed to be static (zero velocity). The other end, the one closest to the moving grip, was assumed to have the same displacement as the one measured during the test. The displacement was extracted from a digital extensometer covering the test gauge.

To calibrate the optical measurement against the actual material damage, it would be necessary to have a method that can correlate damage and change in color at every moment in time for each one of the areas studied. This could be implemented with the aid of microhardness measurements [279], but this approach is not practical to track damage in time. Microhardness requires stopping the test in multiple instances to perform the multiple measurements; also, the micro-indentations could act as stress concentrators that can bias the results. A more suitable approach was to use a microscopic observation of the fracture surface to determine the fraction of voids leading to failure. This provided a direct measurement of damage in the fracture zone (D_{fz}) (Equation 6-1). It was then assumed that the change in color around the fracture zone was directly proportional to this value. The damage in the individual regions (D_{Ai}) used to discretize the AOI was then expressed as a fraction of the damage that occurs at the fracture zone (D_{fz}) (Equation 6-7). The damage fraction (f_{Ai}) was assumed as directly proportional to the ratio between the measured change in color in the region and the change in color in the fracture area (Equation 6-8) at the time of failure.

$$D_{Ai} = f_{Ai} D_{fz}$$

Equation 6-7: Damage in the area as a function of damage at the fracture zone and a proportionality factor

$$f_{Ai} = \frac{C_{Ait} - C_{Ai0}}{C_{fzt} - C_{fz0}}$$

Equation 6-8: Proportionality factor

6.4.2.2 Damage from fracture surfaces

The fracture surfaces were observed with the aid of an opto-digital microscope (ODM) (Keyence VHX-5000, Keyence, Japan) and features such as micro-voids ($r < 10$ μm), voids ($r > 10$ μm) and cracks were identified and measured. The area of all these features, which can be construed as damage, was added together and used to calculate damage using Equation 6-1. The study was made using images at low magnification (80x) and then repeated at high magnification (500x). Identification was first made manually and then, in a different instance, with the aid of different image protocols to confirm the results (Appendix 2). Images analysis was conducted using open source image processing software: Image J [336] and GIMP [337].

6.4.3 Damage measurements for validation

The DP-460NS material has been previously studied as presented through chapters 4 to 5. The damage data in Table 6-1 and Figure 6-2 will be used as a control value for the results using the optical technique. In addition to this data, strains in the material during uniaxial loading were monitored at four different points along the test gauge of the samples (Figure 6-4, bottom). Three points were labeled as P1 (1.5mm to the left of the test gauge right end), P2 (test gauge center), and P3 (1.5mm to the right of the test gauge left end). The fourth point was located at the final fracture plane and labeled as PF. The damage evolution with strain was calculated using Equation 6-5.

For measuring strain, the samples were prepared with a speckle pattern, and the DIC technique [316] was implemented; the VIC-2D 2009 software [225] was used for analysis. Strain measurements were made in two orthogonal views of the test (front and lateral view). On the front view, half of the width of the test gauge was prepared with a speckle pattern to facilitate observation of the strain whitening process while simultaneously measuring the strains using DIC. On the lateral view, the entire test gauge was prepared with a speckle pattern. Having two views at the same time permitted to verify the axial strain measurement and identify strain gradients in the material.

6.5 Results

6.5.1 Strain whitening during uniaxial loading

Mean average pixel value was calculated as a function of time for 10 different locations along the test gauge of samples subjected to uniaxial loading. The average pixel color history for each one of the

zones under analysis was typically described by a sigmoidal curve. Figure 6-5 describes the mean average color detected in Sample AA-6, results for the other two samples are included in Appendix D. Although the measured color history had noise, the variance about the mean value was very small (≤ 0.0004). Of more importance was any noise in the system that could be interpreted as a false positive. For example, at low strains (e≤0.01) minimal changes in average color were distinguished, up to 0.04 in mean pixel value. At this low level of strain, the detected changes in average color can correspond to the inherent noise of the system. The typical noise was calculated as 0.013 (Appendix D). The drift of the system was also verified. Drift was calculated as a change of -0.058 in mean pixel value. Negative slopes in the color history plateau were attributed to signal drifting rather than actual measurable changes in the material.

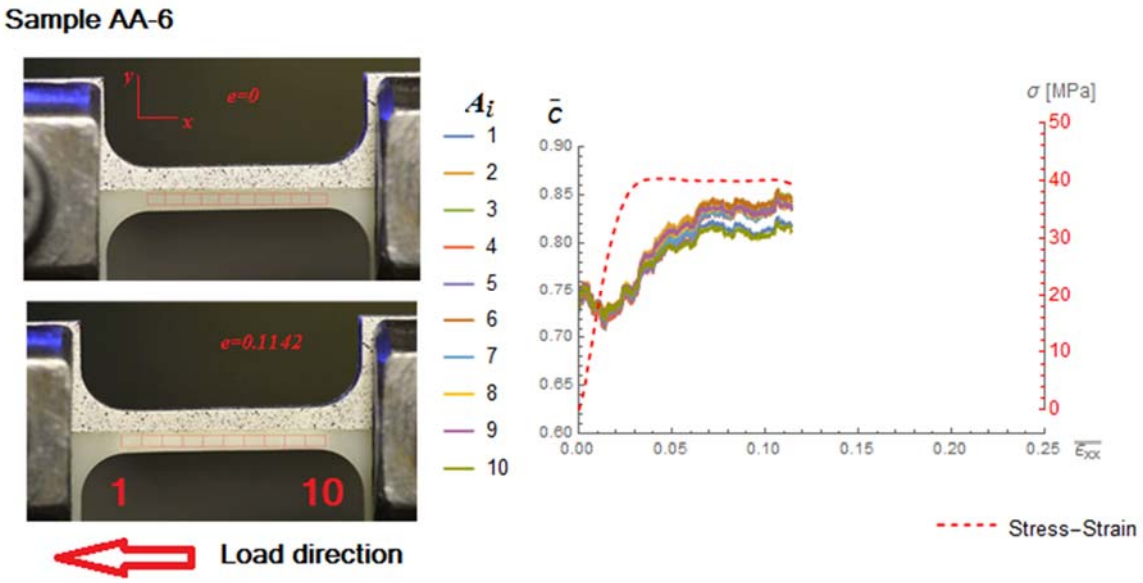

Figure 6-5: Typical Mean pixel average color history for DP-460NS material

Strain whitening typically compromised the entire test gauge for samples AA-6 and AA-7. In the case of sample AA-8, the strain whitening localized mostly in the left-hand side of the test gauge due to necking during the test. This behavior was accurately captured by the measured change in color (ΔC) before failure (Figure 6-6, top). Typically, the highest detected change in pixel color corresponded to the fracture zone or its vicinity. The bottom plot of Figure 6-6 illustrates ΔC as a function of the strain at the locations of the final fracture. Noticeable was the variability in strain to failure for the material,

as high as ~0.46 in the vicinity of the fracture zone for the sample with neck localization (AA-8) while the other two registered strains to failure of 0.12 (AA-6) and 0.24 (AA-7) respectively.

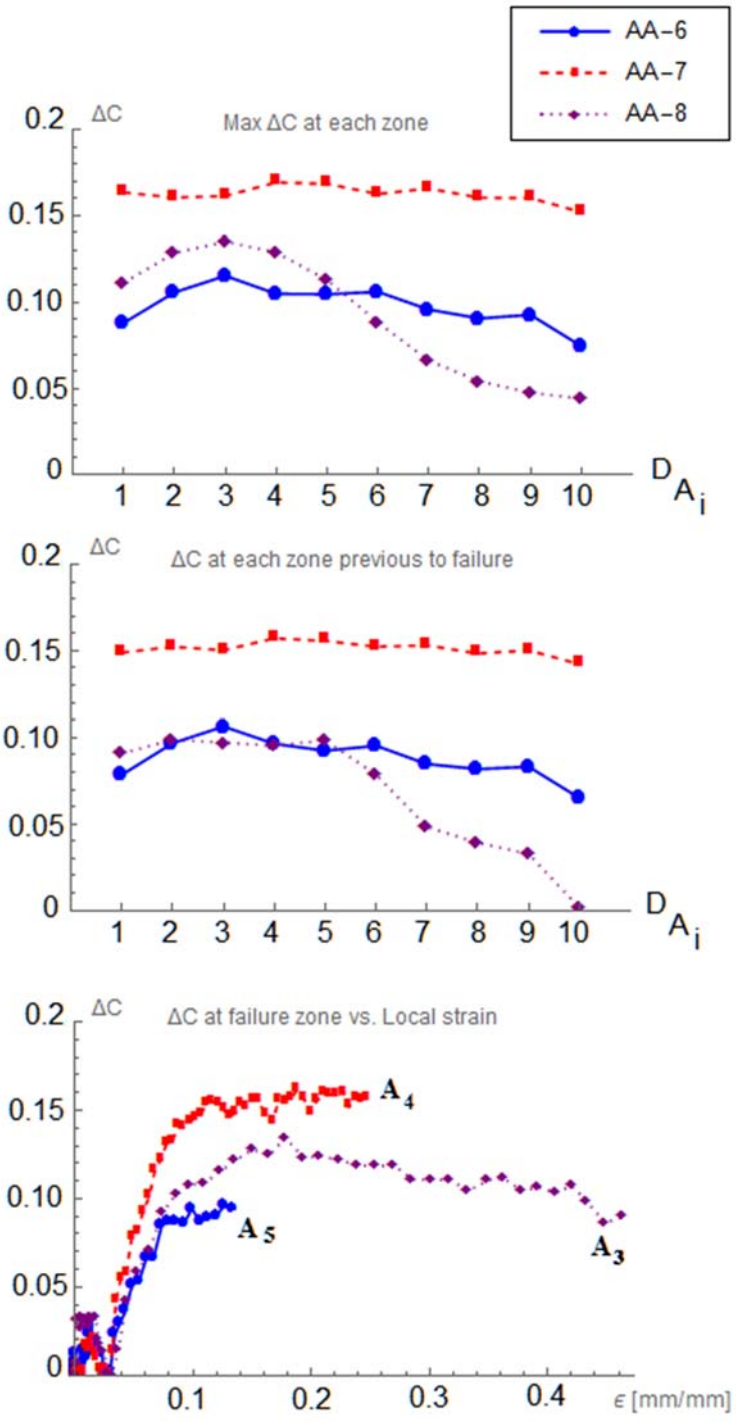

Figure 6-6: Changes in color at the moment of fracture

6.5.2 Damage calculated from fracture surfaces

Identification of voids and cracks in the fracture surface were made using images of the fracture cross section. The area of the features was measured and quantified. In-depth details about the analysis of fracture surface images were provided in Appendix D. The calculate damage in the fracture plane ($D_{\Delta A}$), accounting for the variability, fluctuated between 22 and 60% among the tested samples (Table 6-3). The calculated average damage values (~40%) were comparable between the two magnification levels used. The overall average damage from the fractography was calculated as 41% ± 18%.

Sample	Strain at failure [mm/mm]	Avg. damage at 80x	Avg. damage at 500x	Overall avg. damage fractography
AA-6	0.1142	0.36±0.14	0.41±0.23	0.38±0.16
AA-7	0.2107	0.47±0.20	0.41±0.10	0.44±0.16
AA-8	0.1874	0.47±0.23	0.34±0.20	0.41±0.21

Table 6-3: Damage from fractography ($D_{\Delta A}$) in DP-460NS

6.5.3 Damage with volumetric changes

Strains measurements were made at the front view (camera A) and the side view (Camera B) of each specimen at three different locations and the failure point (Figure 6-7 to 6-9, top row). Axial strains (e_{xx}) and lateral strains (e_{yy} and e_{zz}) were compared between views. There was an agreement in the measured strains between both views in Sample AA-6 at all locations (Figure 6-7, middle row). In the other two samples (AA-7, Figure 6-8 and AA-8 Figure 6-9), in certain instances there was departure between axials strains (e_{xx} Cam A ≠ e_{xx} Cam B) and lateral strains (e_{yy} Cam A ≠ e_{zz} Cam B) although this was only common for strains larger than 0.02, which is after the intrinsic yield of the material. In the few cases where there was a departure, this was at or close to the failure zones, where high strain gradients were detected . Shear strains were negligible during the test ($e_{xy} \cong e_{xz} \leq 0.05$). Typical strain offset error in the DIC analysis was calculated as 0.5% strain for the axial direction (worst case), while 0.01% strain can be expected as error for the lateral deformations. Appendix D includes a detailed analysis of the accuracy of the DIC results with expected errors and includes strain measurements at all points (Appendix D, Figure D4-2).

Damage ($D_{\Delta\varepsilon v}$) was calculated as a function of the measured strains using Tang's method (Equation 6-5) at the three locations where the strain was measured and at the fracture plane (Figure 6-7 to figure 6-9 bottom row). Of note in the results were the differences in calculated damage between the different samples. For sample AA-6 (strain to failure~ 0.012), the damage grew in a linear fashion up to a maximum value of ~5%. The propagation of damage was very even among all locations. The damage curves were compared against the theoretical prediction of the damage equation assuming isotropic elastic behavior before yield (ν=0.4) and volume conservation after yield ($e>0.02$, ν=0.5). Before yield it was determined that in this sample (AA-6), most of the damage followed the linear-elastic prediction. After yield, the calculated damage was attributed to the volumetric changes induced in the material by the uniaxial tensile loading. The damage history from volumetric strains was more complex in the other two samples. The behavior in sample AA-7 (Figure 6-8 bottom) was clearly not linear except at the middle of the test gauge (Point 2). The general trend can be described by initiation of damage in a linear fashion followed by a plateau transitioning then into further linear damage growth until final failure. Damage at fracture was calculated at ~ 8%. Damage in sample AA-8 (Figure 6-9 bottom) can be described by a bilinear process.

At low strains ($e<0.05$) the damage grows very fast that then transitions into a slower rate of growing. Of notice in this sample was that the damage at point one (far away from the fracture zone) stopped at an axial strain of 0.05 and reached a maximum value of ~ 8%. Point 2 (middle of the test gauge) deformed up to a strain of 0.17, and the damage grew up to ~6%. The damage was concentrated around point 3 (extensometer strain reported as e~0.13 at failure), which coincides with the area that developed necking during the test. The measured local strain field reported local axial strains in the order of 0.30 and 0.40. These values of localized strain can be well beyond the practical range of accurate DIC predictions ($e<0.20$) [172,173] for the proposed set-up. For these two samples, the detected damage by volumetric changes was larger than the theoretical damage from volumetric changes due to Poisson effects in the elastic regime.

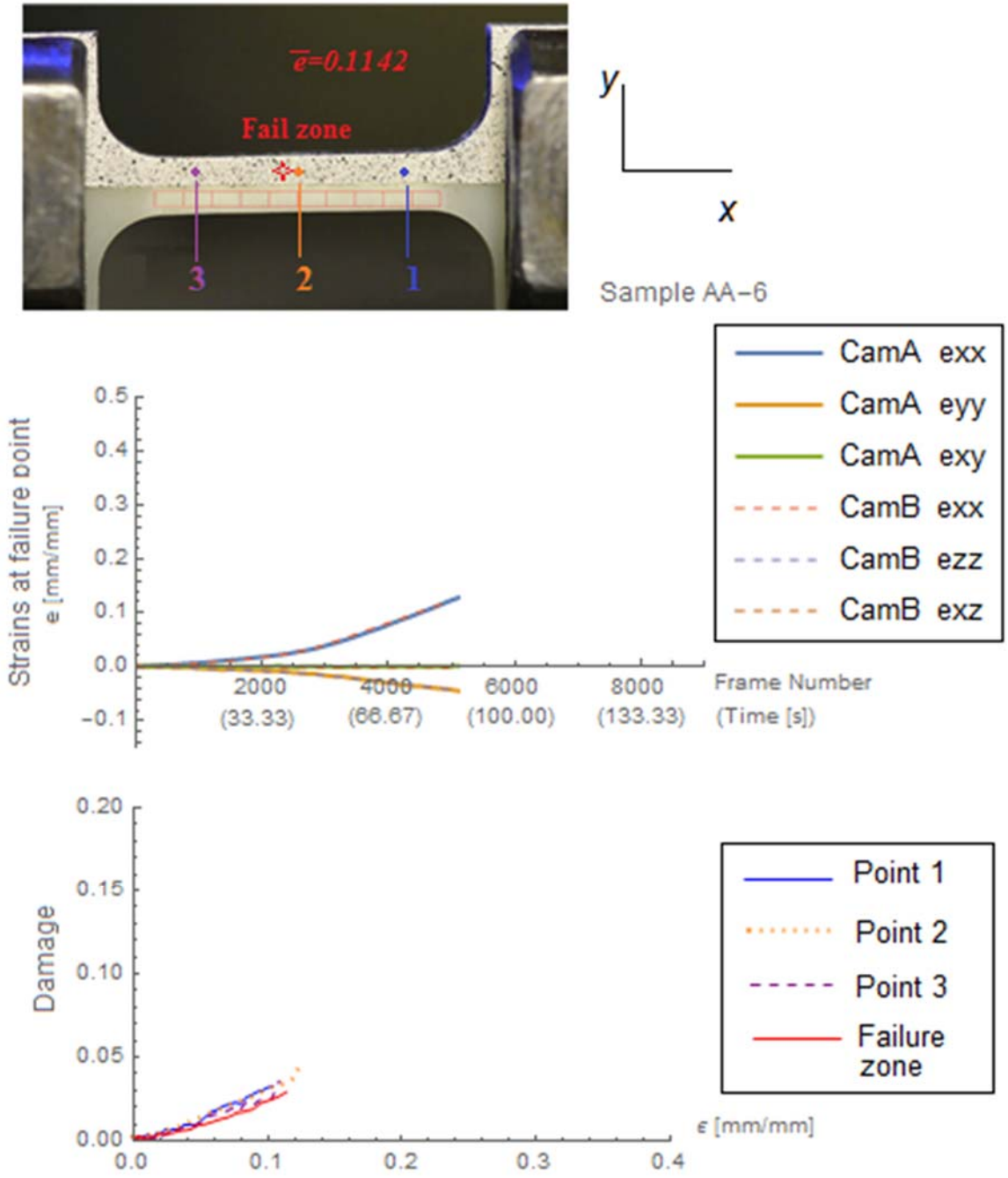

Figure 6-7: Strains and volumetric damage ($D_{\Delta\varepsilon v}$) calculated from DIC measurements in tested sample AA-6

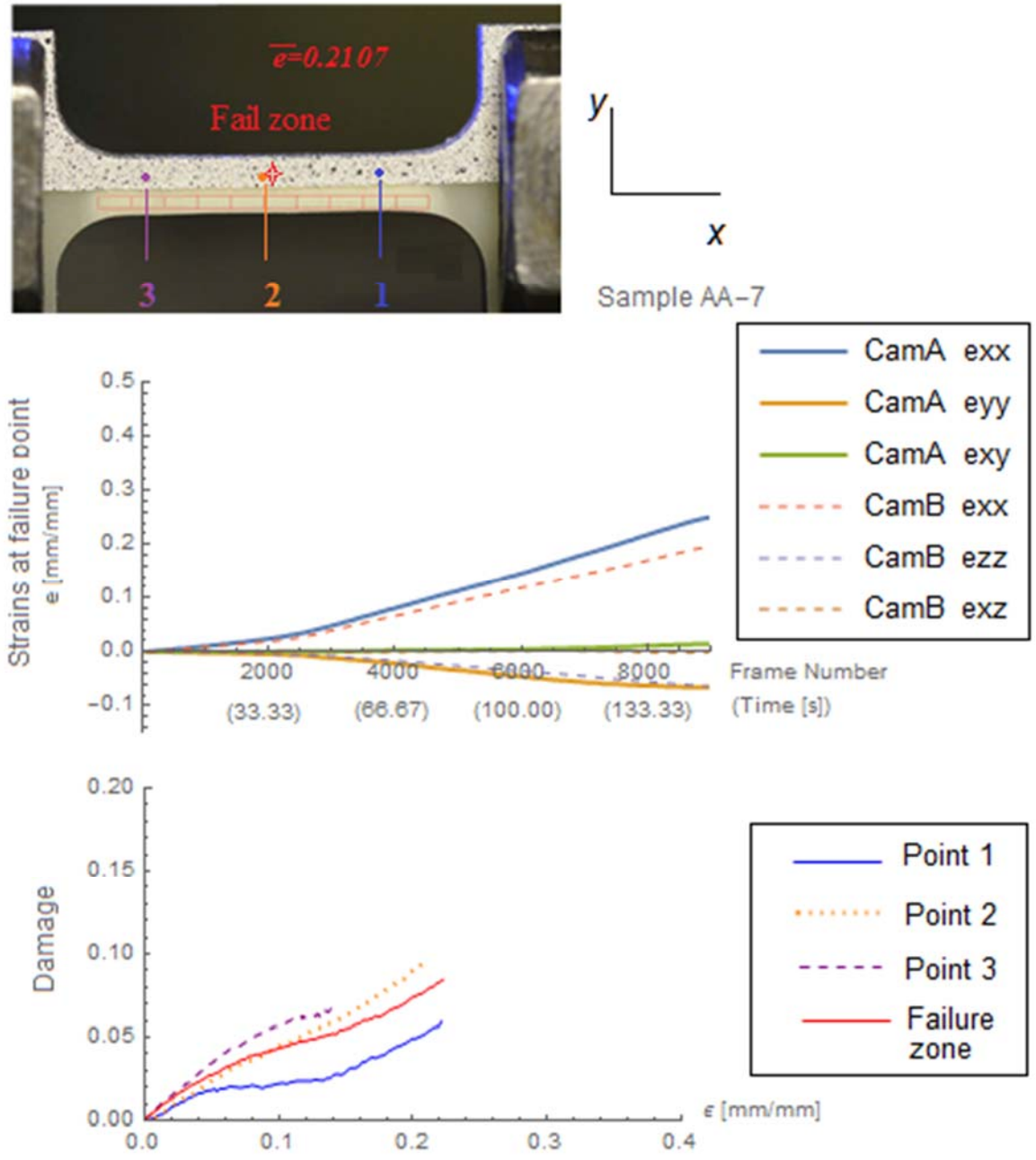

Figure 6-8: Strains and volumetric damage ($D_{\Delta\varepsilon v}$) calculated from DIC measurements in tested sample AA-7

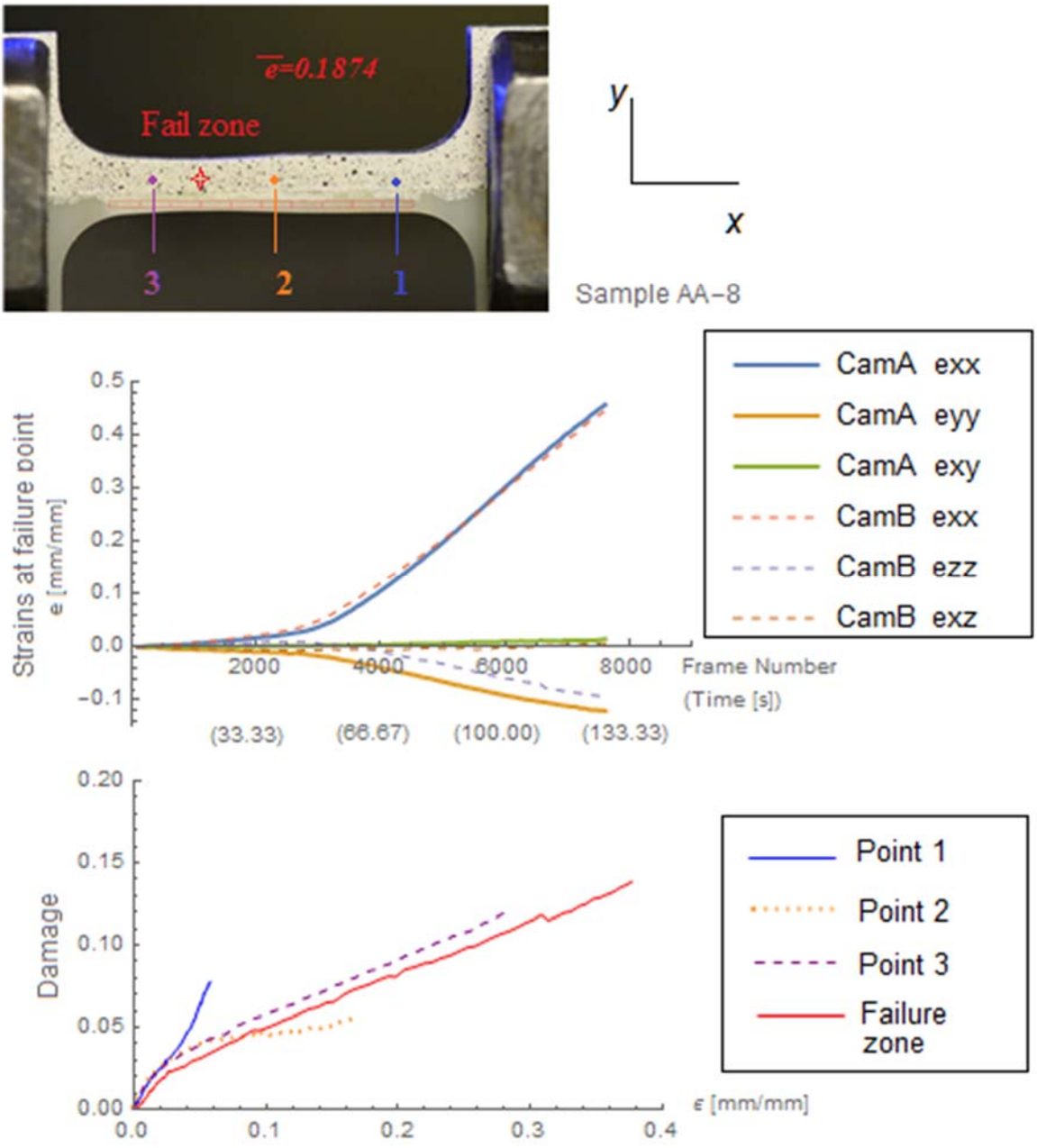

Figure 6-9: Strains and volumetric damage ($D_{\Delta\varepsilon v}$) calculated from DIC measurements in tested sample AA-8

6.5.4 Strain whitening damage with a macroscopic optical technique

Damage measurements using optical image analysis of the strain whitening was implemented by partitioning the test gauge of the coupons into 10 equal zones (Figure 6-5, and Appendix D figures D3-

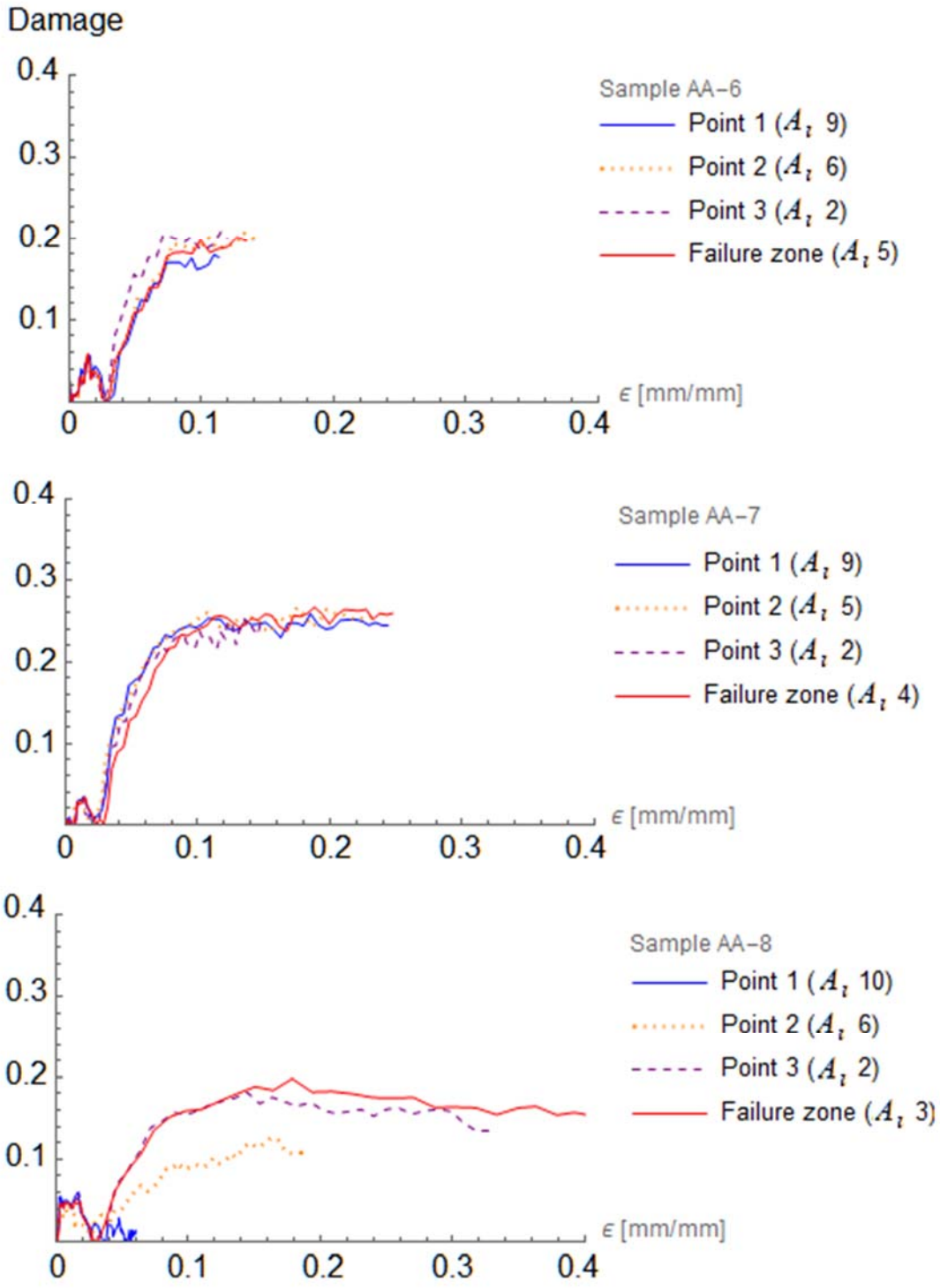

Figure 6-10: Damage calculated from images ΔC and fracture zone calibration

1 and D3-2) and then measuring the changes in color in each individual zone. The strain-damage history in each zone (D_{Ai}) was calculated by calibrating the change in color curves using the damage information from fracture surface void quantification. The lowest damage measurement from the fracture surface (5^{th} column, Table 6-3) was used to calibrate the zone that included the fracture plane; all other zones were considered proportional. Damage measurements fluctuated between 20% and 25% at failure (Figure 6-10). In the figure, the damage was described at the locations used to measure the DIC strains.

In general, the damage evolution as the samples were stretched, can be described by a rapid increase in the damage starting at a strain of ~0.02 until strain around 0.08. Further deformations into the plastic zone (e> 0.08) caused the damage rate to decline towards a plateau which stretched flat until final fracture. The process can be described with the use of a sigmoidal shape and was bounded by saturation, as the end of the slope of the curve was predominantly flat, once a particular value of strain was reached (typically ~0.08).

6.6 Discussion

It was hypothesized that changes in material color could be used as an indirect measurement of damage. To verify this hypothesis, it was necessary to compare the results against measurements of damage using different techniques. To begin, the relevance of the measured changes in color will be discussed. Then, the damage results from the changes in color will be compared against measurements of damage using volumetric strains and the other control techniques.

Color changes were detected by direct observation during the uniaxial testing. Although the changes in color were evident, the signal ratio between the measured average color and the base value (C_0) was used to determine false positives. At a low level of strains, typically less than 0.01, the changes were considered as false positives, since the signal ratio was low (<10 dB). Although it is possible to capture changes using optical techniques, this requires a high magnification setup as used in the previous study with the microscope. The current method uses the average of color changes, this averaging process can wash out any detected changes when they are small. At strains above 0.10, the material experienced a noticeable change towards a lighter color from ~0.72 to ~0.85 in average pixel value; this was typical in all tested samples. This signal change was on the order of 20 dB which highlights the relevance of the change. No further significant changes in average pixel color were detected beyond this level of

strain. The color transition phase, strains between 0.02 and 0.10, corresponds to the development of cavitation and crack opening followed by the development of shear bands. Of importance was the ability of the ΔC curves to correctly pinpoint the location of the fracture zone (Figure 6-6, top and middle), although the exact location can be somewhat hindered by the discretization of the surface and by the tracking scheme used for analysis. The first point was demonstrated with sample AA-7. In this case, the fracture happened between the boundaries of two of the discretization areas. The damage was spread between these two regions preventing the detection of a sharp peak and the subsequent identification of the fracture zone. Nevertheless, the method was robust, and the general region of failure was identified. The second limitation was caused by the inability of the analysis to account for localization since an even distribution of the strain along the test gauge was assumed. This had a more significant impact on sample AA-6 than it did on sample AA-8. On sample AA-6 the fracture zone was determined by manually locating the fracture point, while in sample AA-8 this was done by looking at the maximum value of changes in ΔC (Figure 6-6, top).

A comparison of the results from the different methods used to calculate damage (Figure 6-11), indicates that the average macroscopic changes in color (ΔC~14%) were in good agreement with the average damage from changes in effective strength ($D_{\Delta\sigma}$~15%) and changes in microhardness ($D_{\Delta MHV}$ ~16%). The ΔC values at each zone of analysis (A_i) along the test gauge were used to calculate the statistical spread as a function of the distance from the fracture zone. This data was compared against the damage values expected from changes in microhardness ($D_{\Delta MHV}$) in this material (Figure 6-12). At lengths not greater than 3.75 mm from the fracture zone, the likelihood of agreement between the means fluctuated between 75 and 85%, confirming a relatively good agreement between the two methods. Farther away from the fracture zone, between 4.5 and 7.5mm, the likelihood of agreement between measurements was reduced and fluctuated between 7 and 65%. The likelihood of agreement for distances greater than 8.5mm to the fracture plane increased to levels around 70%. The disagreement in statistical means in the region between 4.5 and 7.5 mm can be explained by the bias towards a higher value of ΔC caused by the even damage spread in one of the samples. The statistical analysis was conducted with a 95% level of confidence.

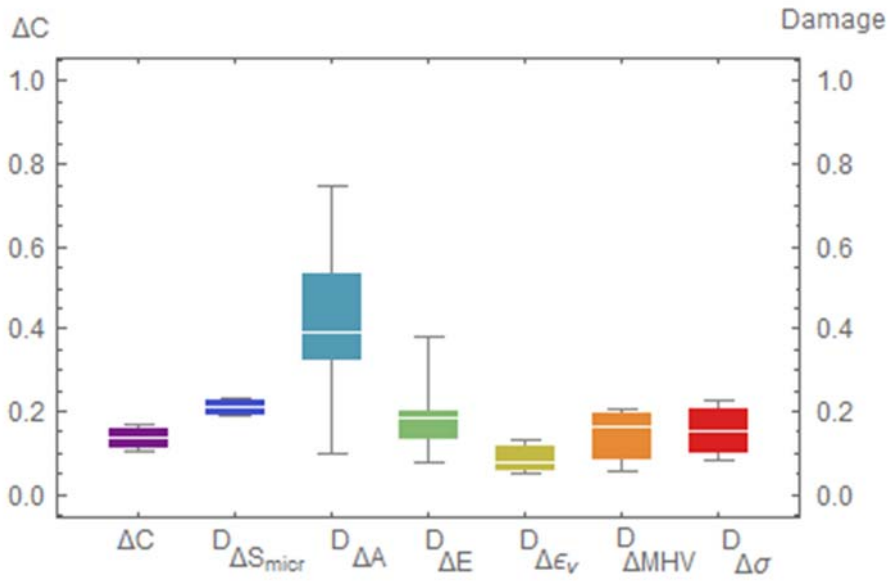

Figure 6-11: Changes in color vs. measurements of damage

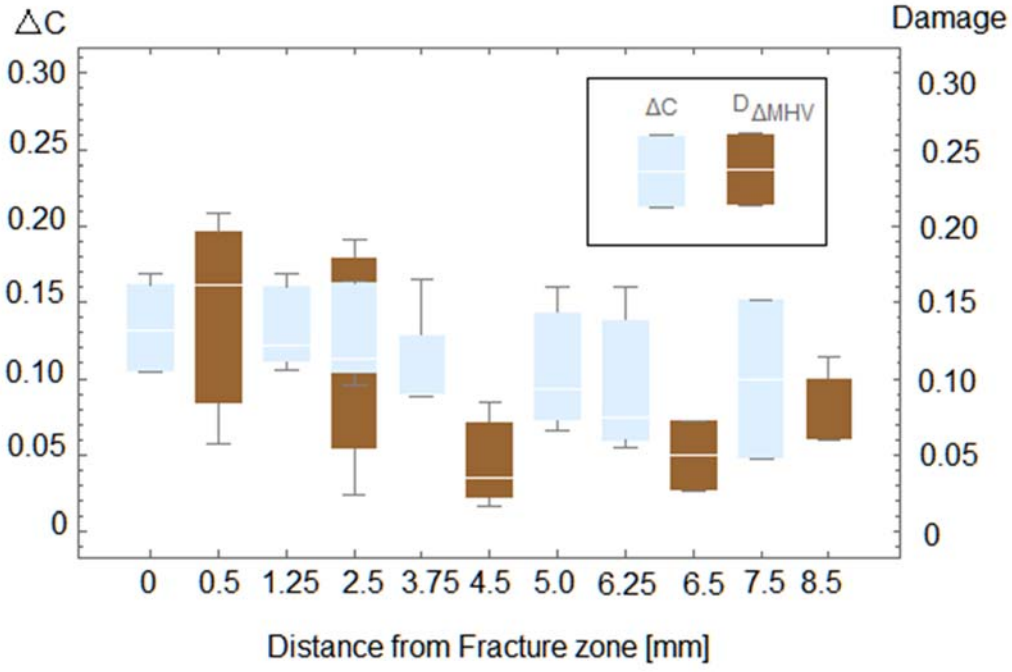

Figure 6-12: Changes in color vs. damage from changes in microhardness ($D_{\Delta MHV}$) in the test gauge

Even though the measured ΔC was in reasonable agreement with at least two methods, it was expected that the average value would be comparable to that of the damages calculated from microscopic changes in the material surface ($D_{\Delta Smic}$~ 21%). The difference can be reconciled by the averaging nature of the ΔC measurement instead of a pixel by pixel comparison as was done with the microscopic images. Also, the smaller resolution with the macroscopic observation can play a part in the differences due to a reduction in detectability.

The damage value at the fracture plane ($D_{\Delta A}$) was calculated by quantification of voids using microscopy. The $D_{\Delta A}$ value (Table 6-3) was compared against available measurements of damage (Figure 6-11). From the figure, the average measured damage value (39%) was not in agreement with any of the damage values calculated from the other methods: microscopic surface changes (21%), changes in modulus of elasticity (~18%), volumetric strains (8%), microhardness (16%) or variations in strength (15%). It must be mentioned though, that the $D_{\Delta A}$ values had quite a considerable variability (14 to 23 %). Although the variability in the measurement could have been the product of limited experience with fractography and image analysis, a variety of procedures were implemented to mitigate this (Appendix D). Automated algorithms exist for such a task too, but in many instances, the software requires either "algorithm training" or manual intervention by the operator, therefore eliminating or reducing the human error is not 100% possible. Even though this problem remains as a limitation of this study, the lower end of the measurements was comparable with damage values from the other methods. The $D_{\Delta A}$ average minus one standard deviation was then considered as the constant for calibration to obtain the damage curves from the changes in average color.

One unexpected finding was the low average damage (~ 8%) calculated from the changes in volumetric strain ($D_{\Delta \varepsilon v}$); this value typically fluctuated between 5% and 13% at the fracture zones. The differences were attributed to two possible explanations. First, error in the DIC measurements. Second, the applicability of Equation 6-5. Significant effort was applied to confirming the DIC results, and it was not possible to find any significant error in the strain measurements other than uncertainty in the results for strains above 0.2. Above this level of strain (e>0.2) it is possible that large deformations in the speckle pattern can introduce correlation errors. Therefore the second reason was explored in more detail. Equation 6-5 has been successfully used in the past to determine damage in other toughened polymers [47,162,166], but limitations such as the size of representative element used for analysis, and the presence of necking need to be considered [46]. In the first instance, the size of the representative

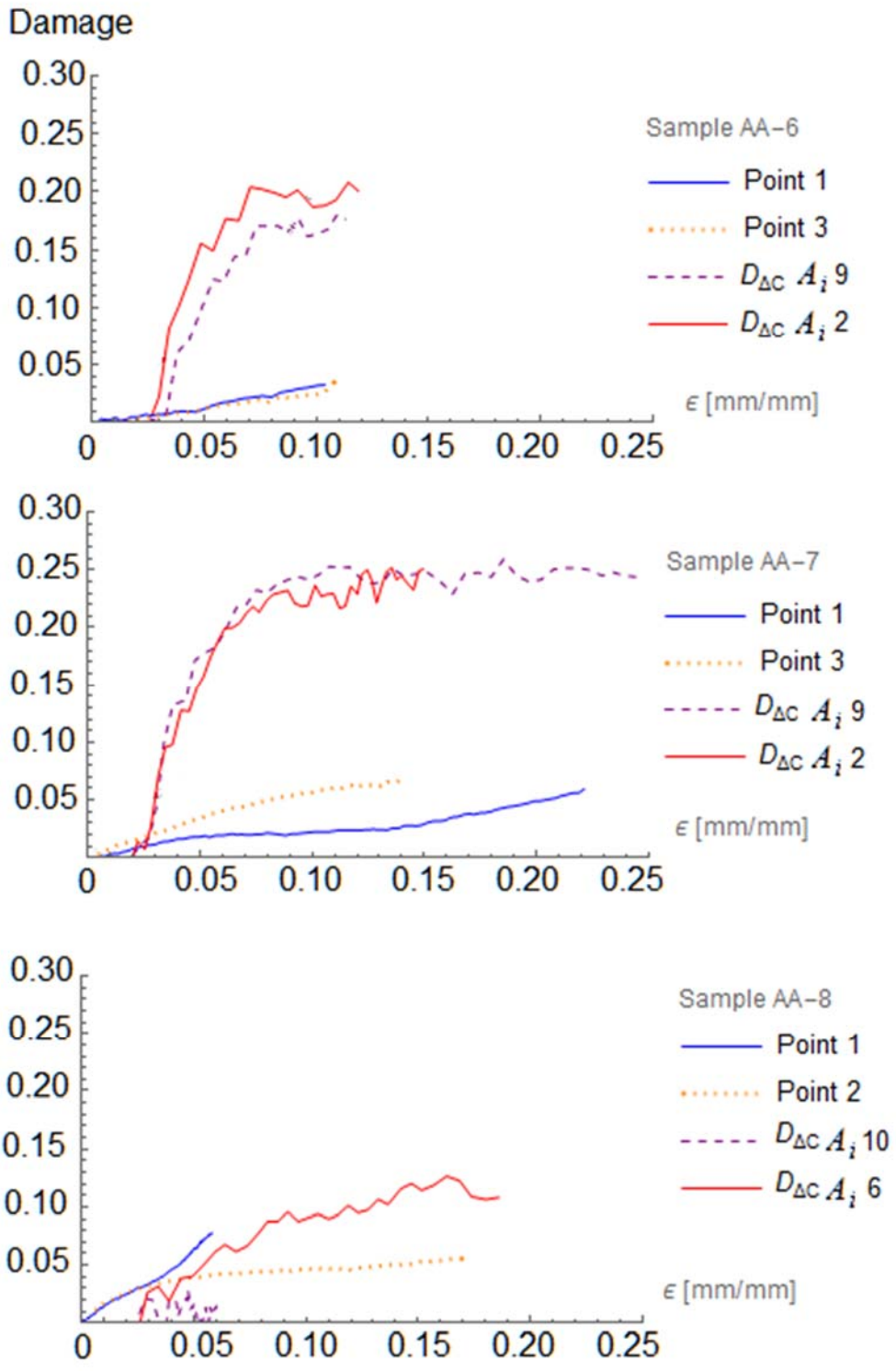

Figure 6-13: Damage from changes in color ($D_{\Delta C}$) vs. damage from volumetric strains ($D_{\Delta \varepsilon v}$)

element must be such that the strain measurements are conducted in the same volume. This constraint was not practical since representative size element for polymers (1 mm) would require measuring strains very close to the sample vertices where high gradients can be present, and the DIC results may not be accurate. Second, the presence of necking induces gradients in the strain field that cannot be accounted for, even though two views were considered for the analysis. Given these considerations, the damage using volumetric strains can only be considered valid away from any necking distortions.

The damage from changes in color ($D_{\Delta C}$) was compared against the volumetric damage ($D_{\Delta \varepsilon v}$) at locations away from the fracture zone (Figure 6-13). From each one of the samples, the measured $D_{\Delta C}$ (15 to 25%) was larger than the $D_{\Delta \varepsilon v}$ ($\leq$5%), although this difference can be dependent on the calibration value applied to build the damage curves from changes in color. However, the discrepancy (difference of at least 10% in average, Figure 6-11) also applies to damage calculated by other methods (changes in modulus of elasticity, changes in strength, changes in microhardness, microscopic observation). Differences between the strain-damage curve characteristics were also important. In the case of the $D_{\Delta C}$ the curves were sigmoidal in nature, demonstrating a rapid increase in damage between the end of the linear behavior (e~ 0.03) until the initiation of the plastic deformation (e~ 0.08) followed by saturation in the plastic regime where a transition from cavitation and crack openings towards shear banding occurs. The changes in color describe a process in which rapid changes in void formation were developed. Once the void growth peaks further energy absorption may be accomplished by accommodating large deformations through shear banding. The plateau in the curve could be interpreted as absence of further damage growth, however it is possible that the damage process is highly localized and further changes related to damage are not being captured. This can be a limitation related to:

1. The size scales used for measurement (optical changes, changes in modulus of elasticity) or,
2. Using a surface observation. Differential changes inside the volume of the material caused by damage may not any longer be reflected or detectable at the surface of the material.

The characteristic shape agrees with damage measurements using changes in modulus of elasticity (Figure 5-13). The $D_{\Delta \varepsilon v}$ curves were mostly linear with slow progressive changes, although some curves demonstrated small changes in slope at strain points that roughly coincide with the strain transition points just described. The volumetric strain depicts a very slow damage process, in which void growth was mostly uninterrupted until final failure. No hint of the significance of shear banding can be accounted for in the damage results from volumetric strains.

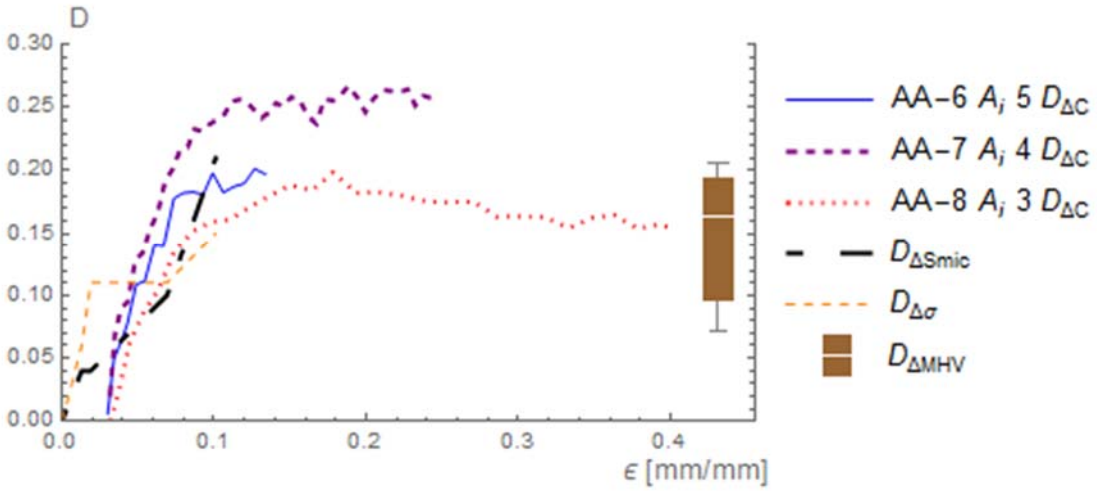

Figure 6-14: Damage at the fracture zones

Since $D_{\Delta \varepsilon v}$ values were not reliable due to necking at the fracture region, $D_{\Delta C}$ results in the fracture region were compared against different measurements of damage (Figure 6-14). It is significant to note that the $D_{\Delta C}$ values at the plateau fluctuated between 18 and 25%, which were comparable to the average of $D_{\Delta MHV}$ (~ 17%) and the measured maximums of $D_{\Delta Smic}$ (~ 21%) and $D_{\Delta \sigma}$ (~15%). Besides agreement in values, the $D_{\Delta \sigma}$ and $D_{\Delta Smic}$ curves also depicted the rapid growth of damage that started in the elastic region and progressed until the beginning of the plastic deformation (e > 0.10). The plateau described by the $D_{\Delta C}$ curves was not captured by the other two methods, but this can be attributed to lack of data rather than a physical disagreement in the described behavior of damage for this material. Although more data points using microscopic observations may be necessary to draw a final conclusion. Reported changes in modulus of elasticity and variations in strength support the presence of the plateau in the damage value (Figures 5-9, 5-10 and 5-13). This characteristic plateau in the damage curve can be tied to the energy absorption required to successively grow and nucleate slip surfaces within the material.

Another essential feature of the proposed technique was the ability to provide a continuous curve that can describe damage as a function of strain. The mechanical response of the material (solid lines) can be compared against the individual damage history (dashed lines) for the tested samples using quasi-static conditions (Figure 6-15). The method can be extended to testing at any rate as long as images can be captured. The stress-strain and strain-damage data are very valuable for the implementation of constitutive models for numerical simulations.

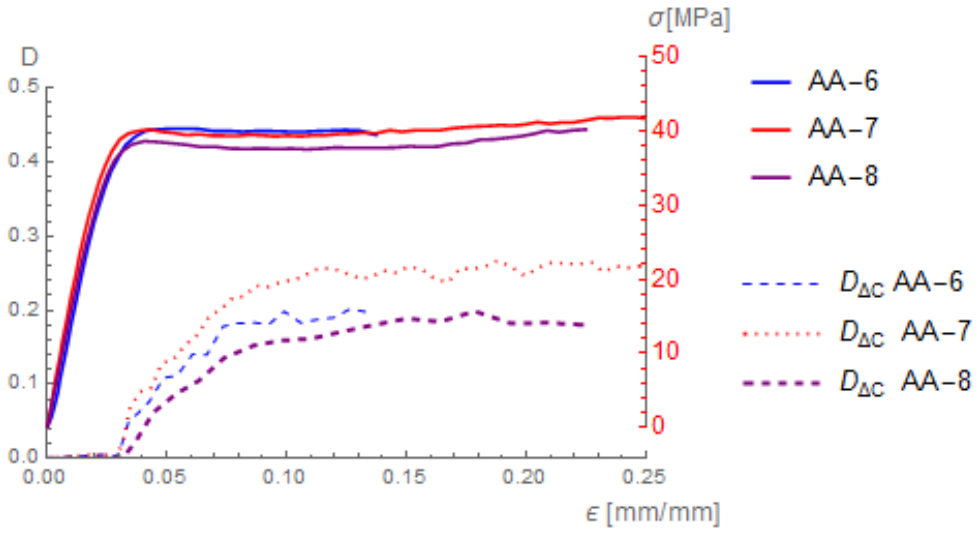

Figure 6-15: Stress-strain and damage-strain history for DP-460NS at quasi-static rates

6.7 Conclusions

During tensile loading of polymeric materials, damage may occur through particle cavitation, crack openings and eventually lead to shear banding, all of which can cause the material to appear as a lighter color when compared to the bulk unloaded material. In this study, a macroscopic optical technique to measure damage taking advantage of the strain whitening phenomenon in polymers was developed. The technique consisted of measuring the average change of material color in a specified area during deformation, then by calibrating the measured change with a known measure of damage, produce a curve that describes the damage evolution as a function of strain.

The fraction of voids in the fracture plane was used for calibration purposes even though this measurement had considerable variability, and required making assumptions regarding the appropriate calibration value. Besides that, proportionality had to be assumed between measurements at different locations. Regardless of these challenges, the technique predicted damage values (15 to 25%) similar to those of other measurements of damage in the same material using changes in strength (15%) and changes in the material surface using microscopic observations (~21%) and proved to be an accurate and simple method of measurement. The method can be improved by using damage from changes in microhardness as the calibration value. Not only was the damage from microhardness in reasonable

agreement with all other damage measurements (Figure 6-11), it has less variability in the results and microhardness can be measure at the same locations where changes in color are measured, which permits direct calibration at every zone of analysis and eliminate the assumption made in regard to proportionality.

Damage from volumetric strains was used as a control measurement. Although this is a powerful and practical technique, the results presented here point to the fact that careful consideration is needed for its implementation. Damage from volumetric strains produced results (~8% on average) that were substantially lower than any of the other techniques (19% on average). The findings support two conclusions. Firstly, there is a limitation in the use of volumetric strains to quantify damage. The technique can only account for damage that is associated with volumetric changes that are detectable. Second, the early discrepancy ($e \leq 0.05$) between the damage prediction of the volumetric changes and the other control techniques, points to the existence of a damage mechanism that does not readily manifest itself trough changes in volume. Later on, the incurred damage triggers the formation of shear bands. Even though shear bands are not typically considered damage[104] since they re a volumetric conserving process, it is necessary to count that they grow and nucleate slip surfaces, which can explain the energy absorption in the material during the plastic deformation at constant stress.

The optical technique can accurately predict the failure point of the material as well as the amount of damage in the fracture zone, but this ability can be limited by the discretization used for the analysis. Discretization issues can be solved by carefully locating the failure zone at the middle of one of the areas used for analysis rather than close to, or at the boundary between analysis zones. Correctly tracking deformation along the area of analysis can also impact the accuracy of the results. In this study, the deformation was assumed to be linearly distributed between the loaded end and the fixed end. This was met with relative success. However, this was a limitation when necking and/or large gradients were present. This can be solved by using multiple tracking points to determine the exact deformation and displacement history for each one of the areas used for analysis.

Damage measurement using changes in average color is a robust experimental technique that offers a new method to qualify, understand and measure damage evolution in polymeric materials with strain whitening. The proposed technique is a simple procedure, which requires little equipment overhead (camera, a personal computer with coding software and a microscope or a micro-indentation machine),

and can easily provide accurate damage information at a variety of strain rates (limited by the image capturing capabilities). Strain-damage curves are much-needed information for the implementation of constitutive material models in the numerical simulation of bonded structures with structural epoxy adhesives.

Chapter 7
Summary

7.1 Conclusions

The main conclusions of this dissertation are:

1. Simulation results indicate that a cohesive zone model (MAT_240) and solid element formulation (MAT_187) can provide an adequate representation of adhesive material for tensile and shear loading across a range of deformation rates. The three tested adhesive materials demonstrated that, at the very least, independent data in tension and shear are needed for modeling. However, deficiencies in current constitutive models for use with structural adhesives were identified. In particular, a constitutive model must be capable of uncoupling strain rate effects for tension and shear loading. This is not the case with current models, and this could introduce significant errors when modeling components subjected to mixed mode load conditions. Additionally, it was shown that the shear stress could not be linked to the tensile stress using traditional yield theories (e.g., von Mises). This will require the implementation of custom subroutines to properly evaluate plastic deformation and failure criteria in the modeling of adhesive materials.

2. Microhardness measurements demonstrated that damage along the gauge length of a strained epoxy adhesive was dependent on both the chemistry of the adhesive and the strain rate. In a non-toughened epoxy (EC-2214), the damage was highly localized around the fracture zone. In toughened epoxies (DP-460NS and SA-9850), the damage extended over much of the sample gauge length and the microhardness variations were linked to the deformation mechanisms. In these two materials, the shear banding generally increased the measured hardness, while crack openings and craze-like behavior decreased the measured hardness. In some cases, these variations offset one another and ultimately affected damage results calculated with the use of microhardness. With increments in strain rate, localization increased. Although microhardness provided insight into the material damage behavior, it was limited to a post-load/post-failure analysis. For acquiring continuous damage data using this method, it would be required to load the material and then stop to perform indentations. The new indentations can serve as stress concentrators if the loading were to be continued

and bias then the next set of measurements. Alternatively, one could load different samples to different levels of load and then take the microhardness measurements.

3. It is possible to take advantage of changes in material surfaces during load to indirectly determine damage. Damage may occur through particle cavitation and crack openings, which eventually can lead to shear banding, all of which can cause changes in the material surface. By comparing pixel values between successive images for a given location, it was possible to quantify the surface changes with increases in load. The process was conducted using analysis of microscopic images. Damage values from microscopic surface changes (21%) were comparable to damage from changes in effective stress (15%), changes in microhardness (17%), and changes in stiffness after accounting for viscoelastic effects (18%). Additionally, the microscopic observations provided values of the local strain fields, but most importantly insight into the crack growth process, values for stress concentration at crack tips, and identification of the role of cavitation in the shear banding process previous to ultimate failure. The optical measurements provided a way to capture damage data without disturbing the material during testing. However, implementing a microscopic observation procedure as a general method for tracking damage was limited in the current study by the size of the field of view.

4. A macroscopic optical technique to measure damage taking advantage of the strain whitening phenomenon in polymers was developed to overcome the limitations of the microscopic observations. The technique consisted of measuring the average change of material color in a specified area during deformation, then by calibrating the measured change with a known measure of damage, produce a curve that describes the damage evolution as a function of strain.

    a. The fraction of voids in the fracture plane was used for calibration purposes although this measurement had considerable variability. Besides that, proportionality had to be assumed between measurements at different locations. Regardless of these limitations, the technique predicted damage values (15 to 25%) similar to those of other measurements of damage in the same material using changes in strength

(15%), changes in the material surface using microscopic observations (21%), and changes in stiffness when accounting for viscoelastic effects (18%). In addition, the macroscopic optical technique predicted a sigmoidal behavior for damage evolution. This was in agreement with the predictions from changes in modulus of elasticity during load-unload, load-reload and changes in strength. Additionally, a traditional technique for damage detection, changes in volumetric strains, was also implemented. Volumetric changes predicted damage at approximately 8% just before failure. The measurements were substantially lower than all the other control techniques.

b. Interestingly, the results indicate that the quantification of the surface changes, both microscopic (changes in pixels) and macroscopic (average change in color), were directly comparable to the measurement of damage calculated using microhardness. Discretization studies were conducted for the macroscopic technique and demonstrated robustness in the method and quick convergence in results. However, how the results can be impacted by variations in the field of view and focal length (i.e. how close the camera is to the specimen) require further study.

c. The macroscopic optical technique can lack sensitivity for detection at small deformations. This limitation can be attributed to the average nature of the implemented calculation to define the changes (average change in color), but also to the sensitivity of the equipment used for detection. The first can be improved by increasing discretization or changing the mathematical scheme that defines the change. The second factor, sensitivity, will always be limited by equipment (type of sensor) and the compromises inherit with capturing the desired field of view (focal length). In other words, it is possible to calculate damage at a small region in the material with high sensitivity by decreasing the focal length (e.g., use of a microscope or a high magnification lens) or to obtain damage information over a large amount of material with reduced sensitivity (DSLR).

d. The proposed optical technique can accurately predict the failure point in the test specimen as well as the amount of damage in the fracture zone. The prediction ability can be limited when the failure plane is located at the boundary of contiguous

analysis zones. Changes in discretization and convergence studies can mitigate this issue.

e. Correctly tracking deformation along the area of analysis used for the optical measurement can also impact the accuracy of the results. The deformation gradient was assumed to be linearly distributed between the loaded end and the fixed end of the test specimens, which was in agreement with DIC measurements. However, this is a limitation when necking and/or large gradients are present. Using multiple tracking points to determine the exact deformation and displacement history for each one of the areas used for analysis can mitigate this problem.

f. The method can be improved by using damage from changes in microhardness along the length of the specimen after testing as the calibration value. Damage from microhardness measurements can be calculated at the same locations where changes in color are measured, which permits direct calibration at every zone of analysis and eliminates the assumption made in regard to proportionality.

5. Different methods were implemented to measure damage in the DP-460NS adhesive. The average damage (38%± 6%) predicted by the changes in modulus (load-unload) previous to failure was comparable to that calculated from counting voids in the fracture surfaces (41% ± 18%). However, these results were substantially higher than the average damage predicted by other methods: 17% damage by changes in microhardness, 8% with volumetric strains, 21% with changes in microscopic surfaces and 15% with changes in strength. The results do not imply that one method is wrong or better than the other, the discrepancies required further understanding in regard to the nature of the material, the active mechanisms present during the material deformation and the limitations of each technique.

   a. The calculated damage using the traditional methodology (i.e. modulus of elasticity during load-unload) did not account for viscoelastic effects in the adhesive material. The viscoelastic effect was noted as a change in the stiffness value measured between the first unload and the second load cycle. It was concluded that a much better measure of damage could be approximated by calculating the damage using the first load modulus of elasticity in combination with the modulus of elasticity

during the second load cycle at the upload portion of the test. The corresponding damage value from load-reload (17.77%± 7.74%) was in better agreement with all the other calculated values for damage.

b. The estimated average damage (41%) from the images at the fracture plane had considerable variability (±18%), this, in turn, was caused by the inherit potential for error in the void counting process, manual or otherwise, even though measures were taken to mitigate observation error. It was hypothesized that the large discrepancy in average value against all other measurements could be explained by the existence of cavitation and craze-like mechanisms. During tension, the toughening particles in areas around cracks can cavitate and act as tendons that absorb energy and prevent further crack tip opening, which in turn allowed the material to continue carrying the load. This behavior has a substantial effect on the effective area that carried the load during straining and after final failure. Before failure, this craze-like behavior is reflected in the response of the modulus of elasticity (hence lower damage); after failure, the cracks reached their maximum extension and this resulted in the identification of more and larger voids at the fracture plane. It is possible that the crack features and cavitated material contributed to calculating a much larger area of voids in the fracture plane, causing then an over prediction in the amount of damage suffered by the material when compared to the damage values from other techniques (i.e., microhardness 17%, microscopic surfaces 21%, changes in strength 15%) before final failure.

c. The presence of crazing or craze-like behavior in epoxy adhesives is controversial. Crazing and cavitation are typically depicted by increases in volume. The damage from volumetric changes was in agreement with other methods at very low amounts of deformation only ($e<<0.01$). This demonstrates that cavitation or cavitation like behaviour were significant in the earlier stages. However, there was a departure in damage prediction as the amount of strain was increased. This difference in the total amount of damage supports the fact that there is a damage mechanism that can not be explained by volumetric changes alone. Modern toughened epoxy adhesives are very complex materials from both composition and molecular structure. Such intricacies compounded with the complex stress fields that can develop in these

materials may help to explain this phenomenon but this study highlights the necessity for further research and forces us to re-evaluate the role of traditional mechanisms such as crazing and cavitation in toughened adhesives.

d. Although shear bands are not typically considered damage, since they are a volume conserving phenomenon, the experimental results hint that further consideration needs to be given to the role that shear bands play in the damage and ultimate failure of polymeric materials. Observations inside the shear banded region at high magnification demonstrated porosity (sponge like surface) and the presence of micro voids. Such appearances can be explained by assuming that cavitation was also a damage mechanism in this stage. Although this assumption seems to be supported by the ever-increasing volumetric change detected with the DIC, it is at the same time at odds with the other damage measurements (changes in modulus of elasticity by load-reload, changes in strength, and the macroscopic optical technique) in which damage saturation was reported. The plateau in the calculated damage value could be interpreted as absence of further damage growth, however it is possible that the damage process is highly localized and further changes are not being detected. This can be a limitation related to the size scale used during measurement (optical changes, changes in modulus of elasticity). Although there was large plastic deformation, very few samples of the toughened epoxy developed necking. In most cases, the material fracture resembled brittle behaviour and no evidence of significant cavitation was apparent on the SEM observation. Other phenomena related to the development of shear bands were the increases in microhardness and the stiffening effect in the measured unload response. Both measurements indicate the presence of strong bonds that need to be deformed, but this is not reflected by an increase of the stress in the plastic portion of the stress-strain response under uniaxial tension. Increases in the strength with strain in the plastic regime, is considered typical of polymers with a high degree of shear banding. No reports in the literature have been found that detail or can explain these contradictory behaviors.

7.2 Contributions

The novel contributions of this dissertation can be summarized as:

1. Material models (constitutive models) are developed based on underlying theory, or as empirical fits to data. In all cases, experimental data is needed but some challenges in experimental testing of adhesives were identified and need to be addressed to support current and future work in this field:

    a. A sample geometry that enables the measurement of fracture toughness and traction-displacement response in Mode I and Mode II loading at high strain rates is required to support the implementation and development of cohesive models.

    b. There is need for experimental techniques that can provide damage data such as damage-strain curves and damage distribution profiles. The first information (damage-strain history) is useful for implementing constitutive models enhanced with damage mechanics formulations. The second is key for the validation and verification of such models.

2. Microhardness is not a 'standard' technique such as the use of changes in modulus of elasticity to measure damage. In this work it was shown that microhardness is a robust tool that can be used not only to identify different trends for different adhesives, but it can also identify characteristics in response at large strains that may not be captured using other techniques. Microhardness also has the capacity of providing field measurements of damage. That is, damage results can be captured along any area of the specimen and provide granularity about damage distribution. Microhardness is traditionally used as an industrial control technique for quality control in polymeric materials. However, it was established that its use can be extended to measure damage in toughed epoxies.

3. The primary objective of this work was the development of a technique that can provide damage-strain data as a field measurement. For this purpose, traditional methods such as measuring changes in microhardness, changes in modulus of elasticity, fractography, volumetric strains and optical techniques were implemented. The findings of this work contribute to expand the current knowledge of toughened adhesives but also points to

limitations in the available techniques. The different studies support the contention that concurrent experimental measurements may be necessary to fully understand damage evolution in structural adhesives. For example:

ii. The use of fractography alone to determine damage can be heavily biased and over predict damage levels in a material previous to failure. This risk can be mitigated by implementing a second technique such as microhardness.

iii. Experimental data supports the development of cavitation followed by shear banding. During the transition between these two mechanisms, the differences in prediction between damage measuring techniques (load-reload, changes in strength and optical techniques vs. volumetric strains) point to the existence of a damage mechanism that is not reflected by changes in volume. Such differences could have not been detected if volumetric changes had been the only technique implemented for measurement.

4. It was determined that viscoelastic effects played a role in the detected differences in the mechanical response and the measured damage values It was identified that in the DP-460NS material, the damage predicted by the changes in stiffness using traditional load-unload measurements (D~35%) could not accurately be used to predict reloading behavior since the actual damage value that can be used to predict changes in stiffness and effective stress during reloading was substantially lower (D~20%). Current numerical implementations to represent adhesive materials (cohesive elements and continuum formulations with damage) may not be able to describe or replicate this mechanical response. This study points to the necessity of implementing a constitutive model, that can differentiate between first load, unload and following re-load. Multi-material structures or engineered components bonded with toughened epoxies that show craze-like behavior followed by shear banding will require such a model when cyclic loading needs to be considered and evaluated.

5. Damage measurement using changes in average color is an accurate and robust experimental technique that offers a new method to qualify, understand and measure damage evolution in

polymeric materials with strain whitening. The technique can provide strain-damage curves, which are much-needed information for the implementation of constitutive material models for structural adhesives and other polymeric materials. The proposed experimental technique has the following advantages:

a. It is a simple procedure that requires little equipment overhead: a camera, a personal computer with coding software and a microscope or micro-indentation machine.
b. It is an enhanced non-destructive measurement method. It provides field information that is missing, or that can be very laborious to obtain when using traditional techniques such as load-unload or analysis of fracture zones.
c. This field information can be used to better understand and quantify damage evolution and distribution in a material.
d. Although the method is limited to strain whitening materials, the measurement can be implemented with any type of testing apparatus (e.g., Split Hopkinson bar) at any strain rate as long as a suitable image capturing device is used. The camera can use either color sensor or black and white with no difference in the implementation.

7.3 Recommendations for future work

The research presented in this dissertation had limitations that can be overcome with further work in the following areas:

1. Deformation along the area of analysis for the optical technique can impact the accuracy of the results. In the study, the deformation was assumed to be linearly distributed; however, this was a limitation when necking and/or large gradients were present around the final fracture region. This can be solved by using multiple tracking points to determine the exact deformation and displacement history for each one of the areas used for analysis. The current code for analysis needs to be enhanced with this feature.

2. The measurement of damage in materials is not a simple task, the resultant strain-damage curves from the optical method developed in this research need to be extended to more adhesive materials and include testing at various strain rates. The additional data will make a valuable addition to the existing literature regarding the mechanical properties of adhesives and polymeric materials given the relevance of these materials for fields such as automotive and aero-space.

3. Engineering design requires the consideration for fatigue life in many instances. Since microhardness was successfully correlated with damage, it is possible that hardness measurements captured at different levels of applied strain can also be correlated with fatigue life. S-N curves are not readily available for structural adhesives, and work is still required in this area. Of interest would be the use of Dynamic Mechanical Analysis. The use of DMA can provide further insight into the development of damage as changes in the mechanical and viscous properties of polymeric materials can be detected with load.

4. Numerical simulation based on micromechanics models were conducted aside from this work. This is not only a powerful and robust way to predict the mechanical response of epoxy structural adhesives, but it also provides insights and understanding about the behavior of the individual components that constitute the adhesive. It will be desirable to incorporate damage data to further refine the capability of available micromechanics models, e.g., Eshelby or Mori-

Tanaka. This enhancement can be used to numerically predict the mechanical response of more complex epoxy adhesive formulations. This is important for two reasons: first, it optimizes the formulation design process previous to manufacturing and actual testing which in terms maximizes the use of resources and enhances economic benefit. Second, the inclusion of damage data for the different individual constituents can facilitate the understanding of the micro-mechanical interactions between the different constitutive phases which in turn can predict the more likely damage mechanisms to occur as well as the circumstances that trigger them in complex polymeric materials.

5. This work demonstrated that the understanding of epoxy adhesive materials is far from complete, especially when considering that new and more complex formulation of modern epoxy adhesives are in the drawing board or already in the production line (i.e., nano particle reinforced epoxies, bio-degradable epoxies, etc.). The role of cavitation in the development of craze-like damage mechanisms and the propagation of shear bands need further in-depth study that can help explain the steps that will lead to the ultimate failure in these new materials.

Copyright Permissions

Figure 2-4 and Figure 2-9

JOHN WILEY AND SONS LICENSE TERMS AND CONDITIONS

Nov 13, 2018

This Agreement between Luis F Trimino ("You") and John Wiley and Sons ("John Wiley and Sons") consists of your license details and the terms and conditions provided by John Wiley and Sons and Copyright Clearance Center.

License Number	4467170938846
License date	Nov 13, 2018
Licensed Content Publisher	John Wiley and Sons
Licensed Content Publication	Journal of Polymer Science Part B: Polymer Physics
Licensed Content Title	Toughening of epoxies via craze-like damage
Licensed Content Author	H.-J. Sue, E. I. Garcia-Meitin, N. A. Orchard
Licensed Content Date	Mar 11, 2003
Licensed Content Volume	31
Licensed Content Issue	5
Licensed Content Pages	14
Type of use	Dissertation/Thesis
Requestor type	University/Academic
Format	Print and electronic
Portion	Figure/table
Number of figures/tables	2
Original Wiley figure/table number(s)	Figure 3 Figure 7
Will you be translating?	No
Title of your thesis / dissertation	Strain Whitening in Epoxy Adhesives, Correlations with Damage and Development of a Macroscopic Optical Method for Damage Characterization
Expected completion date	Jan 2019
Expected size (number of pages)	217
Requestor Location	Luis F Trimino 301-36 River road East kirch2ner, ON N2B2G2 Canada Attn: Luis F Trimino
Publisher Tax ID	EU826007151
Total	0.00 USD
Terms and Conditions	

TERMS AND CONDITIONS

This copyrighted material is owned by or exclusively licensed to John Wiley & Sons, Inc. or one of its group companies (each a"Wiley Company") or handled on behalf of a society with which a Wiley Company has exclusive publishing rights in relation to a particular work (collectively "WILEY"). By clicking "accept" in connection with completing this licensing transaction, you agree that the following terms and conditions apply to this transaction (along with the billing and payment terms and conditions established by the Copyright Clearance Center Inc., ("CCC's Billing and Payment terms and conditions"), at the time that you opened your RightsLink account (these are available at any time at http://myaccount.copyright.com).

Terms and Conditions

- The materials you have requested permission to reproduce or reuse (the "Wiley Materials") are protected by copyright.

Figure 2-5

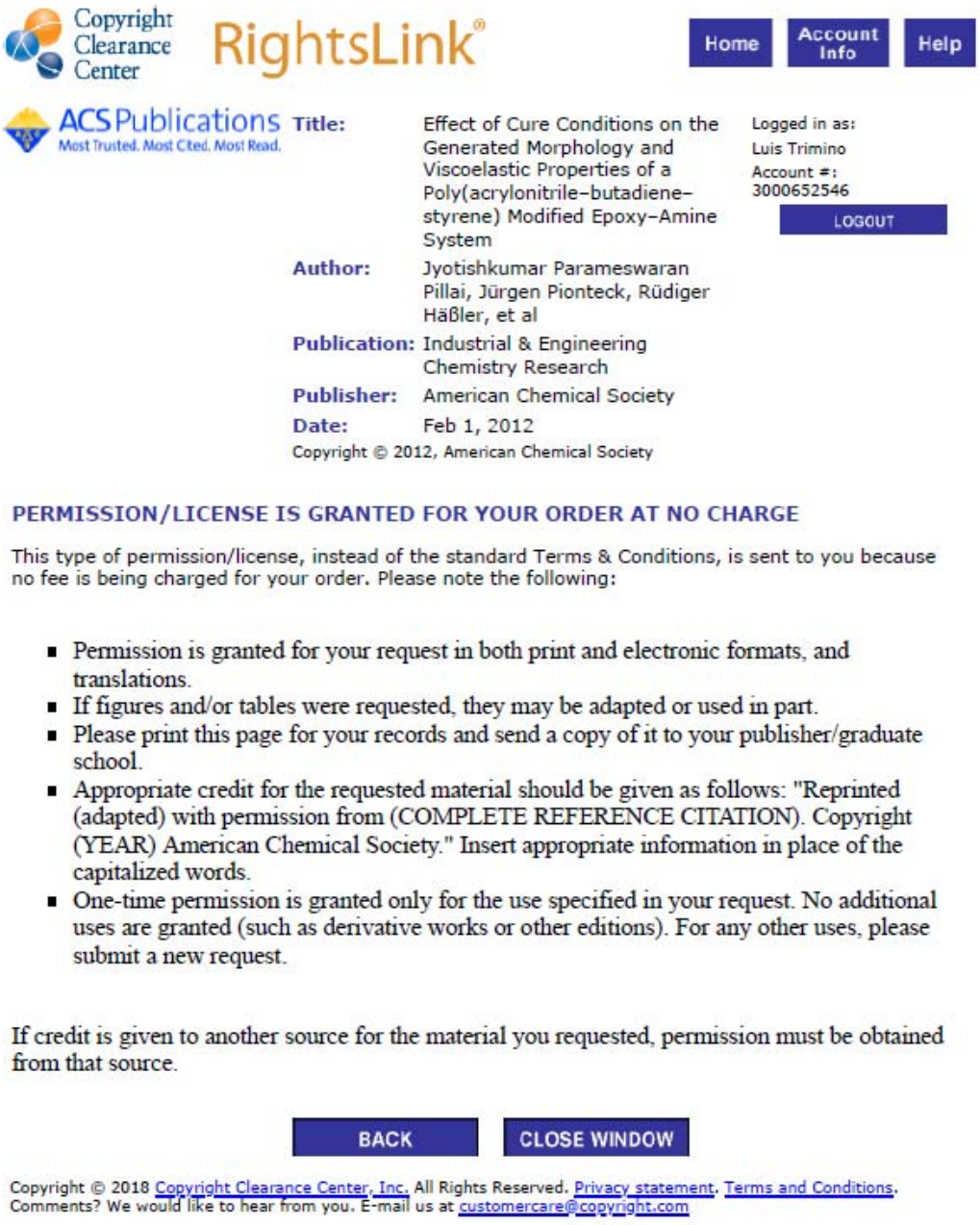
Copyright Clearance Center
RightsLink
Home
Account Info
Help
ACS Publications
Most Trusted. Most Cited. Most Read.
Title: Effect of Cure Conditions on the Generated Morphology and Viscoelastic Properties of a Poly(acrylonitrile–butadiene–styrene) Modified Epoxy–Amine System
Author: Jyotishkumar Parameswaran Pillai, Jürgen Pionteck, Rüdiger Häßler, et al
Publication: Industrial & Engineering Chemistry Research
Publisher: American Chemical Society
Date: Feb 1, 2012
Copyright © 2012, American Chemical Society
Logged in as:
Luis Trimino
Account #:
3000652546
LOGOUT
PERMISSION/LICENSE IS GRANTED FOR YOUR ORDER AT NO CHARGE
This type of permission/license, instead of the standard Terms & Conditions, is sent to you because no fee is being charged for your order. Please note the following:
Permission is granted for your request in both print and electronic formats, and translations.
If figures and/or tables were requested, they may be adapted or used in part.
Please print this page for your records and send a copy of it to your publisher/graduate school.
Appropriate credit for the requested material should be given as follows: "Reprinted (adapted) with permission from (COMPLETE REFERENCE CITATION). Copyright (YEAR) American Chemical Society." Insert appropriate information in place of the capitalized words.
One-time permission is granted only for the use specified in your request. No additional uses are granted (such as derivative works or other editions). For any other uses, please submit a new request.
If credit is given to another source for the material you requested, permission must be obtained from that source.
BACK
CLOSE WINDOW
Copyright © 2018 Copyright Clearance Center, Inc. All Rights Reserved. Privacy statement. Terms and Conditions.
Comments? We would like to hear from you. E-mail us at customercare@copyright.com

Figure 2-6

JOHN WILEY AND SONS LICENSE TERMS AND CONDITIONS

Dec 18, 2018

This Agreement between Luis F Trimino ("You") and John Wiley and Sons ("John Wiley and Sons") consists of your license details and the terms and conditions provided by John Wiley and Sons and Copyright Clearance Center.

License Number	4491990726897
License date	Dec 18, 2018
Licensed Content Publisher	John Wiley and Sons
Licensed Content Publication	Polymer Engineering & Science
Licensed Content Title	Fracture failure processes in polymers. I: Mechanical tests and results
Licensed Content Author	K. Liu, M. R. Piggott
Licensed Content Date	Apr 8, 2004
Licensed Content Volume	38
Licensed Content Issue	1
Licensed Content Pages	9
Type of use	Dissertation/Thesis
Requestor type	University/Academic
Format	Print and electronic
Portion	Figure/table
Number of figures/tables	1
Original Wiley figure/table number(s)	Figure 4
Will you be translating?	No
Title of your thesis / dissertation	Strain Whitening in Epoxy Adhesives, Correlations with Damage and Development of a Macroscopic Optical Method for Damage Characterization
Expected completion date	Jan 2019
Expected size (number of pages)	217
Requestor Location	Luis F Trimino 301-36 River road East kirch2ner, ON N2B2G2 Canada Attn: Luis F Trimino
Publisher Tax ID	EU826007151
Total	0.00 USD
Terms and Conditions	

TERMS AND CONDITIONS

This copyrighted material is owned by or exclusively licensed to John Wiley & Sons, Inc. or one of its group companies (each a"Wiley Company") or handled on behalf of a society with which a Wiley Company has exclusive publishing rights in relation to a particular work (collectively "WILEY"). By clicking "accept" in connection with completing this licensing transaction, you agree that the following terms and conditions apply to this transaction (along with the billing and payment terms and conditions established by the Copyright Clearance Center Inc., ("CCC's Billing and Payment terms and conditions"), at the time that you opened your RightsLink account (these are available at any time at http://myaccount.copyright.com).

Terms and Conditions

- The materials you have requested permission to reproduce or reuse (the "Wiley Materials") are protected by copyright.

Figure 2-7

Luis Trimino Rincon

From: PermissionsFrance <permissionsfrance@elsevier.com>
Sent: January-08-19 1:28 AM
To: Luis Trimino Rincon
Subject: RE: copyright permission

ELSEVIER
MASSON

Issy-Les-Moulineaux, 8-Jan-2019

To the attention of Luis Trimino Rincon

Dear,
As per your request below, we hereby grant you permission to reprint the material detailed in your request at no charge **in your thesis** subject to the following conditions:

1. If any part of the material to be used (for example, figures) has appeared in our publication with credit or acknowledgement to another source, permission must also be sought from that source. If such permissions are not obtained then that materials may not be included in your publication.

2. Any modification of the material is likely to harm the moral right of the authors and therefore should be first submitted and approved by the authors who are the sole owner of the moral right.

3. Suitable and visible acknowledgement to the source must be made, either as a footnote or in a reference list at the end of your publication, as follows:
   "Reproduced from *Authors name. Article title. Journal title year; volume number(issue number):first page-last page*. Copyright © *year [if applicable: name of learned society,* published by*]* Elsevier Masson SAS. All rights reserved."
4. Your thesis may be submitted to your institution in either print or electronic form.

5. Reproduction of this material is confined to the purpose for which permission is hereby given.

6. This permission is granted for non-exclusive world **English** rights only. For other languages please reapply separately for each one required. Permission excludes use in an electronic form other than submission. Should you have a specific electronic project in mind please reapply for permission.

7. Should your thesis be published commercially, please reapply for permission.

Yours sincerely,
Regina

Figure 2-8

SPRINGER NATURE LICENSE TERMS AND CONDITIONS

Nov 13, 2018

This Agreement between Luis F Trimino ("You") and Springer Nature ("Springer Nature") consists of your license details and the terms and conditions provided by Springer Nature and Copyright Clearance Center.

License Number	4467171363398
License date	Nov 13, 2018
Licensed Content Publisher	Springer Nature
Licensed Content Publication	Journal of Materials Science (full set)
Licensed Content Title	Failure-mechanism maps for engineering polymers
Licensed Content Author	Z. Bin Ahmad, M. F. Ashby
Licensed Content Date	Jan 1, 1988
Licensed Content Volume	23
Licensed Content Issue	6
Type of Use	Thesis/Dissertation
Requestor type	academic/university or research institute
Format	print and electronic
Portion	figures/tables/illustrations
Number of figures/tables/illustrations	4
Will you be translating?	no
Circulation/distribution	<501
Author of this Springer Nature content	no
Title	Strain Whitening in Epoxy Adhesives, Correlations with Damage and Development of a Macroscopic Optical Method for Damage Characterization
Institution name	n/a
Expected presentation date	Jan 2019
Portions	Figure 2, Figure 3, Figure 4 and Figure 5
Requestor Location	Luis F Trimino 301-36 River road East kirch2ner, ON N2B2G2 Canada Attn: Luis F Trimino
Billing Type	Invoice
Billing Address	Luis F Trimino 301-36 River road East kirchener, ON N2B2G2 Canada Attn: Luis F Trimino
Total	0.00 USD
Terms and Conditions	

Bibliography

[1] CAFE-legislation n.d. https://www.nhtsa.gov/laws-regulations/corporate-average-fuel-economy (accessed December 12, 2018).

[2] CAFE website n.d. https://one.nhtsa.gov/cafe_pic/CAFE_PIC_home.htm (accessed December 12, 2018).

[3] CAFE Wiki n.d. https://en.wikipedia.org/wiki/Corporate_average_fuel_economy (accessed December 12, 2018).

[4] FMVSS legislation n.d. https://icsw.nhtsa.gov/cars/rules/import/FMVSS/ (accessed December 10, 2018).

[5] Vehicle Safety n.d. https://www.safercar.gov.

[6] Lanzerath, Horst; Pasligh N. Benefit of Structural Adhesives in Full Car Crash Applications. SAE 2014. doi:10.4271/2014-01-0811.

[7] Trimiño L. Analysis and Performance of Adhesively Bonded Crush Tube Structures. University of Waterloo, 2012.

[8] Fish, Jacob; Belytschko T. A First Course in Finite Elements. Hoboken, NJ: Wiley; 2007.

[9] Yu XX, Crocombe AD, Richardson G. Material modelling for rate-dependent adhesives. Int J Adhes Adhes 2001;21:197–210.

[10] Hor A, Morel F, Lebrun J, Germain G. Mechanics of Materials Modelling , identification and application of phenomenological constitutive laws over a large strain rate and temperature range. Mech Mater 2013;64:91–110. doi:10.1016/j.mechmat.2013.05.002.

[11] Weissberg SG, Simha R, Rothman S. Viscosity of dilute and moderately concentrated polymer solutions 1951;47.

[12] Cadell, R.M.;Raghava, R.S.; Atkins AG. A yield criterion for anisotropic and pressure dependent solids such as oriented polymers. J Mater Sci 1973;8:1641–6.

[13] Boyce MC. Large Inelastic Deformation of Glassy Polymers. Massachusetts Institute of Technology, 1986.

[14] Boyce MC, Parks DM, Argon AS. Large inelastic deformation of glassy polymers. part I: rate

dependent constitutive model. Mech Mater 1988;7:15–33. doi:10.1016/0167-6636(88)90003-8.

[15] Kinloch, A J; Kodokian, G.A.; Jaramani B. Impact Properties of Epoxy Polymers. J Mater Sci 1987;22:4111–20.

[16] Todo M, Takahashi K, Ben Jar P-Y, Beguelin P. Toughening mechanisms of rubber toughened PMMA. JSME Int Journal, Ser A 1999;42:585–91.

[17] Mulliken AD, Boyce MC. Mechanics of the rate-dependent elastic–plastic deformation of glassy polymers from low to high strain rates. Int J Solids Struct 2006;43:1331–56. doi:10.1016/j.ijsolstr.2005.04.016.

[18] Anderson KS, Lim SH, Hillmyer MA. Toughening of Polylactide by Melt Blending with Linear Low-Density Polyethylene 2002.

[19] Yang QD, Thouless MD. Mixed-mode fracture analyses of plastically-deforming adhesive joints. Int J Fract 2001;110:175–87.

[20] Stoeckel F, Konnerth J, Gindl-Altmutter W. Mechanical properties of adhesives for bonding wood-A review. Int J Adhes Adhes 2013;45:32–41. doi:10.1016/j.ijadhadh.2013.03.013.

[21] Gilat A, Goldberg RK, Roberts GD. Strain rate sensitivity of epoxy resin in tensile and shear loading. J Aerosp Eng 2007;20:75–89. doi:10.1061/(ASCE)0893-1321(2007)20:2(75).

[22] Farrokh B, Khan AS. A strain rate dependent yield criterion for isotropic polymers: Low to high rates of loading. Eur J Mech A/Solids 2010;29:274–82. doi:10.1016/j.euromechsol.2009.08.004.

[23] Park C, Huh H, Kim J, Ahn C. Determination of true stress-true strain curves of polymers at various strain rates using force equilibrium grid method. J Compos Mater 2012;46:2065–77. doi:10.1177/0021998311429882.

[24] da Silva LFM, Ochsner A. Modeling of adhesively bonded joints. Berlin: Springer; 2008.

[25] Miehe C, Keck J. Superimposed finite elastic-viscoelastic-plastoelastic stress response with damage in filled rubbery polymers. Experiments, modelling and algorithmic implementation. J Mech Phys Solids 2000;48:323–65. doi:10.1016/S0022-5096(99)00017-4.

[26] Makhecha DP, Kapania RK, Johnson ER, Dillard DA. Dynamic Fracture Analysis of

Adhesively Bonded Joints Using Explicit Methods. AIAA J 2007;45:2778–84. doi:10.2514/1.26088.

[27] LS-Dyna Aerospace working group. Modeling guideline document. vol. V13-1. 2013.

[28] Choupani N. Mixed-mode cohesive fracture of adhesive joints: Experimental and numerical studies. Eng Fract Mech 2008;75:4363–82.

[29] Morin D, Bourel B, Bennani B, Lauro F, Lesueur D. A new cohesive element for structural bonding modelling under dynamic loading. Int J Impact Eng 2013;53:94–105. doi:10.1016/j.ijimpeng.2012.02.003.

[30] Kolling S, Haufe A, Feucht M, Du Bois PA. A Constitutive Formulation for Polymers Subjected to High Strain Rates. 9th Int. LS-Dyna Users Conf., Detroit: 2006, p. 15–55.

[31] Børvik T, Hopperstad OS, Berstad T, Langseth M. A computational model of viscoplasticity and ductile damage for impact and penetration 2001;20:685–712.

[32] Joannès S. A micromechanical damage characterization and the modeling of a mineral filled epoxy adhesive. Mech Mater 2014;75:111–24. doi:https://doi.org/10.1016/j.mechmat.2014.04.009.

[33] Balieu R, Lauro F, Bennani B, Haugou G, Chaari F, Matsumoto T, et al. Damage at high strain rates in semi-crystalline polymers. Int J Impact Eng 2015. doi:10.1016/j.ijimpeng.2014.08.013.

[34] Quan D, Cardiff P, Murphy N, Ivankovic A. Damage behaviour of nano-modified epoxy adhesives subject to high stress constraint. J Adhes 2018;94:387–405. doi:10.1080/00218464.2017.1279542.

[35] Edlund ULF, Klarbring A. A Coupled Elastic-Plastic Damage Model for Rubber-Modified Epoxy Adhesives. Int J Solids Struct 1993;30:2693–708. doi:10.1016/0020-7683(93)90107-I.

[36] Biel A, Stigh U. Damage and plasticity in adhesive layer : an experimental study 2010:93–103. doi:10.1007/s10704-010-9508-3.

[37] Mubashar A, Ashcroft IA, Crocombe AD. Modelling Damage and Failure in Adhesive Joints Using A Combined XFEM-Cohesive Element Methodology 2014:682–97. doi:10.1080/00218464.2013.826580.

[38] Desai CS, Toth J. Disturbed state constitutive modeling based on stress-strain and nondestructive behavior. Int J Solids Struct 1996;33:1619–50. doi:https://doi.org/10.1016/0020-7683(95)00115-8.

[39] Molina GJ, Haddad YM. Acousto-ultrasonics approach to the characterization of impact properties of a class of engineering materials. Int J Press Vessel Pip 1996;67:307–15. doi:https://doi.org/10.1016/0308-0161(95)00031-3.

[40] Laiarinandrasana L, Morgeneyer TF, Proudhon H, N'Guyen F, Maire E. Effect of multiaxial stress state on morphology and spatial distribution of voids in deformed semicrystalline polymer assessed by X-ray tomography. Macromolecules 2012;45:4658–68. doi:10.1021/ma3005247.

[41] Schirrer R, Fond C, Lobbrecht A. Volume change and light scattering during mechanical damage in polymethylmethacrylate toughened with core-shell rubber particles 1996;c:6409–22.

[42] Quinn S, Fruehmann RK. Develoment of thermoelastic Stress Analysis as a Non-Destructive Evaluation Tool n.d.;1.

[43] Telenkov SA, Wang Y, Lu Y, Favro LD, Kuo PK, Thomas RL. Infrared imaging of stress-crazing in rubber modified polystyrene. Polym Eng Sci 1998;38:385–91.

[44] Lemaitre J, Dufailly J. Damage measurements. Eng Fract Mech 1987;28:643–61. doi:10.1016/0013-7944(87)90059-2.

[45] Tang CY, Plumtree A. Damage mechanics applied to polymers. Eng Fract Mech 1994;49:499–508. doi:10.1016/0013-7944(94)90044-2.

[46] G'Sell C, Hiver JM, Dahoun A. Experimental characterization of deformation damage in solid polymers under tension, and its interrelation with necking. Int J Solids Struct 2002;39:3857–72. doi:10.1016/S0020-7683(02)00184-1.

[47] Tang CY, Tsui CP, Shen W, Li CC, Peng LH. Modelling of non-linear stress and strain behaviour of HIPS with craze damage in tensile loading and unloading process. Polym Test 2000;20:15. doi:http://dx.doi.org/10.1016/S0142-9418(99)00073-2".

[48] Wen S, Chung DDL. Uniaxial compression in carbon fiber-reinforced cement , sensed by electrical resistivity measurement in longitudinal and transverse directions 2001;31:297–301.

[49] Schang O, Billon N, Muracciole JM, Fernagut F. Mechanical behavior of a ductile polyamide 12 during impact. Polym Eng Sci 1996;36:541–50. doi:10.1002/pen.10440.

[50] Darlix, B.; Montmitonnet, P.; Monasse B. Hardness Measurement as a Means of Determining Simultaneously the Elastic Modulus and Yield Stress of Polymers as a Function of Temperature 1986;6:107–20.

[51] Symietz D. Structural Adhesive Bonding: The Most Innovative Joining Technique for Modern Lightweight Design, Safety and Modular Concepts -Progress Report-. - 2005. doi:-10.4271/2005-01-1747.

[52] ASTM. Standard, D907-12a, 2012, Standard Terminology of Adhesives 2012. doi:10.1520/D0907-12A.

[53] Kinloch AJ. Adhesion and adhesives : science and technology. London: Chapman and Hall; 1987.

[54] Comyn J. Adhesion Science. RSC Paperbacks; 1997.

[55] Fay PA. History of Adhesive Bonding. In: Adams RD, editor. Adhes. Bond. 1st ed., CRC Press; 2005.

[56] Askeland, Donald R.; Phule PP. The Science and Engineering of Materials. 4th editio. Thomson; 2003.

[57] Kellar EJC. Joining Similar and disimilar materials. Adhes. Bond., n.d.

[58] Lee L-H. Preface. In: Lee L-H, editor. Adhes. sealants, coatings Sp. harsh Environ., New York: Plenum Press; n.d.

[59] Ellis B. Introduction to the chemistry, synthesis, manufacture and characterization of epoxy resins. In: Ellis B, editor. Chem. Technol. Epoxy Resins, Dordrecht: Springer Netherlands; 1993, p. 1–36. doi:10.1007/978-94-011-2932-9_1.

[60] Shawn SJ. Epoxy resin adhesives. In: Ellis B, editor. Chemestry Technol. Epoxy Resins. 1st ed., Springer Science+Business Media; n.d.

[61] Goodman SH. 6 - Epoxy Resins. In: Goodman SH, editor. Handb. Thermoset Plast. (Second Ed. Second Edi, Westwood, NJ: William Andrew Publishing; 1998, p. 193–268. doi:https://doi.org/10.1016/B978-081551421-3.50009-6.

[62] Ethylene Oxide n.d. http://www.newworldencyclopedia.org/entry/Ethylene_oxide#Properties (accessed May 2, 2018).

[63] Ethyleneoxide 3rd Ed. 2007.

[64] wikipedia. Ethylene oxide 2013. http://en.wikipedia.org/wiki/Ethylene_oxide.

[65] Meath AR. Epoxy Resin Adhesives. In: Skeist I, editor. Handb. Adhes., Boston, MA: Springer US; 1990, p. 347–58. doi:10.1007/978-1-4613-0671-9_19.

[66] Ashcroft WR. Curing agents for epoxy resins. In: Ellis B, editor. Chem. Technol. Epoxy Resins, Dordrecht: Springer Netherlands; 1993, p. 37–71. doi:10.1007/978-94-011-2932-9_2.

[67] Patel MR. Solvent based epoxy-phenoxy solution and lacquers or inks formed therefrom 2005.

[68] Ellis B. The kinetics of cure and network formation. In: Ellis B, editor. Chem. Technol. Epoxy Resins, Dordrecht: Springer Netherlands; 1993, p. 72–116. doi:10.1007/978-94-011-2932-9_3.

[69] Dillard DA, Pocius A V. Adhesion science and engineering, The mechanics of adhesion. Amsterdam ; Boston: Elsevier; 2002.

[70] Skeist I, editor. Handbook of adhesives. New York: Van Nostrand Reinhold Co; 1977.

[71] Petrova AP, Lukina NF. Behavior of epoxy adhesive joints under service conditions. Polym Sci Ser C 2007;49:99–105. doi:10.1134/S1811238207010225.

[72] Shaw SJ. Additives and modifiers for epoxy resins. In: Ellis B, editor. Chem. Technol. Epoxy Resins, Dordrecht: Springer Netherlands; 1993, p. 117–43. doi:10.1007/978-94-011-2932-9_4.

[73] Sue H-J, Garcia-Meitin E, Orchard NA. Toughening of epoxies via craze-like damage. J Polym Sci Part B (Polymer Physics) 1993;31:595–608. doi:10.1002/polb.1993.090310511.

[74] Zotti, M.A.; Zuppolini, S.; Zarrelli , M.; Borriello A. Fracture Toughening Mechanisms in Epoxy Adhesives. In: Rudawska A, editor. Adhes. Appl. Prop., IntechOpen; n.d. doi:10.5772/62603.

[75] Mousavi SR, Amraei IA. Toughening of dicyandiamide-cured DGEBA-based epoxy resin using MBS core-shell rubber particles 2015. doi:10.1177/0021998314545338.

[76] Pillai JP, Pionteck J, Haessler R, Sinturel C, Mathew VS, Thomas S. Effect of Cure Conditions on the Generated Morphology and Viscoelastic Properties of a Poly(acrylonitrile-butadiene-styrene) Modified Epoxy-Amine System. Ind Eng Chem Res 2012;51:2586–95.

doi:10.1021/ie2011017.

[77] Mills NJ, Mills NJ. Plastics : microstructure, properties and applications. London: London : Edward Arnold; 1986.

[78] Haward RN. The Nature of Polymer Glasses, Their Packing Density and Mechanical Behaviour. In: Haward RN, editor. Phys. Glas. Polym., n.d.

[79] Bowden PB. The yield behaviour of glassy polymers. In: Haward RN, editor. Phys. Glas. Polym., New York: Wiley; 1973, p. 279.

[80] Haward RN. The Post-Yield Behaviour of Amorphous Plastics. In: Haward RN, editor. Phys. Glas. Polym., 1973.

[81] Doll W. Fractography and Failure Mechanisms of Amorphous Polymers. In: Roulin-Moloney AC, editor. Fractography Fail. Mech. Polym. Compos., 1989.

[82] Christensen RM. Theory of Viscoelasticity. 2nd Editio. Dover Publications; 1982.

[83] Liu K, Piggott MR. Fracture failure processes in polymers. I: Mechanical tests and results. Polym Eng Sci 1998;38:60–8.

[84] Bascom WD, Cottington RL, Jones RL, Peyser P. The fracture of epoxy- and elastomer-modified epoxy polymers in bulk and as adhesives. J Appl Polym Sci 1975;19:2545–62. doi:10.1002/app.1975.070190917.

[85] Hodgkin JH, Simon GP, Varley RJ. Thermoplastic toughening of epoxy resins: A critical review. Polym Adv Technol 1998;9:3–10.

[86] Mousavi SR, Amraei IA. Influence of nanosilica and methyl methacrylate-butadiene-styrene core-shell rubber particles on the physical-mechanical properties and cure kinetics of diglycidyl ether of bisphenol-A-based epoxy resin. High Perform Polym 2016;28:809–19. doi:10.1177/0954008315600228.

[87] Goldsmith W. Impact, the theory and physical behaviour of colliding solids. New York: Dober publications; 2001.

[88] Goglio L, Peroni M, Rossetto M. Effect of the strain rate on the mechanical behaviour of epoxy adhesives. Damage Assess. Struct. VII, vol. 347, Dept. of Mechanics, Politecnico Di Torino, C.so Duca Degli Abruzzi 24, 10129 Torino, Italy: Trans Tech Publications Ltd; 2007,

p. 671–6.

[89] Goglio L, Peroni L, Peroni M, Rossetto M. High strain-rate compression and tension behaviour of an epoxy bi-component adhesive. Int J Adhes Adhes 2008;28:329–39.

[90] Morin D, Haugou G, Bennani B, Lauro F. Experimental characterization of a toughened epoxy adhesive under a large range of strain rates. J Adhes Sci Technol 2011;25:1581–602. doi:10.1163/016942410X524417.

[91] Cowper GR, Symonds PS. Strain hardening and strain-rate effects in the impact loading of cantilever beams. vol. 28. New York: Brown University; 1957.

[92] Alves M. Material constitutive law for large strains and strain rates. J Eng Mech 2000;126:215–8.

[93] Bin Ahmad Z, Ashby MF. Failure-mechanism maps for engineering polymers. J Mater Sci 1988;23:2037–50.

[94] Mark 1934- JE. Physical properties of polymers handbook. 2nd ed. CN. New York: Springer; 2007.

[95] Rice JR. The Localization of Plastic Deformation. In: Koiter WT, editor. Int. Congr. Theor. Appl. Mech., Delf: 1976, p. 207–20.

[96] van Melick HGH, Bressers OFJT, den Toonder JMJ, Govaert LE, Meijer HEH. A micro-indentation method for probing the craze-initiation stress in glassy polymers. Polymer (Guildf) 2003;44:2481–91.

[97] Bigoni D, Dal Corso F. The unrestrainable growth of a shear band in a prestressed material. Proc R Soc A Math Phys Eng Sci 2008;464:2365–90. doi:10.1098/rspa.2008.0029.

[98] Bordignon N, Piccolroaz A, Dal Corso F, Bigoni D. Strain Localization and Shear Band Propagation in Ductile Materials. Front Mater 2015;2:1–13. doi:10.3389/fmats.2015.00022.

[99] Cantwell WJ, Roulin-Moloney AC. Fractography and failure mechanisms of unfilled and particulate filled epoxy resins. In: Roulin-Moloney AC, editor. Fractography Fail. Mech. Polym. Compos., London: Elsevier applied science; 1989, p. 233.

[100] Thomas E. MIT polymer physics notes n.d.;April 29 2. http://ocw.mit.edu/courses/materials-science-and-engineering/3-063-polymer-physics-spring-2007/.

[101] Oxborough RJ, Bowden PB. General critical-strain criterion for crazing in amorphous glassy polymers. Philos Mag 1973;28:547–59.

[102] Passaglia E. Crazes and fracture in polymers. J Phys Chem Solids 1987;48:1075–100. doi:10.1016/0022-3697(87)90119-3.

[103] Michler G. Correlation between craze formation and mechanical behaviour of amorphous polymers. J Mater Sci 1990;25:2321–34. doi:10.1007/BF00638022.

[104] Deblieck RAC, van Beek DJM, Remerie K, Ward IM. Failure mechanisms in polyolefines: The role of crazing, shear yielding and the entanglement network. Polymer (Guildf) 2011;52:2979–90.

[105] Ward IM. An introduction to the mechanical properties of solid polymers. Chichester ; New York: Chichester ; New York : J. Wiley & Sons; 1993.

[106] Yee AF, Pearson RA. Fractography and failure mechanisms of rubber modified epoxy resins. In: Roulin-Moloney A, editor. Fractography Fail. Mech. Polym. Compos., London: Elsevier applied science; 1989, p. 291.

[107] Garg, A. C.; Mai YW. Failure Mechanisms in Toughened Epoxy Resins A Review. Compos Sci Technol 1988;31:179–223.

[108] Sue HJ. Craze-like damage in a core-shell rubber-modified epoxy system. J Mater Sci 1992;27:3098–107. doi:10.1007/BF01154125.

[109] Gent AN, Wang C. Fracture mechanics and cavitation in rubber-like solids. J Mater Sci 1991;26:3392–5. doi:10.1007/BF01124691.

[110] Bandyopadhyay S, Science D. Review of the Microscopic and Macroscopic Aspects of Fracture of Unmodified and Modified Epoxy Resins 1990;125:157–84.

[111] Gearing BP, Anand L. On modeling the deformation and fracture response of glassy polymers due to shear-yielding and crazing. Int J Solids Struct 2004;41:3125–50. doi:10.1016/j.ijsolstr.2004.01.017.

[112] Zhou C, Bao XY, Tan ZY, Sun SL, Ao YH, Yang HD, et al. Transition from crazing to shear deformation in ABS/PVC blends. J Polym Sci Part B Polym Phys 2006;44:687–95. doi:10.1002/polb.20656.

[113] Berger LL, Kramer EJ. The effect of temperature on the transition from crazing to shear deformation in crosslinked polystyrene. J Mater Sci 1988;23:3536–43.

[114] Berger LL. Relationship between craze microstructure and molecular entanglements in glassy polymers. 1. Macromolecules 1989;22:3162–7.

[115] Cheung, M.F.; Plummer Jr H. lzod Impact Fracture Morphology of Rubber-toughened Polysulfone and Poly (Phenyene Sulfide) Blends. Polym Eng Sci 1996;36:15–22.

[116] Gao G, Zhang J, Yang H, Zhou C, Zhang H. Deformation mechanism of polystyrene toughened with sub-micrometer monodisperse rubber particles 2006;1221:1215–21. doi:10.1002/pi.

[117] Wu, J.; Yu, D-M.;Mai, Y.W.;Yee AF. Fracture toughness and fracture mechanisms of PBT/PC/IM blends. J Mater Sci 2000;35:307–15.

[118] Kytopoulos, V.N.; Badalouka, B.G.; Bourkas, G.D.; Sideridis E. A SEM-Fractographic Study of Dynamic Crack Propagation Effects in Particulate Epoxy Systems under Impact Loading Conditions. Reinf Plast Compos 2009;28. doi:10.1177/0731684408094743.

[119] Roulin-Moloney AC. Preface. Fractography Fail. Mech. Polym. Compos., 1989.

[120] Price JN. Stress Corrosion Cracking in Glass Reinforced Composites. In: Roulin-Moloney AC, editor. Fractography Fail. Mech. Polym. Compos., 1989.

[121] Smith JW. Optical Microscopy. In: Roulin-Moloney AC, editor. Fractography Fail. Mech. Polym. Compos., Elsevier applied science; 1989, p. 3–42.

[122] Roulin-Moloney AC. Scanning Electron Microscopy. In: Roulin-Moloney AC, editor. Fractography Fail. Mech. Polym. Compos., Elsevier applied science; 1989, p. 43–86.

[123] Henkee CS. Transmission Electron Microscopy. In: Roulin-Moloney AC, editor. Fractography Fail. Mech. Polym. Compos., Elsevier applied science; 1989, p. 87–144.

[124] Smith JW. Fractography and failure mechanisms of polymers and composites. In: Roulin-Moloney AC, editor., London: Elsevier Applied Science; 1989, p. 28.

[125] da Silva LFM. Advances in numerical modelling of adhesive joints. Berlin ; Heidelberg: Springer; 2012.

[126] García JA, Chiminelli A, García B, Lizaranzu M, Jiménez MA. Characterization and material

model definition of toughened adhesives for finite element analysis. Int J Adhes Adhes 2011;31:182–92. doi:10.1016/j.ijadhadh.2010.12.006.

[127] Bala S. Tie-Break Contacts in LS-DYNA n.d.

[128] Bala S. Contact Modeling in LS-DYNA. FEA Inf 2001.

[129] LSTC. LS-DYNA Keyword user manual, Version 971. vol. 1. Livermore: Livermore software technology Corporation, (LSTC); 2007.

[130] LSTC. LS-DYNA Keyword user manual, Material Models, Version 971. vol. 2. Livermore: Livermore Software Technology Corporation, (LSTC); 2007.

[131] Matzenmiller A, Gerlach S, Fiolka M, Mechanik I, Kassel U. Progressive Failure Analysis of Adhesively Bonded Joints in Crash Simulations 2006:11–20.

[132] Marzi S, Hesebeck O, Brede M, Kleiner F. A rate-dependent cohesive zone model for adhesively bonded joints loaded in mode I. J Adhes Sci Technol 2009;23:881–98.

[133] Su C, Wei YJ, Anand L. An elastic-plastic interface constitutive model: Application to adhesive joints. Int J Plast 2004;20:2063–81.

[134] Davila, C.; Camanho, P.P.; Turin A. Cohesive Elements for Shells. Langley, VA, USA: 2007.

[135] Moura MFSF De, Gonc JPM, Chousal JAG, Campilho RDSG. Cohesive and continuum mixed-mode damage models applied to the simulation of the mechanical behaviour of bonded joints. Int J Adhes Adhes 2008;28:419–26. doi:10.1016/j.ijadhadh.2008.04.004.

[136] Lulei F, Miehe C. A physically-based constitutive model for finite viscoelastic deformations in rubbery polymers based on a directly evaluated micro-macro-transition. In: Besdo, D and Schuster, RH and Ihlemann, J, editor. Const. Model. RUBBER II, 2001, p. 117–25.

[137] Duan Y, Saigal A, Greif R, Zimmerman MA. A uniform phenomenological constitutive model for glassy and semicrystalline polymers. Polym Eng Sci 2001;41:1322–8. doi:10.1002/pen.10832.

[138] Borvik T, Hopperstad OS, Berstad T, Langseth M. Numerical simulation of plugging failure in ballistic penetration. Int J Solids Struct 2001;38:6241–64. doi:10.1016/S0020-7683(00)00343-7.

[139] Huang H, Talreja R. Numerical simulation of matrix micro-cracking in short fiber reinforced

polymer composites : Initiation and propagation. Compos Sci Technol 2006;66:2743–57. doi:10.1016/j.compscitech.2006.03.013.

[140] Besson J. Continuum Models of Ductile Fracture: A Review. Int J Damage Mech 2010;19:3–52. doi:10.1177/1056789509103482.

[141] Lemaitre J. A course on damage mechanics. Berlin: Springer-Verlag; 1992.

[142] Gurson AL. Continuum theory of ductile rupture by boid nucleation and growth -1. Yield criteria and flow rules for porous ductile media. Am Soc Mech Eng 1976.

[143] Wilkins, R.L.; Streit, R.D.; Reaugh JE. Cumulative- Str ain-D amage Model of Ductile Fracture: Simulation and Prediction of Engineering Fracture Tests. Livermore, CA, USA: 1980.

[144] Matzenmiller A, Lubliner J, Taylor RL. A constitutive model for anisotropic damage in fiber-composites. Mech Mater 1995;20:125–52. doi:10.1016/0167-6636(94)00053-0.

[145] Todo M, Fukuya Y, Hagihara S, Arakawa K. Finite element modeling of damage formation in rubber-toughened polymer. vol. 297–300 II, Research Institute for Applied Mechanics, Kyushu University, Kasuga, Japan: Trans Tech Publications Ltd; 2005, p. 1019–24.

[146] Armero F, Oller S. A general framework for continuum damage models. I. Infinitesimal plastic damage models in stress space. Int J Solids Struct 2000;37:7409–36. doi:https://doi.org/10.1016/S0020-7683(00)00205-5.

[147] Armero F, Oller S. A general framework for continuum damage models. II. Integration algorithms, with applications to the numerical simulation of porous metals. Int J Solids Struct 2000;37:7437–64. doi:https://doi.org/10.1016/S0020-7683(00)00206-7.

[148] Celentano, C.J.; Chaboche J-L. Experimental and numerical damage evolution in steels. Int J Plast 2007;23:1739–62.

[149] Diel S. A Continuum Damage Mechanics Model for the 2017:1–21. doi:10.3390/ma10080951.

[150] Llobet J, Maimí P, Mayugo JA, Essa Y, de la Escalera FM. A fatigue damage and residual strength model for unidirectional carbon/epoxy composites under on-axis tension-tension loadings. Int J Fatigue 2017;103:508–15. doi:https://doi.org/10.1016/j.ijfatigue.2017.06.026.

[151] Davis LS, Rosenfeld A, Weszka JS. Region Extraction by Averaging and Thresholding. IEEE

Trans Syst Man Cybern 1975;SMC-5:383–8.

[152] Zurek AK. Dynamic ductile evolution and tensile fracture: new experimental insights for models evaluation. In: Staudhammer, KP and Murr, LE and Meyers M, editor. Fundam. issues Appl. Shock. high-strain rate phenomena, Proc., Elsevier Science BV; 2001, p. 125–34. doi:10.1016/B978-008043896-2/50108-X.

[153] Topolar L, Pazdera L, Cikrle P. Acoustic Emission Monitoring during Static Modulus Elasticity Test of Concrete Specimen. In: Petrenko, A, editor. Exp. Stress Anal. 51, vol. 486, 2014, p. 267+. doi:10.4028/www.scientific.net/AMM.486.267.

[154] Artar M, Daloglu AT. Damage Detection in Simulated Space Frames Using Genetic Algorithms. Sigma J Eng Nat Sci 2015;33:166–87.

[155] May A, Belouchrani MA, Manaa A, Bouteghrine Y. Influence of fatigue damage on the mechanical behaviour of 2024-T3 aluminum alloy. In: Guagliano, M and Vergani, L, editor. 11TH Int. Conf. Mech. Behav. Mater., vol. 10, 2011. doi:10.1016/j.proeng.2011.04.132.

[156] Cuong LN, Quang ND, Cuong TQ, Khanh DN, Khanh NP. Experimental Investigation and Modeling of the Thermal Cycling Effect on the Mechanical Properties of CFRP. Proc. 2016 7TH Int. Conf. Mech. Aerosp. Eng., 2016, p. 41–5.

[157] Kytyr D, Valach J, Doktor T, Jirousek O. Assesment of C/PPS Composites Degradation Indicators Using Accoustic Measurement. In: Fuis V, editor. Eng. Mech. 2011, 2011, p. 355–8.

[158] Garnier V, Piwakowski B, Abraham O, Villain G, Payan C, Chaix JF. Acoustic techniques for concrete evaluation: Improvements, comparisons and consistency. Constr Build Mater 2013;43:598–613. doi:10.1016/j.conbuildmat.2013.01.035.

[159] Zheng S, Ashcroft IA. A depth sensing indentation study of the hardness and modulus of adhesives. Int J Adhes Adhes 2005;25:67–76. doi:10.1016/j.ijadhadh.2004.02.004.

[160] Ziadi A, Galmiche F, Maldague X. Pulse shaping in infrared thermography for nondestructive evaluation. Rev Sci Instrum 2003;74:411–3. doi:10.1063/1.1517737.

[161] G'Sell C, Addiego F, Dahoun A, Hiver J-M. In-situ characterization of cavitation during the deformation of semi-crystalline polymers. ANTEC 2004 - Annu. Tech. Conf. Proceedings, May 16, 2004 - May 20, vol. 2, Lab. de Phys. Des Materiaux, Ecole Des Mines de Nancy,

Parc de Saurupt, 54042 Nancy, France: Society of Plastics Engineers; 2004, p. 2013–7.

[162] Addiego F, Dahoun A, G'Sell C, Hiver J-M. Characterization of volume strain at large deformation under uniaxial tension in high-density polyethylene. Polymer (Guildf) 2006;47:4387–99. doi:10.1016/j.polymer.2006.03.093.

[163] Sutton MA. Image correlation for shape, motion and deformation measurements basic concepts, theory and applications. New York: New York : Springer; 2009.

[164] Pierron F. Identification of materials mechanical properties from full-field measurements: Latest advances in the virtual fields method. 6th Int. Conf. Adv. Exp. Mech. Sept. 9, 2008 - Sept. 11, vol. 13–14, LMPF, Arts et Metiers ParisTech, Rue St-Dominique, 51000 Chalons En Champagne Cedex, France: Trans Tech Publications; 2008, p. 3–9.

[165] Lauro F, Bennani B, Morin D, Epee AF. The SEE method for determination of behaviour laws for strain rate dependent material: Application to polymer material. Int J Impact Eng 2010;37:715–22. doi:10.1016/j.ijimpeng.2009.11.007.

[166] Balieu R, Lauro F, Bennani B, Haugou G, Chaari F, Matsumoto T, et al. Damage at high strain rates in semi-crystalline polymers. Int J Impact Eng 2015;76:1–8. doi:10.1016/j.ijimpeng.2014.08.013.

[167] Lecompte D, Smits A, Bossuyt S, Sol H, Vantomme J, Van Hemelrijck D, et al. Quality assessment of speckle patterns for digital image correlation. Opt Lasers Eng 2006;44:1132–45. doi:10.1016/j.optlaseng.2005.10.004.

[168] Lambros J, Patel J. Microscale digital image correlation study of irradiation induced ductile-to-brittle transition in polyethylene. Spec Issue Micro Nano-Scale Deform Meas 2011;46:347–60. doi:10.1177/0309324711406474.

[169] Grédiac M, Hild F (François), editors. Full-field measurements and identification in solid mechanics. London : Hoboken, NJ: London : ISTE Ltd. ; Hoboken, NJ : John Wiley & Sons, Inc; 2013.

[170] Sutton MA, Yan JH, Tiwari V, Schreier HW, Orteu JJ. The effect of out-of-plane motion on 2D and 3D digital image correlation measurements. Opt Lasers Eng 2008;46:746–57.

[171] Schreier HW, Braasch JR, Sutton MA. Systematic errors in digital image correlation caused by intensity interpolation. Opt Eng 2000;39:2915–21. doi:10.1117/1.1314593.

[172] Goh CP, Ratnam MM, Ismail H. Large in-plane Deformation Mapping and Determination of Young's Modulus of Rubber Using Scanner-Based Digital Image Correlation 2016:1117–27.

[173] Tang Z, Liang J, Xiao Z, Guo C. Large deformation measurement scheme for 3D digital image correlation method. Opt Lasers Eng 2012;50:122–30. doi:10.1016/j.optlaseng.2011.09.018.

[174] Genovese K, Sorgente D. A morphing-based scheme for large deformation analysis with stereo-DIC. Opt Lasers Eng 2018;104:159–72. doi:10.1016/j.optlaseng.2017.06.020.

[175] Luo W, Liu W. Incubation time to crazing in stressed poly(methyl methacrylate). Polym Test 2007;26:413–8. doi:http://dx.doi.org/10.1016/j.polymertesting.2006.12.013.

[176] Xiu, L.; Luo, W.; Boyuan Y. Strain-amplitude and strain-rate dependent craze damage of polymethyl methacrylate. Polym Polym Compos 2014;22:737–41.

[177] VW, FIAT, RENAULT, OPEL, DAIMLER, VOLVO. SuperLight Car program n.d.;2013. http://www.superlightcar.com/public/index.php.

[178] Lightweight Vehicle Structure Conference. Innov. Dev. Light Weight Veh. Struct., Wolfsburg, Germany: VolksWagen Group; 2009.

[179] Kochan A. Lotus: aluminium extrusions and adhesives. Assem Autom 1996;16:19–21. doi:10.1108/01445159610150990.

[180] Peroni L, Avalle M. Experimental investigation of the energy absorption capability of bonded crash boxes. 9th Int. Conf. Struct. Under Shock Impact 2006, SUSI 2006, SU06, July 3, 2006 - July 5, vol. 87, Department of Mechanics, Politecnico Di Torino (Technical University of Turin), Italy: WITPress; 2006, p. 445–54.

[181] Peroni L, Avalle M, Belingardi G. Comparison of the energy absorption capability of crash boxes assembled by spot-weld and continuous joining techniques. Int J Impact Eng 2009;36:498–511.

[182] Avalle M, Peroni L, Peroni M, Scattina A. Bi-material joining for car body structures: Experimental and numerical analysis. Durab. Adhes. Joints, vol. 86, Politecnico Di Torino, Corso Duca Degli Abruzzi 24, 10129 Torino, Italy: Taylor and Francis Inc; 2010, p. 539–60.

[183] Fay PA, Suthurst GD. Redesign of adhesively bonded box beam sections for improved impact performance. Int J Adhes Adhes 1990;10:128–38. doi:DOI: 10.1016/0143-7496(90)90095-F.

[184] Belingardi G, Goglio L, Rossetto M. Impact behaviour of bonded built-up beams: experimental results. Int J Adhes Adhes 2005;25:173–80. doi:10.1016/j.ijadhadh.2004.06.004.

[185] ASTM. Standard D1876-08, 2015, Standard Test Method for Peel Resistance of Adhesives (T-Peel test) 2015. doi:10.1520/D3433-99.

[186] ASTM. Standard D1002-10, 2015, Standard Test Method for Aparent Shear Strength of Single-Lap-Joint Adhesively Bonded Metal Specimens by Tension Loading (Metal-to-Metal)Peel Resistance of Adhesives (T-Peel test) 2015. doi:10.1520/D3433-99.

[187] ASTM Website n.d. http://compass.astm.org/CUSTOMERS/filtrexx40.cgi?index.frm.

[188] Zhao X, Adams RD, Da Silva LFM. Single lap joints with rounded adherend corners: Experimental results and strength prediction. J Adhes Sci Technol 2011;25:837–56. doi:10.1163/016942410X520880.

[189] Zhao X, Adams RD, da Silva LFM. A new method for the determination of bending moments in single lap joints. Int J Adhes Adhes 2010;30:63–71. doi:10.1016/j.ijadhadh.2009.09.001.

[190] Adams RD, Harris JA. The influence of local geometry on the strength of adhesive joints. Int J Adhes Adhes 1987;7:69–80. doi:10.1016/0143-7496(87)90092-3.

[191] 3M. 3M Scoth Weld, EC-2214 Technical data sheet n.d.

[192] 3M. 3M Scoth Weld, DP-460NS Technical data sheet n.d.

[193] Kinloch AJ, Kodokian GA, Jamarani MB. Impact properties of epoxy polymers. J Mater Sci 1987;22:4111–20.

[194] Jang BZ, Uhlmann DR, Vander Sande JB. Rubber particle size dependence of crazing in Polypropylene. Polym Eng Sci 1985;25:643–51.

[195] Mostovoy S, Ripling EJ, Bersch CF. Fracture Toughness of Adhesive Joints. J Adhes 1971;3:125-. doi:10.1080/00218467108081159.

[196] Kinloch AJ, Kodokian GKA, Jamarani MB. Impact of properties of engineering adhesives. Adhes. ’87 - Second Int. Conf., Heslington, United Kingdom: Publ by Plastics & Rubber Inst; 1987, p. 1400.

[197] Cheng CM, Hiltner A, Baer E, Soskey P, Mylonakis SG. Deformation of Rubber-Toughened Polycarbonate - Macroscale Analysis of the Damage Zone. J Appl Polym Sci 1994;52:177–93.

doi:10.1002/app.1994.070520206.

[198] Nagai T, Iwamoto T, Sawa T, Sekiguchi Y, Kuramoto H, Uesugi N. An experimental study on the impact deformation and the strain rate sensitivity in some structural adhesives. 9th AEPA 2008 - Eng. Plast. it's Appl. - From Nanoscale to Macroscale, Grad. Sch. of Eng., Hiroshima Univ., Higashi-Hiroshima, Japan: World Scientific Publishing Co. Pte. Ltd; 2008, p. 218–23.

[199] Yokoyama T, Nakai K. Determination of impact tensile properties of structural epoxy adhesive butt joints using a hat-shaped specimen. J Phys IV 2006;134:789–95.

[200] Beguelin P, Barbezat M, Kausch HH. Mechanical Characterization of Polymers and Composites with a Servohydraulic High-Speed Tensile Tester. J Phys Iii 1991;1:1867–80.

[201] Georgiou I, Ivankovic A, Kinloch AJ, Tropsa V. Rate Dependent Fracture Behaviour of Adhesively Bonded Joints. Eur Struct Integr Soc 2003;32:317–28. doi:http://dx.doi.org/10.1016/S1566-1369(03)80105-X.

[202] Jamarani MB, Reed PE, Davies WR. Fracture behaviour of UPVC thin tubes at high loading rates. Part 2. Validity of fracture toughness tests and the effects of rate. J Mater Sci 1989;24:2917–22.

[203] Khalil AA, Bayoumi MR. Effect of loading rate on fracture toughness of bonded joints. Eng Fract Mech 1991;39:1037–43.

[204] Loo S, Zhang X, Ng H, Tee T, Mhaisalkar SG. Impact of Thermal, Moisture, and Mechanical Loading Conditions on Interfacial Fracture Toughness of Adhesively Bonded Joints. J Electron Mater 2007;36:110–6. doi:10.1007/s11664-006-0065-5.

[205] Selby K, Miller LE. Velocity Dependent Fracture Toughness of Epoxy-Resins - Reply. J Mater Sci 1975;10:2003.

[206] Marzi S, Hesebeck O, Brede M, Kleiner F. A Rate-dependent, elasto-plastic cohesive zone mix-mode model for crash analysis of adhesively bonded joints, Salzburg, Austria: DYNAmore Gmbh; 2009.

[207] Richardson G, Crocombe AD, Smith PA. Comparison of two- and three-dimensional finite element analyses of adhesive joints. Int J Adhes Adhes 1993;13:193–200.

[208] Castagnetti D, Dragoni E. Standard finite element techniques for efficient stress analysis of adhesive joints. Int J Adhes Adhes 2009;29:125–35.

[209] Wu G, Crocombe AD. Simplified finite element modelling of structural adhesive joints. Comput Struct 1996;61:385–91. doi:10.1016/0045-7949(96)00101-0.

[210] van Hoof J. Modelling of Impact induced Delamination in Composite Materials. Carleton University, 1999.

[211] Iwamoto T, Nagai T, Sawa T. Experimental and computational investigations on strain rate sensitivity and deformation behavior of bulk materials made of epoxy resin structural adhesive. Int J Solids Struct 2010;47:175–85. doi:10.1016/j.ijsolstr.2009.09.026.

[212] Needleman A. An analysis of tensile decohesion along an interface. J Mech Phys Solids 1990;38:289–324. doi:DOI: 10.1016/0022-5096(90)90001-K.

[213] Yang QD, Thouless MD, Ward SM. Numerical simulations of adhesively-bonded beams failing with extensive plastic deformation. J Mech Phys Solids 1999;47:1337–53.

[214] Mi Y, Crisfield MA, Davies GAO, Hellweg H-B. Progressive delamination using interface elements. J Compos Mater 1998;32:1246–72.

[215] Needleman A. Some Issues in Cohesive Surface Modeling. Mech World Proc 23rd Int Congr Theor Appl Mech ICTAM2012 2014;10:221–46. doi:http://dx.doi.org/10.1016/j.piutam.2014.01.020.

[216] Boqaileh K. Experimental Testing and Modelling of Adhesively Joined T-structures. University of Waterloo, 2015.

[217] Belingardi G, Chiandussi G. Stress flow in thin-walled box beams obtained by adhesive bonding joining technology. Int J Adhes Adhes 2004;24:423–39.

[218] Cavalli MN, Thouless MD, Yang QD. Cohesive-zone modeling of the deformation and fracture of weld-bonded joints. Weld J (Miami, Fla) 2004;83:133–S–139–S.

[219] 3M. 3M Scoth Weld, EC-2214 Safety data sheet n.d.

[220] 3M. 3M Scoth Weld, DP-460NS Safety data sheet n.d.

[221] Caruso Dailey MM, Trimiño LF, Cronin DS. 3M Scoth Weld, SA-9850 Preliminary Technical data sheet n.d.

[222] Smerd R, Winkler S, Salisbury C, Worswick M, Lloyd D, Finn M. High strain rate tensile testing of automotive aluminum alloy sheet. Fifth Int Symp Impact Eng 2006;32:541–60.

doi:10.1016/j.ijimpeng.2005.04.013.

[223] ASTM. Standard, D638-08, 2008, Standard Test Method for Tensile Properties of Plastics 2008. doi:10.1520/D0638-08.

[224] Bardelcik A, Worswick MJ, Wells MA. The influence of martensite, bainite and ferrite on the as-quenched constitutive response of simultaneously quenched and deformed boron steel - Experiments and model. Mater Des 2014;55:509–25. doi:10.1016/j.matdes.2013.10.014.

[225] VIC-2D 2009.

[226] ASTM. Standard D5656-10, 2012, Standard Test Method for Thick Adherend Metal Lap-Shear Joint for Determination of the Stress-Strain Behavior of Adhesives in Shear by Tension Loading 2012. doi:10.1520/D5656-10.

[227] Doghri I, Muller A, Taylor RL. A general three-dimensional contact procedure for implicit finite element codes. Eng Comput (Swansea, Wales) 1998;15:233–59. doi:10.1108/02644409810202639.

[228] Greve L, Andrieux F. Deformation and failure modelling of high strength adhesives for crash simulation. Int J Fract 2007;143:143–60. doi:10.1007/s10704-007-9054-9.

[229] Trimino LF, Cronin DS, Caruso Dailey MM. Characterization of Structural Epoxy Adhesives. Annu. Conf. Expo. Exp. Appl. Mech. SEM 2014, June 2, 2014 - June 5, vol. 65, Green Ville, S.C.: Springer New York LLC; 2015, p. 185–91. doi:10.1007/978-3-319-06995-1_28.

[230] LSTC. LS-DYNA 2014;ls971_d_R5.

[231] ASTM. Standard, D3433-99, 2012, Standard Test Method for Fracture Strength in Cleavage of Adhesives in Bonded Metal Joints 2012. doi:10.1520/D3165.

[232] Sridharan S. Delamination behaviour of composites. vol. 1st editio. Woodhead publishing; 2008.

[233] Blackman BRK, Kinloch AJ, Paraschi M. On the Mode II Loading of Adhesive Joints. Eur Struct Integr Soc 2003;32:293–304. doi:http://dx.doi.org/10.1016/S1566-1369(03)80103-6.

[234] Kafkalidis MS, Thouless MD, Yang QD, Ward SM. Deformation and fracture of adhesive layers constrained by plastically-deforming adherends. J Adhes Sci Technol 2000;14:1593–607.

[235] Tvergaard V, Hutchinson JW. Relation between crack growth resistance and fracture process parameters in elastic-plastic solids. J Mech Phys Solids 1992;40:1377.

[236] Turon A, Davila CG, Camanho PP, Costa J. An engineering solution for mesh size effects in the simulation of delamination using cohesive zone models. Eng Fract Mech 2007;74:1665–82.

[237] Blazynski TZ. Materials at high strain rates. London: Elsevier Applied Science; 1987.

[238] ASTM. Standard,E11-04, 2010, Standard Test Method for Young's Modulus, Tangent modulus. and Chord modulus 2010. doi:10.1520/D3165.

[239] Chen W, Zhang B, Forrestal MJ. A split Hopkinson bar technique for low-impedance materials. Exp Mech 1999;39:81–5.

[240] Chen W, Lu F, Cheng M. Tension and compression tests of two polymers under quasi-static and dynamic loading. Polym Test 2002;21:113–21. doi:http://dx.doi.org/10.1016/S0142-9418(01)00055-1.

[241] Rae PJ, Brown EN. The properties of poly(tetrafluoroethylene) (PTFE) in tension. Polymer (Guildf) 2005;46:8128–40. doi:10.1016/j.polymer.2005.06.120.

[242] ASTM. Standard, B831-14, 2014, Standard Test Method for Shear Testing of thin Aluminum Products 2014. doi:10.1520/D3165.

[243] Morin D, Haugou G, Bennani B, Lauro F. Identification of a new failure criterion for toughened epoxy adhesive. Eng Fract Mech 2010;77:3481–500. doi:10.1016/j.engfracmech.2010.09.016.

[244] Banks-Sills L, Arcan M, Bortman Y. Mixed Mode Fracture Specimen for Mode II Dominant Deformation. Eng Fract Mech 1984;20:145–57. doi:10.1016/0013-7944(84)90122-X.

[245] Jamarani MB, Reed PE, Davies WR. Fracture behaviour of UPVC thin tubes at high loading rates. J Mater Sci 1988;23:4437–44.

[246] Selby K, Miller LE. Fracture Toughness and Mechanical-Behavior of an Epoxy-Resin. J Mater Sci 1975;10:12–24. doi:10.1007/BF00541027.

[247] Needleman A, Tvergaard V. An analysis of ductile rupture in notched bars. J Mech Phys Solids 1984;32:461–90. doi:10.1016/0022-5096(84)90031-0.

[248] Trimiño LF, Cronin DS. Evaluation of Numerical Methods to Model Structural Adhesive Response and Failure in Tension and Shear Loading. J Dyn Behav Mater 2016;2:122–37. doi:10.1007/s40870-016-0045-7.

[249] Todo M, Takahashi K, Beguelin P, Kausch HH. Effect of displacement rate on the Mode I fracture behavior of rubber toughened PMMA. JSME Int Journal, Ser A 1999;42:49–56.

[250] Bucknall CB. Quantitative approaches to particle cavitation, shear yielding, and crazing in rubber-toughened polymers. J Polym Sci Part B Polym Phys 2007;45:1399–409. doi:10.1002/polb.21171.

[251] Brostow W. Mechancical properties. In: Mark JE, editor. Phys. Prop. Polym. Handb. 2nd editio, Springer; 2007, p. 423–45.

[252] Berger LL. On the mechanism of craze fibril breakdown in glassy polymers. Macromolecules 1990;23:2926–34.

[253] Andrews EH. Cracking and crazing in polymeric glasses. In: Haward RN, Holliday L, Kelly A, editors. Phys. Glas. Polym., New York: New York, Wiley c1973; 1973, p. 394.

[254] Donald AM, Kramer EJ. Craze Initiation and Growth in High-Impact Polystyrene 1982;27:3729–41. doi:10.1002/app.1982.070271009.

[255] Woo CW, Li DL. A universal physically consistent definition of material damage. Int J Solids Struct 1993;30:2097–108. doi:10.1016/0020-7683(93)90053-A.

[256] Tabor D. Indentation hardness: Fifty years on a personal view. Philos Mag A 1996;74:1207–12. doi:10.1080/01418619608239720.

[257] Baltá-Calleja FJ. Microhardness of polymers. Cambridge, U.K.: Cambridge University Press; 2000.

[258] Oyen ML. Analytical techniques for indentation of viscoelastic materials. Philos Mag 2017;86:5625–41. doi:10.1080/14786430600740666.

[259] Chen X, Ashcroft IA, Wildman RD, Tuck CJ. An inverse method for determining the spatially resolved properties of viscoelastic – viscoplastic three-dimensional printed materials Subject Areas : R Soc London -- Philos Trans 2015.

[260] Mix AW, Giacomin AJ. Standardized Polymer Durometry. J Test Eval 2011;39:103205.

doi:10.1520/JTE103205.

[261] Apostolov AA, Boneva D, Baltá Calleja FJ, Krumova M, Fakirov S. Microhardness under Strain. 2. Microhardness Behavior during Stress-Induced Polymorphic Transition in Block Copolymers of Poly(butylene Terephthalate). J Macromol Sci - Phys 1998;37:543–55.

[262] Paplham WP, Seferis JC, Balta Calleja FJ, Zachmann HG. Microhardness of carbon fiber reinforced epoxy and thermoplastic polyimide composites. Polym Compos 1995;16:424–8.

[263] Lopez J. Microhardness Testing of Plastics : Literature Review 1993;12:437–58.

[264] Boneva D, Baltá Calleja FJ, Fakirov S, Apostolov AA, Krumova M. Microhardness under strain. III. Microhardness behavior during stress-induced polymorphic transition in blends of poly (butylene terephthalate) and its block copolymers. J Appl Polym Sci 1998;69:2271–6.

[265] Fakirov S, Boneva D, Baltá Calleja FJ, Krumova M, Apostolov AA. Microhardness under strain: Part I Effect of stress-induced polymorphic transition of poly(butylene terephthalate) on microhardness. J Mater Sci Lett 1998;17:453–7.

[266] 3M. 3M technical data sheets n.d. http://solutions.3m.com/wps/portal/3M/en_EU/Industrial-Adhesives-Tapes/-/Resources/DataSheets/.

[267] Todo M, Takahashi J, Watanabe H, Nakamoto J, Arakawa K. Effect of loading-rate on fracture micromechanism of methylmethacrylate-butadiene-styrene polymer blend. Polymer (Guildf) 2006;47:4824–30. doi:10.1016/j.polymer.2006.04.042.

[268] Bucknall CB, Kingdom U. Quantitative Approaches to Particle Cavitation , Shear Yielding , and Crazing in Rubber-Toughened Polymers 2006:1399–409. doi:10.1002/polb.

[269] ASTM. Standard E384-16, 2016, Standard Test Method for Microindentation Hardness of Materials 2016.

[270] Bernal CR, Frontini PM. Determination of fracture toughness in rubber modified glassy polymers under impact conditions. Polym Eng Sci 1995;35:1705–12.

[271] Kinloch AJ. Fracture behaviour of polymers. London: Applied Science Publishers; 1983.

[272] Multi Material Light-weight Vehicle 2013.

[273] Cui X, Zhang H, Wang S, Zhang L, Ko J. Design of lightweight multi-material automotive bodies using new material performance indices of thin-walled beams for the material selection

with crashworthiness consideration. Mater Des 2011;32:815–21. doi:10.1016/j.matdes.2010.07.018.

[274] Belingardi G, Goglio L, Tarditi A. Investigating the effect of spew and chamfer size on the stresses in metal/plastics adhesive joints. Int J Adhes Adhes 2002;22:273–82. doi:DOI: 10.1016/S0143-7496(02)00004-0.

[275] Wang CN. On the fracture of constrained layers. Int J Fract 1998;93:227–46.

[276] Meng Q. Nanosilica-toughened polymer adhesives. Mater Des 2014;61:75–86.

[277] Raghavan D, He J, Hunston D, Hoffman D. Strain rate dependence of fracture in a rubber-toughened epoxy system. J Adhes 2002;78:723–39.

[278] Akhavan-Safar A, Barbosa AQ, da Silva LF, Ayatollahi MR. Micro failure analysis of adhesively bonded joints enhanced with natural cork particles: Impact of overlap length and particles volume fraction. Frat ED INTEGRITA Strutt 2018:266–74. doi:10.3221/IGF-ESIS.46.24.

[279] Trimiño LF, Cronin DS. Damage measurements in epoxy structural adhesives using microhardness. Int J Adhes Adhes 2018;82:211–20. doi:10.1016/j.ijadhadh.2018.01.014.

[280] Dufour L, Bourel B, Lauro F, Haugou G, Leconte N. International Journal of Adhesion & Adhesives A viscoelastic - viscoplastic model with non associative plasticity for the modelling of bonded joints at high strain rates 2016;70:304–14. doi:10.1016/j.ijadhadh.2016.07.015.

[281] Kinloch, A J; Shawn, S.J.; Hunston, D.L.; Tod DA. Deformation and fracture behaviour of a rubber-toughned epoxy: 1. Microstructure and fracture studies. Polymer (Guildf) 1983;24:1341–54.

[282] Hourston DJ, Lane S, Zhang HX. Toughened thermoplastics: 2. Impact properties and fracture mechanisms of rubber modified poly(butylene terephthalates). Polymer (Guildf) 1991;32:2215–20. doi:10.1016/0032-3861(91)90049-O.

[283] Gent AN. Hypothetical Mechanism of Crazing in Glassy Plastics 1970;5:925–32.

[284] Inglis CE. No Title. Trans Inst Nav Archit 1913;55:219.

[285] Paterson MS. Effect of Pressure on Young's Modulus and the Glass Transition in Rubbers. J Appl Phys 1964;35:176.

[286] Shen W, Tang CY, Tsui CP, Peng LH. Effects of two damage mechanisms on effective elastic properties of particulate composites. Compos Sci Technol 2002;62:1397–406. doi:10.1016/S0266-3538(02)00085-4.

[287] Xin H, Brown HR, Naficy S, Spinks GM. Mechanical recoverability and damage process of ionic-covalent PAAm-alginate hybrid hydrogels. J Polym Sci Part B Polym Phys 2016;54:53–63. doi:10.1002/polb.23899.

[288] Shui G, Wang Y, Huang P, Qu J. Nonlinear ultrasonic evaluation of the fatigue damage of adhesive joints. NDT E Int 2015;70:9–15. doi:10.1016/j.ndteint.2014.11.002.

[289] Akbarzadeh P, Farhangdoost K. Fatigue life assessment of adhesive joints based on ratchetting strain evolution. Mech Adv Mater Struct 2016;23:681–8. doi:10.1080/15376494.2015.1029157.

[290] Cheng P, Gong X-J, Aivazzadeh S, Xiao X. Experimental observation of tensile behavior of patch repaired composites. Polym Test 2014;34:146–54. doi:10.1016/j.polymertesting.2014.01.007.

[291] Grave JHL, Echtermeyer AT. Strain fields in adhesively bonded patch repairs of damaged Metallic beams. Polym Test 2015;48:50–8. doi:10.1016/j.polymertesting.2015.09.013.

[292] de Freitas ST, Sinke J. Failure analysis of adhesively-bonded skin-to-stiffener joints: Metal-metal vs. composite-metal. Eng Fail Anal 2015;56:2–13. doi:10.1016/j.engfailanal.2015.05.023.

[293] Chiu WK, Galea SC, Koss LL, Rajic N. Damage detection in bonded repairs using piezoceramics. SMART Mater Struct 2000;9:466–75. doi:10.1088/0964-1726/9/4/309.

[294] Tsamasphyros GJ, Kanderakis GN, Marioli-Riga ZP. Thermal analysis by numerical methods of debonding effects near the crack tip under composite repairs. Appl Compos Mater 2003;10:149–58. doi:10.1023/A:1023945121389.

[295] Pavlopoulou S, Worden K, Soutis C. On the Structural Health Monitoring of Repaired Aerospace Structures. In: Chang, FK, editor. Struct. Heal. Monit. 2013, VOLS 1 2, 2013, p. 956+.

[296] Yavas D, Shang X, Hong W, Bastawros AF. Utilization of nanoindentation to examine bond line integrity in adhesively bonded composite structures. Int J Fract 2017;204:101–12.

doi:10.1007/s10704-016-0165-z.

[297] Wu G, Qin Z, Zhang L, Yang K. Strain response analysis of adhesively bonded extended composite wind turbine blade suffering unsteady aerodynamic loads. Eng Fail Anal 2018;85:36–49. doi:10.1016/j.engfailanal.2017.12.009.

[298] de Ulzurrun ID, Lopez F, Herreros MA, Suarez JC. Tests of deck-to-hull adhesive Joints in GFRP boats. Eng Fail Anal 2007;14:310–20. doi:10.1016/j.engfailanal.2006.02.012.

[299] DEejong E, Duchatinier JG, Vannisselroij JJM. A Straightforward Ultrasonic Technique for the Inspection of Adhesively Bonded Connections and Sizing of Impact Damage in GRP Pipeines. INSIGHT 1994;36:683–5.

[300] Salamone S, Fasel T, Bartoli I, Srivastava A, di Scalea FL, Todd M. Health Monitoring Approach for Adhesively Bonded Joints. Mater Eval 2009;67:828–36.

[301] Ni X, Rizzo P. Use of Highly Nonlinear Solitary Waves in Nondestructive Testing. Mater Eval 2012;70:561–9.

[302] Severin F, Seviaryna I, Maeva E. Industrial Applications of Scanning Acoustic Microscopy. Mater Eval 2013;71:867–74.

[303] Crawford A, Droubi MG, Faisal NH. Analysis of Acoustic Emission Propagation in Metal-to-Metal Adhesively Bonded Joints. J Nondestruct Eval 2018;37. doi:10.1007/s10921-018-0488-y.

[304] Landini G. Image J, Auto Threshold 2017. https://imagej.net/Auto_Threshold (accessed April 9, 2016).

[305] Glasbey CA. An Analysis of Histogram-Based Threshold Algorithms. Graph Model Image Process 1993;55:532–7.

[306] Sezgin M. Survey over image thresholding techniques and quantitative performance evaluation 2004;13:146–65. doi:10.1117/1.1631316.

[307] Gonzales-Barron U, Butler F. A comparison of seven thresholding techniques with the k-means clustering algorithm for measurement of bread-crumb features by digital image analysis 2006;74:268–78. doi:10.1016/j.jfoodeng.2005.03.007.

[308] Surový P, Dinis C, Marušák R, Ribeiro NDA. Importance of automatic threshold for image

segmentation for accurate measurement of fine roots of woody plants Význam automatického prahovania na obrazovú segmentáciu pre presné merania jemných koreňov drevín 2014;60:244–9.

[309] Low I, Mai Y. Micromechanisms of Crack Extension in Unmodified and Modified Epoxy Resins. Compos Sci Technol 1988;33:191–212.

[310] Silicone Rubber mechanical properties n.d. http://www.azom.com/properties.aspx?ArticleID=920 (accessed August 11, 2016).

[311] Oxtoby DW. Principles of modern chemistry. Philadelphia: Saunders College Pub.; 1987.

[312] Shackelford JF. Introduction to materials science for engineers. 4th ed. Upper Saddle River, N.J.: Prentice Hall; 1996.

[313] Qi HJ, Joyce K, Boyce MC. Durometer Hardness and the Stress-Strain Behavior of Elastomeric Materials. Rubber Chem Technol 2003;76:419–35. doi:10.5254/1.3547752.

[314] Lange FF. Interaction between overlaping paralell cracks; a photoelastic study. Int J Fract Mech 1968;4.

[315] Swain M V, Hagan JT. Some observations of overlaping interacting cracks. Eng Fract Mech 1978;10:299–304.

[316] Chu TC, Ranson WF, Sutton MA, Peters WH. Applications of Digital-Image Correlation techniques to experimental mechanics. Exp Mech 1985;25:232–44.

[317] Cuadra J, Vanniamparambil PA, Hazeli K, Bartoli I, Kontsos A. Damage quantification in polymer composites using a hybrid NDT approach. Compos Sci Technol 2013;83:11–21. doi:10.1016/j.compscitech.2013.04.013.

[318] Prudencio EE, Bauman PT, Williams S V, Faghihi D, Oden JT. Real-time inference of stochastic damage in composite materials. Compos Part B 2014;67:209–19. doi:10.1016/j.compositesb.2014.07.004.

[319] Harizi W, Chaki S, Bourse G, Ourak M. Mechanical damage assessment of Glass Fiber-Reinforced Polymer composites using passive infrared thermography. Compos Part B 2014;59:74–9. doi:10.1016/j.compositesb.2013.11.021.

[320] Steenbrink, A.C.; Van der Giessen E. On cavitation, post-cavitation and yield in amorphous

polymer-rubber blends. J Mech Phys Solids 1999;47:843–76.

[321] van Melick HGH, Govaert LE, Meijer HEH. Localisation phenomena in glassy polymers: influence of thermal and mechanical history. Polymer (Guildf) 2003;44:3579–91. doi:10.1016/S0032-3861(03)00089-2.

[322] Zebarjad SM, Bagheri R, Lazzeri A, Serajzadeh S. Dilatational shear bands in rubber-modified isotactic polypropylene. Mater Des 2004;25:247–50. doi:10.1016/j.matdes.2003.10.001.

[323] Tomita Y, Lu W. Computational characterization of micro- to macroscopic mechanical behavior and damage of polymers containing second-phase particles. Int J Damage Mech 2002;11:129–49. doi:10.1106/105678902023084.

[324] Dal Corso F, Bigoni D. Growth of slip surfaces and line inclusions along shear bands in a softening material. Int J Fract 2010;166:225–37. doi:10.1007/s10704-010-9534-1.

[325] Lou Y, Huh H, Lim S, Pack K. New ductile fracture criterion for prediction of fracture forming limit diagrams of sheet metals. Int J Solids Struct 2012;49:3605–15. doi:10.1016/j.ijsolstr.2012.02.016.

[326] Kambour RP. Review of Crazing and Fracture in Thermoplastics. J Polym Sci Macromol Rev 1973;7:1–154. doi:10.1002/pol.1973.230070101.

[327] George M, Nziakou Y, Goerke S, Genix A, Bresson B, Roux S. In situ AFM investigation of slow crack propagation mechanisms in a glassy polymer. J Mech Phys Solids 2018;112:109–25. doi:10.1016/j.jmps.2017.11.019.

[328] Jähne B. Digital image processing : concepts, algorithms, and applications. Berlin: Springer-Verlag; 1991.

[329] Radke RJ, Andra S, Al-Kofahi O, Roysam B. Image change detection algorithms: a systematic survey. Image Process IEEE Trans 2005;14:294–307. doi:10.1109/TIP.2004.838698.

[330] Patra S, Ghosh S, Ghosh A. Histogram thresholding for unsupervised change detection of remote sensing images. Int J Remote Sens 2011;32:6071–89.

[331] Pun T. A new method for grey-level picture thresholding using the entropy of the histogram. Signal Processing 1980;2:223. doi:http://dx.doi.org/10.1016/0165-1684(80)90020-1".

[332] Sahoo PK, Soltani S, Wong AKC. A survey of thresholding techniques. Comput Vision,

Graph Image Process 1988;41:233. doi:http://dx.doi.org/10.1016/0734-189X(88)90022-9".

[333] Jia L, Liu Y. A novel thresholding approach to background subtraction. 2008 IEEE Work. Appl. Comput. Vision, WACV, January 7, 2008 - January 9, School of Electronic and Information Engineering, Xi'an Jiaotong University, Xi'an 710049, China: Inst. of Elec. and Elec. Eng. Computer Society; 2008. doi:10.1109/WACV.2008.4544007.

[334] Photron FASTCAM viewer V3.6.3 n.d.

[335] Wolfram S. Mathematica V11.0 2016.

[336] Rasband W. Image J V1.51h n.d.

[337] Kimball, S.; Mattis P. GNU Image Manipulation Program GIMP V2.8.16 2015.

[338] Argon AS, Salama MM. Growth of crazes in glassy polymers. Philos Mag 1977;36:1217–34. doi:10.1080/14786437708239790.

[339] Kramer EJ. Craze Fibril Formation and Breakdown. Polym Eng Sci Sci 1984;24:761–9.

[340] Zhang H, Liu N, Ran X, Han C, Han L, Zhuang Y, et al. Toughening of Polylactide by Melt Blending with Methyl Methacrylate – Butadiene – Styrene Copolymer. J Appl Polym Sci 2012;125:E550–61. doi:10.1002/app.

[341] Brown D. Tracker, video analysis and modeling tool 2014;4.87.

Appendix A

Mechanical properties and numerical simulation study

A1: Material properties summary

This section presents a summary of material properties for the three structural adhesives tested.

Strain Rate / Material	Quasi-static from Manufacturer	0.001 [1/s]	0.1 `[1/s]	0.77 [1/s]	10 [1/s]	100 [1/s]
EC-2214	5.17	5.12	N/A	N/A	5.94±1.63	6.93±0.92
DP-460NS	2.13	2.52±0.34	N/A	2.17±0.08	2.58±0.08	2.30±0.16
SA-9850	N/A	2.27±0.13	1.73±0.1	N/A	2.34±0.07	2.19±0.13

Table A1-1: Modulus of Elasticity [GPa] ± 1 standard deviation

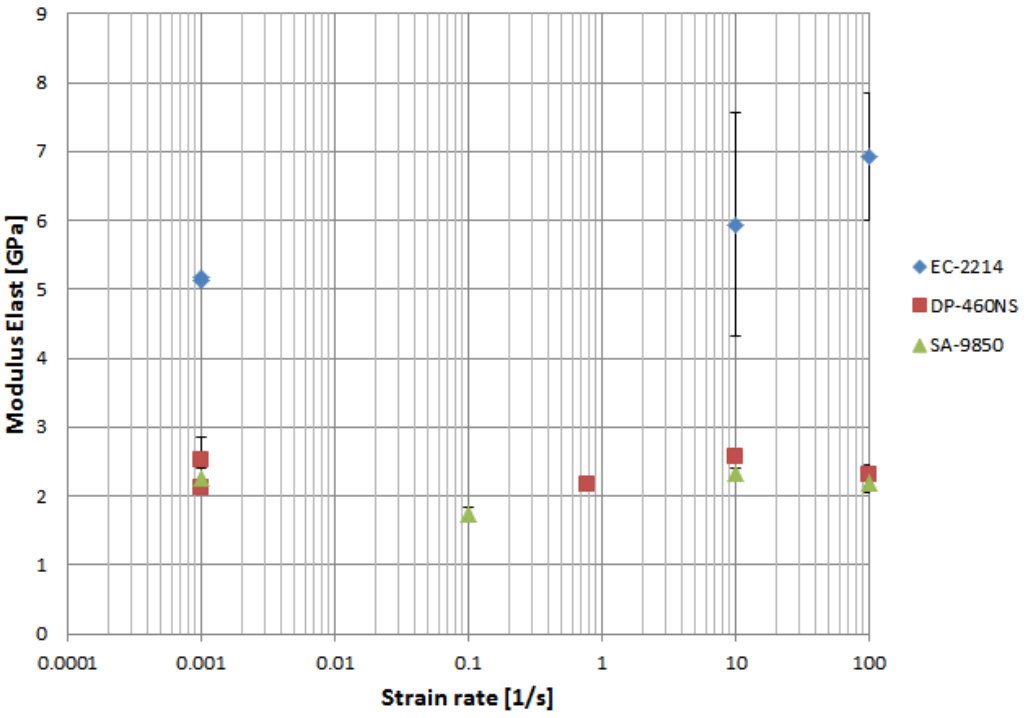

Figure A1-1: Modulus of Elasticity as per Table A1-1

MATERIAL	ρ [kg/m³]	G_{Ic} [MPa/m]	G_{II} [MPa/m]	E [GPa]	G [GPa]	ν
EC-2214-	1540	1.82	5.46	5.17	1.87	0.38
DP-460NS	1200	2.82	10	2.13	0.77	0.41
SA-9850	1200	2.97	15	2.40	0.85	0.41

Table A1-2: Cohesive model parameters

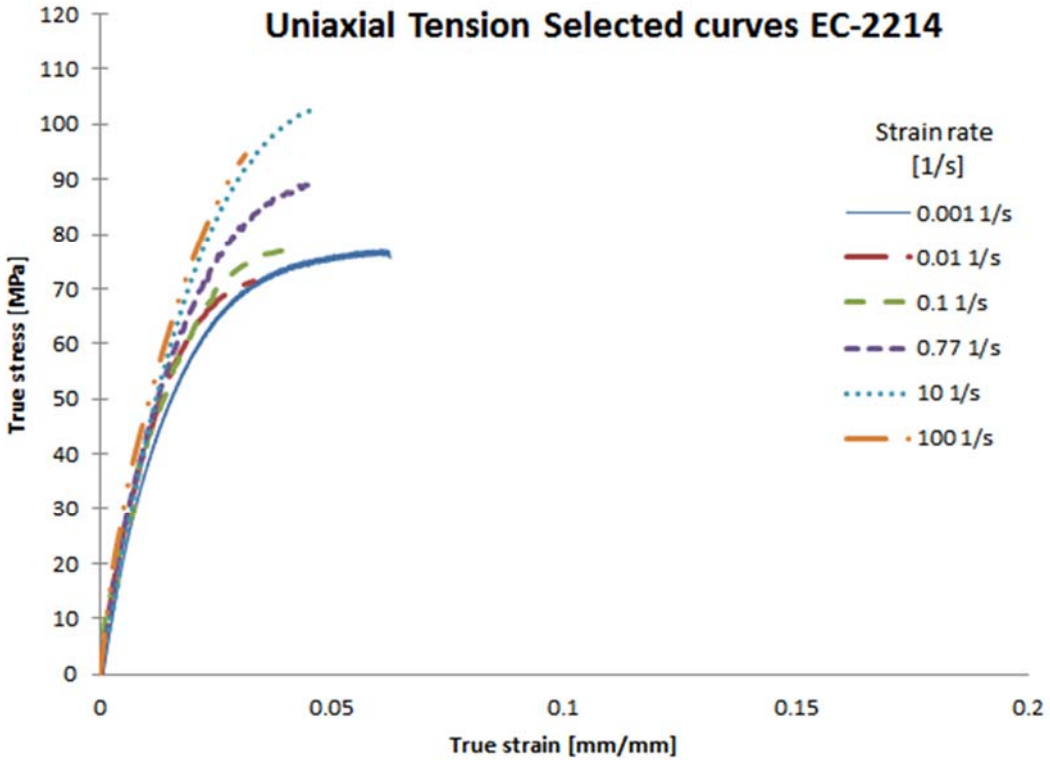

Figure A1-2: Tensile testing results for EC-2214

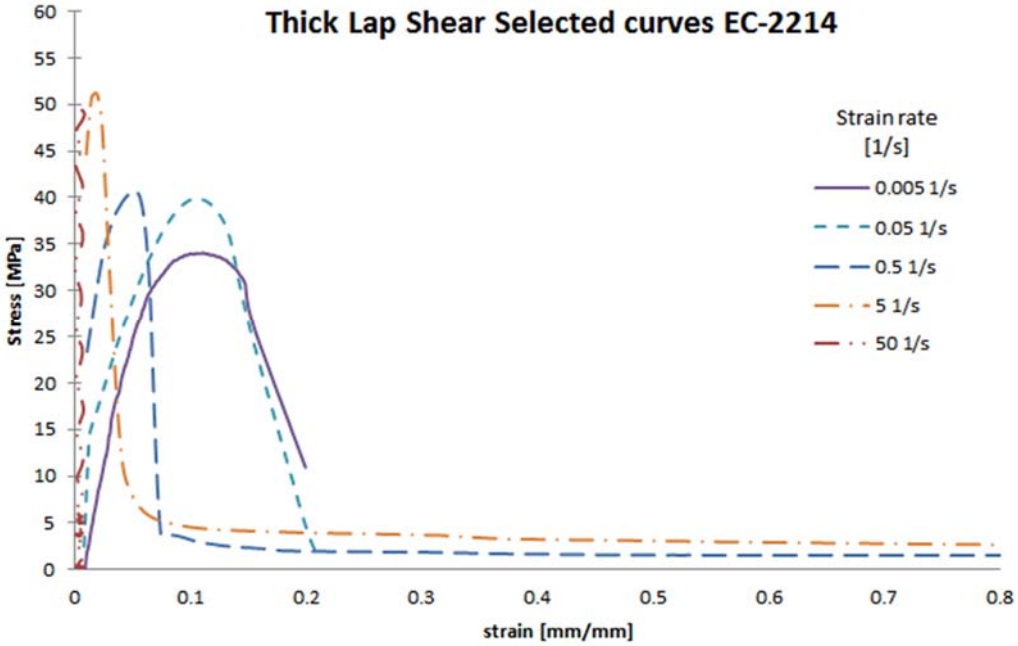

Figure A1-3: Shear testing results for EC-2214

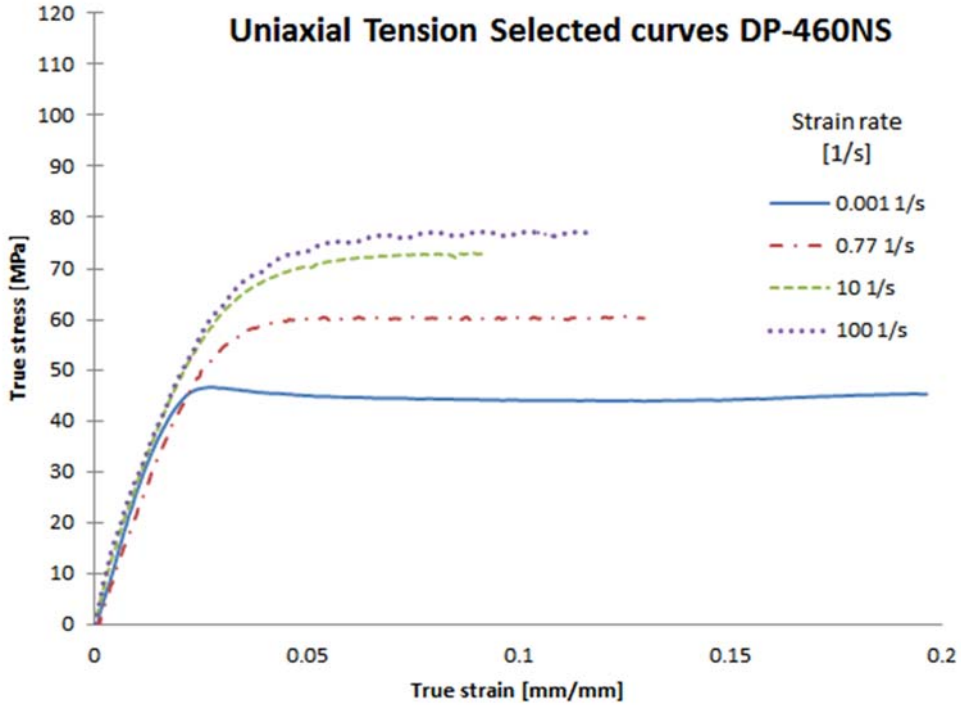

Figure A1-4: Tensile testing results for DP-460NS

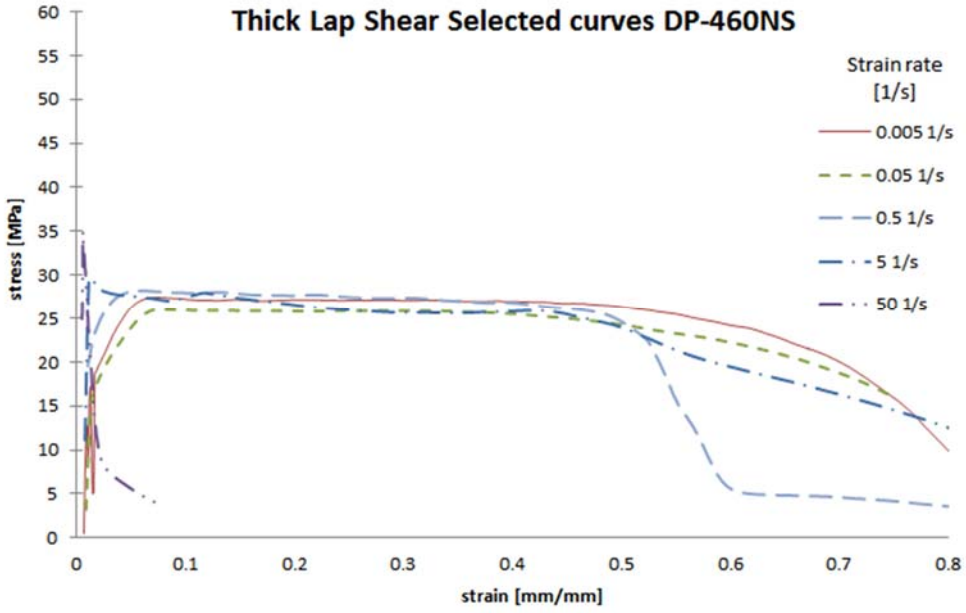

Figure A1-5: Shear testing results for DP-460NS

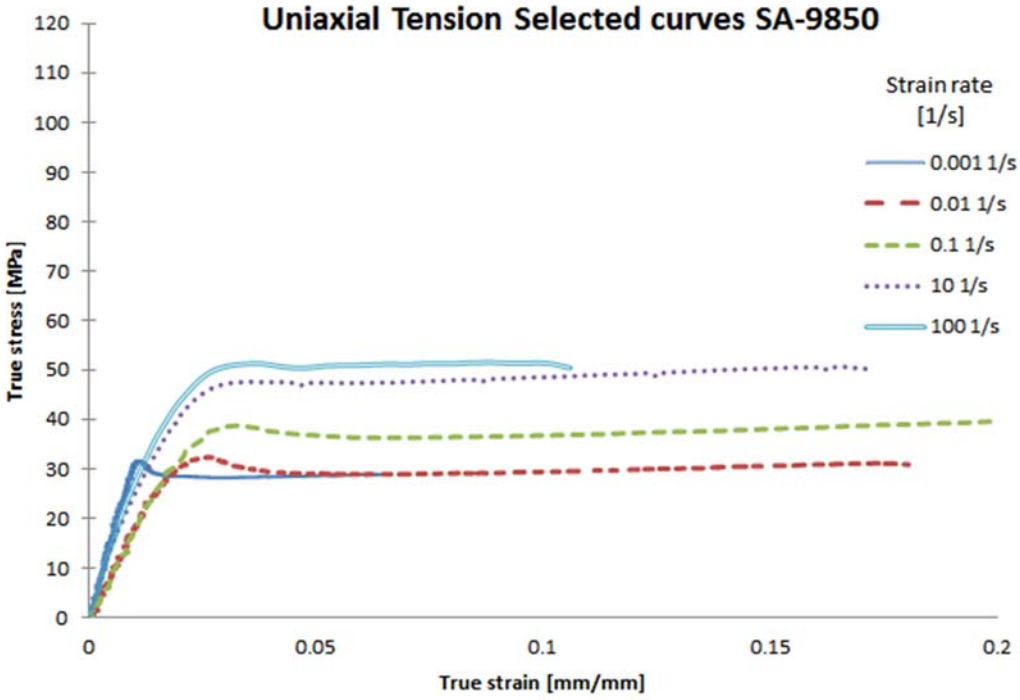

Figure A1-6: Tensile testing results for SA-9850

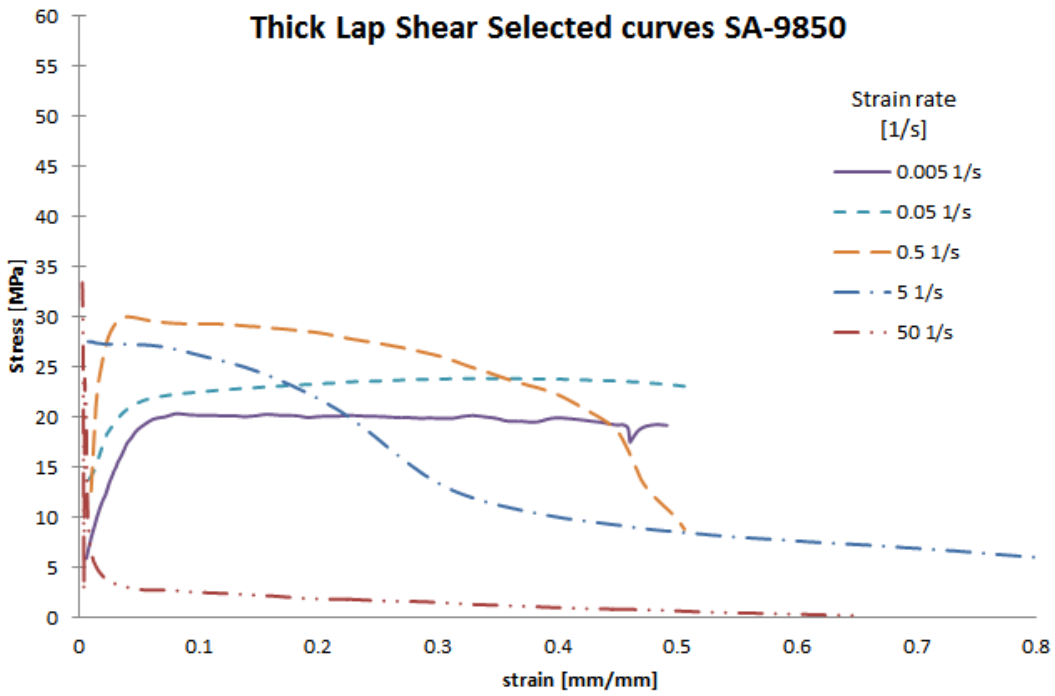

Figure A1-7: Shear testing results for SA-9850

A2: LS-DYNA cards

LS-Dyna cards for cohesive elements with strain rate dependency (Mat 240), the material properties were defined in the mm-sec-tonne-Newton unit system [129], commonly used in vehicle and structural models.

*MAT_COHESIVE_MIXED_MODE_ELASTOPLASTIC_RATE							
MID	**Ro**	**RoFLAG**	**INTFAIL**	**EMOD**	**GMOD**	**THICK**	**OUTPUT**
_	1.54 E-9	0	0	5.17E3	1.87E3	0	-
GIc_0	**GIc-INF**	**EDOT_GI**	**To**	**T1**	**EDOT_T**	**FGI**	**-**
1.82	0	0	-69.73	-2.79	0.001	0.25	
GIIc_0	**GIIc-INF**	**EDOT_GII**	**So**	**S1**	**EDOT_S**	**FGII**	**-**
5.46	0	0	-31.79	-1.88	0.0049	0.77	

Table A2-1: CZM Material Properties for EC-2214

*MAT_COHESIVE_MIXED_MODE_ELASTOPLASTIC_RATE							
MID	**Ro**	**RoFLAG**	**INTFAIL**	**EMOD**	**GMOD**	**THICK**	**OUTPUT**
-	1.20E-9	0	0	2.13E3	0.77E3	0	-
GIc_0	**GIc-INF**	**EDOT_GI**	**To**	**T1**	**EDOT_T**	**FGI**	**-**
2.82	0	0	-13.04	-3.45	5.34E-7	0.75	
GIIc_0	**GIIc-INF**	**EDOT_GII**	**So**	**S1**	**EDOT_S**	**FGII**	**-**
15	0	0	-23.89	-1.01	0.005	0.77	

Table A2-2: CZM Material Properties for DP-460NS

*MAT_COHESIVE_MIXED_MODE_ELASTOPLASTIC_RATE							
MID	**Ro**	**RoFLAG**	**INTFAIL**	**EMOD**	**GMOD**	**THICK**	**OUTPUT**
-	1.20E-9	0	0	2.4E3	0.85E3	0	-
GIc_0	**GIc-INF**	**EDOT_GI**	**To**	**T1**	**EDOT_T**	**FGI**	**-**
2.97	0	0	-21.05	-2.68	6.84E-5	0.7	
GIIc_0	**GIIc-INF**	**EDOT_GII**	**So**	**S1**	**EDOT_S**	**FGII**	**-**
15	0	0	-17	-0.3	4.41E-13	0.78	

Table A2-3: CZM Material Properties for SA-9850

A3: Cohesive element (MAT#240) single element response

Cohesive model response using single element simulations for tension and shear loading vs. experimental data (Figure A3-1 to A3-6).Cohesive model response metrics in single element simulations for tension and shear loading (Table A3-1 to A3-6).

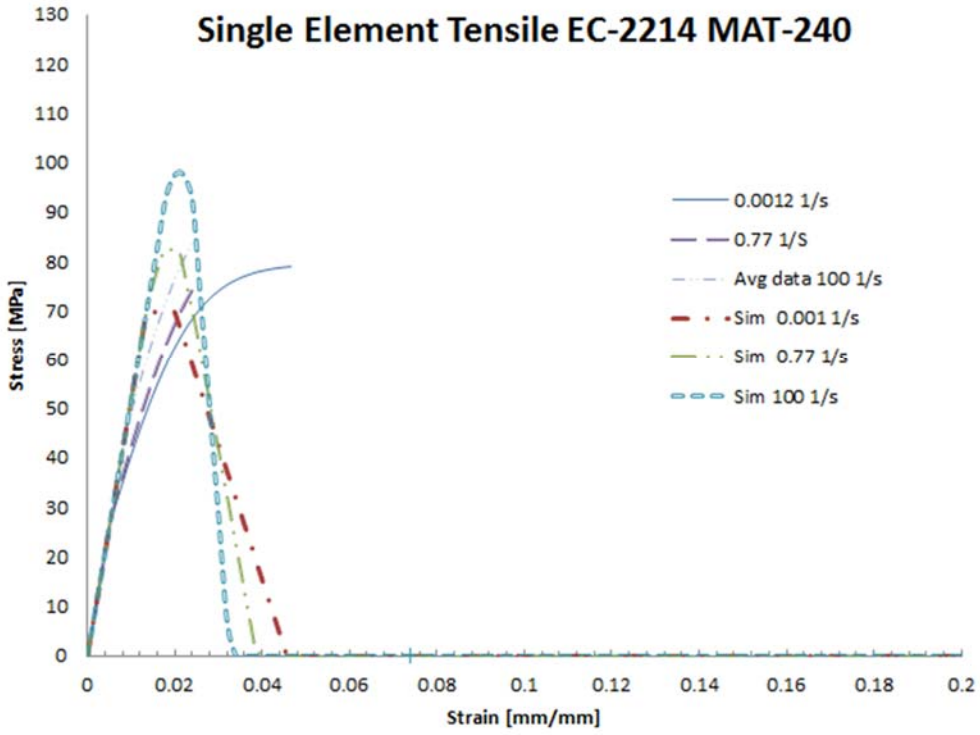

Figure A3-1: Single element MAT-240 tensile simulations results EC-2214

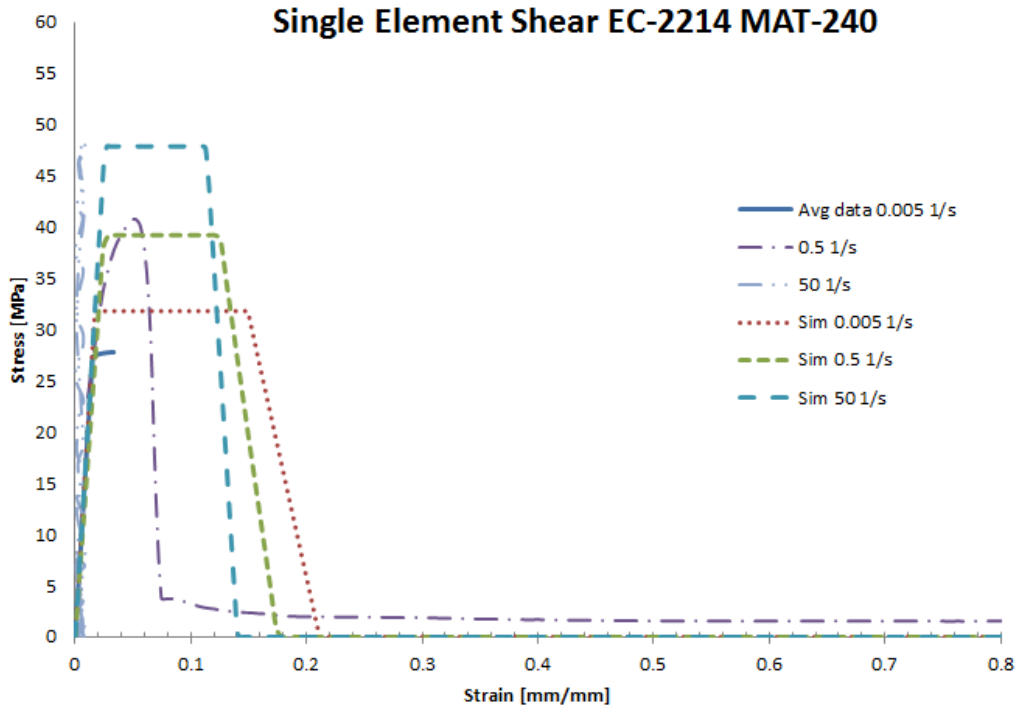

Figure A3-2: Single element MAT-240 shear simulations results EC-2214

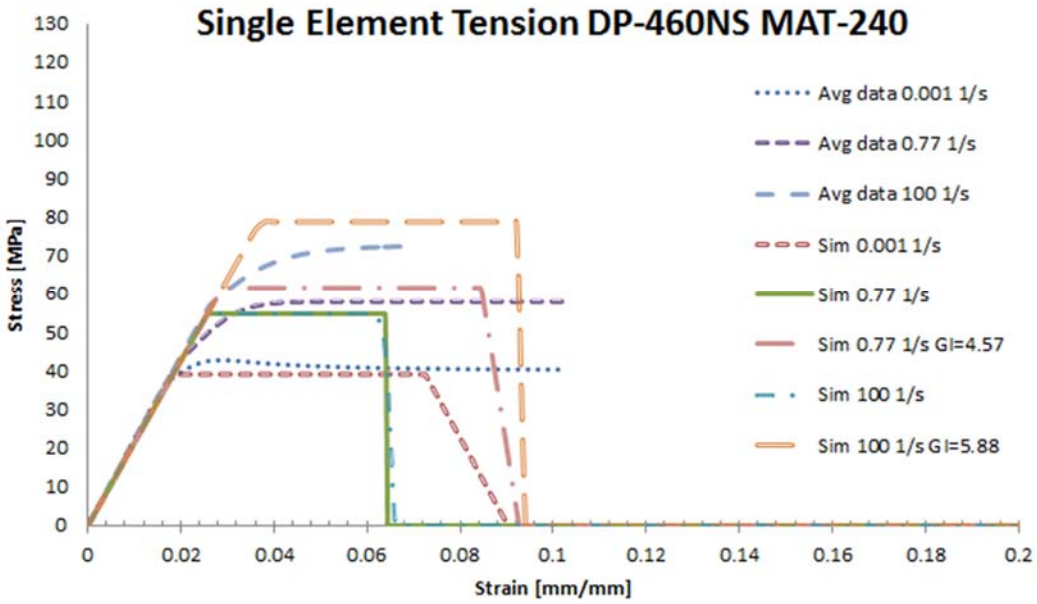

Figure A3-3: Single element MAT-240 tensile simulations results DP-460NS

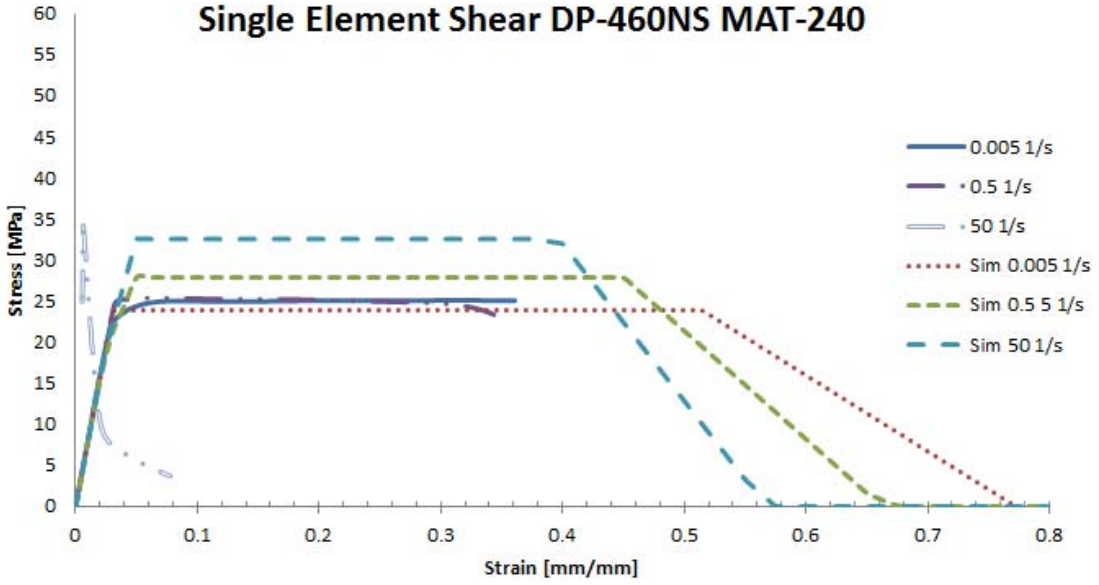

Figure A3-4: Single element MAT-240 shear simulations results DP-460NS

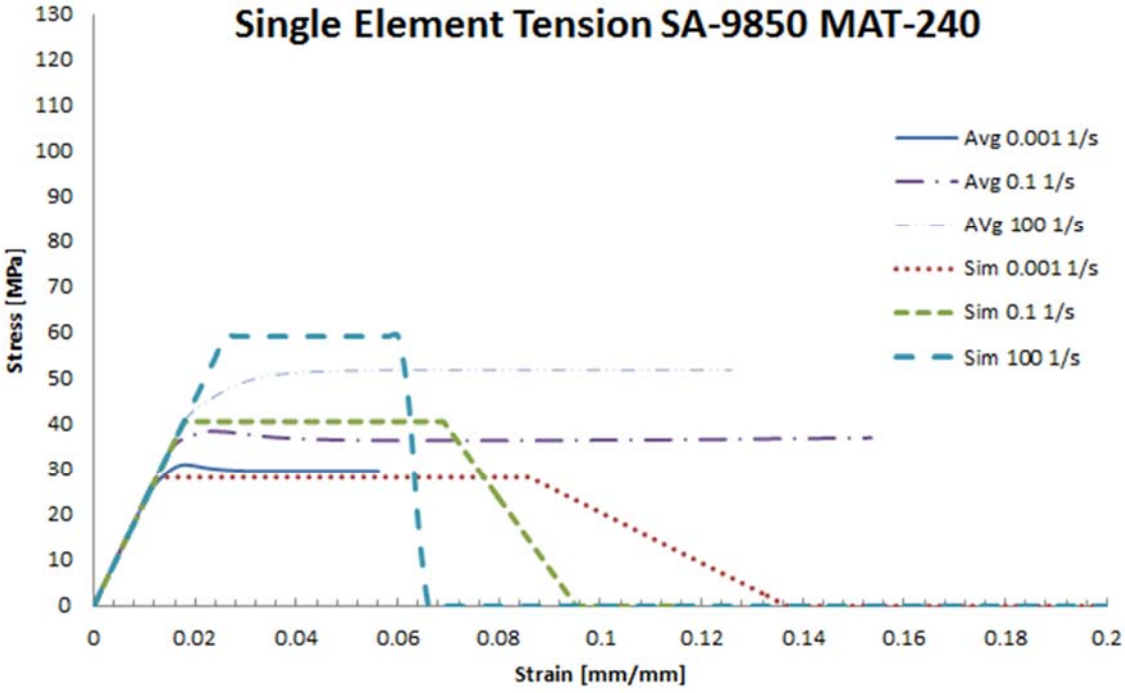

Figure A3-5: Single element MAT-240 tensile simulations results SA-9850

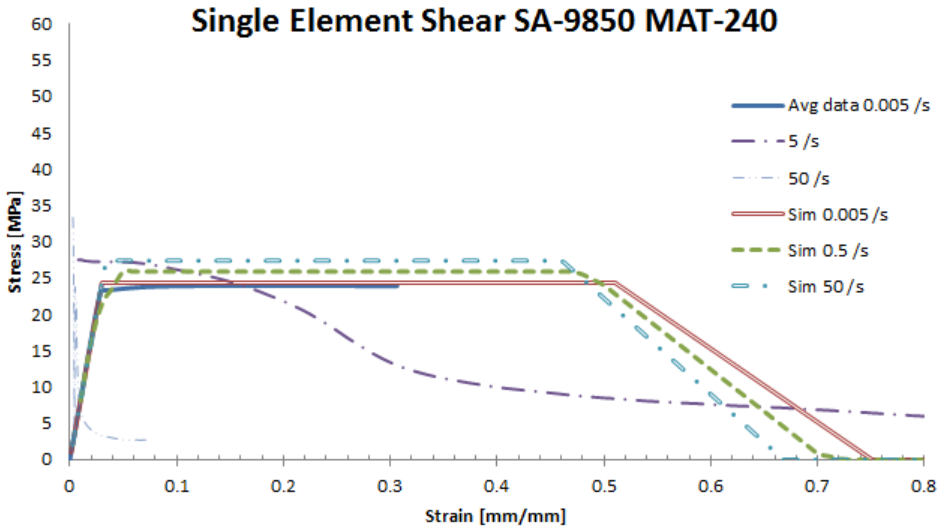

Figure A3-6: Single element MAT-240 shear simulations results SA-9850

EC-2214 Tensile results						
Strain Rate [1/s]	**Data curve fit Stress [MPa]**	**Expmt. Avg. Stress [MPa]**	**Expmt. Std. Dev. [MPa]**	**Sim. Stress [MPa]**	**Difference %**	**r^2**
0.001	62.32	77.11	8.58	69.73	11.89	0.65
0.77	82.66	75.64	N/A	82.38	0.33	0.50
100	97.55	84.66	2.64	97.57	0.02	0.96

Table A3-1: Cohesive model response metrics single element simulations EC-2214 in Tension

EC-2214 Shear results						
Strain Rate [1/s]	**Data curve fit Stress [MPa]**	**Expmt. Avg. Stress [MPa]**	**Expmt. Std. Dev. [MPa]**	**Sim. Stress [MPa]**	**Difference %**	**r^2**
0.005	31.79	27.78	5.86	31.79	14.43	0.68
0.5	40.47	40.77	0.24	39.20	3.85	0.83
50	49.14	48.26	5.00	47.87	0.81	0.07

Table A3-2: Cohesive model response metrics single element simulations EC-2214 in Shear

DP-460NS Tensile results						
Strain Rate [1/s]	**Data curve fit Stress [MPa]**	**Expmt. Avg. Stress [MPa]**	**Expmt. Std. Dev. [MPa]**	**Sim. Stress [MPa]**	**Difference %**	**r^2**
0.001	39.04	42.7	4.68	39.04	0.01	0.83
0.77 (GI=2.88)	61.97	57.91	N/A	54.75	11.65	N/A
0.77 (GI=4.57)	61.97	57.91	N/A	61.64	0.53	0.94
100 (GI=2.88)	78.76	75.90	4.45	54.75	30.49	N/A
100 (GI=5.82)	78.76	75.90	4.45	78.76	0.00	0.96

Table A3-3: Cohesive model response metrics single element simulations DP-460NS in Tension

DP-460NS Shear results						
Strain Rate [1/s]	**Data curve fit Stress [MPa]**	**Expmt. Avg. Stress [MPa]**	**Expmt. Std. Dev. [MPa]**	**Sim. Stress [MPa]**	**Difference %**	**r^2**
0.005	23.89	25.08	3.56	23.89	4.74	0.86
0.5	28.57	25.37	3.16	28.57	12.61	0.98
50	33.24	34.86	1.65	33.24	4.65	0.01

Table A3-4: Cohesive model response metrics single element simulations DP460NS in Shear

SA-9850 Tensile results						
Strain Rate [1/s]	**Data curve fit Stress [MPa]**	**Expmt. Avg. Stress [MPa]**	**Expmt. Std. Dev. [MPa]**	**Sim. Stress [MPa]**	**Difference %**	**r^2**
0.001	28.24	31.05	3.57	28.24	0.01	0.82
0.1	40.58	38.41	6.55	40.58	0.00	0.76
100	59.09	51.88	2.20	59.09	0.00	0.91

Table A3-5: Cohesive model response metrics single element simulations SA-9850 in Tension

SA-9850 Shear results						
Strain Rate [1/s]	**Data curve fit Stress [MPa]**	**Expmt. Avg. Stress [MPa]**	**Expmt. Std. Dev. [MPa]**	**Sim. Stress [MPa]**	**Difference %**	**r^2**
0.005	26.10	23.93	5.65	24.37	1.84	0.95
0.5	26.86	27.51	5.19	25.88	5.93	0.95
50	27.61	33.4	6.33	27.4	17.96	0.01

Table A3-6: Cohesive model response metrics single element simulations SA-9850 in Shear

A4: SAMP-1 solid element (MAT#187) single element response

Solid constitutive model response using single element simulations for tension and shear loading vs. experimental data (Figure A4-1 to A4-6). Solid constitutive model response metrics in single element simulations for tension and shear loading (Table A4-1 to A4-6).

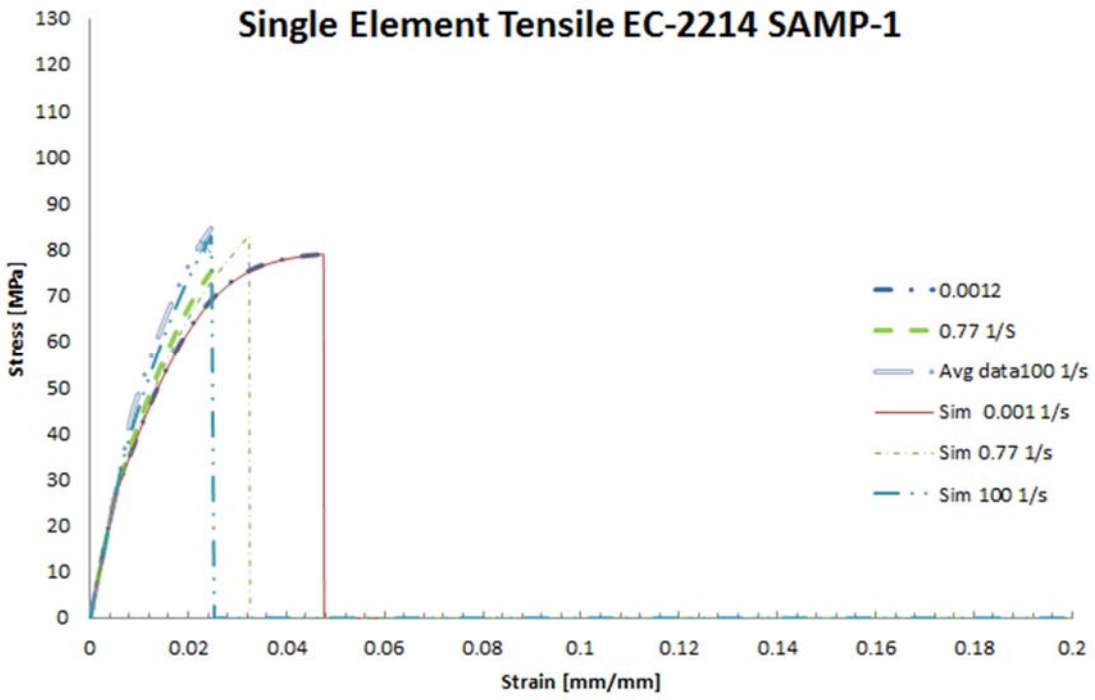

Figure A4-1: Single element SAMP-1 tensile simulation results EC-2214

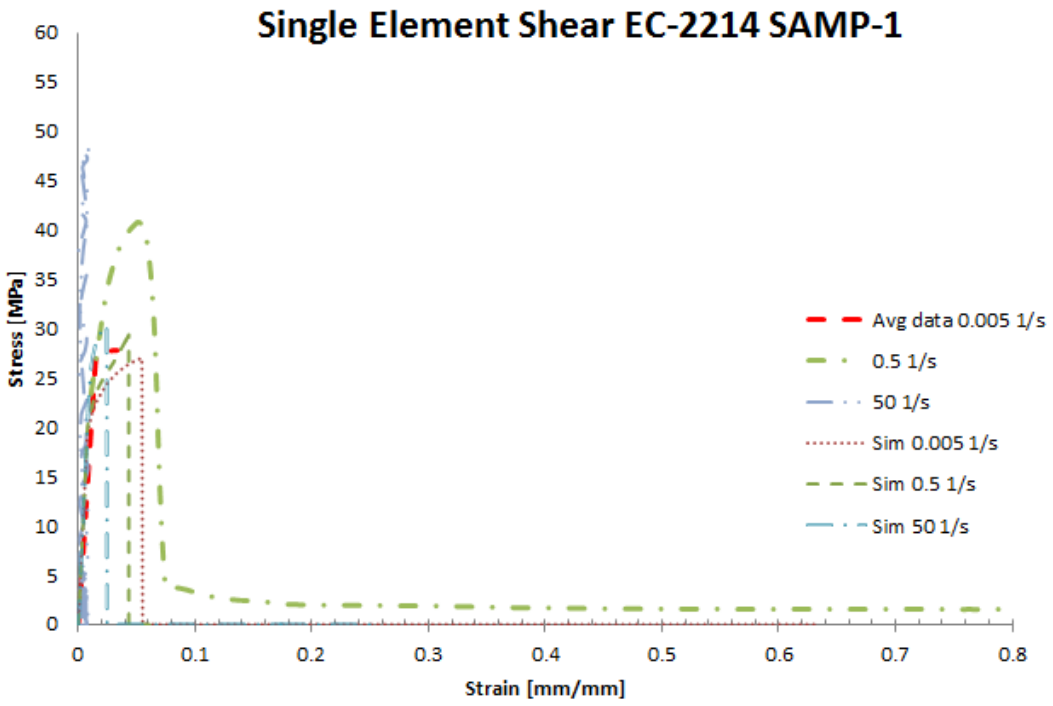

Figure A4-2: Single element SAMP-1 shear simulation results EC-2214

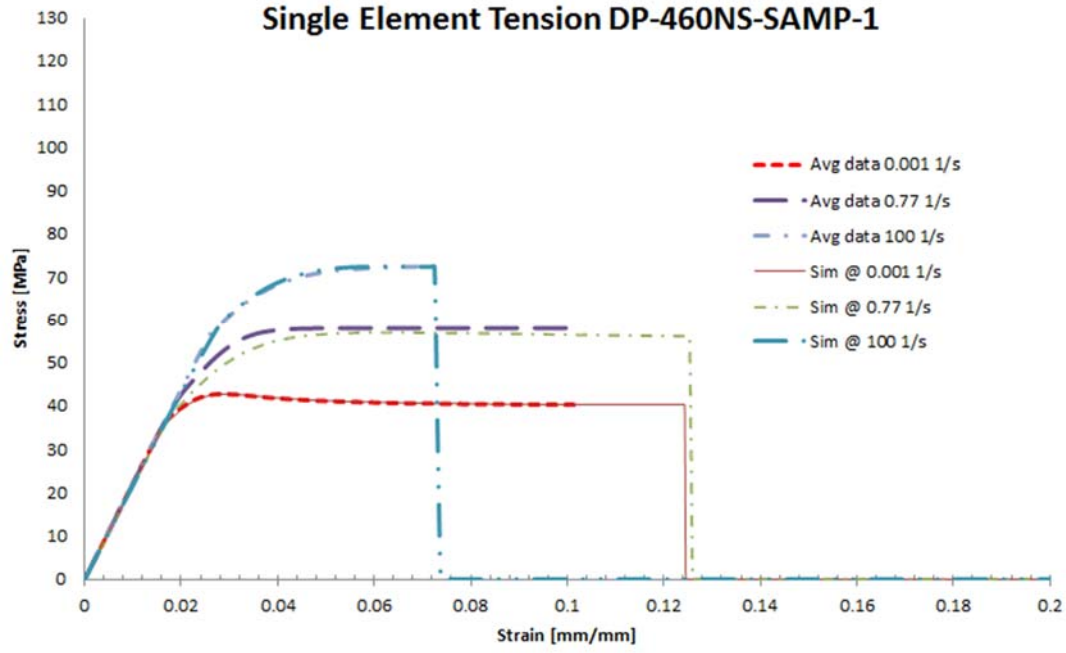

Figure A4-3: Single element SAMP-1 tension simulation results DP-460NS

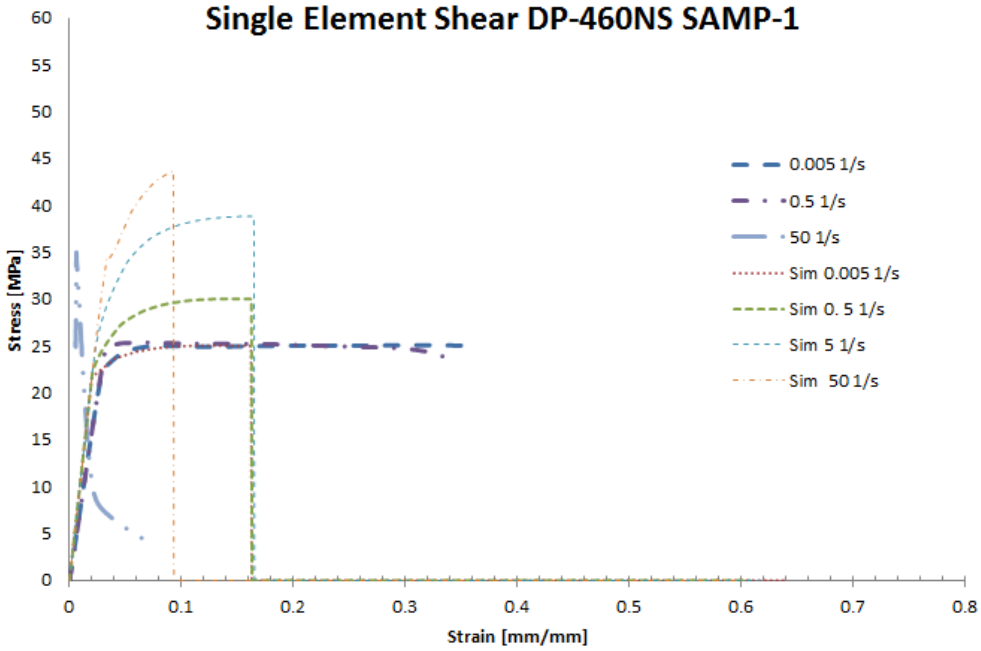

Figure A4-4: Single element SAMP-1 shear simulation results DP-460NS

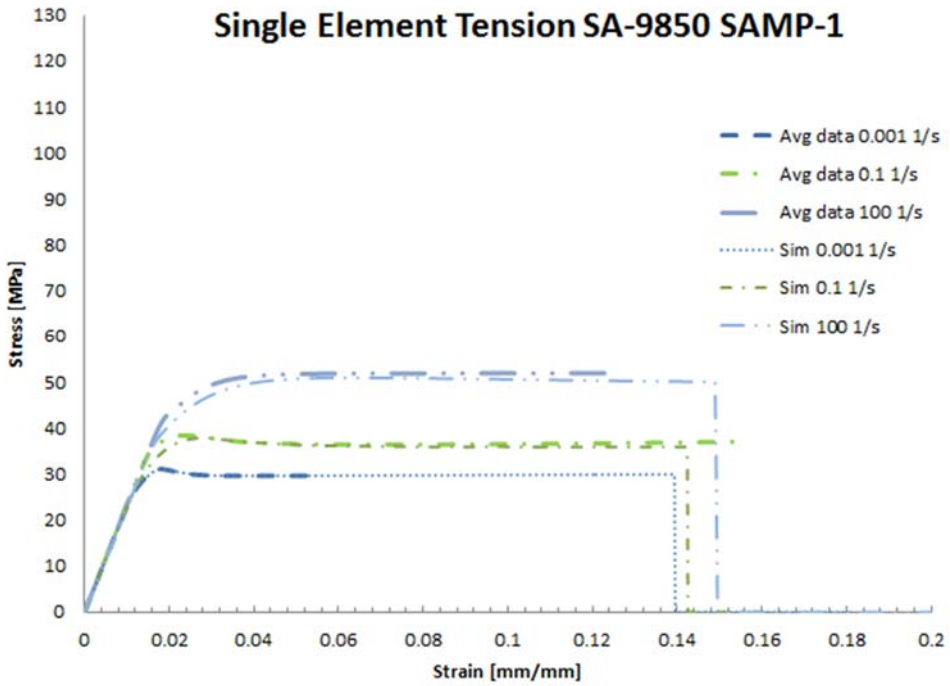

Figure A4-5: Single element SAMP-1 tension simulation results SA-9850

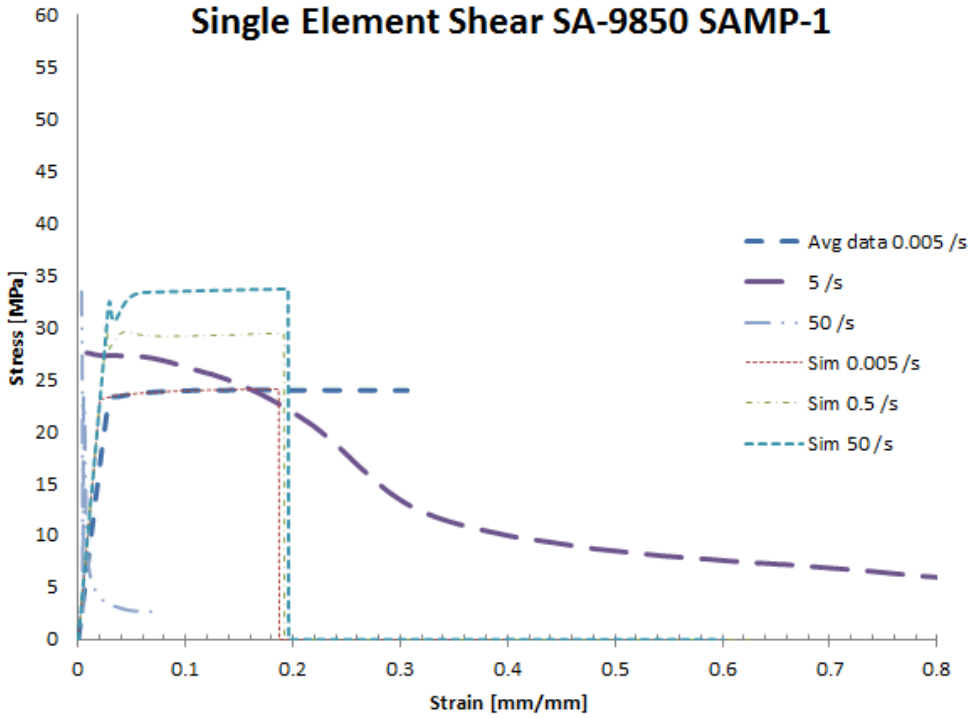

Figure A4-6: Single element SAMP-1 shear simulation results SA-9850

EC-2214 Tension results					
Strain Rate [1/s]	**Expmt. Avg. Stress [MPa]**	**Expmt. Std. Dev. [MPa]**	**Sim. Stress [MPa]**	**Difference %**	**r^2**
0.001	78.97	8.58	79.00	0.04	0.99
0.77	75.64	N/A	83.10	9.87	0.94
100	84.66	2.64	82.82	2.17	0.96

Table A4-1: SAMP-1 model response metrics single element simulation EC-2214 Tension

EC-2214 Shear results					
Strain Rate [1/s]	**Expmt. Avg. Stress [MPa]**	**Expmt. Std. Dev. [MPa]**	**Sim. Stress [MPa]**	**Difference %**	**r^2**
0.005	27.78	5.86	27.01	2.78	0.89
0.5	40.77	0.24	29.38	27.95	0.36
50	48.26	5.00	30.31	37.19	0.05

Table A4-2: SAMP-1 model response metrics single element simulation EC-2214 Shear

DP-460NS Tension results					
Strain Rate [1/s]	**Expmt. Avg. Stress [MPa]**	**Expmt. Std. Dev. [MPa]**	**Sim. Stress [MPa]**	**Difference %**	**r^2**
0.001	42.73	4.68	42.75	0.04	0.99
0.77	57.93	N/A	56.93	1.73	0.99
100	72.42	4.45	72.46	0.05	0.98

Table A4-3: SAMP-1 model response metrics single element simulation DP-460NS Tension

DP-460NS Shear results					
Strain Rate [1/s]	**Expmt. Avg. Stress [MPa]**	**Expmt. Std. Dev. [MPa]**	**Sim. Stress [MPa]**	**Difference %**	**r^2**
0.005	25.08	3.56	25.04	0.16	0.99
0.5	25.37	3.16	30.03	18.36	0.65
50	34.86	1.65	43.68	25.31	0.01

Table A4-4: SAMP-1 model response metrics single element simulation DP-460NS Shear

SA-9850 Tension results					
Strain Rate [1/s]	**Expmt. Avg. Stress [MPa]**	**Expmt. Std. Dev. [MPa]**	**Sim. Stress [MPa]**	**Difference %**	**r^2**
0.001	31.05	3.57	31.06	0.03	0.99
0.1	38.41	6.55	37.83	1.52	0.99
100	51.88	2.20	50.76	2.15	0.95

Table A4-5: SAMP-1 model response metrics single element simulation SA-9850 Tension

SA-9850 Shear results					
Strain Rate [1/s]	**Expmt. Avg. Stress [MPa]**	**Expmt. Std. Dev. [MPa]**	**Sim. Stress [MPa]**	**Difference %**	**r^2**
0.005	23.93	5.65	24.04	0.44	0.99
0.5	27.51	5.19	29.66	7.80	0.5
50	33.38	6.33	33.64	0.76	0.33

Table A4-6: SAMP-1 model response metrics single element simulation SA-9850 Shear

Appendix B
Damage with microhardness

B1: Preliminary study

A preliminary study was conducted to determine if the fixture support method, to support the samples during micro-indentation, would affect the results compared to mounting the sample in epoxy mounting resin. Additionally, in all three materials, the effect of changes in applied load during the indentation process was studied as micro-indentation results should be independent of applied load.

The DP-460NS sample was mounted in an epoxy resin (NAPA polyester resin, E ~ 3.0GPa, ultimate strength ~70+MPa) and measurements were made at different levels of applied weight (200–1000gr), which were then compared against measurements made in the jig. A T-test statistical analysis demonstrated that the average mean of the support fixture-mounted sample was statistically indistinguishable from the data measured in the epoxy-mounted material (Table B1-1). Additional hardness measurements using the Vickers machine were taken to verify independence from the applied load during indentation [256]. In most cases a T-test analysis proved independence of load to be true for DP-460NS and EC-2214 materials (Table B1-1), but there were a few cases where this principle was challenged for SA-9850 (Table B1-1). The data for SA-9850 was plotted in detail (Figure B1-1), and considerable variability detected only at the two extremes of the loads applied during indentation. The variability of the data in all the adhesives was studied to assess differences (Table B1-2). Much lower variability was present in DP-460NS, and this material microhardness was consistent for all load levels investigated. The variability in the other materials can be related to the inherent error in the measurements since an optical filar micrometer and an optical microscope were used for the measurements at that time, and detectability at the lowest load setting was a challenge. Further investigation with the ODM could be warranted here for SA-9850 and EC-2214, but in general, assuming independence of load to determine microhardness using a Vickers machine is accurate. For each material, the load level that provided the least variability in the microhardness results, without compromising appropriate optical detectability, was selected.

Experiment	DP-460NS Epoxy mount vs. Jig	EC-2214 200g vs. 300g	SA-9850 500g vs. 300g	SA-9850 500g vs. 200g	SA-9850 500g vs. 1000g
T_{obs}	2.79	1.38	0.36	4.65	3.59
T_{crit}	3.52	3.30	1.70	1.72	1.71

Table B1-1: T-test statistical analysis with 95% confidence

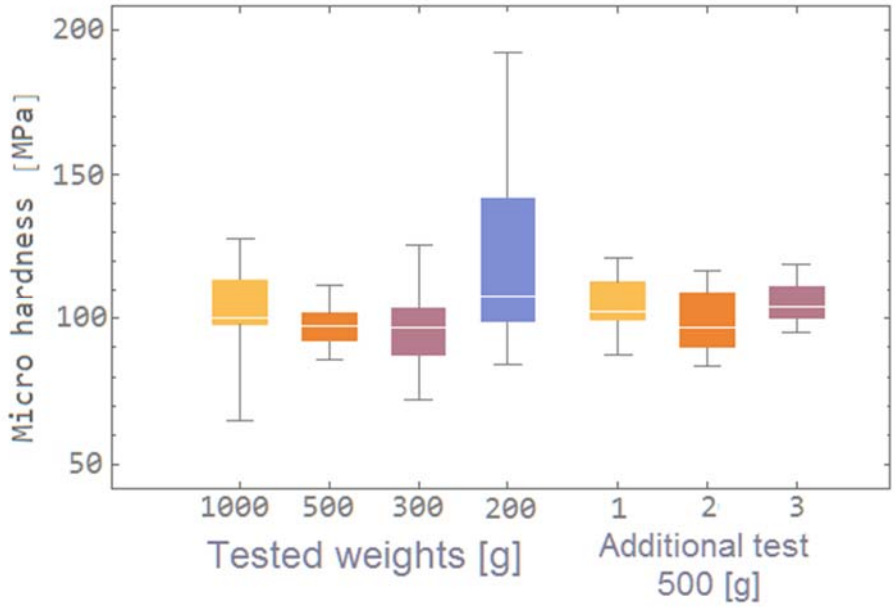

Figure B1-1: Microhardness measurements in SA-9850

Weight [g]	200	300	500	1000
DP-460NS	10.90	79.52	18.42	24.80
SA-9850	766.92	209.43	72.15	254.34
EC-2214	704.20	1447.11	-	-

Table B1-2: Variance of HV for different applied weights during indentation

B2: Statistical relevance of measured microhardness

The tables below summarize the analysis results for each material at each measured location. Each table contains the observed value (T_{obs}) and the critical value (T_{crit}) for the T-test, with a significance level of 95%. Locations, where the mean measured value was deemed statistically different from the material average mean microhardness (Table 3-4), are marked with the star symbol (*) in Figures 3-6 to 3-8. Calculations were made for all three materials for all tested strain rates.

Strain rate [1/s]	**T values**	**Distance from fracture zone[mm]**							
		0.5	**2.5**	**4.5**	**6.5**	**8.5**	**10.5**	**12.5**	**14.5**
0.002	T_{obs}	3.03	0.65	0.59	0.11	3.04	0.35	-	-
	T_{crit}	1.88	2.06	1.93	2.33	1.85	1.92	-	-
0.01	T_{obs}	1.66	4.32	5.03	7.20	7.73	4.44	-	-
	T_{crit}	1.89	1.79	1.77	1.76	1.71	1.77	-	-
0.1	T_{obs}	0.04	2.13	1.18	1.89	2.14	0.67	-	-
	T_{crit}	1.97	1.83	1.81	1.85	1.74	1.91	-	-
100	T_{obs}	0.56	1.17	0.95	0	1.50	-	-	-
	T_{crit}	1.93	1.87	1.95	1.95	1.85	-	-	-

Table B2-1: T-test for EC-2214 measured microhardness values against undamaged material microhardness

Strain rate [1/s]	T values	Distance from fracture zone[mm]							
		0.5	2.5	4.5	6.5	8.5	10.5	12.5	14.5
0.002	T_{obs}	23.09	5.95	22.35	78.14	22.71	20.12	3.43	-
	T_{crit}	1.89	1.97	1.91	1.75	1.91	2.02	1.97	-
0.01	T_{obs}	23.40	100	67.72	36.05	7.12	127	0.47	-
	T_{crit}	1.90	1.71	1.77	1.87	1.97	1.71	2.00	-
0.1	T_{obs}	8.86	10.76	11.78	67.28	76.65	4.39	3.02	-
	T_{crit}	1.87	1.87	1.88	1.75	1.73	1.97	1.89	-
100	T_{obs}	17.38	144.06	66.56	19.45	-	-	-	-
	T_{crit}	1.89	1.92	1.77	1.89	-	-	-	-

Table B2-2: T-test for SA-9850 measured microhardness values against undamaged material microhardness

Strain rate [1/s]	T values	Distance from fracture zone[mm]							
		0.5	2.5	4.5	6.5	8.5	10.5	12.5	14.5
0.002	T_{obs}	1.13	1.02	1.06	1.65	2.97	0.51	2.99	-
	T_{crit}	1.97	1.96	1.97	1.99	1.89	1.95	1.91	-
0.01	T_{obs}	11.95	12.58	14.42	5.52	6.68	0.02	3.50	10.31
	T_{crit}	1.89	1.90	1.87	1.88	1.87	1.94	1.90	1.86
0.1	T_{obs}	49.06	17.36	7.09	12.81	5.86	12.16	3.82	3.96
	T_{crit}	1.86	1.86	1.93	1.89	1.90	1.87	1.87	1.87
100	T_{obs}	1.12	4.13	1.04	0.76	5.52	1.57	-	-
	T_{crit}	1.79	1.79	1.81	1.77	1.77	1.79	-	-

Table B2-3: T-test for DP-460NS measured microhardness values against undamaged material microhardness

B3: DP-460NS analysis at high strain rate ($100s^{-1}$)

To clearly understand the overall increase in microhardness (132.5MPa on average vs. 120MPa) in the undamaged material, and the variability recorded, the individual samples were examined in detail (Figure B3-1). In addition, each sample was subjected to a T-test against the base material measurement (Table B3-1). Sample AF-1 developed mostly crazing, while shear bands were present only in the area immediately adjacent to the fracture zone, hence the only significant increases in microhardness occurred at this particular point, while all others were softer. The AF-5 sample had crazing followed by mild shear banding along the gauge length; therefore the microhardness measurements were still softer than that of the undamaged material. Lastly, AF-3 developed crazing, but it was followed by a high degree of shear banding, and the resultant microhardness was substantially higher. For the three samples tested at the high strain rate, the T-test analysis supported the finding that the changes in microhardness were statistically significant.

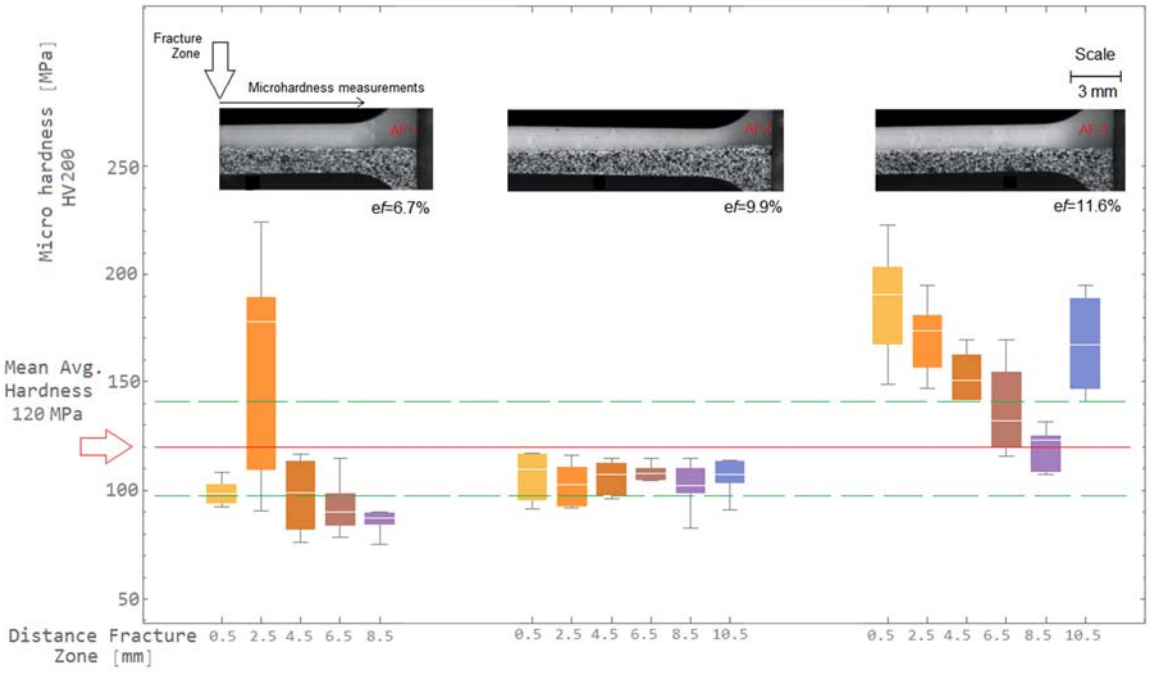

Figure B3-1: DP-460NS individual samples, microhardness measurements at $100s^{-1}$ strain rate. Material average (solid line) with +/- three standard deviations (dashed line)

Sample	T values	Distance from fracture zone[mm]					
		0.5	**2.5**	**4.5**	**6.5**	**8.5**	**10.5**
AF-1	T_{obs}	28.39	0.96	2.45	9.99	56.97	--
	T_{crit}	1.82	2.01	2.29	1.94	1.79	--
AF-5	T_{obs}	6.69	10.85	13.59	31.59	8.47	11.56
	T_{crit}	1.92	1.89	1.86	1.74	1.92	1.87
AF-3	T_{obs}	5.52	10.17	14.37	2.40	0.19	6.09
	T_{crit}	2.00	1.97	1.92	1.98	1.90	1.98

Table B3-1: T-test DP-460NS individual samples at high strain rate ($100s^{-1}$)

Appendix C

Damage in an Epoxy Adhesive

C1: Viscoelastic effects in microhardness measurements

To clearly understand the potential for viscoelastic effects in DP-460NS, the undamaged material was subjected to micro-indentation. The micro-indentations were made using a Micro Vickers Hardness Machine (Leco MHD-200 model), and measurements were conducted using an opto-digital microscope (Keyence VHX-5000) at high magnification (1000x). Optical measurements of the indentations were conducted immediately after indentation and after a period of one week (Table C1-1). The microhardness measurements were compared against the published microhardness for the material [279] (Figure C1-1). The figure includes the microhardness average value (solid line) and the three standard deviation limits (dashed lines) of this figure. Statistical analysis was used to identify differences between the data sets mean average. The analysis was conducted using a T-test with 95% confidence (α=0.05). The T-test results (Table C1-2) report that recorded differences in the mean value of the measurements were not statistically significant. Therefore viscoelastic effects on this material are not expected.

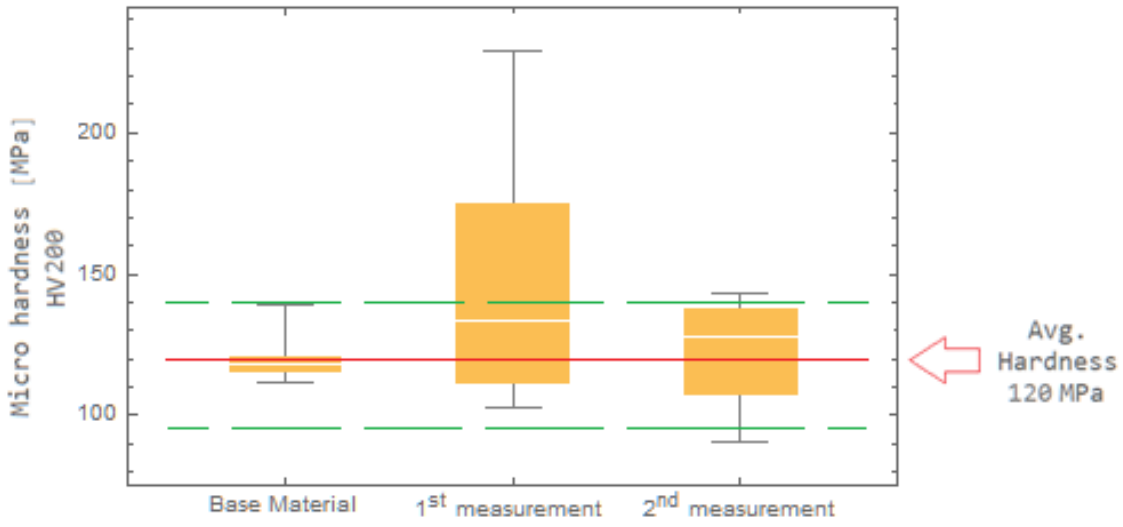

Figure C1-1: Microhardness values

1st measurement		2nd measurement	
Diagonal length [µm]	**HVN**	**Diagonal length [µm]**	**HVN**
165	136.23	165.1	136.06
189.3	103.50	182.5	111.35
127.4	228.50	160.9	143.26
134.8	204.10	170.9	126.98
159.2	146.33	170.3	127.88
168.4	130.78	163	139.59
176.7	118.78	189.7	103.06
190	102.74	201.6	91.25
Average	146.4		122.4
Std. dev	46.18		18.65

Table C1-1: Microhardness indentations measurements

Set	T_{obs}	T_{crit}	P-Value
Base vs 1st	1.60	1.89	0.15
Base vs 2nd	0.33	1.86	0.75
1st vs 2nd	1.35	1.83	0.21

Table C1-2: Statistical analysis

C2: Additional microscope observations: polished sample under load and post failure fracture plane

Additional observations were made at the surface of a polished sample under tension, at different levels of strain. Of notice was the detection of strain whitening at an embedded particle. The particle can be described as a circular black shell (~ 167 µm in diameter) with an interior white core (~66 µm in diameter). The color change started at the equator of the particle core and extended towards the shell

with increases in strain. Finally, the strain whitening extended beyond the shell towards the surrounding area (Figure C2-1, middle and far right) and the particle deformed into an ellipsoid for its final shape.

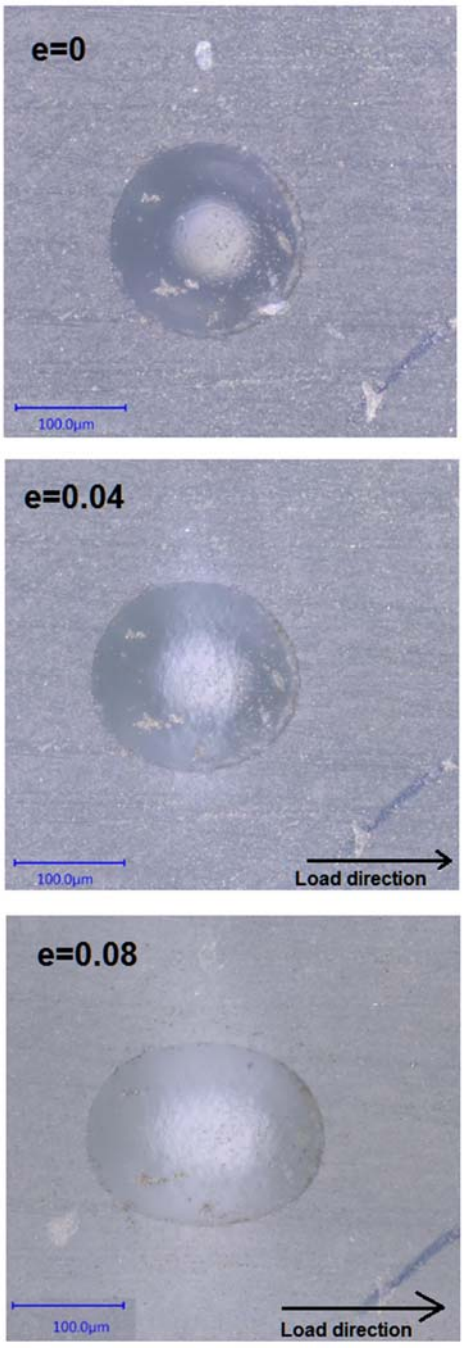

Figure C2-1: Particle cavitation during increased axial loading

A fracture surface was studied using scanning electron microscopy (SEM). Although the fracture surface under SEM at various magnifications (Figure C2-2) resembles the typical appearance of a toughened epoxy with thermoplastic toughening [86], the morphology of the fracture resembles that of furrows and steps. According to Low and Mei [309], this type of morphology is evidence of crack growth and arrest, and it is similar to those observed in other toughened polymers [115]. No evidence of particle debonding was evident in the SEM observations.

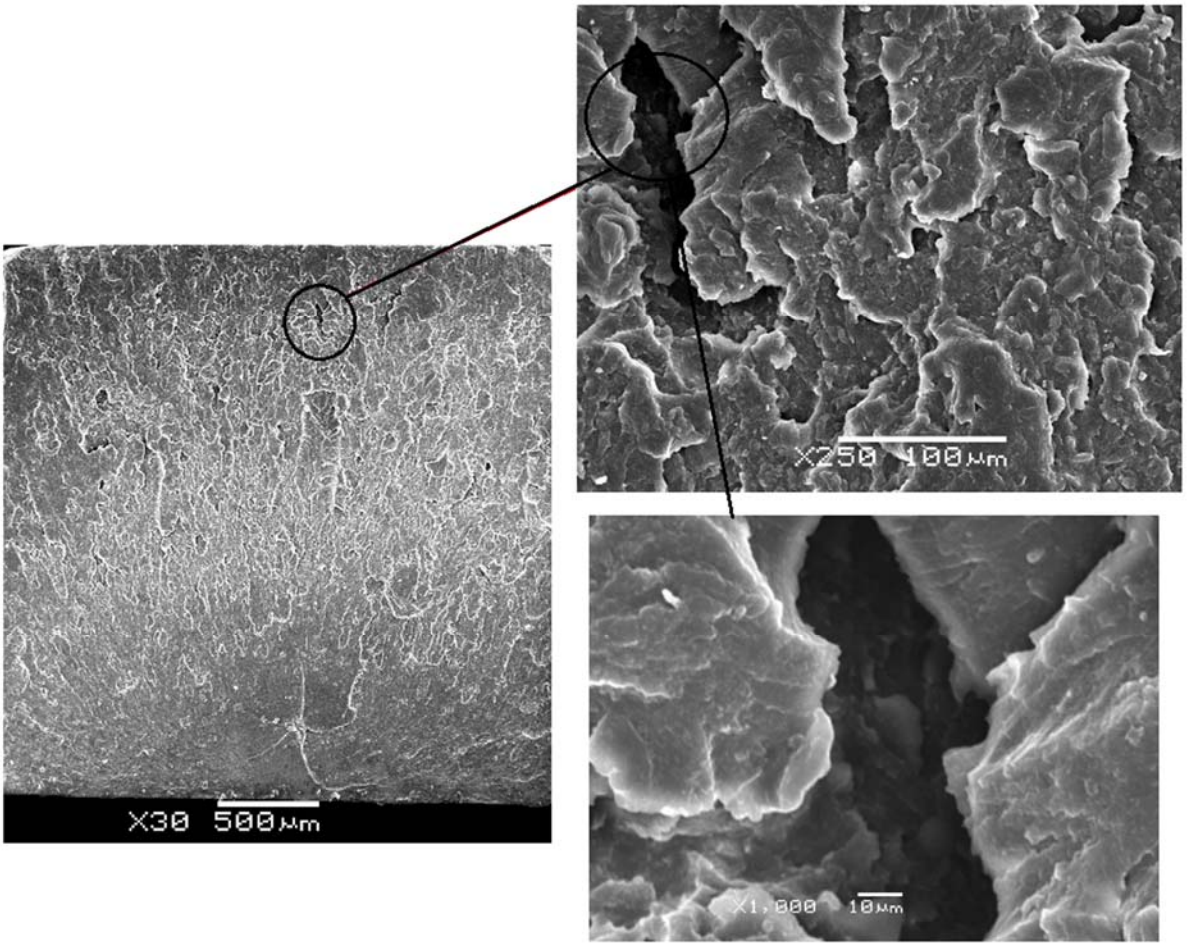

Figure C2-2: Fracture plane on a sample tested to failure under quasi-static uniaxial tensile load

C3: Load-Unload measurements

The measurements of the modulus of elasticity during load and unload are summarized in Tables C3-1 to C3-4. Each table corresponds to the tested displacements as per Table 5-3, and each table includes the coefficient of determination (r^2) and coefficient of variation (V_1).

Sample # and cycle	Load cycle			Unload cycle		
	E [GPa]	r^2	V_1 [%]	E [GPa]	r^2	V_1 [%]
A-LU-A2-cycle1	2.06	0.99	0.25	2.11	0.99	0.13
A-LU-A2-cycle2	1.93	0.99	0.17	1.98	0.99	0.13
A-LU-A2-cycle3	2.02	0.99	0.21	2.02	0.99	0.18
A-LU-A3-cycle 1	1.97	0.99	0.28	1,98	0.99	0.18
A-LU-A3-cycle 2	1.83	0.99	0.22	1.83	0.99	0.20
A-LU-A3-cycle 3	1.84	0.99	0.34	1.89	0.99	0.34
A-LU-A4-cycle 1	1.96	0.99	0.29	2.06	0.99	0.26
A-LU-A4-cycle 2	1.88	0.99	0.25	2.08	0.99	0.51
A-LU-A4-cycle 3	1.98	0.99	0.33	1.96	0.99	0.50

Table C3-1: Modulus of elasticity measurements and calculation coefficients for the applied strain of ~1.3% (Strain point A, Table 5-3)

Sample # and cycle	Load cycle			Unload cycle		
	E [GPa]	r^2	V_1 [%]	E [GPa]	r^2	V_1 [%]
A-LU-B2-cycle1	2.12	0.99	0.14	1.98	0.99	0.17
A-LU-B2-cycle2	1.91	0.99	0.13	1.91	0.99	0.19
A-LU-B2-cycle3	1.88	0.99	0.15	2.00	0.99	0.18
A-LU-B3-cycle 1	1.95	0.99	0.31	1.90	0.99	0.26
A-LU-B3-cycle 2	1.99	0.99	0.24	1.91	0.99	0.15
A-LU-B3-cycle 3	2.11	0.99	0.25	2.17	0.99	0.21
A-LU-B4-cycle 1	1.92	0.99	0.26	2.15	099	0.29
A-LU-B4-cycle 2	1.95	0.99	0.24	1.83	0.99	0.18
A-LU-B4-cycle 3	1.91	0.99	0.29	2.06	0.99	0.25

Table C3-2: Modulus of elasticity measurements and calculation coefficients for the applied strain of ~2% (Strain point B, Table 5-3)

Sample # and cycle	Load cycle			Unload cycle		
	E [GPa]	r^2	V_1 [%]	E [GPa]	r^2	V_1 [%]
A-LU-C4-cycle1	1.92	0.99	0.29	1.37	0.99	0.43
A-LU-C4-cycle2	1.73	0.99	0.73	1.39	0.98	0.77
A-LU-C4-cycle3	1.54	0.99	0.56	1.17	0.98	0.64
A-LU-C5-cycle 1	1.78	0.99	0.27	1.27	0.99	0.65
A-LU-C5-cycle 2	1.45	0.99	0.55	1.25	0.98	0.69
A-LU-C5-cycle 3	1.28	0.99	0.60	1.22	0.98	0.71
A-LU-C6-cycle 1	1.87	0.99	0.18	1.12	0.99	0.43
A-LU-C6-cycle 2	1.66	0.99	0.21	1.26	0.99	0.39
A-LU-C6-cycle 3	1.39	0.99	0.40	1.08	0.98	0.60

Table C3-3: Modulus of elasticity measurements and calculation coefficients for the applied strain of ~7% (Strain point C, Table 5-3)

Sample # and cycle	Load cycle			Unload cycle		
	E [GPa]	r^2	V_1 [%]	E [GPa]	r^2	V_1 [%]
A-LU-D1-cycle1	1.95	0.99	0.59	1.06	0.99	0.47
A-LU-D1-cycle2	1.58	0.98	1.09	1.31	0.98	0.67
A-LU-D1-cycle3	1.52	0.99	0.77	--	--	--
A-LU-D3-cycle 1	1.81	0.99	0.28	1.16	0.97	0.80
A-LU-D3-cycle 2	1.67	0.99	0.48	1.21	0.97	0.88
A-LU-D3-cycle 3	1.32	0.98	0.87	1.25	0.97	0.83
A-LU-D10-cycle 1	1.99	0.99	0.33	1.05	0.98	0.66
A-LU-D10-cycle 2	1.57	0.99	0.49	1.05	0.97	0.78
A-LU-D10-cycle 3	1.50	0.99		--	--	--

Table C3-4: Modulus of elasticity measurements and calculation coefficients for the applied strain of 8–10% (Strain point D, Table 5-3)

C4: Energy balance to check cavitation

Strain whitening has been linked to particle cavitation .Gent developed an expression that predicts the required critical internal pressure (or local dilatant stress) to cause cavitation (Equation 5-1) in an embedded particle in a material. It is possible to calculate the required stress to initiate cavitation in a material and therefore the strain whitening using an energy balance. Assuming that the material is linear elastic, the stored strain energy can be equated to the energy required for a phase transition towards a liquid material that can cavitate (Equation C4-1). The softer material favors then the formation of Taylor meniscus instabilities at regions of high stress from which fibrils/tendons can be drawn [338,339] and in turn leads to the creation of voids. Changes in temperature (ΔT), the material density (ρ), its volume (V) and the heat capacity (C^p) can describe the phase transition.

$$\rho\, V\, C^P\, \Delta T = \frac{V\, \sigma^2}{2E}$$

Equation C4-1: Energy balance between phase changes and strain energy

The required data to use this equation with MBS is scarce. However, reasonable approximations can be made using general data from polymers and available data for both MBS and DP-460NS. The modulus of Elasticity for MBS as reported by Zhang [340] was 101±19 MPa. Testing of the adhesive material using differential scanning calorimetry (TA Instruments DSC Model Q2000) has identified the glass transition temperature to be between 65 and 67°C. The exact heat capacity of MBS or DP-460NS has not been measured, but for polymers, this property typically varies between 0.318 and 2.08 kJ/(kg K) [94].

To calculate the stress to initiate cavitation using Equation C4-1 required some assumptions: it was assumed that the volume of the particle was equal to the volume of surrounding material causing the stress field; also the average density of the adhesive (1,200 kg/m^3, Table 5-1) was used for calculations. The exact value of the material heat capacity is unknown. This value was narrowed down using typical values of heat capacity for polymers (between 0.318 and 2.08 kJ/(kg K)). A temperature differential equal to the difference between room temperature (25°C) and the glass transition temperature in the material (66°C) was assumed for the calculation. This was a reasonable value considering the thermodynamic conditions of the test (adiabatic behavior without heat transfer) and the fact that at the glass transition temperature, the material can develop the required soft phase that can initiate a cavitation process. In this particular material, the cavitation stress predicted by the energy balance (Equation C4-1) was between 255 and 652 MPa. In this case, the calculated values need to be interpreted as the stresses around an inclusion or defect and not the average across the bulk cross section measured during uniaxial tension. In the case of the MBS toughening material, the required stress for cavitation from the energy balance was approximated in the range of 62 to 158 MPa.

An alternate method to predict cavitation based on an energy balance was proposed. With the measured average stresses and the calculated tip concentration factors, it was possible to demonstrate that there was enough strain energy around crack tips to propitiate the material phase transition required for the development of cavitation. The predicted stress range from the energy balance (255 to 652 MPa) was in agreement with the calculated stresses using the stress concentration factors (300 to 800 MPa) and the predictions of Equation 5-1.

Appendix D

Macroscopic Optical Technique

D1: Preliminary study

A preliminary study was conducted to determine the best method to detect and quantify the changes in color for a region. Different methods for image analysis were considered to identify and quantify changes in image pixel values, such as histograms (Figure D1-1), segmentation and mask operations. Although they are well-established methods, they were either computationally expensive (histograms) or not well suited to compare images in which deformations play a significant role (mask operations), and pixel correspondence between one image and the next is not 1 to 1. To easily differentiate between changes, the use of the mean average value of the pixels in a specific region was deemed to be practical. Conceptually it clearly represents an average of the histogram changes in time while being computationally efficient and eliminating the 1 to 1 pixel correspondence problem.

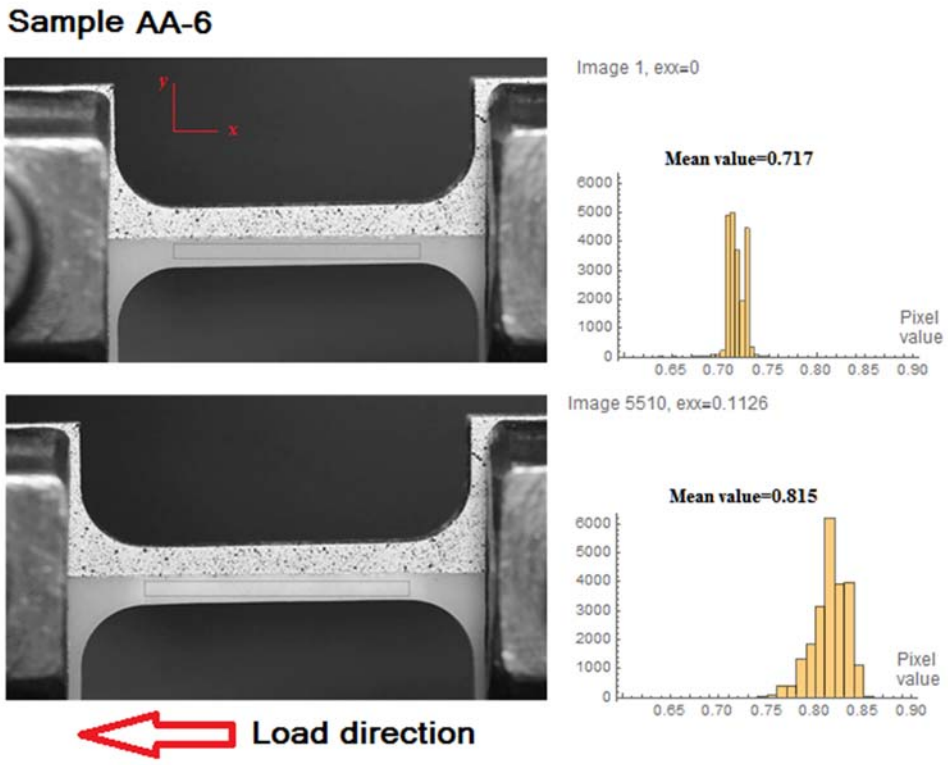

Figure D1-1: Pixel color histogram changes with strain

To define the average pixel value in a region two methods were considered. Firstly, decomposition of pixel color into three different signals followed by calculation of the average value in the area of analysis for each signal. Secondly, implementation of the Jia method [333], in which the color is treated as a vector; in this method, the magnitude of the vector represents the illumination component (lighter or darker) while the angle represents the actual color (blue, red, etc.). Figure D1-2 presents analysis results for the same area using signal decomposition as well as color vector analysis for a sample tested during the preliminary study. In both cases the magnitude of the changes for all practical purposes was identical; the absolute magnitude of the measured deltas (final value minus initial value) was around 8 to 10% (Table D1-1).

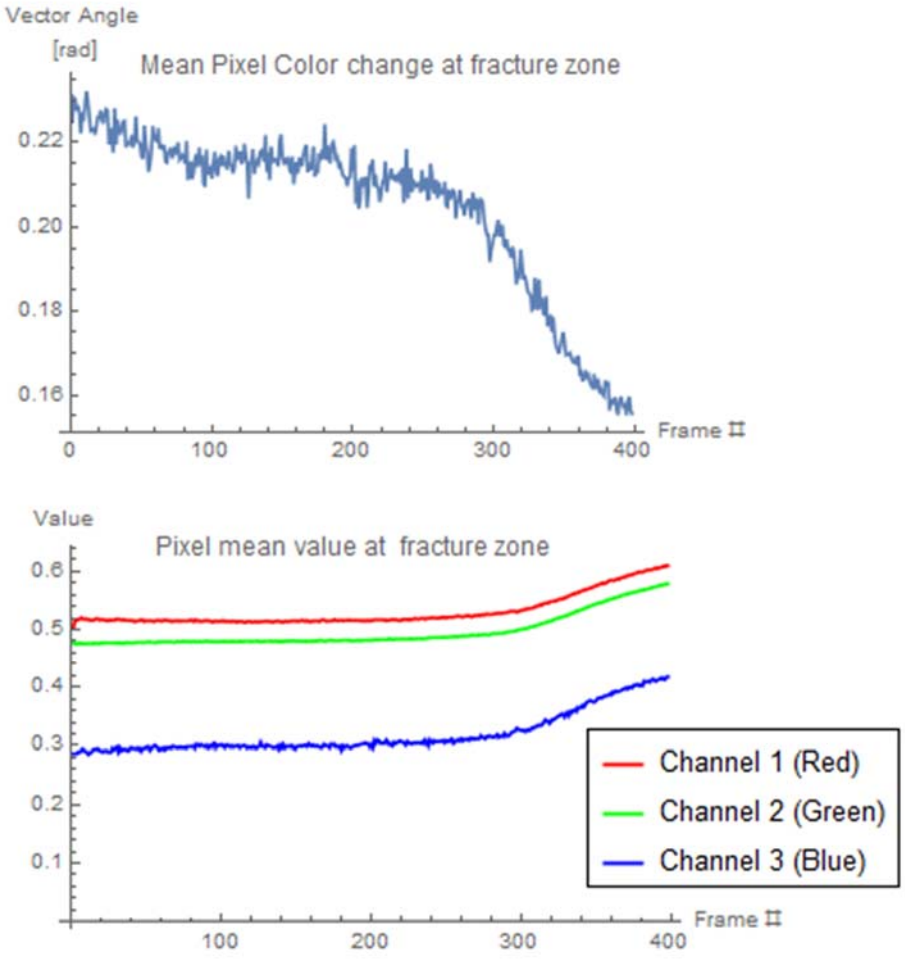

Figure D1-2: Mean pixel value at failure zone. Color vector approach (left hand), RGB decomposition (right hand)

Method	Quantity	Initial	Final	|Δ|
RGB	R	0.51	0.60	0.09
	G	0.47	0.56	0.09
	B	0.29	0.38	0.09
Color vector	Angle [Rad]	0.225	0.155	0.07

Table D1-1: Figure D1-2 change in color results

Pragmatically the change detected in any of the channels was comparable and hence the analysis could be carried using any of the three signals. A priori the measured intensity in the red channel was more significant (higher pixel value) without a significant level of noise hence this signal was used for analysis in this material.

Besides analysis technique, numerical methods that use discretization require convergence verification in the results. To verify the impact of the discretization in the studied area, a convergence analysis was performed by dividing the test gauge zone of the sample into 5,10,15,20 and 40 sections, then the implemented algorithm for analysis was used to calculate the mean pixel color value for each individual zone, and the results were compared. The method consistently identified similar levels of color change in correspondent areas of the material (Figure D1-3); independently of the number of divisions used for the analysis. Also, the code properly distinguished the area containing the fracture zone, as the location with the most significant change in mean color. The same amount of net change was predicted for the fracture zone independent of the number of zones used for the analysis (Figure D1-4), demonstrating the robustness of the method.

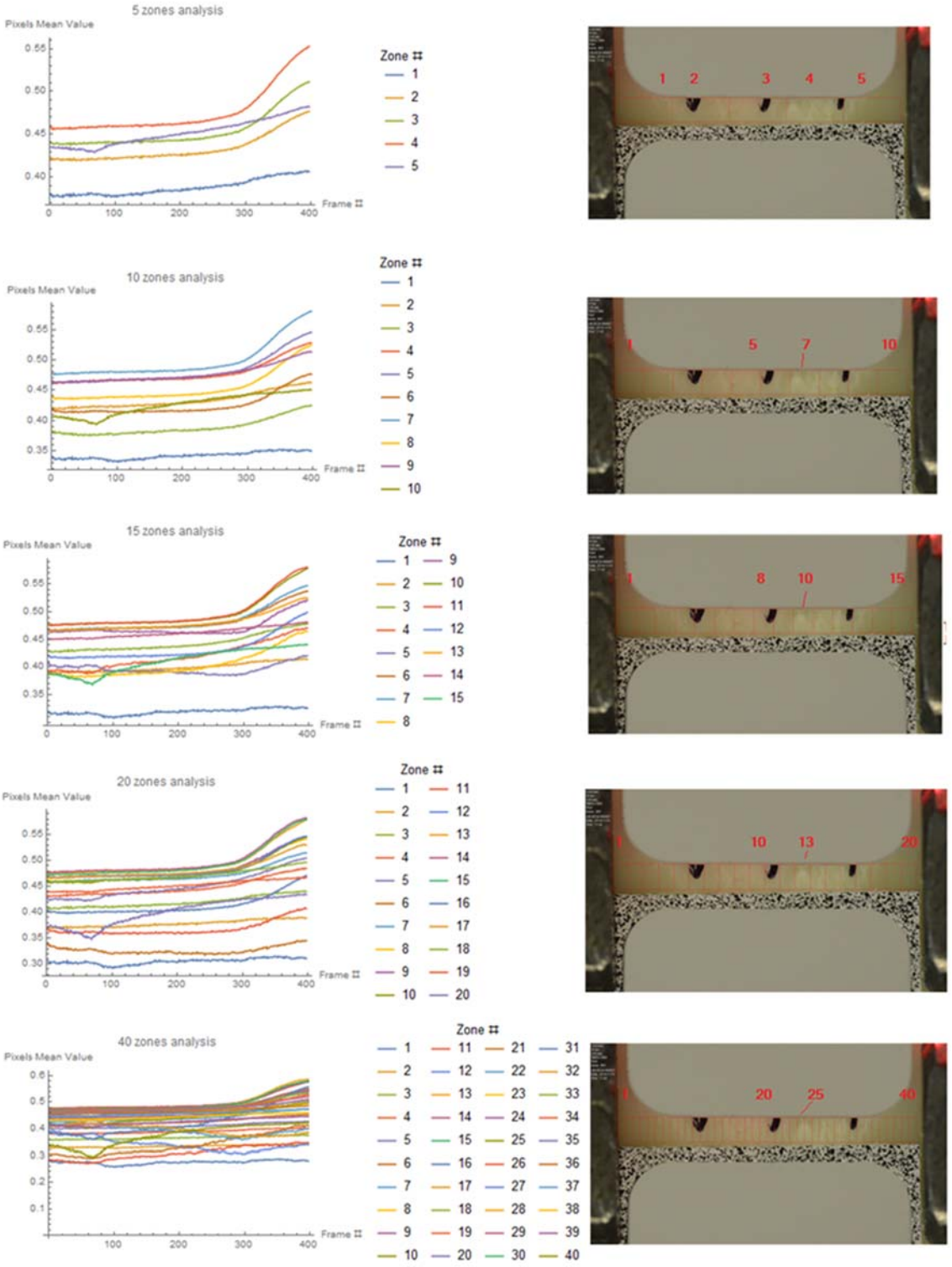

Figure D1-3: Convergence analysis

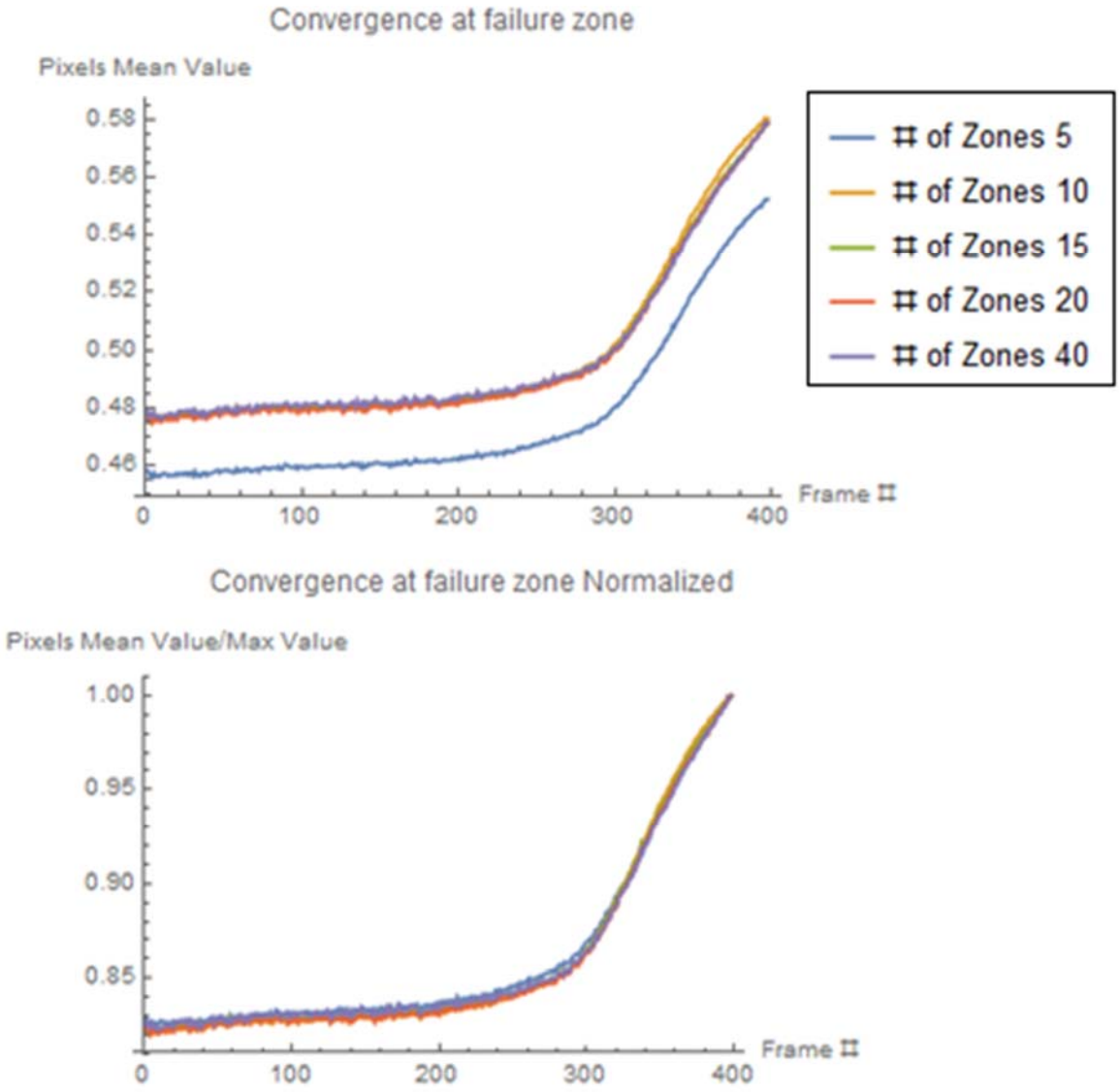

Figure D1-4: Failure zone convergence. Data from the analysis (left hand), and normalized results (right hand)

D2: Fractography

Study of fracture surfaces is not an easy task; it is time-consuming and requires insight and skill to correctly identify the relevant features. With current image processing tools, this job can be expedited, but the operator needs to assure that the measured features are not significantly distorted and that the

results are reasonable. This section provides a brief summary of the fractography process done to arrive at the results summarized in Table 6-3 of the main text.

The first task for identification of features in fracture surfaces is to accurately determine the working area; this is typically done by cropping the image to determine the area of interest (AOI). Once an AOI is established, features such as cracks and voids can be identified and quantified by individually selecting pixels or by using selection tools that can isolate the contour of the feature. In this work, the low magnification images were used to manually identify voids and cracks to establish a baseline value. The onboard software of the microscope was used with a threshold value to separate and quantify the features of interest. Additional processing was performed with the aid of Image J. Morphological operations in a specific order (image processing protocol) were performed to isolate and quantify the features of interest (Table D2-1). Figure D2-1 illustrates typical results for one of the samples.

Protocol	Description
Manual	Manual selection of features with mouse and lasso tool. Features identified in three different layers using GIMP
Color threshold	Onboard Keyence software. Use 4 different shades of gray to isolate the relevant features
Protocol 1	Sharpening, despeckle, contrast enhance, remove outliers, morphological top hat w element radius > 20, 8-bit conversion, binarization
Protocol 2	From previous protocol add closing operation follow by despeckling, run to times to eliminate textures
Protocol 3	From protocol 1 after removing outliers, gray attribute filtering closing with a minimum area of 122, morphological gradient r=2, 8-bit conversion, threshold of darker features
Protocol 4	From protocol 1 after removing outliers, subtract background, sharpen, binary, closing operation and despeckle 2x

Table D2-1: Image processing protocols

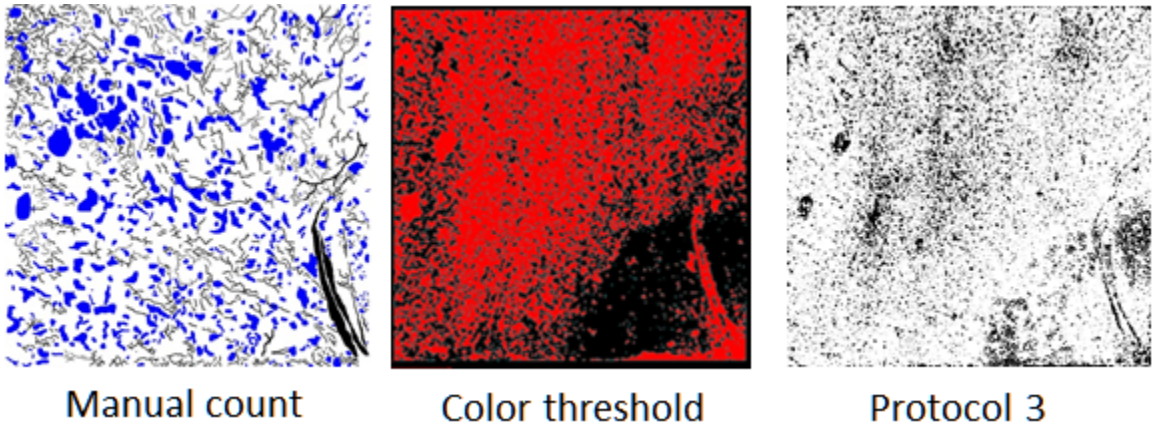

Figure D2-1: Image feature identification for sample AA-7 under three different methods

To assure the quality of the results, 3 typical features per image were used as a control. The typical features selected were a micro-void (r< 10µm), a void (r>20µm) and a crack. Figure D2-2 and Table D2-2 illustrate the process. Table D2-3 summarizes the quantification of damage in the observed fracture surfaces.

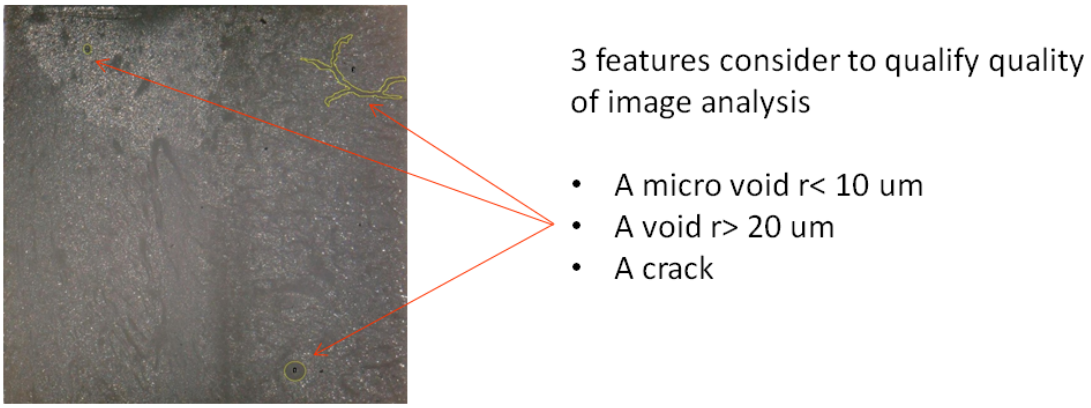

Figure D2-2: Image features for image processing quality control

Sample		Area of feature			Differences [%]	
		Original image (A)	Prot. 1 (B)	Prot. 2 (C)	A vs. B	A vs. C
Feature 1	AA-6	6083.069	6861.136	6486.249	12.79	6.63
	AA-7	17881.394	24021.05	22210.276	34.34	24.21
	AA-8	14594.701	15266.661	16394.393	4.60	12.33
Feature 2	AA-6	9626.811	17414.554	20321.695	80.90	111.09
	AA-7	56480.591	46882.073	44696.412	16.99	20.86
	AA-8	2668.906	2290.704	2199.076	14.17	17.60
Feature 3	AA-6	2687.868	2426.154	2157.368	9.74	19.74
	AA-7	1952.241	1358.081	2249.321	30.43	15.22
	AA-8	40454.994	52284.439	46441.381	29.24	14.80

Table D2-2: Image features for image processing quality control

Sample #	80 x					500 x			
	Microscope	GIMP	Image J			Image J			
	Color threshold processing	Manual Selec.	Prot. 1	Prot. 2	Prot. 3	Prot. 1	Prot. 2	Prot. 3	Prot. 4
AA-6	0.32	0.31	0.58	0.41	0.20	0.63	0.49	0.17	0.33
AA-7	0.66	0.38	0.64	0.49	0.16	0.55	0.35	0.40	0.35
AA-8	0.61	0.34	0.75	0.48	0.16	0.50	0.35	0.10	0.39

Table D2-3: Damage calculations from image features in tested samples

D3: Changes in color measurements

D3-1 Changes in color

The three following figures summarize the changes in color measurements. The first two figures (Figure D3-1 and D3-2) depict the color history in two of the tested specimens for the material while the third (Figure D3-3) one describes the calculated change in mean average pixel color with strain for all zones used for analysis along the area of interest in all tested samples. Following these results, there is a detailed description of measured noise in the system.

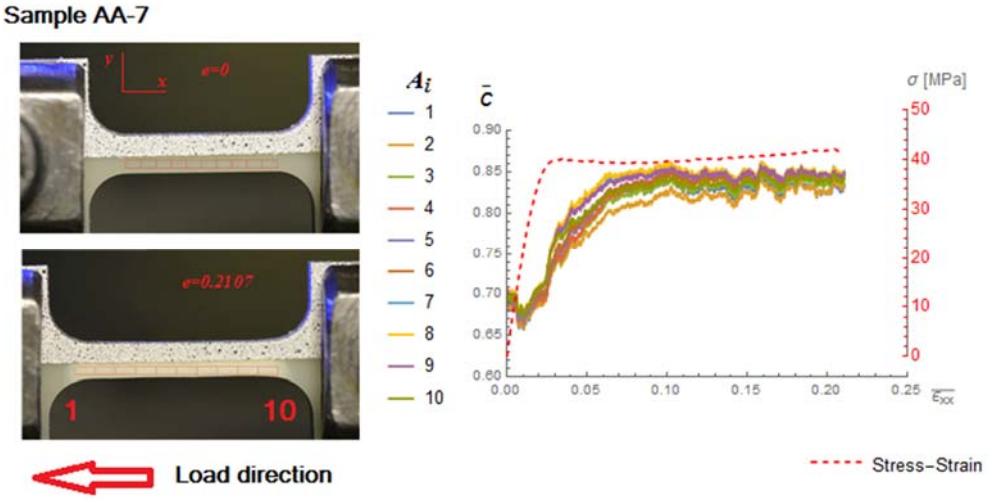

Figure D3-1: Color history DP-460NS, sample AA-7

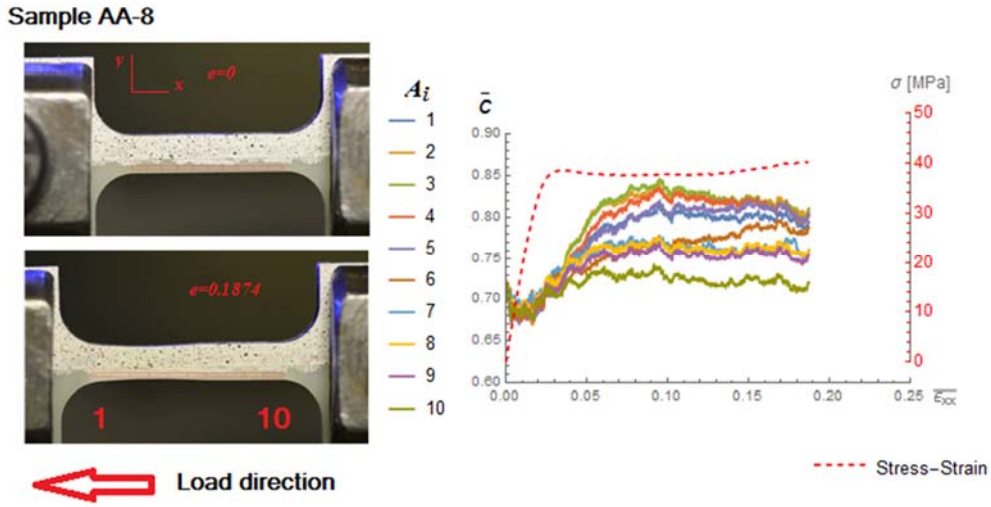

Figure D3-2: Color history DP-460NS, sample AA-8

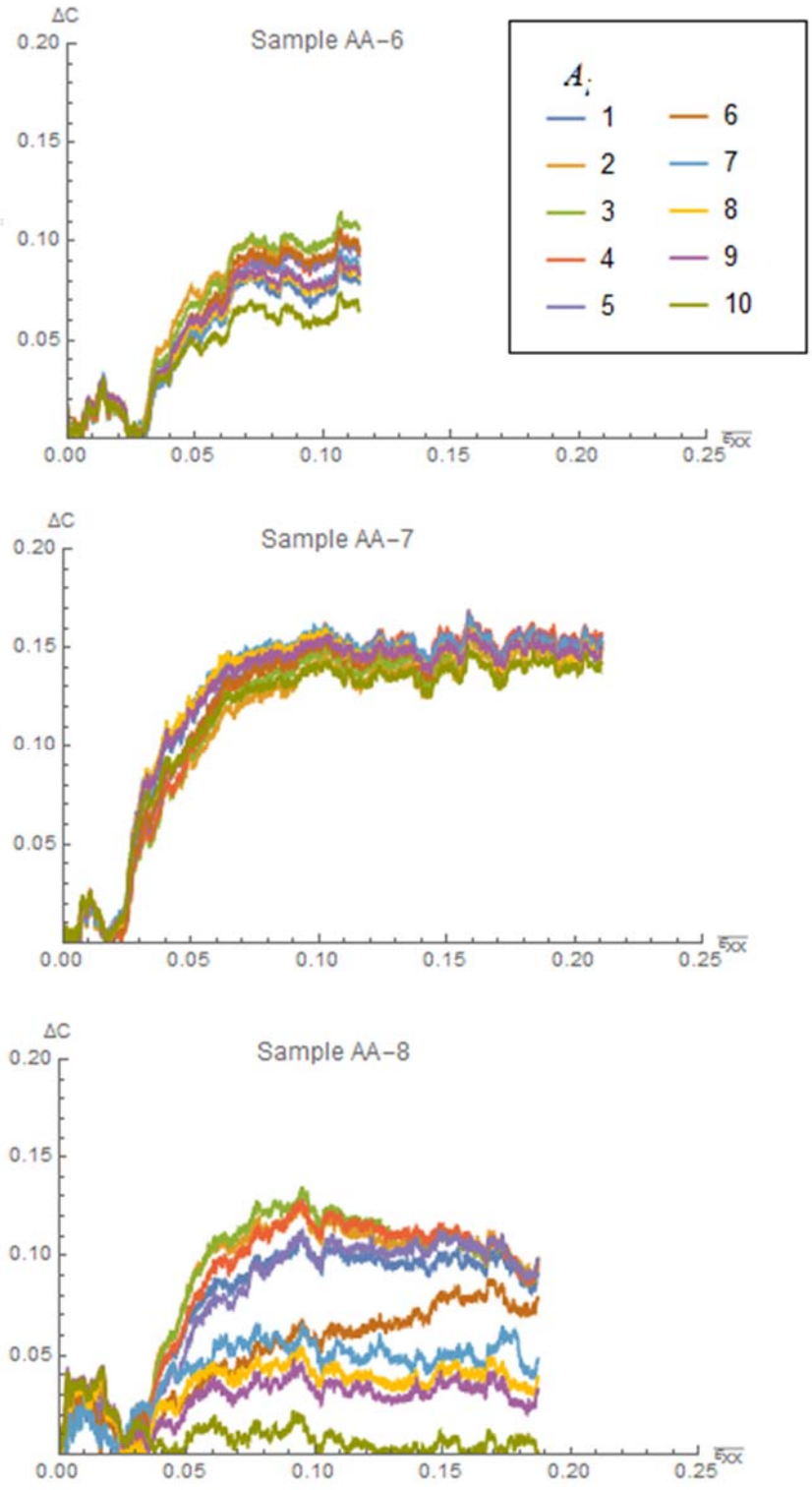

Figure D3-3: Mean pixel color change (channel 1) with strain in DP-460NS, all tested samples

D3-2 System noise and illumination variability

Noise in the system had to be understood and quantified so only relevant changes in color were acknowledged avoiding then false positives. Noise in the system can be introduced by sensor drifting and/or saturation in the signal, besides variations in illumination that can affect the image. System noise was measured using the standard deviation of the average pixel value. The measurement was implemented in two regions of the image background: above and below the sample test gauge. Figure D3-4 illustrates the areas of interest for noise in sample AA-6. Table D3-1 summarizes the measured average pixel value with its standard deviation in the regions tested for noise. The average noise was used to calculate the signal to noise ratio (Equation D3-1, Figure D3-5) for the measurements. This was used to determine the relevance of the change in the color history (Figure D3-5). Besides the relevance of the signal in comparison to noise, the variability of color in time at each one of the zones used for analysis was considered. The measurement was done at the correspondent area on the speckle pattern. Since the speckle zone is relatively unchanged during the test, the changes in mean value were measured (Figure D3-6)

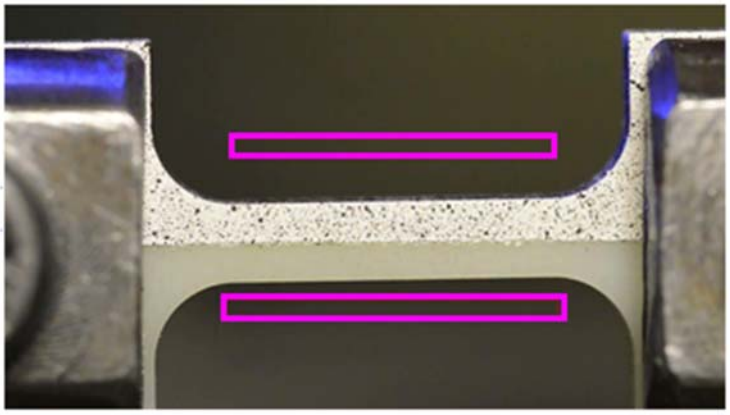

Figure D3-4: Areas of interest for noise analysis and signal drifting (Sample AA-6)

Sample	AA-6	AA-7	AA-8
Upper	0.219±0.013	0.214±0.016	0.207±0.012
Lower	0.201±0.012	0.209±0.015	0.205±0.012
System noise		0.013±0.002	

Table D3-1: Measurements of noise in the images, the average pixel value ± standard deviation

$$SNR = 20 * Log_{10} \frac{Signal}{Ref.value}$$

Equation D3-1: Signal to noise ratio definition

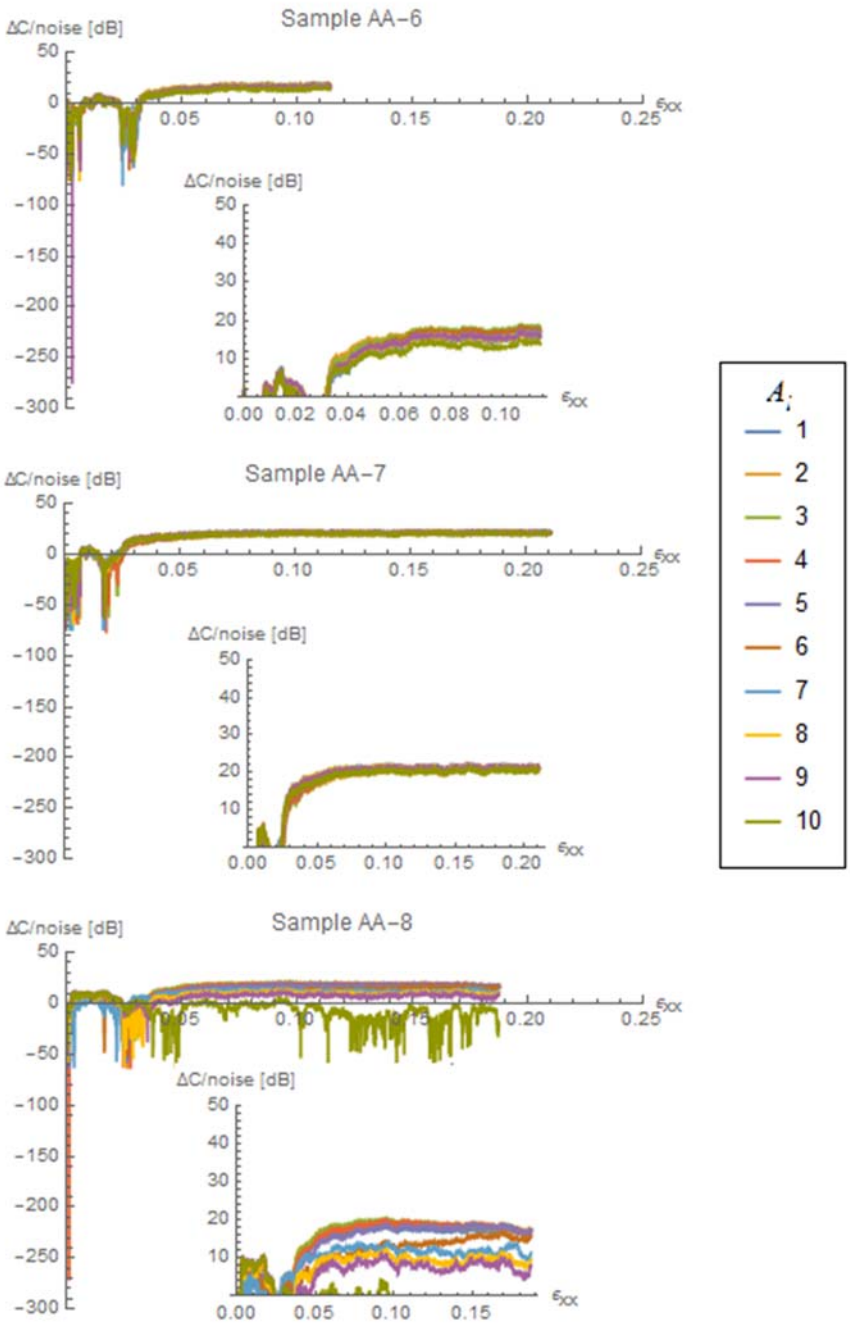

Figure D3-5: Signal to noise ratio in the measurements

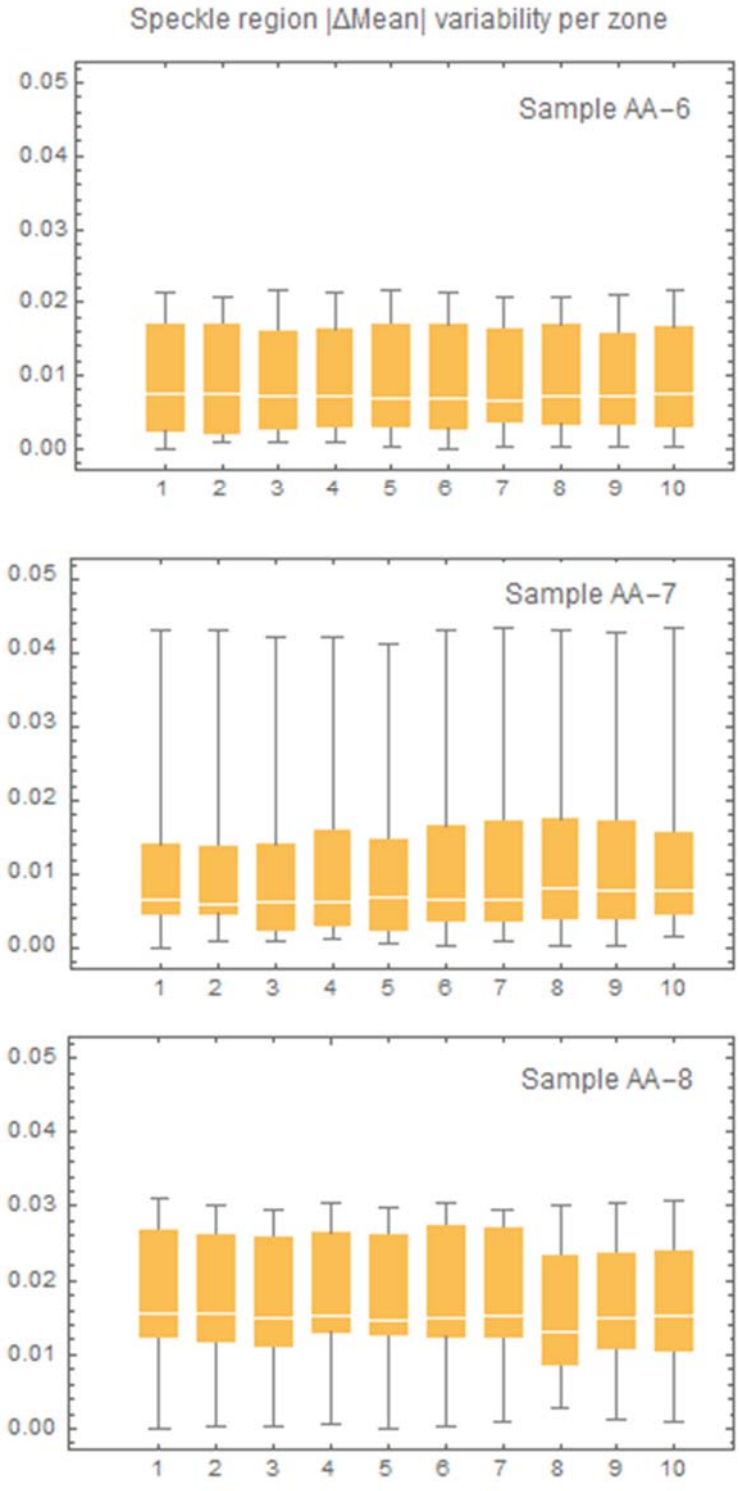

Figure D3-6: Speckle region absolute mean changes for each sample

D3-3 Sensor drift

The drift of the system was verified by calculating the average pixel value in the noise region as well as in the speckle pattern area of the sample test gauge. Average pixel value typically drifted towards a lower value by 0.058.

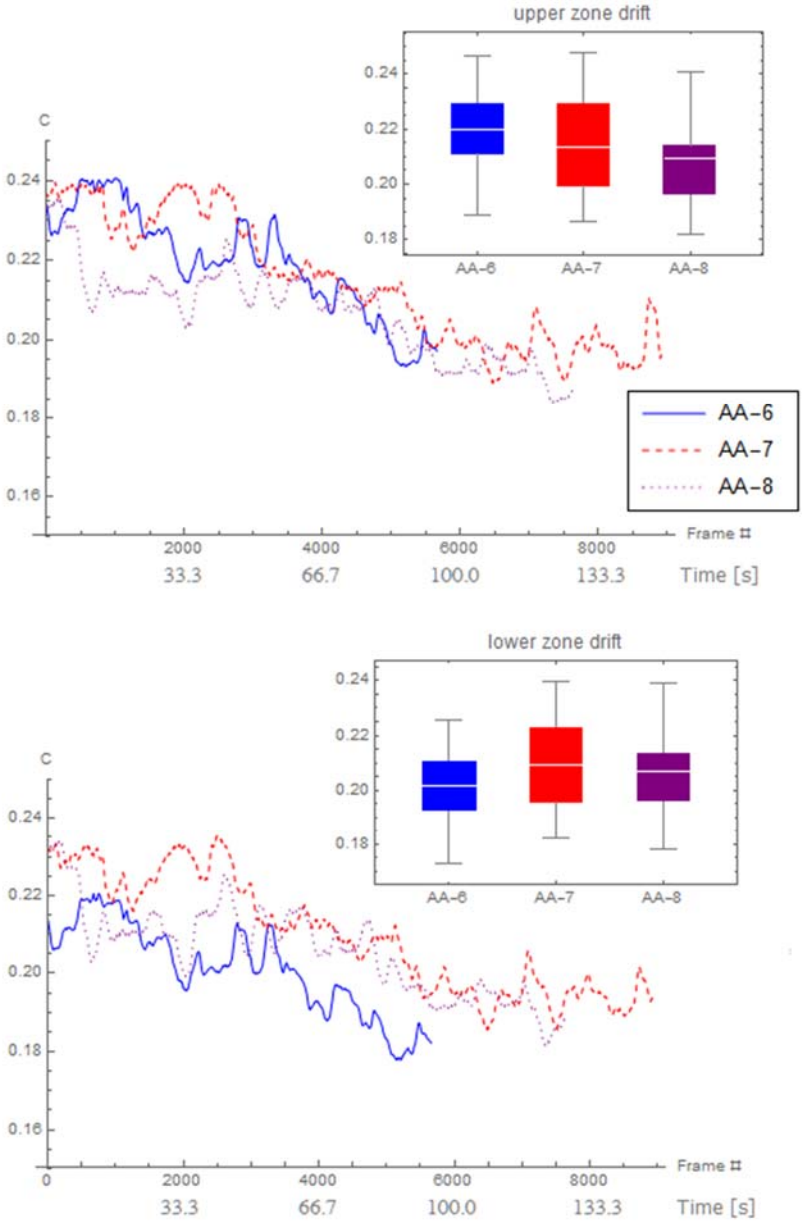

Figure D3-7: Signal drift in time at the tested zones for noise (Moving average 50 points, unfiltered data for inserts)

D4: DIC

This section verifies the quality of the DIC analysis and summarizes the DIC measurements used to calculate volumetric damage in the coupons tested for this study and summarizes the strain values at the measurement points.

D4-1 DIC quality and expected measurement error

In the first instance, the digital extensometer results used to define the stress-strain curve response of the material was compared to stress-strain curves obtained with the use of contact extensometer (Figure D4-1, left hand). The strain response was measured using digital extensometers from tracker software[341] and compare against DIC results (Figure D4-1, right hand).

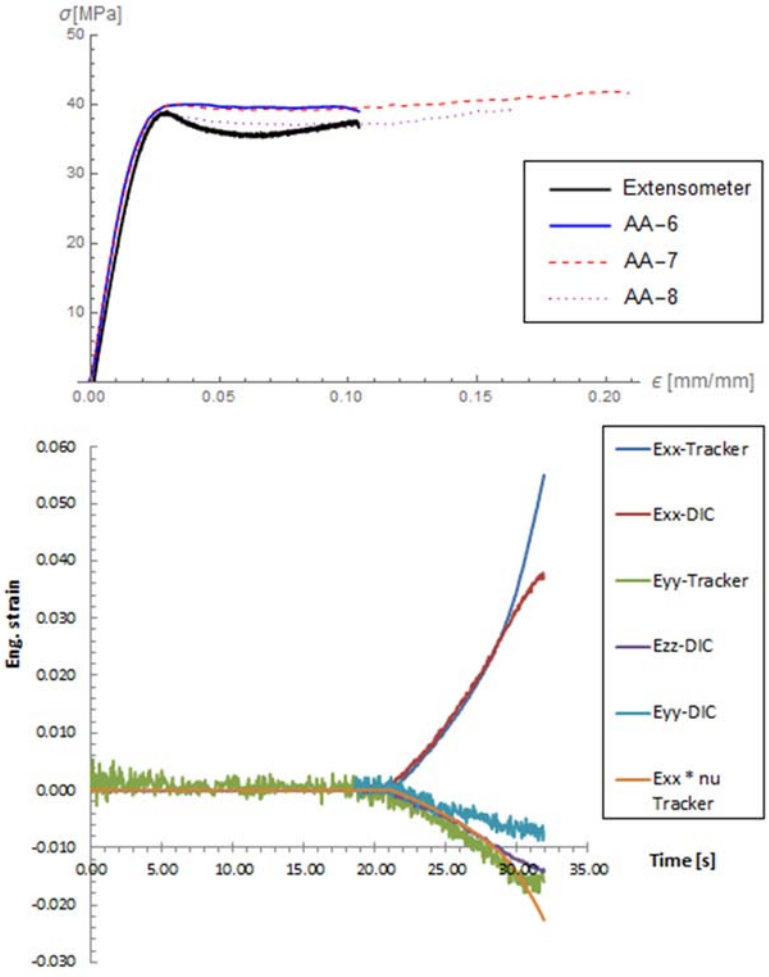

Figure D4-1: DIC quality control

Data for this study was collected using a single camera setup for each view; this requires that the material deforms in a plane perpendicular to the axis of the camera. As is noticeable in some of the sample images (Figure 6-5 in the main text, and Figures D2-1 and D2-2 in this appendix) the material demonstrated large deformations. Such deformations induce out-of-plane translations (a1-errors) as well as out-of-plane rotations (a-2 errors) as explained by Sutton [170]. For error calculation, the lens distance to the specimen was approximately 600 mm. Strains were also calculated by direct measuring in the images previous to failure (Tables D4-1 to D4-3). Additional systemic errors can be introduced by the quality of the speckle pattern affecting the interpolation routines used for calculation [171]. Although there is no direct way to calculate or correct this error that the authors know of, the analysis included the use of low pass filters and high interpolation orders to minimize the errors that could be induced by the bi-modal distribution of the speckle pattern as recommended by Sutton [171].

Camera	Out of Plane δ [mm]	Out of plane rotation angle [Deg]	a-1		a-2		Expected strains	
			e_{yy}	e_{xx}	e_{yy}	e_{xx}	Axial	lateral
A	0.105	5.56	-1.7E-4	-1.7E-4	-4.7E-4	-5.64E-3	0.107	-0.008
B	0.180	1.00	-2.9E-4	-2.9E-4	-8.40E-5	-3.2E-4	0.107	-0.061

Table D4-1: Sample AA-6, DIC errors and expected strains previous to failure

Camera	Out of Plane δ [mm]	Out of plane rotation angle [Deg]	a-1		a-2		Expected strains	
			e_{yy}	e_{xx}	e_{yy}	e_{xx}	Axial	lateral
A	0.149	5.41	-2.4E-4	-2.4E-4	-4.5E-4	-5.3E-3	0.178	-0.128
B	0.119	1.00	-1.9E-4	-1.9E-4	-8.40E-5	-3.2E-4	0.178	-0.077

Table D4-2: Sample AA-7, DIC errors and expected strains previous to failure

Camera	Out of Plane δ [mm]	Out of plane rotation angle [Deg]	a-1		a-2		Expected strains	
			e_{yy}	e_{xx}	e_{yy}	e_{xx}	Axial	lateral
A	0.278	5.12	-4.5E-4	-4.5E-5	-4.3E-4	-4.9E-4	0.145	-0.153
B	0.370	1.00	-6.0E-4	-6.0E-4	-8.40E-5	-3.2E-4	0.145	-0.179

Table D4-3: Sample AA-8, DIC errors and expected strains previous to failure

D4-2 Strain measurements

Figure D4-2 illustrates a summary of strain values at the measurement points using DIC analysis. The figure includes axial strains (e_{xx}) for the frontal view (Cam A) and side view (Cam B). The figure includes the lateral strains (e_{yy} and e_{zz}) as well as the shear strains (e_{xy} and e_{xz}).

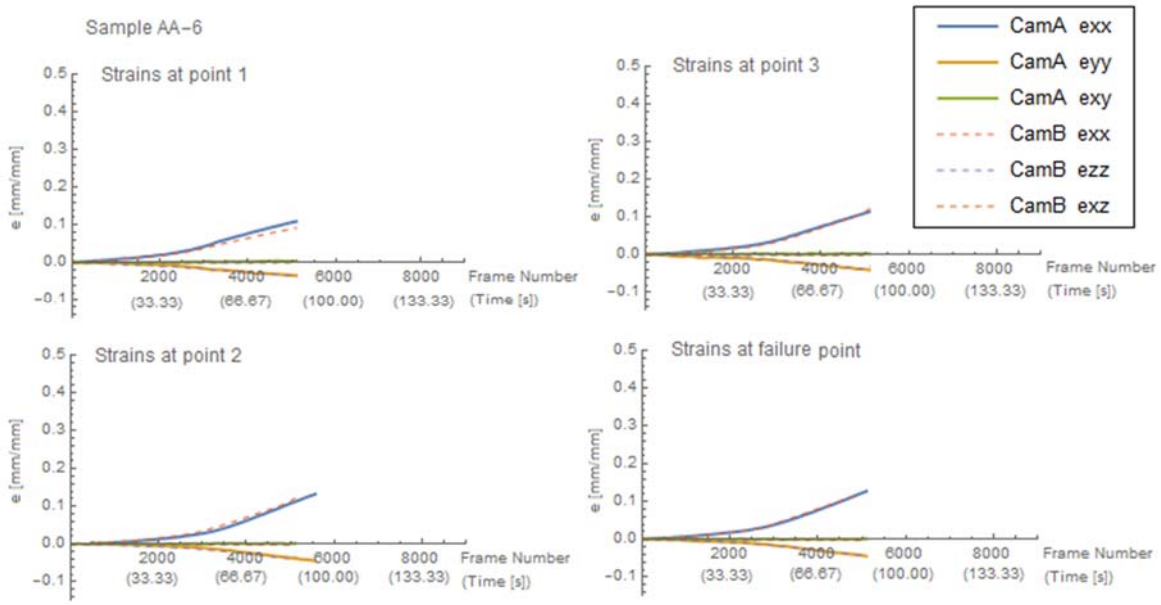

Figure D4-2: Strain measurements from DIC

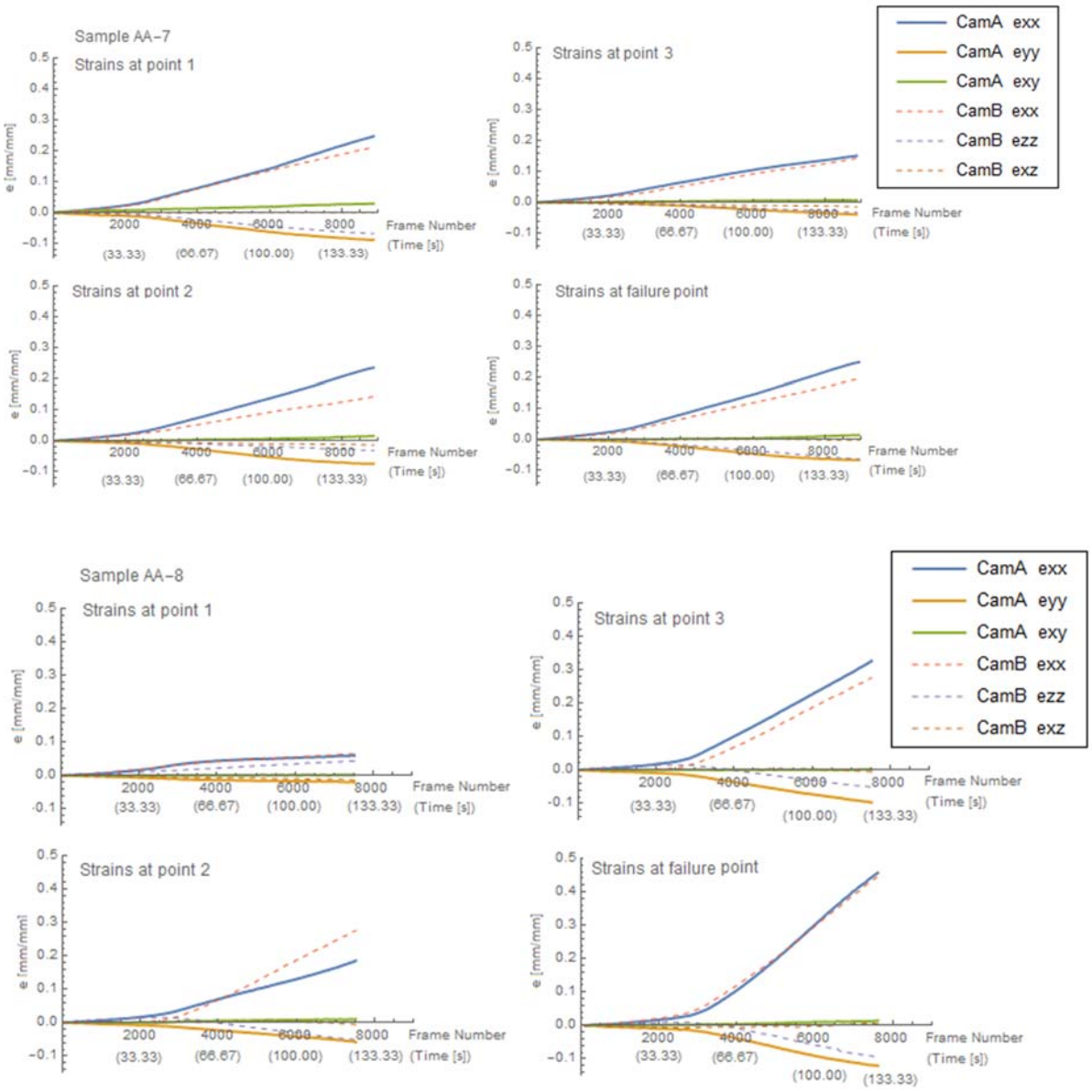

Figure D4-2: Strain measurements from DIC (continued)